

**Stable isotope development in ground ice along an alpine tundra slope
in the Ogilvie Mountains, Yukon Territory**

by

Casey Alexander Buchanan

A thesis submitted in partial fulfillment of the requirements for the degree of

Master of Science

Department of Earth and Atmospheric Sciences
University of Alberta

© Casey Alexander Buchanan, 2021

Abstract

Stable isotopic ratios of oxygen and hydrogen ($\delta^{18}\text{O}$ and δD) from ground ice have been used to reconstruct paleoclimate temperatures spanning the Late Pleistocene and Holocene in subarctic and arctic regions. This is possible due to the strong relations between the isotopic composition of atmospheric moisture and air temperature. Pore and texture ice, common forms of ground ice in permafrost regions, have been used to qualitatively infer the timing of centennial- and millennial-scale climate fluctuations spanning the Holocene and late Pleistocene. However, these records can be difficult to interpret because their source waters may become isotopically altered by local hydrological and phase-change (water-ice) processes before undergoing long-term preservation into the underlying permafrost record. The manifestations and relative contributions of these “secondary” isotopic modifications, which occur within the active layer and underlying transition layer, are poorly understood. In this study, we investigate spatially-varying processes that drive isotopic development in pore and texture ice from a catena within the Southern Ogilvie Mountains, Yukon Territory. The objectives of this study are to (1) establish the history of local permafrost formation using geochemical and traditional cryostructure analyses; (2) examine the stable isotopic relations between the active layer, transition layer, and relict pore and texture ice; (3) assess the impacts of local processes on the stable isotope development of pore and texture ice; and (4) build upon existing evidence for 20th century warming captured by stable isotope records in pore and texture ice

Preface

This thesis consists of six chapters, of which chapter 5 will ultimately become a manuscript for publication. Chapter 5 is co-authored by myself (Casey Buchanan) and collaborating researchers Drs. Duane Froese, Trevor Porter, Jeffrey Kavanaugh. Duane Froese guided the structure of the manuscript, the methodology, and provided feedback and edits. Trevor Porter and Jeffrey Kavanaugh provided feedback and edits. I (Casey Buchanan) wrote the manuscript and created the figures. The results of this study also contain modified Copernicus Climate Change Service information 2022. Neither the European Commission nor ECMWF is responsible for any use that may be made of the Copernicus information or data it contains.

The manuscript is in preparation to be submitted for publication at a journal to be determined as: Buchanan, C.A.; Froese, Duane G., Kavanaugh, J.L., Porter, T.J. Stable isotope development in ground ice along an alpine tundra slope in the Ogilvie Mountains, Yukon

Acknowledgements

I would first like to thank my supervisor, Dr. Duane Froese, for everything he has taught me over the last several years, for the innumerable experiences I have had in the field and in the lab, support during times of difficulty, and funding to make my work possible. Through my experiences with his lab group, I have engendered an enduring passion for permafrost science and the Canadian North. I thank Brielle Andersen, Dr. Sophie Norris, and Alejandro Alvarez, for your invaluable assistance during some of the hardest field work I think I've experienced and also some of the most beautiful. I'll always remember the spirit of adventure during our hikes under the midnight sun. Thank you to Alistair Monteath for his time and work processing tephra from my sites, for teaching and assisting me with macro-fossil selection for radiocarbon dating, and for his assistance on other lab activities, and to Sasiri Bandara for teaching me the ropes around the lab when I first started with the lab group during my undergraduate degree. Sasiri also taught me many of the primary lab techniques for permafrost sampling and isotope work that I used in this thesis. I am also thankful for the advice, support, and mentorship of Drs. Alberto Reyes and Britta Jensen during the directed studies I took with them, for always being there to offer advice, and who reminded me to pump the breaks if I began taking on too much. Thank you to all of the wonderful people in my lab community for your friendship, advice, and support, and all of the fun times that we have had together. And on that note, a special shout-out to the DnD group who made the COVID years more bearable. Lastly, I thank my parents for everything they have done to support me and encourage me.

Contents

LIST OF TABLES	vii
LIST OF FIGURES	viii
1. INTRODUCTION	1
1.1. Introduction	1
1.2. Objectives	3
1.3. Thesis Organization	3
References	4
2. LITERATURE REVIEW	8
2.1. Introduction	8
2.2. Methods of Ground Ice Characterization	10
2.2.1. Visual characterization	10
2.2.2. Physical properties.....	10
2.3. Classification of Ground Ice	15
2.3.1. Non-genetic classifications.....	16
2.3.2. Genetic classifications	19
2.4. Stratigraphic Division of Permafrost Soils	23
2.5. Stable Isotopes in Permafrost	25
2.5.1. Isotopic fractionation.....	26
2.5.2. Co-isotopic relations in precipitation	28
2.5.3. Co-isotopic relations in ice.....	29
2.5.4. Stable isotope development in ground ice.....	32
References	40
3. REGIONAL SETTING AND SITE DESCRIPTIONS	51
3.1. Geography	51
3.2. Bedrock Geology and Quaternary History	52
3.2.1. Bedrock geology.....	52
3.2.2. Quaternary history	54
3.3. Climate	55
3.4. Soils, Vegetation and Hydrology	55
3.5. Collection Area Description	57
References	60
4. METHODOLOGY	63
4.1. Water Sample Collection	63
4.2. Permafrost Core Recovery, Subsampling, and Depth Corrections	63
4.3. Thaw Depth Measurement	64

4.4. Thaw Depth Modeling.....	64
4.5. pH and Electrical Conductivity.....	65
4.6. Gravimetric Water Content	66
4.7. Stable Isotope Analysis	66
References	66
5. STABLE ISOTOPE DEVELOPMENT IN GROUND ICE ALONG AN ALPINE TUNDRA SLOPE IN THE OGILVIE MOUNTAINS, YUKON TERRITORY	68
5.1. Introduction	68
5.2. Regional Setting and Site Description	71
5.3. Materials and Methods	74
5.3.1. Water sample collection	74
5.3.2. Permafrost core recovery, subsampling, and depth corrections	75
5.3.3. Thaw depth measurement.....	75
5.3.4. Thaw depth modeling.....	76
5.3.5. Stable isotope analysis.....	76
5.3.6. Ice and water content.....	77
5.3.7. Electrical conductivity and pH	77
5.4 Results.....	78
5.4.1. Precipitation and basal active layer water stable isotopes and geochemistry.....	78
5.4.2. Stratigraphic framework.....	80
5.4.3. Ground ice geochemistry and stable isotopes.....	82
5.4.4. Thaw depth modeling.....	99
5.5. Discussion.....	100
5.5.1. Isotopic development of 2019 basal active layer waters	100
5.5.2. Geochemical and isotopic development of the 2018 active layer ice.....	104
5.5.3. Cryophysical, geochemical, and isotopic development of hillslope ground ice	110
5.5.4. Cryophysical, geochemical, and isotopic development of ground ice in the degrading polygon area and fen	115
5.5.5. Role of down-hill enrichment in the isotopic development of ground ice	118
5.5.6. Modern climate change and recent stable isotope record formation	119
5.6. Conclusions	120
References	122
6. CONCLUSIONS AND FUTURE WORK.....	127
6.1. Conclusions	127
6.1.1. Cryostratigraphy and History of Ground Ice Formation	127
6.1.2. Formation of stable isotopic patterns in pore and texture ice.....	128
6.1.3. Influence of downhill basal active layer water $\delta^{18}\text{O}$ increase on pore and texture ice isotope chemistry	130
6.1.4. Evidence of recent warming in stable isotope records of pore and texture ice	130
6.2. Future Work.....	131
Bibliography.....	132
APPENDIX.....	145
Appendix 1. Stable isotope data of BS19 ground ice.....	145

Appendix 2. September 2019 Active Layer Profile Water Stable Isotopes.....	159
Appendix 3. September 2019 Basal Active Layer Waters.....	161
Appendix 4. September 2019 Thaw Depths.....	161
Appendix 5. Electrical Conductivity, pH, and GWC of Permafrost Ice.....	162
Appendix 6. Core Names and Designations.....	171
Appendix 7. Methodology for correcting core segment depths.....	171
Appendix 8. Methodology for correcting subsample depths.....	173
Appendix 9. Local Meteoric Water Line.....	173
Appendix 10. Correcting a flipped core segment at Site 3.....	174
Appendix 11. Methods for modeling 2018 thaw depth using thawing degree-days.....	175
Appendix 12. R Studio script for cumulative TDD calculations.....	179

LIST OF TABLES

- Table 5.1. δD - $\delta^{18}\text{O}$ regressions of stratigraphic units for Site 1, Site 2, Site 3, and Site 4.
- Table 5.2. $\delta^{18}\text{O}$ values of 2019 basal active layer waters, 2018 first ice, and average relict permafrost ice for each of the four sites
- Table 5.3. Table 5.3. δD - $\delta^{18}\text{O}$ regressions of relict permafrost ice and basal waters in Fig. 5.16.
- Table 5.4. Summary of TDD-modeled 2018 ALT_{max} and isotope-estimated 2018 ALT_{max} .

LIST OF FIGURES

- Figure 2.1. Circumpolar map of permafrost distribution (National Snow and Ice Data Center).
- Figure 2.2. A representative “trumpet curve” ground temperature profile with anatomical labels for various thermal characteristics (from Osterkamp and Burn, 2003).
- Figure 2.3. Ground temperature time series at 50cm depth in peatland permafrost near Chapman Lake, Ogilvie Mountains, Yukon Territory.
- Figure 2.4. Non-genetic classification of cryostructures in minerogenic matrix permafrost (from Murton and French, 1994).
- Figure 2.5. Representative cryofacies classifications of typical ground ice from the Tuktoyaktuk Coastlands (from Murton and French, 1994).
- Figure 2.6. Micro-cryostructural classification (from Kanevskiy et al., 2011).
- Figure 2.7. The succession of permafrost accumulation following lake drainage in A) continuous permafrost zones, and B) discontinuous permafrost zones (from Kanevskiy et al., 2014).
- Figure 2.8. Representative profile of 1) active layer, 2) transition layer, 3) intermediate horizon, 4) relict permafrost (from French and Shur, 2010).
- Figure 2.9. Example of modelled freezing regression line of slope (from Jouzel and Souchez, 1982).
- Figure 2.10. Example of “C”-shaped $\delta^{18}\text{O}$ profile in the active layer within continuous permafrost (from Michel and Fritz, 1982).
- Figure 3.1. Regional map of the Yukon showing study site locations and general boundaries of permafrost zones (adapted from Scudder, 1997).
- Figure 3.2. Bedrock geology within the Chapman Lake region (adapted from Yukon Geological Survey bedrock map for NTS regions 116B and 116C).
- Figure 3.3. Extent of Pliocene and Pleistocene Cordilleran and continental glaciations in northwestern Canada and eastern Alaska (from Duk’Rodkin et al., 2004).
- Figure 3.4. Soil classification map of Yukon Territory (from Scutter, 1997, after Agriculture Canada Expert Committee on Soil Survey 1987).
- Figure 3.5. Map of sites and zones at the BS19 collection area (satellite imagery from Google Earth).
- Figure 3.6. BS19 vegetation and topography at the hilltop, degrading polygon area, and fen.
- Figure 5.1. Conceptual model illustrating the development of a “C”-shaped $\delta^{18}\text{O}$ or δD profile in the active layer as a result of bi-directional freezing.
- Figure 5.2. Map of the Blackstone 2019 collection area (satellite imagery from Google Earth).
- Figure 5.3. BS19 vegetation and topography at the hilltop, degrading polygon area, and fen.
- Figure 5.4. Stable isotope development of basal active layer waters (BW).
- Figure 5.5. Stable isotopic profiles of June 2019 active layer waters.

- Figure 5.6. Representative stable isotope and GWC characteristics of the Unit 1-2 and Unit 2-3 boundaries.
- Figure 5.7. Cryostructures, stable isotopes, geochemistry, and unit divisions for Site 1.
- Figure 5.8. $\delta\text{D}-\delta^{18}\text{O}$ relations of stratigraphic units in Site 1.
- Figure 5.9. Cryostructures, stable isotopes, geochemistry, and unit divisions for Site 2.
- Figure 5.10. $\delta\text{D}-\delta^{18}\text{O}$ relations of stratigraphic units in Site 2.
- Figure 5.11. Cryostructures, stable isotopes, geochemistry, and unit divisions for Site 3.
- Figure 5.12. $\delta\text{D}-\delta^{18}\text{O}$ relations of stratigraphic units in Site 3.
- Figure 5.13. Cryostructures, stable isotopes, geochemistry, and unit divisions for Site 4.
- Figure 5.14. $\delta\text{D}-\delta^{18}\text{O}$ relations of stratigraphic units in Site 4.
- Figure 5.15. Comparison of the $\delta^{18}\text{O}$ values of average relict ground ice, 2018 first ice at the predicted 2018 active layer base, and September 2019 basal active layer water.
- Figure 5.16. $\delta\text{D}-\delta^{18}\text{O}$ regressions of relict ground ice at each site.
- Figure 5.17. Relations between 2019 probed thaw depth and thawing degree-days (TDDs) for each of the four sites in the Blackstone study area.
- Figure 5.18. Conceptual model of stable isotope development in ground ice along sloping terrain.

1. INTRODUCTION

1.1. Introduction

Permafrost peatlands in northern environments are archives of paleoclimatic and environmental proxies. These include plant macrofossil remains (Booth et al., 2004; Van Bellen et al., 2011; Turunen and Turunen, 2003), trace metals (Bandara et al. 2019, Shotykh, 1996), paludification (Mangan et al., 2019), testate amoeba (Van Bellen et al., 2018), diatoms (Carballeira and Pontevedra-Pombal, 2020), pollen (Booth et al., 2004), and peat geochemistry (Rantala et al., 2016; Zaccone et al., 2018). These archives have been used to constrain past climate and environmental parameters, including air temperature, soil moisture regimes, contaminant deposition and the history of peatland development.

The development of paleoclimate records from ice cores has been one of the most significant contributions to climatology by providing robust records of past temperatures (e.g. Johnson et al., 2001; Augustine et al., 2004). In some ice cores, the relations between past air temperatures and enclosed gases (Brook and Buizert, 2018). This is possible due to the strong relations between the isotopic composition of atmospheric moisture with air temperature and relative humidity (Dansgaard, 1964). However, one of the most challenging aspects of ice core records is that they are only present where glaciers exist today.

Stable isotopes ($\delta^{18}\text{O}$ and δD) from permafrost archives, similar to ice cores, show potential for reconstructing past climate. The veracity of stable isotope-based reconstructions derived from permafrost depends on the reliability of these ground ice archives as faithful recorders of meteoric precipitation, with minimal isotopic fractionation or diagenesis as the ground ice forms and becomes part of the permafrost. For example, the fidelity of polygonal wedge ice in this regard has made it an attractive and promising means of reconstructing both relative and absolute winter temperatures (e.g. Vasil'chuk and Vasil'chuk, 2014; Meyer et al., 2002; Nikolayev and Mikhalev, 1995). This is largely possible because the source waters (primarily snow melt) contribute to wedge growth during spring, when daily air temperatures are cool and evaporative enrichment is limited (Porter and Opel, 2020).

Stable isotopes from *pore ice* – microscopic ice occupying the soil pore space – and *texture ice* – ground ice distinguished by visible cryostructures – have also been used for paleoclimatic and paleoenvironmental reconstruction (e.g. Vardy et al. 1997, Bandera et al., 2020; Schwamborn et al., 2006; Porter et al., 2019). The isotopic composition of pore and texture ice reflect the composition of active layer waters – a mixture of summer and winter precipitation (Michel, 2011; Porter et al., 2016, Bandara et al., 2020) – at the time of formation. Growing evidence also suggests pore and texture ice record a multi-annual (decadal to sub-decadal) blend of water from the active layer – the upper-most soil layer that thaws and refreezes every year – owing to repeated mixing during freeze-thaw cycles (Porter et al., 2019; Bandara et al., 2020).

However, the relations between past climate and stable isotope records in pore and texture ice can be difficult to interpret due to varying annual contributions of winter and summer precipitation to the active layer, and the isotopic alteration of active layer waters preceding its long-term archival in permafrost (Nikolayev and Mikhalev, 1995, Wetterich et al., 2014; Dereviagin et al., 2003). Alterations may arise from isotopic fractionation during freezing (Lacelle et al., 2014; Wetterich et al., 2014; Schwamborn et al., 2006), evaporation in the upper active layer (Wetterich et al., 2014), or multi-annual blending (Porter et al., 2019; Wetterich et al., 2014; Lacelle et al., 2014). For these reasons, existing studies generally supplement stable isotope data from pore and texture ice with other proxies.

The potential for syngenetic pore ice – ground ice that aggrades in tandem with ground surface aggradation – in permafrost peatlands as archives of past climate via stable isotope reconstructions has been explored. Porter et al. (2019) presented a stable isotope record from syngenetic peatland pore ice with a remarkably smooth, stable $\delta^{18}\text{O}$ and δD trends spanning the last 13.6ka. This trend includes an enrichment at the top of the permafrost, which is interpreted to have formed in response to 20th century warming. The smooth isotopic trend of the *relict* pore ice – the pore ice underlying the long-term maximum thaw depth – contrasts with the strong variability in the active layer. Yet the process by which isotopically stable permafrost evolves from an isotopically noisy active layer remains unclear. The role of the transition layer - the layer of permafrost that occasionally rejoins the active layer during exceptionally deep thaw

penetration, and has properties of both the active layer and permafrost (Shur et al., 2005) – in the isotopic development of pore and texture ice is equally unclear.

1.2. Objectives

This thesis looks at the isotopic relations between precipitation, active layer waters, transition layer ice, and relict pore and texture ice from the Blackstone Plateau in central Yukon Territory to better understand how isotopic values become preserved in ground ice. The study is guided by four overarching aims:

- (1) To establish the history of local permafrost formation using geochemical and traditional cryofacies methods;
- (2) To infer the conditions of stable isotope development of pore and texture ice in the active layer, transition layer, and relict permafrost;
- (3) To assess the impacts of the local environment on the stable isotope development of pore and texture ice; and
- (4) To build upon existing evidence for 20th century warming captured by stable isotope records in pore and texture ice.

These aims were approached through a combination of field observation and geochemical analyses. Permafrost cores and active layer waters were extracted along a transect spanning a hillslope peatland and fen in the Ogilvie Mountains of central Yukon. Geochemical and stable isotopic associations between precipitation, basal active layer waters, and relict permafrost ice along this transect were used to identify the transition layer and establish the history of ground ice formation.

1.3. Thesis Organization

This thesis is divided into five chapters. *Chapter 2* provides a review of literature concerning areas of permafrost science relevant to the thesis. Topics covered include freezing processes in permafrost, isotopic fractionation during freezing, methods of ground ice characterization, and classification schemes of ground ice. *Chapter 3* consists of a description of the regional setting. This includes descriptions of general physical properties of the study area

including bedrock geology, Quaternary (glacial) setting, and regional climate. This chapter also discusses surficial and shallow subsurface characteristics, including soil properties, vegetation assemblages, hydrologic regimes, and regional and site-specific permafrost conditions. *Chapter 4* presents the methodology for both field and laboratory work, as well as project design and rationale. *Chapter 5*, formatted as a manuscript for future submission for publication, presents results obtained through field observation, laboratory analyses, and interpretations. *Supplementary* information including results and more detailed methodologies are included as an appendix to the thesis.

References

- Augustin, L., Barbante, C., Barnes, P. R., Barnola, J. M., Bigler, M., Castellano, E., ... & Dreyfus, G. (2004). Eight glacial cycles from an Antarctic ice core. *Nature*, *429*, 623-628.
- Bandara, S., Froese, D. G., St. Louis, V. L., Cooke, C. A., & Calmels, F. (2019). Postdepositional mercury mobility in a permafrost peatland from central Yukon, Canada. *ACS Earth and Space Chemistry*, *3*(5), 770-778.
- Booth, R. K., Jackson, S. T., & Gray, C. E. (2004). Paleoecology and high-resolution paleohydrology of a kettle peatland in upper Michigan. *Quaternary Research*, *61*(1), 1-13.
- Brook, E. J., & Buizert, C. (2018). Antarctic and global climate history viewed from ice cores. *Nature*, *558*(7709), 200-208.
- Carballeira, R., & Pontevedra-Pombal, X. (2020). Diatoms in Paleoenvironmental Studies of Peatlands. *Quaternary*, *3*(2), 10.
- Dansgaard, W. (1964). Stable isotopes in precipitation. *tellus*, *16*(4), 436-468.
- Dereviagin, A. Y., Chizhov, A. B., Meyer, H., Hubberten, H. W., Siegert, C. (2003). Recent ground ice and its formation on evidence of isotopic analysis. In *Proceedings of 8th International Conference on Permafrost* (pp. 21-25).
- Jackson, S. T., Charman, D., Newman, L., & Kiefer, T. (2010). *Peatlands: Paleoenvironments and carbon dynamics*. Pages International Project Office.
- Johnsen, S. J., Dahl-Jensen, D., Gundestrup, N., Steffensen, J. P., Clausen, H. B., Miller, H., Masson-Delmotte, V., Sveinbjörnsdóttir, A. E., & White, J. (2001). Oxygen isotope and

- palaeotemperature records from six Greenland ice-core stations: Camp Century, Dye-3, GRIP, GISP2, Renland and NorthGRIP. *Journal of Quaternary Science: Published for the Quaternary Research Association*, 16(4), 299-307.
- Lacelle, D., Fontaine, M., Forest, A. P., & Kokelj, S. (2014). High-resolution stable water isotopes as tracers of thaw unconformities in permafrost: A case study from western Arctic Canada. *Chemical Geology*, 368, 85-96.
- Mackay, J. R. (1983). *Oxygen isotope variations in permafrost, Tuktoyaktuk Peninsula area, Northwest Territories* (No. GSCAN-P--83-1B).
- Meyer, H., Dereviagin, A., Siegert, C., Schirrmeister, L., & Hubberten, H. W. (2002). Palaeoclimate reconstruction on Big Lyakhovsky Island, North Siberia—hydrogen and oxygen isotopes in ice wedges. *Permafrost and periglacial processes*, 13(2), 91-105.
- Meyer, H., Derevyagin, A. Y., Siegert, C., & Hubberten, H. W. (2002). Paleoclimate studies on Bykovsky Peninsula, North Siberia-hydrogen and oxygen isotopes in ground ice. *Polarforschung*, 70, 37-51.
- Michel, F. A. (1990). Isotopic composition of ice-wedge ice in northwestern Canada. In *Proceedings, Fifth Canadian Permafrost Conference, Nordicana* (Vol. 54, pp. 5-9).
- Nikolayev, V. I., & Mikhalev, D. V. (1995). An oxygen-isotope paleothermometer from ice in Siberian permafrost. *Quaternary Research*, 43(1), 14-21.
- Porter, T. J., & Opel, T. (2020). Recent advances in paleoclimatological studies of Arctic wedge and pore-ice stable-water isotope records. *Permafrost and Periglacial Processes*, 31(3), 429-441.
- Porter, T. J., Schoenemann, S. W., Davies, L. J., Steig, E. J., Bandara, S., & Froese, D. G. (2019). Recent summer warming in northwestern Canada exceeds the Holocene thermal maximum. *Nature communications*, 10(1), 1-10.
- Porter, T. J., Froese, D. G., Feakins, S. J., Bindeman, I. N., Mahony, M. E., Pautler, B. G., ... & Weijers, J. W. (2016). Multiple water isotope proxy reconstruction of extremely low last glacial temperatures in Eastern Beringia (Western Arctic). *Quaternary Science Reviews*, 137, 113-125.
- Rantala, M. V., Nevalainen, L., Rautio, M., Galkin, A., & Luoto, T. P. (2016). Sources and controls of organic carbon in lakes across the subarctic treeline. *Biogeochemistry*, 129(1-2), 235-253.

- Schwamborn, G., Meyer, H., Fedorov, G., Schirrmeister, L., & Hubberten, H. W. (2006). Ground ice and slope sediments archiving late Quaternary paleoenvironment and paleoclimate signals at the margins of El'gygytgyn Impact Crater, NE Siberia. *Quaternary Research*, 66(2), 259-272.
- Shotyk, W. (1996). Peat bog archives of atmospheric metal deposition: geochemical evaluation of peat profiles, natural variations in metal concentrations, and metal enrichment factors. *Environmental Reviews*, 4(2), 149-183.
- Shur, Y., Hinkel, K. M., & Nelson, F. E. (2005). The transition layer: implications for geocryology and climate-change science. *Permafrost and Periglacial Processes*, 16(1), 5-17.
- Turunen, C., & Turunen, J. (2003). Development history and carbon accumulation of a slope bog in oceanic British Columbia, Canada. *The Holocene*, 13(2), 225-238.
- van Bellen, S., Magnan, G., Davies, L., Froese, D., Mullan-Boudreau, G., Zaccone, C., ... & Shotyk, W. (2018). Testate amoeba records indicate regional 20th-century lowering of water tables in ombrotrophic peatlands in central-northern Alberta, Canada. *Global change biology*, 24(7), 2758-2774.
- Van Bellen, S., Garneau, M., & Booth, R. K. (2011). Holocene carbon accumulation rates from three ombrotrophic peatlands in boreal Quebec, Canada: impact of climate-driven ecohydrological change. *The Holocene*, 21(8), 1217-1231.
- Vardy, S. R., Warner, B. G., & Aravena, R. (1997). Holocene Climate Effects on the Development of a Peatland on the Tuktoyaktuk Peninsula, Northwest Territories I. *Quaternary Research*, 47(1), 90-104.
- Vasil'chuk, Y., & Vasil'chuk, A. (2014). Spatial distribution of mean winter air temperatures in Siberian permafrost at 20– 18 ka BP using oxygen isotope data. *Boreas*, 43(3), 678-687.
- Vasil'chuk, Y. K., & Vasil'chuk, A. C. (1998). Oxygen-isotope and C14 data associated with Late Pleistocene syngenetic ice-wedges in mountains of Magadan region, Siberia. *Permafrost and Periglacial Processes*, 9(2), 177-183.
- Vasil'chuk, Y. K., & Vasil'chuk, A. C. (1997). Radiocarbon dating and oxygen isotope variations in Late Pleistocene syngenetic ice-wedges, northern Siberia. *Permafrost and Periglacial Processes*, 8(3), 335-345.

- Vasil'chuk, Y. K., Vasil'chuk, A. C., & Stanilovskaya, J. V. (2017). Early Holocene climate signals from stable isotope composition of ice wedge in the Chara Basin, Northern Transbaikalia, Russia. *Geoscience Frontiers. Scopus*, 8(5), 1.
- Vasil'chuk, Y. K. (2013). Syngenetic Ice Wedges: Cyclical Formation, Radiocarbon Age and Stable Isotope Records by Yuriy K. Vasil'chuk, Moscow University Press, Moscow, 2006. 404 pp. ISBN 5-211-05212-9. *Permafrost and Periglacial Processes*, 24(1), 82-93.
- Wetterich, S., Tumskey, V., Rudaya, N., Andreev, A. A., Opel, T., Meyer, H., Schirrmeister, L., Hüls, M. (2014). Ice Complex formation in arctic East Siberia during the MIS3 Interstadial. *Quaternary Science Reviews*, 84, 39-55.
- Zaccone, C., Plaza, C., Ciavatta, C., Miano, T. M., & Shotyk, W. (2018). Advances in the determination of humification degree in peat since: Applications in geochemical and paleoenvironmental studies. *Earth-Science Reviews*, 185, 163-178.

2. LITERATURE REVIEW

2.1. Introduction

Permafrost is defined as ground that remains at or below 0°C for two or more years (Burn, 2013). Permafrost underlies ~20-25% of the Earth's surface (e.g. Anisimov and Nelson, 1996; Osterkamp and Burn, 2003) and ~50% of Canada (Throop et al., 2012) (Fig.1). Permafrost affected regions in the Northern Hemisphere are estimated at around 24%, though only ~12.8-17.8% of the exposed land surface in the Northern Hemisphere is underlain by permafrost, the rest underlying near-shore coastal regions (Zhang et al., 2000). Permafrost regions can be geographically separated into continuous (90-100% permafrost), discontinuous (50-90%), sporadic (10-50%), and isolated patches (0-10%) (Zhang et al., 2000). Although the physical presence of ground ice is not a prerequisite for defining ground as permafrost, permafrost-affected regions nonetheless typically contain a significant portion of ground ice in a variety of forms.



Figure 2.1. Circumpolar map of permafrost distribution (National Snow and Ice Data Center).

Ground ice is a generic term for all ice found within permafrost (NRCC, 1989). Perturbations in ground ice content and distribution due to current and future climate changes are expected to result in significant environmental changes in northern regions (Lee et al., 2014). Understanding ground ice distribution and its response to climate change carries critical ramifications for water quality (e.g. Kokelj et al., 2009), ecological changes (e.g. Wolter et al., 2016), sediment transport (e.g. Mann et al., 2010), carbon storage and mobilization (e.g. Shuur et al., 2008; Couture et al., 2018), watershed dynamics (e.g. Mann et al., 2010; Wright et al., 2009), and infrastructure (e.g. Couture and Pollard, 2007). The physical and chemical characteristics of ground ice - including stable isotopes, cryostratigraphy, lithostratigraphy, and chemostratigraphy - indicate how the ice formed and the past environment in which it formed (Murton and French, 1994). Ground ice is therefore a powerful source of paleoclimate and paleoenvironmental data (Porter et al., 2016). The significance of ground ice in northern regions

has spurred the development of many methods of characterization and classification over the past century, allowing geocryologists to better understand and communicate their scientific findings regarding genetic interpretation, response to environment and climate changes, and guide infrastructure planning.

This chapter provides a review of common techniques of ground ice characterization, classification, and genetic interpretation. These techniques, which include physical, geophysical, geochemical, and remote sensing methods, are summarized. Non-genetic and genetic classification schemes are considered and discussed separately. The latter part of this chapter is dedicated to summarizing the use of the oxygen and hydrogen stable isotopes of ground ice as a paleoclimate proxy and hydrological tracer. Literature important to this thesis on these topics will be presented.

2.2. Methods of Ground Ice Characterization

2.2.1. Visual characterization

Visual techniques for ground ice characterization describe the physical shape and geometry of the ice. In both Russian and North American literature these physical characteristics are often grouped and described stratigraphically by cryotexture, cryostructure and cryofacies (see Section 2.3 for detailed discussion on classification). These visual techniques are a readily available tool for permafrost scientists in both field and laboratory settings, and can often be conducted without the use of expensive lab instrumentation. However, visual techniques naturally require the availability of exposed ground ice in the field or cores extracted from the field. Accessing northern field sites and collecting permafrost samples can be expensive, time consuming, and physically strenuous. The use of drones has seen limited use in some field projects to observe otherwise difficult-to-reach parts of the landscape. Scanning techniques in a laboratory setting show potential for augmenting visual characterization of ground ice properties (Calmels et al., 2010).

2.2.2. Physical properties

Ground ice can be characterized by its physical properties and its response to different stresses. Such properties include, but are not limited to: ice content (Murton and French, 1994), cementation (Pihlainen and Johnston, 1963), plasticity (Lewkowicz and Harris, 2005), density,

texture, and heat capacity. The following list of ground ice properties is not exhaustive, but covers some of the most common properties of interest.

Ice content

Ice content is generally reported as gravimetric water content (GWC) or volumetric water content (VWC). These are commonly used parameters in studies of ground ice (e.g. Lacelle et al., 2014;) and are given by equations (1) and (2):

$$GWC(\%) = \left(\frac{\text{moist soil mass (g)}}{\text{dry soil mass (g)}} \right) * 100 \quad (2.1)$$

$$VWC(\%) = \left(\frac{\text{moisture volume (cm}^3\text{)}}{\text{bulk soil volume (cm}^3\text{)}} \right) * 100 \quad (2.2)$$

GWC is best applied in scenarios where the ground material is homogeneous because changes in ice content are difficult to differentiate from changes in soil lithology using GWC. Although VWC is generally more difficult to manually measure, it is not affected by changes in lithology in the same way as GWC.

When ice volume exceeds that of the available pore space, the portion of the ice that exceeds the pore space is termed *excess ice* (Lee et al., 2014). Excess ice causes ground heaving, making it a common geomorphological agent in permafrost landscapes, as well as a hazard to infrastructure integrity. Excess ice comes in the form of segregated ice lenses and ice wedges. Fine-textured soils are the preferred medium in which excess ice accumulates because the high mineral surface area of the soil provides a continuous network of connected film water along the grain boundaries, allowing moisture to move through the soil to the freezing front, adding to the ice (Hivon and Segoy, 1995; Fisher et al., 2019; Osterkamp and Burn, 2003). The amount of excess ice is generally reported as the percentage of volume over the total pore volume (e.g. Kokelj and Burn, 2003). Permafrost is considered “ice-rich” when excess ice is >20% (Grosse et al., 2011). The presence of excess ice can alter the bulk thermal conductivity and heat capacity of the soil (Lee et al., 2014). Though layers of ice-rich ground can thermally protect underlying ground ice from deep thaw penetration (Woo, 1986), final melting and loss of that ice can cause significant environmental changes. When excess ice thaws, the ground subsides and water pools at the surface (Grosse et al., 2011), driving continued thawing and reducing ground stability.

Thawing of excess ice also changes the subsurface hydrology and carbon fluxes across permafrost landscapes (Lee et al., 2014).

Ground temperature regime and heat capacity

Ground temperature is typically measured using a thermistor string installed down a borehole (e.g. Throop et al., 2012). This is frequently done at regular depth intervals, including a sensor at the ground surface to measure surface air temperature. Data are collected across seasons so that full annual ground temperature ranges and depth-dependent shifts are observed. The summer and winter ground temperature profiles form “trumpet curves” (Fig. 3) as the shallow subsurface temperature swings between positive and negative between these two seasons, with more stable temperature profiles at depth. The top of the permafrost corresponds to the depth at which the trumpet curve crosses 0°C at the peak of the summer ground temperature oscillation. The effects of latent heat release during freezing produce a *zero-curtain effect* that steadies the ground temperature at 0°C at a given depth until freezing is complete (Muller, 1947 via Cook, 1955), a phenomenon observable in time-series analysis (Fig. 4).

The propagation of a thermal front (either thawing or freezing) into the ground is commonly modelled using the Stefan Equation (Riseborough et al., 2008). Kurlyk and Hayashi (2016) present a version of the Stefan Equation that incorporates correction factors to account for varying phase-change conditions in the soil, such as a non-zero initial temperature:

$$X = \sqrt{\frac{2 k_u I(t)}{\phi \rho_w L}}, \quad (2.3)$$

$$I(t) = \int_0^t T_s(\tau) d(\tau) \quad (2.4)$$

and where,

X: depth from surface to frozen-thawed interface (m)

k_u : bulk thermal conductivity of upper unfrozen zone ($\text{W m}^{-1} \text{ }^\circ\text{C}^{-1}$)

I(t): surface thawing index (or surface degree-day total)

T_s : surface temperature ($^\circ\text{C}$)

τ : time over which mean daily surface temperature is $>0^{\circ}\text{C}$ or $<0^{\circ}\text{C}$ (for thawing and freezing regimes, respectively)

ϕ : volumetric moisture content that has undergone phase change

ρ_w : density of water (kg m^{-3})

L : mass-based latent heat of fusion for water (J kg^{-1})

This equation assumes that the heat capacity of the soil is negligible and a uniform thermal conductivity above the thaw front, producing a linear temperature distribution in the upper thaw zone (Kurlyk and Hayashi, 2016). The Stefan Equation is used as the foundation for many ground temperature models, such as the Frost Index model from Nelson and Outcalt (1987). Though beyond the scope of this work, thaw front and freezing front propagation have been modelled using a variety of methods other than the Stefan Equation alone, such as the Kudryavtsev model (Riseborough et al., 2008) and Neumann solution (Kurylyk and Hayashi, 2016), all of which, including the Stefan Equation, are founded on Fourier's laws (Yershov, 1996). Fundamental consequences of Fourier's first and second laws are that temperature fluctuations 1) decrease in amplitude with depth, and 2) are shifted in time with depth (Yershov, 1996), empirically evident phenomena measurable by time series analysis of ground temperature at varying depths (Fig. 4).

Thermal conductivity and heat capacity in permafrost soils are important thermal indices that control ground temperature regimes and depend on the soil material, water content, and ice content. Thermal conductivity describes the amount of heat energy conducted through a given mass due to an energy gradient (without advection, convection, or other mass movements). Heat capacity describes the amount of energy required to raise a given amount of mass by a given temperature. The water-ice ratio forms an important thermal feedback with heat capacity and thermal conductivity in the active layer that varies seasonally and influences permafrost aggradation in the soil below. In the summer the active layer thaws, releasing large amounts of water. The high heat capacity and low thermal conductivity of the water retards downward heat penetration protecting deeper permafrost from warming. This protects underlying permafrost during the summer. In the fall and winter, however, this water freezes. Ice has a much lower heat capacity and higher thermal conductivity than water, allowing cool temperatures to penetrate deep into the ground, promoting permafrost growth (Osterkamp and Burn, 2003). This seasonal

thermal bias is especially true for peats, which are able to absorb large amounts of water like a sponge, but can dry in the summer. Peatlands therefore make excellent thermal regulators in permafrost environments that protect ground ice (Osterkamp and Burn, 2003).

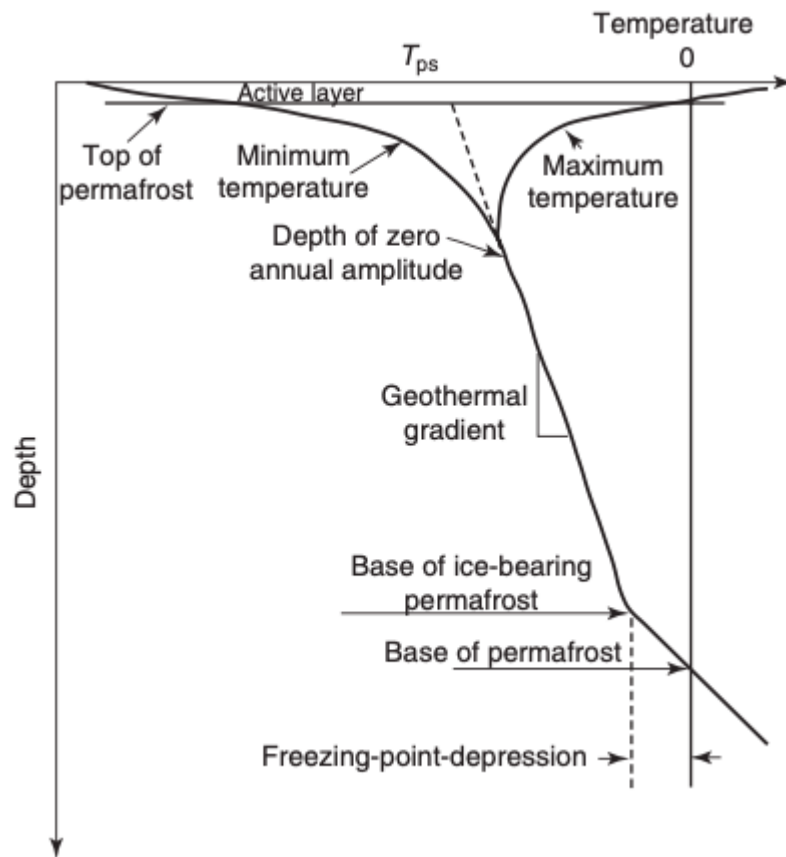


Figure 2.2. A representative “trumpet curve” ground temperature profile with anatomical labels for various thermal characteristics (from Osterkamp and Burn, 2003).

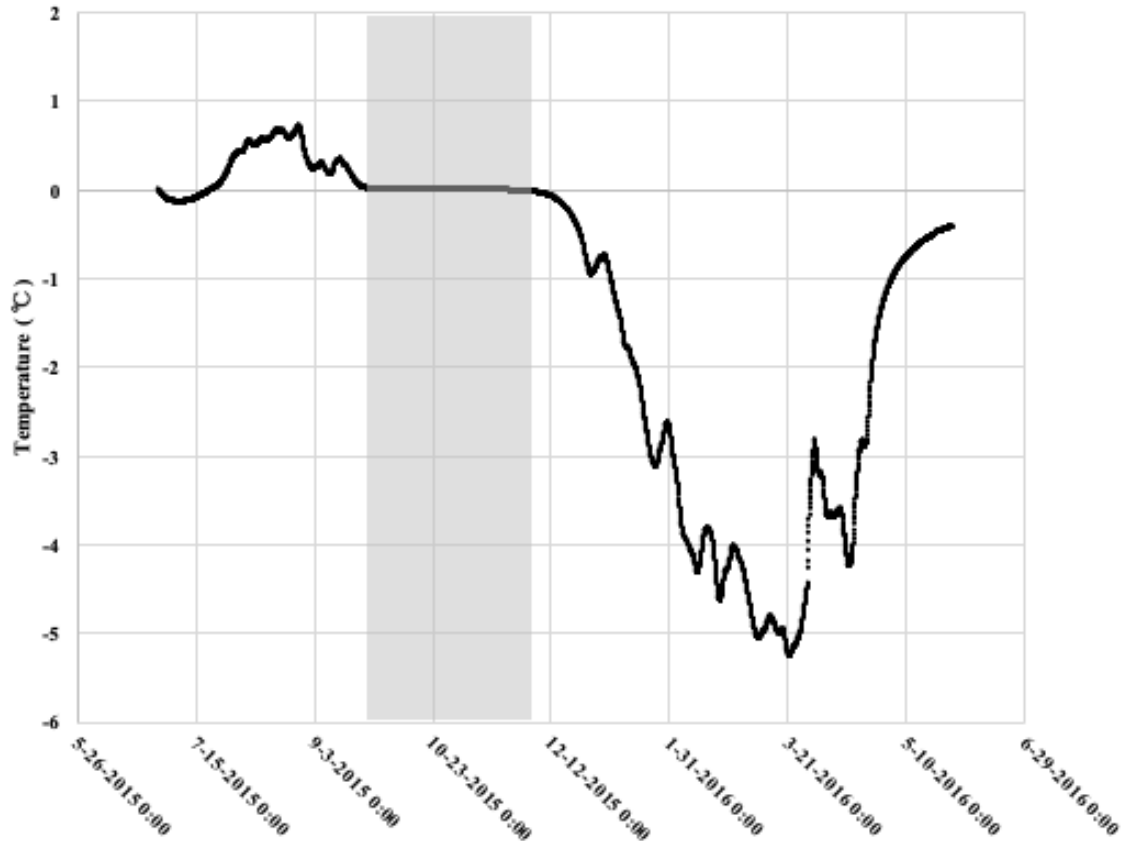


Figure 2.3. Ground temperature time series at 50cm depth in peatland permafrost near Chapman Lake, Ogilvie Mountains, Yukon Territory. The grey region represents the zero-curtain effect observed during fall freeze back between approximately Sept 26 - Dec 2 2015.

2.3. Classification of Ground Ice

Ground ice is complex, resulting from thermal history, host sediment characteristics, sedimentation and erosion, topography, water sources, and water source chemistry. This complexity has led to a variety of different ground ice classification systems. In addition, different traditions - namely those of the Russian and North American scientists - have arisen (French, 2018). Broadly speaking, the various ground ice classification systems can be regarded as either *genetic* or *non-genetic*. Genetic classifications are designed to both describe the physical and (or) geochemical properties of the ground ice while simultaneously offering a mechanism of formation for those properties. Non-genetic classifications do not describe how

ground ice types form, but simply describe the physical and (or) geochemical characteristics of the ground ice. Although ground ice classifications generally focus on the ice itself, it is worth noting that significant amounts of unfrozen water can remain at sub-zero temperatures below the permafrost table, a factor that is not included within current classification schemes.

2.3.1. Non-genetic classifications

Visual frameworks of ground ice classification provide readily available modes of classification to geocryologists in the field and laboratory. Traditionally, visual characterization usually involves the identification of cryostratigraphic units based on physical manifestations of the ice within the soil matrix. Such classifications provide the basis for understanding the genesis of ice growth within soil (French, 2018). Physical manifestations of ground ice may be grouped and described as cryotextures, cryostructures, and cryofacies (Murton and French, 1994). *Cryotexture* refers to the size and shape of ice grains and crystals that form the ice, as well as the nature of the contacts between the ice grains and crystals. *Cryostructures* are classifications of the physical arrangement, size, and shape of ground ice bodies. In Russian literature “cryotexture” is used interchangeably with “cryostructure”, whereas North American literature generally distinguishes between the two. *Cryofacies* are groupings of associated cryotextures, cryostructures, and ice content. Strictly speaking, cryofacies are not unique to any particular genesis, as similar cryofacies can have different origins depending on other contextual factors. However, as the highest order of non-genetic classification, cryofacies provide a framework for inferring the genetic history of ice growth

Murton and French (1994) developed one of the most widely used classifications of cryostructures found in current North American literature and also include a basic framework for cryofacies classification (Fig. 5). Their classification consists of seven main cryostructural categories: structureless (Sl), layered (La), lenticular (Le), regular reticulate (Rr), irregular reticulate (Ri), crustal (Cr), and suspended (Su). “Suspended” structures are equivalent to “ataxitic” structures in Russian literature (e.g. Kanevskiy et al., 2013). Furthermore, six subcategories can be applied to both the lenticular and layered categories based on whether the structures are *parallel* or *non-parallel*, and whether they are *planar*, *wavy*, or *curved*.

Murton and French’s cryofacies classification scheme, at its broadest level, is divided first by volumetric ice content. The second division occurs by identifying minor and major soil

matrix types. The third and final division occurs on the basis of cryostructures present. The presence of multiple cryofacies is referred to as a *cryofacies assemblage*.

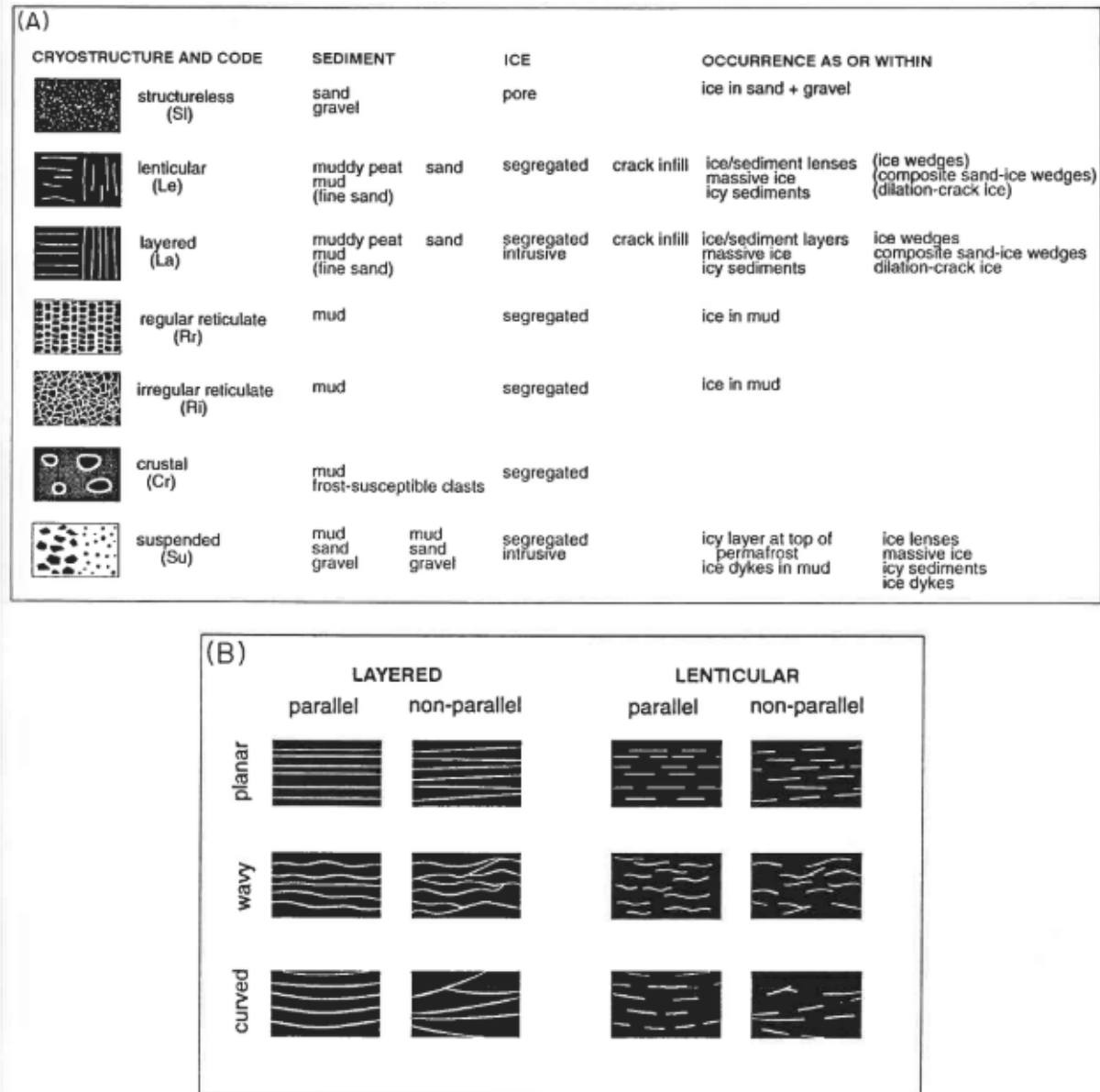


Figure 2.4. Non-genetic classification of cryostructures in minerogenic matrix permafrost (Murton and French, 1994). Layered ice is millimeters to meters thick; reticulate ice, a few millimeters to ~10cm thick; and lenticular ice, 1 mm to ~3cm thick.

Cryofacies type	Volumetric ice content (%)	Cryofacies	Code	Cryostructures
Pure ice	100	Pure ice	I	Le, Le
Sediment-poor ice	>75	Sand-poor ice	SPI	Le, La, Su
		Aggregate-poor ice	API	
Sediment-rich ice	>5 to ≤75	Sand-rich ice	SRI	Le, La, Su
		Aggregate-rich ice	ARI	
Ice-rich sediment	>25 to ≤50	Ice-rich sand	IRS	Sl, Le, La
		Ice-rich mud	IRM	Le, La, Rr, Ri, Cr
		Ice-rich diamicton	IRD	
Ice-poor sediment	≤25	Ice-poor mud	IPM	Sl; various non-ice
		Ice-poor sand	IPS	sedimentary structures
		Ice-poor gravel	IPG	
		Ice-poor diamicton	IPD	
		Ice-poor peat	IPP	

Figure 2.5. Representative cryofacies classifications of typical ground ice from the Tuktoyaktuk Coastlands (from Murton and French, 1994).

Cryostructures can also be found on much smaller scales that require close examination, potentially with a hand lens, to observe. Kanevskiy et al. (2011) defined a classification scheme for such ‘micro-structures’, based on examples found in minerogenic matrices hosting syngenetic permafrost (Fig. 7). Broadly speaking, this classification scheme adopts the terminology for equivalent larger cryostructures. In the experience of the present author, the micro-cryostructure types in this classification fall along a continuum of increasing ice lens continuity and overlap, often indicative of increasing ice content.

These cryostructure and cryofacies classifications provide quick and versatile ways to categorize ground ice in the field or in the lab. A potential disadvantage of these classification schemes, like many existing cryostructural classifications, is the focus on predominantly minerogenic soil materials, and disclusion of organic host materials.

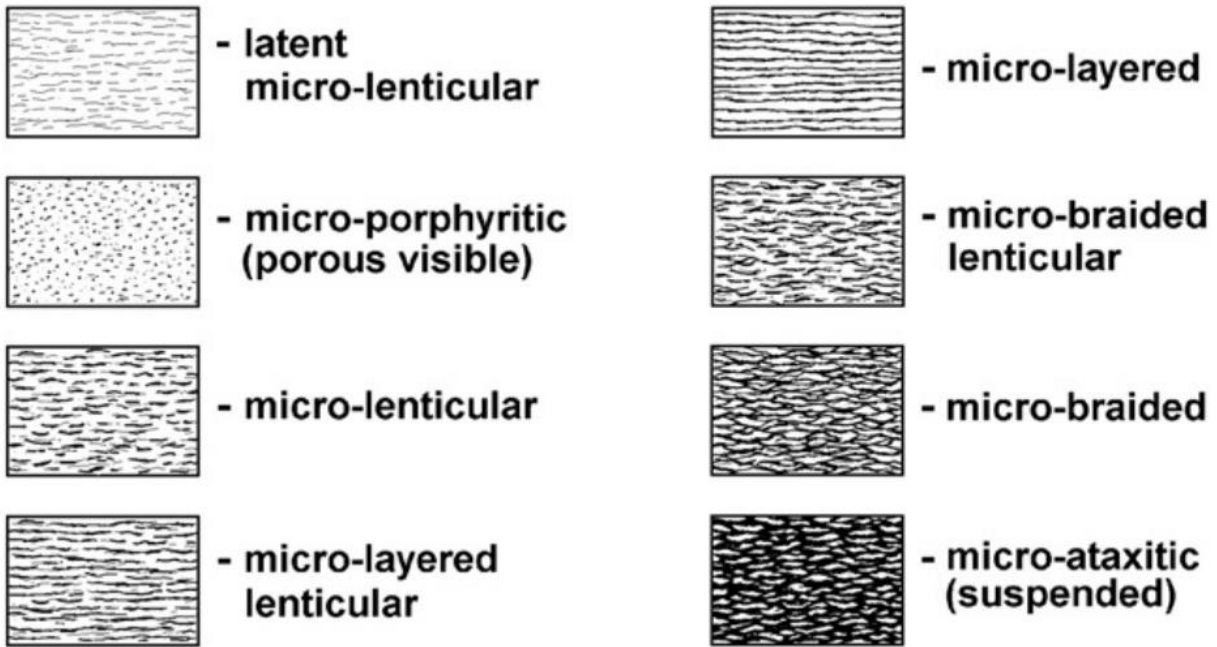


Figure 2.6. Micro-cryostructural classification (from Kanevskiy et al., 2011). Such micro structures are common in syngenetic minerogenic permafrost, and is widely adopted in this study to characterize cryostructures observed in peatland permafrost. These micro structures are less than 1mm thick and can be up to several millimeters long.

2.3.2. Genetic classifications

Genetic classifications ascribe an interpretation of the ice beyond its physical properties. These interpretations may indicate the behavior of ice accumulation over time, the dominant mechanism that led to ice growth, or the original source or environment of ice formation. Naturally, frequent overlaps exist between these classifications.

Syngenetic and epigenetic classification

Genetic classification can be conceptualized by the behavior of ice accumulation over time, and is commonly divided into either syngenetic or epigenetic ground ice growth. *Syngenetic* ground ice develops due to, and in tandem with, the aggradation of the ground surface from either sedimentation or peat accumulation (Fig. 8) (French and Shur, 2010). Syngenetic ground ice is older with increasing depth (Gilbert et al., 2016). *Epigenetic* ground ice

forms after the host material has been deposited. Freezing of lacustrine sediments following lake drainage is an example of epigenetic ice growth because the lake sediments were deposited first and the pore ice formed later (Fig. 8a) (French and Shur, 2010; Kanevskiy et al., 2014). Ice is younger with increasing depth in epigenetic permafrost sequences (Gilbert et al., 2016).

Anti-syngenetic is a temporally-defined genetic term used to describe ground ice that has formed in tandem with the removal of surface material through erosion. Anti-syngenetic ground ice formation was described by Mackay (1990) in the context of ice wedges. These ice wedges were characterized by simultaneous outward and downward growth into the host material, in a direction normal to the ground surface.

Quasi-syngenetic ice growth refers to ground ice that forms in a syngenetic and epigenetic sense simultaneously (Gilbert et al., 2016). This has been attributed to a sudden change in surface conditions, such as permafrost growth in lacustrine sediments following pond or lake drainage (Fig. 8b). In such a scenario, the sudden exposure of lake bottom sediments initiates the epigenetic ice growth and the development of an active layer, while paludification and the aggradation of organics on the exposed surface initiates concurrent syngenetic ice growth and thinning of the newly formed active layer (Kanevskiy et al., 2014).

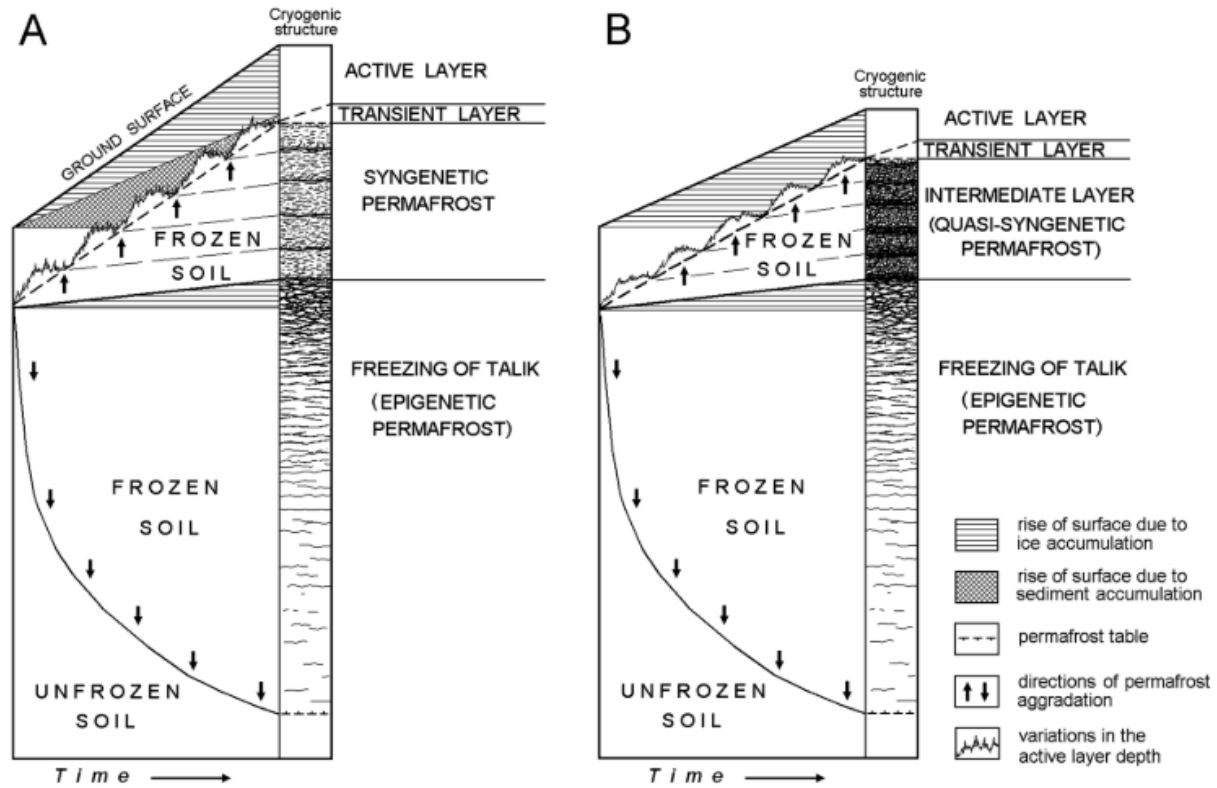


Figure 2.7. The succession of permafrost accumulation following lake drainage in A) continuous permafrost zones, and B) discontinuous permafrost zones (from Kanveskiy et al., 2014).

Provenancial and mechanistic classifications

Provenancial genetic classifications define the ice by its original source or environment of formation. Mechanistic classifications define the dominant process that led to ice growth. Mechanistic ice types are commonly used in tandem with syngenetic or epigenetic designations.

Segregated ice

Segregated ice is a mechanistic term describing ground ice that has grown by the migration of soil moisture by cryosuction to an existing ice body (Harris and Matthews, 1984). This process generally accompanies the rejection of sediment aggregates and dissolved impurities from the ice (Lacelle et al., 2014). Segregated ice may take the form of lenses, layers, crustal ice, or larger bodies (see *massive ice* below). Many forms of *texture ice* develop by segregation.

Aggradational ice

Aggradational ice is a mechanistic term for ground ice that is formed by the incorporation of ice lenses and layers into the permafrost during upward aggradation of the permafrost table (Mackay, 1972) and is generally associated with syngenetic ice growth. Because these ice lenses and layers form by segregation, aggradational ice can be thought of as being composed of segregation ice (French and Shur, 2010), although downward flux during summer is greater than upward flux during winter (Guodong, 1983). The permafrost table can migrate upwards in a number of ways. A common scenario involves the upward migration of the active layer of constant thickness due to sediment or organic deposition at the surface. A different scenario involves thinning of the active layer driven by a cooling climate or accumulation of surface organics. While a cooling climate does not necessitate any surface aggradation to transpire, active layer thinning due to the accumulation of surface organics results in active layer thinning disproportionately greater than the thickness of the new organic layer. Either way, the active-layer-thinning scenario results in the formation of a quasi-syngenetic intermediate layer (previously discussed). However, aggradational ice can also form after the formation of major thaw unconformities, such as during active layer thinning following a deep fire-driven thaw (Lacelle et al., 2014).

Massive ice and its variations

Though massive ice is, strictly speaking, a non-genetic term - physically defined as having >250% GWC (Permafrost Subcommittee, 1988) - it encompasses a host of provenancial and large mechanistic (i.e. genetic) ground ice types with this physical property. Subforms of massive ice include: buried ice, ice wedges, intrasedimental ice, intrusive ice, thermokarst cave ice (e.g. Douglas et al., 2011), ice wedges, and pingo ice. Glacial ice, snowpack, lake and sea ice, and aufeis are all potential sources (provenances) of *buried ice*. *Intrasedimental ice* is a mechanistic term for massive ice that has grown in-situ within the soil and can be either segregated, segregation-intrusive, or intrusive in origin (Mackay and Dallimore, 1992). *Intrusive ice* is a mechanistic term sometimes referred to as “injection ice”, and forms by water experiencing pressure-induced migration (Mackay, 1972). *Aufeis* is a provenancial term for layered ice that develops on the surface of rivers and streams during or by spring water discharge (Permafrost Subcommittee, 1988).

2.4. Stratigraphic Division of Permafrost Soils

Permafrost soils are classically divided into two primary horizons: the *active layer* and *permafrost*. The active layer is *mechanically* defined at the horizon that physically thaws and refreezes every year (Burn, 1998). In contrast, permafrost is *thermally* defined as ground that remains at or below 0°C for more than two years (Muller, 1943). Because the bottom of the active layer is mechanically defined and the top of the permafrost is thermally defined, the two boundaries may not coincide with one another if the presence of dissolved solutes or molecular interactions between the water and soil grains depresses the freezing point of the soil water (Burn, 1994).

Thaw frequency and depth are not necessarily consistent between years or over longer periods of time. The *transient layer* is the layer of upper permafrost that occasionally thaws and rejoins the active layer and is controlled by fluctuations in the surface energy driven by climate and environment variations operating usually over sub-decadal to centennial time scales (Yanovsky, 1933; Shur et al., 2005). Although the transition layer is defined by the recurrence of mechanical thawing (similar to the active layer), it is still part of the permafrost if it has been frozen, and therefore cryotic, for two or more years between episodes of rethawing. In minerogenic materials such as loess, the transition layer is typically characterized by low to moderate ice content and can result in a rhythmic sequence of layered and lenticular cryostructures in syngenically aggrading ground ice (Shur et al., 2005). In this context, layered ice is thought to form during periods when upward transition layer migration is slow, giving time for ice to accumulate. In contrast, lenticular and micro-lenticular cryostructures are thought to form during comparatively rapid upward transition layer migration. For comparison, these mechanisms have also been invoked by Kokelj and Burn (2003) to describe for the accumulation of ground ice during active layer recovery following deep thaw penetration.

The *transition layer*, coined by Shur et al. (1988), is composed of the transient layer and a deeper *intermediate layer* (Fig. 9). Thus, ideal syngenetic soil profiles can be divided into the active layer, transition layer, and relict permafrost. However, the intermediate layer begins to form when surface sedimentation stops and the transition layer becomes stationary. Consequently, aggradational ice begins to accumulate at the bottom of the transition layer, providing increasing protection against deep thaw penetration. Aggradational ice continues to form and aggrade pseudo-syngenetically in response to increasing thermal buffering with

increasing ice content, causing the transition layer to slowly migrate upwards and the active layer to thin. A thinning active layer can also be perpetuated by the onset of thermally-protective organic growth at the surface. The pseudo-syngenetic aggradational ice that makes up the intermediate horizon is generally characterized by layered (banded) and suspended (atactic) cryostructures and is generally between 0.5-1.5m thick (Shur, 1988; Kanevskiy et al., 2011). The ice-rich nature of the transition layer, particularly the intermediate horizon, is critical for the thermal stability of permafrost in the face of changing climate and environment (Shur et al. 2005). Nonetheless, it is liable to undergo thawing over multi-decadal to multi-centennial time scales driven by shifts in climate (Shur et al., 2005, 2010; Kanevskiy et al., 2011, 2014).

In practice, uncertainty remains within the definition of the intermediate horizon. In a 2011 study of a syngenetic Yedoma Ice Complex sequence along the Itkillik River, Alaska, Kanevskiy et al. defined the intermediate horizon as an ice-rich (GWC varied between 54-223% and averaged 148%), usually 0.5-1.5m thick, and formed in consequence of active layer thinning in response to environmental changes such as vegetation growth, peat accumulation, and other local factors after surface sedimentation had stopped. While this definition emphasizes the physical characteristics and process-oriented aspects of intermediate horizon definition from Shur et al. (2005), it does not indicate whether they consider potential future thaw recurrence as a criterion for defining the intermediate horizon in their study. In this context, the question could be asked of whether potentially relict portions of the lower intermediate horizon can still be counted as part of the modern intermediate (and transition) horizon.

The definition of the intermediate horizon becomes further complicated when the *genesis* of its formation is considered. Kanevskiy et al. (2014) described intermediate horizon formation within lacustrine sediments following lake drainage. Subaerial exposure of the lacustrine sediments following lake drainage initiated downward, epigenetic ground ice formation and (presumably) the formation of an active layer. Concurrently, organics began to grow at the surface, causing active layer thinning and the formation of an ice-rich intermediate horizon. They assert that the concurrent epigenesis and pseudo-syngenetic ice growth of this layer is a characteristic of the intermediate horizon. Pseudo-syngensis is also relevant to the formation of the intermediate horizon in Kanevskiy et al. (2011) (previously discussed) which was driven by the growth of surface organics, increased thermal buffering, and thinning of the active layer.

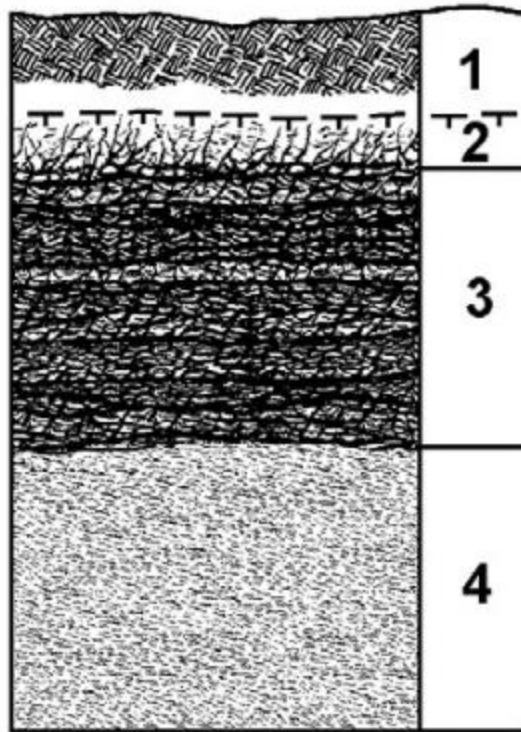


Figure 2.8. Representative profile of 1) active layer, 2) transition layer, 3) intermediate horizon, 4) relict permafrost. The transition layer consists of the transient and intermediate layers. Black regions below the active layer are representative of cryostructures. Note the greater density of cryostructures in the intermediate horizon coincident with greater ice content (from French and Shur, 2010).

2.5. Stable Isotopes in Permafrost

The stable isotopes of ground ice oxygen (^{16}O and ^{18}O) and hydrogen (^1H and ^2H) provide information about the environment and climate at the time the ice formed, how that ice has formed, and processes that affected the ice after it formed. However, using stable isotopes for this purpose must be done so with caution because ground ice can be formed in a broad manner of environmental and hydrological settings with unique physical and thermal properties that control the behavior of cryofractionation. As such, stable isotope records from ground ice must be interpreted within their individual genetic contexts. This section reviews basic tenants of isotope notation and fractionation, discusses how oxygen and hydrogen isotopes behave in natural cryogenic systems, and reviews how oxygen and hydrogen isotopes have been used to infer the history of permafrost environments and climate.

2.5.1. Isotopic fractionation

The stable isotopes of oxygen (^{16}O and ^{18}O) and hydrogen (^1H and ^2H) group in different combinations to create water molecules that vary in total mass due to differing numbers of neutrons. These mass-differing molecules are known as “isotopologues”. Although there are nine possible isotopologues, the most common, and therefore most relevant for O and H stable isotope interactions discussed in this work are (in decreasing atmospheric frequency): $^1\text{H}_2^{16}\text{O}$, $^1\text{H}_2^{18}\text{O}$, and $^1\text{H}^2\text{H}^{16}\text{O}$. Stable isotope values are expressed as the ratio of heavy to light isotopes of a sample, divided by the ratio of the heavy to light isotopes of the standard (Vienna Standard Mean Ocean Water, V-SMOW):

$$\delta (\text{‰}) = \left[\left(\frac{R_x}{R_s} \right) - 1 \right] \times 1000 \quad (2.5)$$

Where,

R_s : S_h/S_l

R_x : X_h/X_l

Because the bracketed portion of this equation produces very small values, it is multiplied by 1000 to make handling of these values easier to use. δ is thus expressed in units of “permil” (‰).

Isotopic fractionation refers to the differential partitioning of isotopic species between different phases in a chemical system (Hoefs, 2015). This occurs due to differences in atomic and molecular masses, bond energies, and corresponding vibrational states (Hoefs, 2015).

Isotopic fractionation between water and ice during freezing has been dubbed “cryofractionation” (Porter and Opel, 2020). During cryofractionation the ice becomes more enriched in heavier isotopes than the parent water because heavy water isotopologues form more stable bonds in ice than lighter isotopologues (Hoefs, 2015). When the forward and backward exchange rates of various isotopic species equalize, the system is said to be in “isotopic equilibrium” (Hoefs, 2015). However, if the forward and backward exchange rates of isotopic species do not equalize, the resulting fractionation is said to be “kinetic” in nature.

Cryofractionation under equilibrium conditions is quantified by the equilibrium fractionation factors for D and ^{18}O . Equilibrium fractionation factors for hydrogen ($\alpha_{2\text{H}(i-w)}$) and oxygen ($\alpha_{18\text{O}(i-w)}$) range between 1.0195-1.0206 and 1.0028-1.0031, respectively (Suzuoki and Kimura, 1973; O'Neil, 1968), corresponding to ‰-equivalent fractionation values (ϵ_{i-w}) of 19.5 - 20.6‰ and 3.1 - 2.8‰, respectively. These values were produced in the lab under near-ideal conditions for isotopic equilibrium fractionation: pure (deionized) water, slow freezing rates (0.7-1.9mm/hr, Suzuoki and Kimura), well mixed liquid reservoirs (reduces thin diffusive layer at ice-water interface), and constant temperature at the ice-water interface (0°C, partly moderated by the release of latent heat during freezing). However, they represent only very close approximations of true equilibrium fractionation values since a small degree of non-equilibrium conditions will always exist if freezing rates are >0mm/h (Suzuoki and Kimura, 1973). Diminished isotopic fractionation (due to non-equilibrium conditions and a smaller fractionation factor) is produced under faster freezing conditions because the isotopologues have less time to partition between the liquid and solid phases (Suzuoki and Kimura, 1973; Lacelle, 2011).

Freezing in natural systems is more complicated than freezing under ideal laboratory conditions. The theoretical fractionation factors are further modified by 1) the initial isotopic composition of the water, 2) the freezing rate, 3) the degree of reservoir mixing, and 4) the thickness of the boundary layer separating the ice and water phases (Suzuoki and Kimura, 1973; Lacelle, 2011). The equilibrium fractionation factor between ice and water increases with increasing initial δ value of the source water and with decreasing freezing rate (Lacelle, 2011). In addition, the fractionation factor decreases faster with increasing freezing in response to increasing boundary layer thickness, the thin (mm-scale) zone at the ice-water interface (Lacelle, 2011).

Cryofractionation in the subsurface is generally treated as a Rayleigh-style fractionation process because the backward reaction from ice to water during freezing is small enough that the reactants and products are virtually isolated from one another (Dansgaard, 1964). As adapted from Lacelle (2011), Rayleigh fractionation can be described by the equation:

$$R_w = R_{0,w} f^{(\alpha_{i-w}-1)} + (\alpha_{i-w} - 1) \quad (2.6)$$

Where,

R_w : ratio of the heavy to light isotope in the water.

$R_{0,w}$: initial ratio of heavy to light isotope in the source water

α_{i-w} : equilibrium fractionation factor between water and ice
 f : fraction of remaining source water

Note that before fractionation begins ($f=1$), R represents the isotopic ratio of the water caused by the first iteration of fractionation. Expressed in δ notation Eq. 2.2 becomes:

$$\delta_i = \delta_0 + \ln(\alpha_{i-w}) \cdot 1000 \cdot \ln(f) + \ln(\alpha_{i-w}) \cdot 1000 \quad (2.7)$$

Where,

δ_i : delta value of ice

δ_0 : initial delta value of ice

α_{i-w} : equilibrium fractionation factor between water and ice

f : fraction of remaining source water

2.5.2. Co-isotopic relations in precipitation

Co-isotopic ($\delta^{18}\text{O}$ - δD) regressions are commonly used to infer fractionation processes and conditions of water phase transitions. $\delta^{18}\text{O}$ and δD in water samples are closely related to one another and form a linear relation:

$$\delta D = (S \cdot \delta^{18}O) + B \quad (2.8)$$

Where,

S : co-isotopic regression slope

B : y-axis (δD -axis) intercept

Craig (1961), for example, determined the relation between $\delta^{18}\text{O}$ and δD in global precipitation, known as the *global meteoric water line (GMWL)*, to be:

$$\delta D = (8 \cdot \delta^{18}O) + 10 \quad (2.9)$$

The GMWL has commonly been employed as a datum for assessing the isotopic similarity of environmental waters to precipitation. The δD -axis intercept (or '*d*-excess', see below) of 10‰ indicates that, on average worldwide, kinetic fractionation accompanies the initial evaporation of moisture from the ocean (Lacelle, 2011). The slope of 8 reflects the predominant effects of equilibrium fractionation during atmospheric condensation following this initial evaporation

(Dansgaard, 1964). Atmospheric waters that have undergone little to no isotopic modification during atmospheric transport should have a slope very similar to those of the GMWL.

In more recent years, a stronger emphasis has been placed on the use of *local meteoric water lines* (LMWLs) as references comparing environmental waters (Lacelle, 2011). Local meteoric water lines are co-isotopic lines for precipitation gathered within the area or region of interest. The slopes and intercepts of LMWLs are particular to the processes that influenced the isotopic development of the moisture in that region. For example, LMWLs in northwestern Canada have slopes between 6 and 7 (Lacelle, 2011).

D-excess, defined as the δD -axis intercept of a water sample in $\delta^{18}O$ - δD space when a regression slope of 8 is assumed. *D*-excess is derived by rearranging eq. (2.9) and solving for the intercept:

$$d = \delta D - (8 * \delta^{18}O) \quad (2.10)$$

In locations where the LMWL slope reasonably approximates the GMWL slope of 8, variations in precipitation *d*-excess can be interpreted as differences in marine moisture source arising from variable amounts of kinetic fractionation during initial evaporation from the ocean surface (Frohlich et al., 2002). However, because other kinetic effects can influence precipitation *d*-excess such as during the formation of solid precipitation and recycling of terrestrial moisture (Porter et al., 2016), caution should be taken when interpreting precipitation *d*-excess.

2.5.3. Co-isotopic relations in ice

The $\delta^{18}O$ - δD relations in ice have also been explored as a tool to evaluate system conditions during freezing. Under closed-system Rayleigh fractionation conditions, the first ice to form will be more enriched than the parent water (Souchez and Jouzel, 1984; Lacelle, 2011; Dansgaard, 1964). Although ice will always be more enriched than its source water, ice formed after the first ice becomes progressively depleted as the residual water reservoir becomes more depleted, and does so more dramatically as the liquid reservoir is used up (Lacelle, 2011) (Fig. 2.9).

The isotopic depletion of freezing water falls along a *freezing line* in $\delta^{18}O$ - δD space, a term coined by Jouzel and Souchez (1982) (Fig. 2.9). They posited that the slope of the freezing line under ideal conditions is estimated by:

$$S = S_0 \frac{1000 + \delta_i D}{1000 + \delta_i^{18}O}, S_0 = \frac{\alpha^{18}O_{i-w} - 1}{\alpha D_{i-w} - 1} \quad (2.11)$$

Where,

S: freezing slope

S_0 : $(\alpha D_{i-w} - 1) / (\alpha^{18}O_{i-w} - 1)$; ideal, closed-system co-isotopic slope

$\alpha^{18}O_{i-w}$: equilibrium fractionation factor for

^{18}O between ice and water

αD_{i-w} : equilibrium fractionation factor for D between ice and water

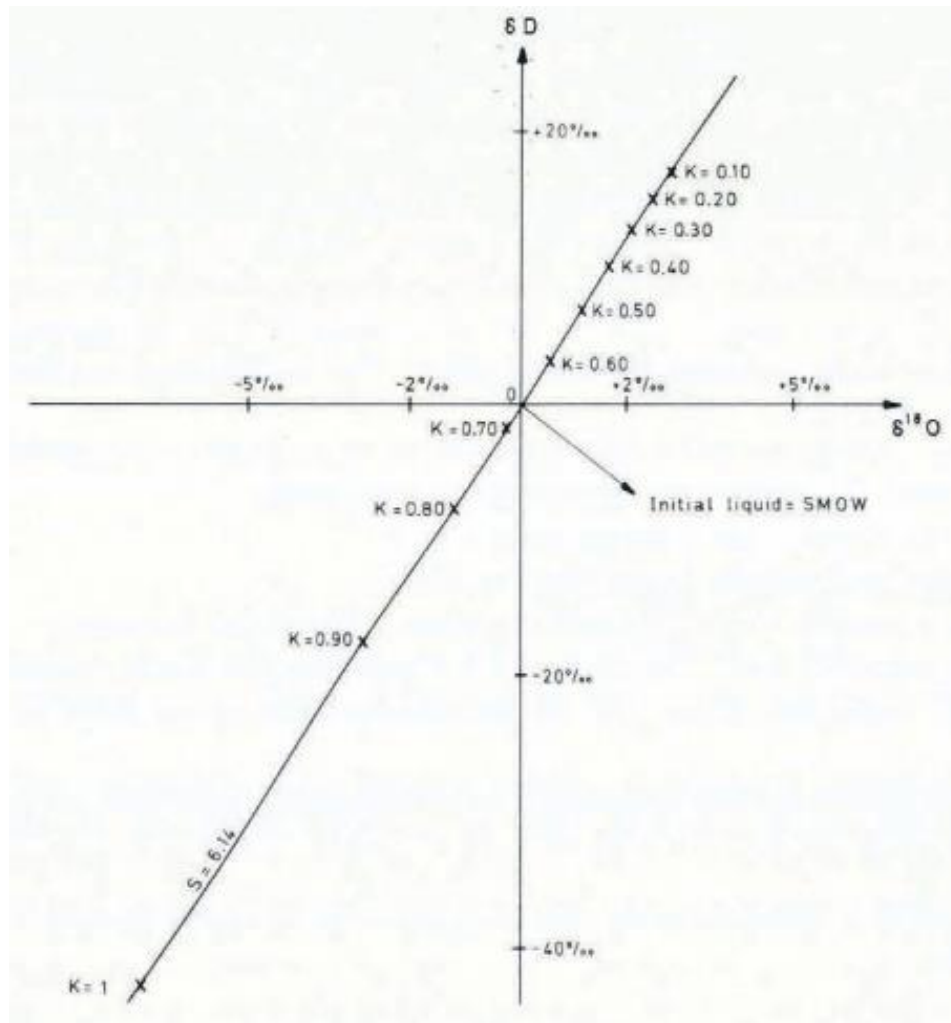


Figure 2.9. Example of modelled freezing regression line of slope (S) calculated from an equivalent form of Eq. 2.3 and using the equilibrium fractionation factors from O’Neil (1968) of $\alpha^{18}O_{i-w} = 1.003$ and $\alpha^2H_{i-w} = 1.0186$. K is the fraction of the system that is ice. Note the accelerating depletion of new ice with increasing K (figure from Jouzel and Souchez, 1982).

Freezing slopes (S) are shallower than the GMWL (Yang et al., 2017), where slopes between 6.2 and 7.3 generally indicate ideal Rayleigh-style cryofractionation (Lacelle, 2011). Slopes less than 6.2 indicate freezing occurred kinetically rather than as an equilibrium process.

Further information regarding the isotopic composition of the initial waters can be gleaned from the freezing slope. When the isotopic compositions of the ice and parent water are

known, and the observed freezing slope (S) between them closely approximates S_0 , freezing conditions are approximated by closed-system, ideal Rayleigh-style cryofractionation (Jouzel and Souchez, 1982). This method has been applied by a number of studies (Michel, 1986; Fritz et al., 2011; Lacelle et al., 2009). Conversely, when the initial parent water $\delta^{18}\text{O}$ and $\delta^2\text{H}$ are not known, they can be approximated by the intersection point between the observed freezing regression line and the source water regression line (Jouzel and Souchez, 1982). This method has been utilized in studies involving basal glacier ice (Jouzel and Souchez, 1982), syngenetic ground ice (Yang et al., 2017), and frost blisters (Michel, 1986).

2.5.4. Stable isotope development in ground ice

Lithalsas

Calmels et al. (2008) used stable isotopes to establish the dynamics of lithalsa formation at Nunavik. Assuming equilibrium fractionation at 0°C in an open system (3.1‰ $\delta^{18}\text{O}$ enrichment in the ice), they estimated that the original source waters were between -17.4 and -19.3‰ $\delta^{18}\text{O}$. From these values they used the equation from Dansgaard (1964) relating $\delta^{18}\text{O}$ and MAAT to determine that MAAT ranged between -5.5 and -8.2°C . Based on these values, they believe the lithalsa formed sometime during the last few centuries during colder MAATs than those reported for the 20th century. Furthermore, they reported an overall “cool to warm” trend going down-core according to $\delta^{18}\text{O}$ and δD at 20cm resolution. However, large variability of 1.39‰ and 9.82‰ for $\delta^{18}\text{O}$ and δD respectively due to 1) variations in the isotopic composition of the source water, 2) cryosuction and cryofractionation at the centimeter scale occurs as a semi-closed system (distillation never reaches peak effectiveness).

Pingos

Stable isotopes have provided insight into freezing conditions during the development of pingo ice cores. Mackay (1990) examined the isotopic profile of Pingo 20 from the Mackenzie River Delta, noting it had a $\delta\text{D}-\delta^{18}\text{O}$ freezing slope of 7.2. Mackay noted this was similar to the $\delta\text{D}-\delta^{18}\text{O}$ freezing slopes Souchez and Jouzel (1984) reported of precipitation-sourced glacier ice ($S_{\delta\text{D}-\delta^{18}\text{O}} > 6.7$) (i.e. glacial ice that had not undergone regelation), and used this to exemplify the difficulties that arise when trying to interpret the genesis of ice solely using co-isotopic slopes.

Yoshikawa et al. (2012) uses stable isotopes in tandem with major ion geochemistry to infer freezing conditions and developmental history of the Mongot Pingo (Mongolia) and Weather Pingo (Prudhoe Bay, Alaska). Ice cores extracted from these two sites were composed primarily of segregated and intrusive ice. Different phases of ice core development in both were marked by changes in the isotopic profiles, suggesting either changes in closed or open conditions, freezing rate, amount of available source water, or a combination of these factors. The Mongot Pingo ice core developed primarily under open-system conditions, which produced relatively homogeneous stable isotopic layers, while the Weather Pingo ice core generally developed in a closed system.

Vasil'chuk et al. (2014, 2016) found that equilibrium fractionation dominated during ice core formation in two closed-system pingos – the Pestsovoye Pingo, as indicated by δD - $\delta^{18}O$ and d -excess- δD freezing slopes, though variations in freezing rate produced isotopic fluctuations.

Frost blisters

Michel (1986) measured the $\delta^{18}O$ and δD values of a frost blister ice core from the North Fork Pass along the Dempster Highway, and observed that both $\delta^{18}O$ and δD decrease curvilinearly with depth, consistent with closed-system Rayleigh cryofractionation. However, where the $\delta^{18}O$ profile followed the type curve for ideal Rayleigh-style fractionation, the δD data were characterized by an α value smaller than that expected of ideal Rayleigh-style fractionation. He interpreted this as indicative of non-equilibrium processes with respect to 2H . Van Everdingen (1982) presented $\delta^{18}O$ and δD trends from seasonal frost mounds at Bear Rock Spring near Fort Norman, N.W.T. Isotopic values in this profile decrease from approximately -21 to -26‰ $\delta^{18}O$ and from approximately -142 to -197‰ δD . They interpret these trends as indicative of slow freezing of water in a closed system. d - δD slopes were not calculated. However, they posit that rupture and drainage of the sub-blisters water lens is represented by the isotopic record by a slight increase in delta values, followed by a resumed decreasing trend with depth.

Massive tabular ice

The origin of massive tabular ice in northwestern Canada has long been debated (Fritz et al., 2011). Fritz et al. (2011) utilized stable isotopic methods to investigate the origins of massive

ground ice on Herschel Island, including one novel specimen. They used the “ S_x - S_{th} comparison method” to indicate that freezing took place at near equilibrium conditions. A negative, well-correlated d - δD slope further supported equilibrium fractionation. Concomitant $\delta^{18}O$ and δD with d enrichment from the outside of the ice body towards the center indicated that freezing took place in an isolated reservoir of water from the outside-inwards. The “MWL-FL intercept method”, valid because freezing seems to have taken place in a closed or mostly closed system, indicated that the initial isotopic composition of the water was approximately -32.7‰ $\delta^{18}O$ and -251‰ δD . Such low values suggest it formed some time during MIS-2. However, they do not offer an explicit genetic classification of the ice body. At a separate site on the opposite side of Herschel Island, Fritz et al. suggest a basal regelation origin for massive tabular beds, partly on the basis of strongly depleted $\delta^{18}O$ and δD values that lack profile trends. Respectively, these findings suggest: a) a full Wisconsinan glacial water source, and b) isotopic modification during regelation, mixing, and refreezing of the ice body. They also note that a segregated or segregated-intrusive origin cannot be ruled out.

Buried aufeis, surface icings, and snowpack

Though studies of the isotopic composition of buried aufeis is rare, studies have been conducted on the isotopic composition of fresh (non-buried) aufeis. The isotopic composition of aufeis relates to freezing rate, isotopic composition of the river water, and closed vs. open (or semi-open) conditions (Gibson and Prowse 1999, 2002). Gibson and Prowse (1999) reported $\delta^{18}O$ and δD depth profiles for congelation ice in the Liard River basin in northwestern Canada. Non-varying isotopic profiles enriched relative to the underlying river water are indicative of freezing in an open system while isotopic enrichment of this profile geometry relative to underlying river water is inversely proportional to freezing rate. Profiles that deplete in $\delta^{18}O$ and δD with depth are indicative of slow freezing in a closed system. This depletion trend becomes less pronounced under increasing freezing rates. Finally, profiles that enrich in $\delta^{18}O$ and δD with depth are indicative of open system conditions in which the water source is becoming more enriched.

The isotopic composition of surface icings from groundwater discharge at springs have been investigated by few studies. Michel (2011) reports an isotopic profile of a surface icing from spring discharge along the Alaska Highway in southwestern Yukon Territory. The lower

~40cm is isotopically consistent, indicating fast freezing of a constant water source. The upper ~190cm is characterized by frequent strong oscillations of up to ~4‰ $\delta^{18}\text{O}$ and an average of ~2‰ $\delta^{18}\text{O}$, indicative of periodic snow and groundwater mixing.

Buried snowpack stable isotopic composition reflects the isotopic composition of the original snow (Michel, 2011). Lacelle et al. (2009) reported stable isotopic compositions of massive tabular ice exposed along a thaw slump at Red Creek in the Ogilvie Mountains of central Yukon Territory. $\delta^{18}\text{O}$ values of the massive ice ranged between -30.2‰ to -27.8‰. These values are more negative than modern precipitation at Mayo, the adjacent stream water, candle ice underneath the sample section, and values reported for late Holocene ice wedges. They were, however, consistent with Pleistocene ice wedges. A S_x - S_{th} comparison indicated that the ice was not formed by equilibrium freezing of groundwater, $\delta^{18}\text{O}$ - δD slope matching that of the modern LMWLs at Mayo and Inuvik. Ultimately, the molar gas ratios and stable isotopic compositions of entrapped air in the ice were able to confirm the ice was derived from firn.

Pore and texture Ice

Pore and texture ice have been used to infer qualitative (i.e., cooler vs. warmer) (Michel, 1986, Schwambor et al., 2006; Opel et al., 2017) and quantitative (Nikolayev and Mikhalev, 1995; Porter et al., 2019) paleoclimate temperature, permafrost hydrology and source waters (Vardy et al., 1997; Michel and Fritz, 1982), and the depths of thaw unconformities (Lacelle et al., 2014; Burn et al., 1986; Murton et al., 2005). However, studies that employ these records often grapple with a wide-range of potential environmental and climatological factors that modify these isotopic signatures and make interpretation difficult (Schwamborn et al., 2006). This section provides an overview of our current understanding of the stable isotopic development of pore and texture ice.

Isotopic development of source waters

The isotopic composition of pore and texture ice reflect the isotopic composition of local precipitation. Isotopic variations in atmospheric moisture are expressions of regional weather and climate, and are known to vary predictably with latitude, altitude, and distance from marine moisture source (Lachniet et al., 2016). The last of these factors is related to ‘continentality’, which is produced by Rayleigh distillation as moisture travels from source to point of deposition

(Stumpp et al., 2014). During transport over land, atmospheric moisture may also undergo multiple cycles of precipitation and re-evaporation. Consequently, local meteoric water lines (LMWLs) are often shallower in slope than the global meteoric water line (GMWL), reflecting the kinetic fractionation effects of evaporation. Finally, precipitation feeds active layer waters, which then feed underlying ground ice.

The water source of pore and texture ice is active layer water. Active layer water is a seasonal mixture of spring snowmelt, melted seasonal active layer ice (potentially including transition layer ice if thaw penetration is deep enough), and summer precipitation (Throckmorton et al., 2016; Zhu et al., 2017; Porter et al., 2016). The relative contributions of these sources vary between locations (e.g. Wang et al., 2018; Yang et al., 2017; Zhu et al., 2017; Boike et al., 1998). While the active layers of some environments receive most of their moisture from winter precipitation (e.g. Nikolayev and Mikhalev, 1995), summer precipitation usually makes up the bulk of late summer active layer waters (e.g. Porter et al., 2019; Vardy et al., 1997).

Active layer water isotopes can undergo kinetic fractionation by evaporation (Sugimoto et al., 2003; Bandera et al., 2019; Zhu et al., 2019; Throckmorton et al., 2016). Evaporation primarily affects the upper several centimeters of the active layer, presumably above the water table where some air space is available for vapor transport (e.g. Zhu et al., 2019). The strength of evaporative fractionation depends on air temperature, relative humidity, wind speed, and net total radiation (Zhang et al., 2007). However, the presence of evaporative effects does not mean the active layer will be impacted similarly. Some active layer soils studied by Zhu et al. (2019) in late summer, for example, indicated evaporative $\delta^{18}\text{O}$ enrichment in the upper active layer, but isotopic depletion in the lower active layer, potentially because of the greater precipitation input to the soil column at the time. Porter et al. (2019) also indicate that pore ice from a soligenic peatland in the Ogilvie Mountains plots tightly along the LMWL, indicating a lack of evaporative enrichment on basal active layer waters.

Active Layer Isotope Patterns

The stable isotope profile geometry of frozen active layers is commonly characterized by a “C”-shaped pattern (e.g. Michel and Fritz, 1982; Yang et al., 2017; Vardy et al., 1998). This isotope profile geometry is caused by Rayleigh-type cryofractionation during bi-directional freezing (from top-down and bottom-up) of the active layer in the fall and winter (Michel, 2011).

The most enriched values are found at the top and bottom of the active layer and represent the first ice to form, while the last ice to form (located within the mid-sections of the active layer) is the most depleted, reaching values below that of the initial source water (Fig. 11). Ultimately, the bottom-most first ice of this C-type profile becomes incorporated by aggrading permafrost (Porter et al., 2019). As explained in previous sections, under slow freezing conditions and a thin boundary layer, fractionation of 2.8-3.1‰ $\delta^{18}\text{O}$ and 19.5 - 20.6‰ δD are potentially achieved. However, ice enrichment is often less in the active layer because these conditions are not always met during freeze-back (Lacelle et al., 2014). Nonetheless, many researchers believe rates of freeze-back at the bottom of the active layer is generally slow enough to approximate ideal fractionation conditions.

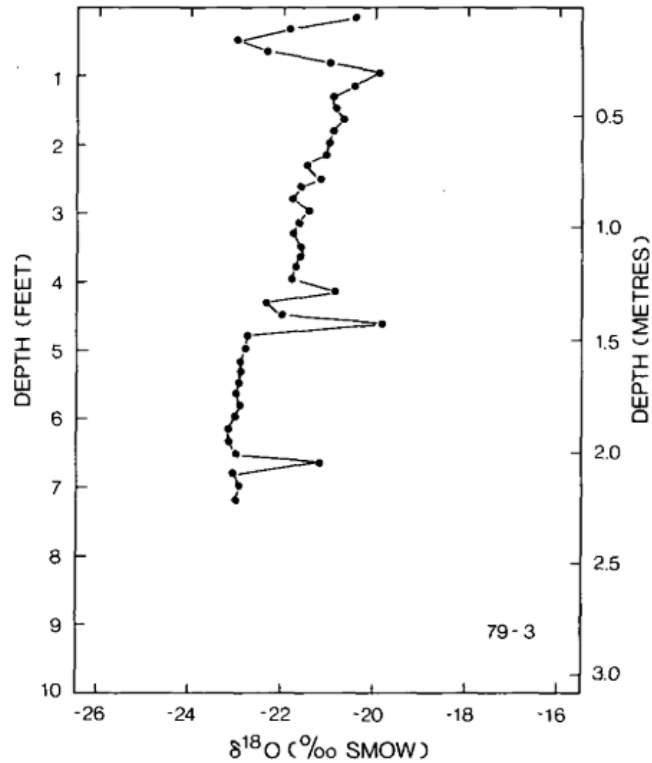


Figure 2.10. $\delta^{18}\text{O}$ depth profile of core 79-3 from Michel and Fritz (1982) taken from outside the experimental lake basin at Illisarvik. Note the “C”-shaped isotope profile of the frozen active layer in the upper foot. First ice at the top and bottom are approximately -20‰ $\delta^{18}\text{O}$, while last ice is $\sim -23\text{‰}$.

Ground ice recycling and multi-year blending

Cycles of thawing and freezing in the active layer recycles and mixes active layer waters over multiple years (Nikolayev and Mikhalev, 1995; Porter et al. 2016, 2019). This is caused by cycles of thawing and freezing in the active layer which recycles and mixes old active layer waters from past years with new precipitation. The isotopic values of old and new waters become

averaged, repressing more extreme isotope fluctuations. This might be one reason for the relatively consistent $\delta^{18}\text{O}$ and δD records of relict pore ice (Porter et al., 2016, 2019).

Water mixing and isotopic blending continues within the transition layer, the zone that undergoes freeze-thaw cycles less frequently than the active layer (Shur et al., 2005). Furthermore, because the probability of thawing decreases with increasing depth through the transition layer, the deepest transition layer ice could therefore be considered the penultimate stage before becoming relict ground ice. Because only the warmest years are capable of thawing the deepest transition layer ice, pore and texture ice are potentially biased towards warmer-than-average summer temperatures because exceedingly deep thaw penetration and source water homogenization is unlikely to recur again before further surface aggradation and permanent ground ice preservation (Porter et al., 2019). However, the role of the transition layer in the isotopic development of pore and texture ice has not been fully explored and is one of the objectives of this thesis.

Cryotic water migration in pore and texture ice

In late summer, when the active layer has reached its greatest depth for the year, thawed active layer waters continue to migrate down into the upper permafrost due through gravity and cryosuction under a negative temperature gradient (Mackay 1983; Cheng, 1983). This is possible because the presence of dissolved solutes and surface tension along soil particles depress the freezing temperature, allowing thin films of unfrozen, cryotic water to exist interstitially within the ice (Hivon and Segó, 1995). Cryosuction is transmitted along the network of films, pulling basal active layer waters deeper into the upper permafrost. Elevated tritium concentration within the upper upper layer of modern permafrost support this theory (Burn and Michel, 1988). Not many studies directly examine the effects of this cryosuction and subsequent freezing on the isotopic composition of the ice. Lacelle et al. (2014) posit that the freezing of cryotic, downward-translocated waters in the upper part of the transition layer is very slow due to the small thermal gradient, resulting in cryofractionation enrichment of the ice approximating ideal fractionation values. In the winter, however, when the ground thermal regime flips and cryotic waters begin to freeze, fractionation becomes increasingly kinetic due to progressively faster freezing and significantly diminishing water volumes. Furthermore, Lacelle et al. (2014) demonstrate that this

property results in isotopically enriched spikes in pore and texture ice produced at the base of the active layer during deep thaw and the formation of a thaw unconformity.

References

- Anderson, D. M., & Tice, A. R. (1973). The unfrozen interfacial phase in frozen soil water systems. In *Physical aspects of soil water and salts in ecosystems* (pp. 107-124). Springer, Berlin, Heidelberg.
- Anisimov, O. A., & Nelson, F. E. (1996). Permafrost distribution in the Northern Hemisphere under scenarios of climatic change. *Global and Planetary Change*, 14(1-2), 59-72.
- Arcone, S. A., Lawson, D. E., Delaney, A. J., Strasser, J. C., & Strasser, J. D. (1998). Ground-penetrating radar reflection profiling of groundwater and bedrock in an area of discontinuous permafrost. *Geophysics*, 63(5), 1573-1584.
- Arenson, L. U., Springman, S. M., & Segó, D. C. (2007). The rheology of frozen soils. *Applied Rheology*, 17(1), 12147-1.
- Bandara, S., Froese, D. G., St Louis, V. L., Cooke, C. A., & Calmels, F. (2019). Postdepositional Mercury Mobility in a Permafrost Peatland from Central Yukon, Canada. *ACS Earth and Space Chemistry*, 3(5), 770–778. <https://doi.org/10.1021/acsearthspacechem.9b00010>
- Beuselinck, L., Govers, G., Poesen, J., Degraer, G., & Froyen, L. (1998). Grain-size analysis by laser diffractometry: comparison with the sieve-pipette method. *Catena*, 32(3-4), 193-208.
- Bockheim, J. G. (2015). *Cryopedology* (p. 173). London: Springer.
- Boike, J., Roth, K., & Overduin, P. P. (1998). Thermal and hydrologic dynamics of the active layer at a continuous permafrost site (Taymyr Peninsula, Siberia). *Water Resources Research*, 34(3), 355-363.
- Brandt, O., Langley, K., Kohler, J., & Hamran, S. E. (2007). Detection of buried ice and sediment layers in permafrost using multi-frequency Ground Penetrating Radar: A case examination on Svalbard. *Remote Sensing of Environment*, 111(2-3), 212-227.
- Brooks, H., Doré, G., & Smith, S. L. (2018). Permafrost geotechnical index property variation and its effect on thermal conductivity calculations. *Cold Regions Science and Technology*, 148, 63-76.

- Burn, C. R. (1994). Permafrost, tectonics, and past and future regional climate change, Yukon and adjacent Northwest Territories. *Canadian Journal of Earth Sciences*, 31(1), 182-191.
- Burn, C. R. (1998). The active layer: two contrasting definitions. *Permafrost and Periglacial Processes*, 9(4), 411-416.
- Burn, C. (2013). Permafrost. In *Encyclopedia of Quaternary Science: Second Edition* (pp. 464–471). doi:10.1016/B978-0-444-53643-3.00099-6
- Burn, C. R., & Michel, F. A. (1988). Evidence for recent temperature-induced water migration into permafrost from the tritium content of ground ice near Mayo, Yukon Territory, Canada. *Canadian Journal of Earth Sciences*, 25(6), 909-915.
- Calmels, F., & Allard, M. (2004). Ice segregation and gas distribution in permafrost using tomodesitometric analysis. *Permafrost and Periglacial Processes*, 15(4), 367-378.
- Calmels, F., Delisle, G., & Allard, M. (2008). Internal structure and the thermal and hydrological regime of a typical lithalsa: significance for permafrost growth and decay. *Canadian Journal of Earth Sciences*, 45(1), 31-43.
- Calmels, F., Clavano, W., & Froese, D. G. (2010). Progress on X-ray computed tomography (CT) scanning in permafrost studies. In *Proceedings of the 5th Canadian Conference on Permafrost, GEO2010 Calgary, Alberta* (pp. 1353-1358).
- Cook, F.A. (1955). Near Surface Soil Temperature Measurements at Resolute Bay, Northwest Territories. *Arctic*, 8(4), 237–249.
- Couture, N. J., Irrgang, A., Pollard, W., Lantuit, H., & Fritz, M. (2018). Coastal erosion of permafrost soils along the Yukon Coastal Plain and fluxes of organic carbon to the Canadian Beaufort Sea. *Journal of Geophysical Research: Biogeosciences*, 123(2), 406-422.
- Couture, N. J., & Pollard, W. H. (2007). Modelling geomorphic response to climatic change. *Climatic Change*, 85(3), 407-431.
- Craig, H. (1961). Isotopic variations in meteoric waters. *Science*, 133(3465), 1702-1703.
- Dansgaard, W. (1964). Stable isotopes in precipitation. *Tellus*, 16(4), 436-468.
- Douglas, T. A., Fortier, D., Shur, Y. L., Kanevskiy, M. Z., Guo, L., Cai, Y., & Bray, M. T. (2011). Biogeochemical and geocryological characteristics of wedge and thermokarst-cave ice in the CRREL permafrost tunnel, Alaska. *Permafrost and Periglacial Processes*, 22(2), 120-128.

- Fisher, D. A., Lacelle, D., & Pollard, W. (2019). A model of unfrozen water content and its transport in icy permafrost soils: Effects on ground ice content and permafrost stability. *Permafrost and Periglacial Processes*, 31(1), 184-199.
- French, H. M. (2017). *The periglacial environment*. John Wiley & Sons.
- French, H., & Shur, Y. (2010). The principles of cryostratigraphy. *Earth-Science Reviews*, 101(3-4), 190-206.
- Fritz, M., Wetterich, S., Meyer, H., Schirrmeister, L., Lantuit, H., & Pollard, W. H. (2011). Origin and characteristics of massive ground ice on Herschel Island (western Canadian Arctic) as revealed by stable water isotope and hydrochemical signatures. *Permafrost and Periglacial Processes*, 22(1), 26-38.
- Froehlich, K., Gibson, J. J., & Aggarwal, P. K. (2002). *Deuterium excess in precipitation and its climatological significance* (No. IAEA-CSP--13/P).
- Gibson, J. J., & Prowse, T. D. (1999). Isotopic characteristics of ice cover in a large northern river basin. *Hydrological Processes*, 13(16), 2537-2548.
- Gibson, J. J., & Prowse, T. D. (2002). Stable isotopes in river ice: Identifying primary over-winter streamflow signals and their hydrological significance. *Hydrological Processes*, 16(4), 873-890.
- Gilbert, G. L., Kanevskiy, M., & Murton, J. B. (2016). Recent advances (2008–2015) in the study of ground ice and cryostratigraphy. *Permafrost and Periglacial Processes*, 27(4), 377-389.
- Grosse, G., Romanovsky, V., Jorgenson, T., Anthony, K. W., Brown, J., & Overduin, P. P. (2011). Vulnerability and feedbacks of permafrost to climate change. *Eos, Transactions American Geophysical Union*, 92(9), 73-74.
- Cheng, G. (1983). The mechanism of repeated-segregation for the formation of thick layered ground ice. *Cold Regions Science and Technology*, 8(1), 57-66.
- Harris, C., & Matthews, J. A. (1984). Some observations on boulder-cored frost boils. *Geographical Journal*, 63-73.
- Hayashi, M., McClymont, A., Christensen, B., Bentley, L., & Quinton, W. (2011). Thawing of permafrost peatlands: Effects of water-energy feedback on landscape evolution. In *Proceedings of the joint meeting of the International Association of Hydrogeologists Canadian National Chapter and the Canadian Quaternary Association*, Quebec City.

- Hilbich, C., Marescot, L., Hauck, C., Loke, M. H., & Mäusbacher, R. (2009). Applicability of electrical resistivity tomography monitoring to coarse blocky and ice-rich permafrost landforms. *Permafrost and Periglacial Processes*, 20(3), 269-284.
- Hivon, E. G., & Segoy, D. C. (1995). Strength of frozen saline soils. *Canadian Geotechnical Journal*, 32(2), 336-354.
- Hoefs, J. (2015). *Stable isotope geochemistry* (Vol. 285). Berlin: Springer.
- Hossain, S., Kibria, G., & Khan, S. (2018). *Site Investigation Using Resistivity Imaging*. CRC Press.
- Jørgensen, A. S., & Andreasen, F. (2007). Mapping of permafrost surface using ground-penetrating radar at Kangerlussuaq Airport, western Greenland. *Cold Regions Science and Technology*, 48(1), 64-72.
- Jouzel, J., & Souchez, R. A. (1982). Melting–refreezing at the glacier sole and the isotopic composition of the ice. *Journal of Glaciology*, 28(98), 35-42.
- Judge, A. S., Tucker, C. M., Pilon, J. A., & Moorman, B. J. (1991). Remote sensing of permafrost by ground-penetrating radar at two airports in Arctic Canada. *Arctic*, 40-48.
- Kanevskiy, M., Shur, Y., Fortier, D., Jorgenson, M. T., & Stephani, E. (2011). Cryostratigraphy of late Pleistocene syngenetic permafrost (yedoma) in northern Alaska, Itkillik River exposure. *Quaternary research*, 75(3), 584-596.
- Kanevskiy, M., Shur, Y., Jorgenson, M. T., Ping, C. L., Michaelson, G. J., Fortier, D., ... & Tumskoy, V. (2013). Ground ice in the upper permafrost of the Beaufort Sea coast of Alaska. *Cold Regions Science and Technology*, 85, 56-70.
- Kanevskiy, M., Jorgenson, T., Shur, Y., O'Donnell, J. A., Harden, J. W., Zhuang, Q., & Fortier, D. (2014). Cryostratigraphy and permafrost evolution in the lacustrine lowlands of west-central Alaska. *Permafrost and Periglacial Processes*, 25(1), 14-34.
- Kokelj, S. V., & Burn, C. R. (2003). Ground ice and soluble cations in near-surface permafrost, Inuvik, Northwest Territories, Canada. *Permafrost and Periglacial Processes*, 14(3), 275-289.
- Kokelj, S. V., Zajdlik, B., & Thompson, M. S. (2009). The impacts of thawing permafrost on the chemistry of lakes across the subarctic boreal-tundra transition, Mackenzie Delta region, Canada. *Permafrost and Periglacial Processes*, 20(2), 185-199.

- Kurylyk, B. L., & Hayashi, M. (2016). Improved Stefan equation correction factors to accommodate sensible heat storage during soil freezing or thawing. *Permafrost and Periglacial Processes*, 27(2), 189-203.
- Lacelle, D., St-Jean, M., Lauriol, B., Clark, I. D., Lewkowitz, A., Froese, D. G., ... & Zazula, G. (2009). Burial and preservation of a 30,000 year old perennial snowbank in Red Creek valley, Ogilvie Mountains, central Yukon, Canada. *Quaternary Science Reviews*, 28(27-28), 3401-3413.
- Lacelle, D. (2011). On the $\delta^{18}\text{O}$, δD and D-excess relations in meteoric precipitation and during equilibrium freezing: theoretical approach and field examples. *Permafrost and Periglacial Processes*, 22(1), 13-25.
- Lacelle, D., Fontaine, M., Forest, A. P., & Kokelj, S. (2014). High-resolution stable water isotopes as tracers of thaw unconformities in permafrost: A case study from western Arctic Canada. *Chemical Geology*, 368, 85-96.
- Lachniet, M. S., Lawson, D. E., Stephen, H., Sloat, A. R., & Patterson, W. P. (2016). Isoscapes of $\delta^{18}\text{O}$ and $\delta^2\text{H}$ reveal climatic forcings on Alaska and Yukon precipitation. *Water Resources Research*, 52(8), 6575-6586.
- Lapalme, C. M., Lacelle, D., Davila, A. F., Pollard, W., Fortier, D., & McKay, C. P. (2015, September). Cryostratigraphy of near-surface permafrost in University Valley, McMurdo Dry Valleys of Antarctica. In Conference Paper: GeoQuebec (p. 2015).
- Lee, H., Swenson, S. C., Slater, A. G., & Lawrence, D. M. (2014). Effects of excess ground ice on projections of permafrost in a warming climate. *Environmental Research Letters*, 9(12), 124006.
- Lewkowitz, A. G., & Harris, C. (2005). Morphology and geotechnique of active-layer detachment failures in discontinuous and continuous permafrost, northern Canada. *Geomorphology*, 69(1-4), 275-297.
- Li, H., Yang, Z. J., & Wang, J. (2018). Unfrozen water content of permafrost during thawing by the capacitance technique. *Cold Regions Science and Technology*, 152, 15-22.
- Mackay, J. R. (1972). The world of underground ice. *Annals of the Association of American Geographers*, 62(1), 1-22.
- Mackay, J. R. (1983). Downward water movement into frozen ground, western arctic coast, Canada. *Canadian Journal of Earth Sciences*, 20(1), 120-134.

- Mackay, J. R. (1990). Seasonal growth bands in pingo ice. *Canadian Journal of Earth Sciences*, 27(8), 1115-1125.
- Mackay, J. R., & Dallimore, S. R. (1992). Massive ice of the Tuktoyaktuk area, western Arctic coast, Canada. *Canadian Journal of Earth Sciences*, 29(6), 1235-1249.
- Mann, D. H., Groves, P., Reanier, R. E., & Kunz, M. L. (2010). Floodplains, permafrost, cottonwood trees, and peat: What happened the last time climate warmed suddenly in arctic Alaska?. *Quaternary Science Reviews*, 29(27-28), 3812-3830.
- McCave, I. N., & Syvitski, J. P. (1991). Principles and methods of geological particle size analysis. Principles, methods and application of particle size analysis, 3-21.
- McClymont, A. F., Hayashi, M., Bentley, L. R., & Christensen, B. S. (2013). Geophysical imaging and thermal modeling of subsurface morphology and thaw evolution of discontinuous permafrost. *Journal of Geophysical Research: Earth Surface*, 118(3), 1826-1837.
- Michel, F. A. (1986). Isotope geochemistry of frost-blister ice, North Fork pass, Yukon, Canada. *Canadian Journal of Earth Sciences*, 23(4), 543–549. <https://doi.org/10.1139/e86-054>
- Michel, F. A. (1990, June). Isotopic composition of ice-wedge ice in northwestern Canada. In *Proceedings, Fifth Canadian Permafrost Conference, Nordicana* (Vol. 54, pp. 5-9).
- Michel, F. A. (2011). Isotope Characterisation of Ground Ice in Northern Canada Eureka, 12(November 2009), 3–12. <https://doi.org/10.1002/ppp.721>
- Michel, F. A., Fritz, P., & French, H. M. (1982). Significance of isotope variations in permafrost waters at Illisarvik, NWT. In *Proceedings of the Fourth Canadian Permafrost Conference* (pp. 173-181). National Research Council of Canada.
- Muller, S. W. (1943). Permafrost or permanently frozen ground and related engineering problems. US. Engineer. Office, Strat. Engineer. Study Spec. Rep, 62.
- Muller, S. W. (1947). *Permafrost or permanently frozen ground and related engineering problems*. J.W. Edwards, Inc.
- Murton, B., & French, H. M. (1994). Cryostructures in permafrost, Tuktoyaktuk coastlands, western arctic Canada. *Canadian Journal of Earth Sciences*, 31, 737–747.
- “National Snow and Ice Data Center.” *SOTC: Permafrost and Frozen Ground | National Snow and Ice Data Center*, 4 Apr. 2017, nsidc.org/cryosphere/sotc/permafrost.html.

- Nelson, F. E., & Outcalt, S. I. (1987). A computational method for prediction and regionalization of permafrost. *Arctic and Alpine Research*, 19(3), 279-288.
- Nikolayev, V. I., & Mikhalev, D. V. (1995). An oxygen-isotope paleothermometer from ice in siberian permafrost. *Quaternary Research*, 43, 14–21.
<https://doi.org/10.1016/j.solener.2019.02.027>
- National Research Council Canada (1989). Glossary of permafrost and related ground-ice terms. Associate Committee on Geotechnical Research, National Research Council of Canada, Ottawa, 156.
- O’Neil, J. R. (1968). Hydrogen and oxygen isotope fractionation between ice and water. *Journal of Physical Chemistry*, 72(10), 3683–3684. <https://doi.org/10.1021/j100856a060>
- Opel, T., Wetterich, S., Meyer, H., Dereviagin, Y. A., Fuchs, C. M., & Schirmer, L. (2017). Ground-ice stable isotopes and cryostratigraphy reflect late Quaternary palaeoclimate in the Northeast Siberian Arctic (Oyogos Yar coast, Dmitry Laptev Strait). *Climate of the Past*, 13(6), 587–611. <https://doi.org/10.5194/cp-13-587-2017>
- Osterkamp, T. E., & Burn, C. R. (2003). Permafrost.
- Pihlainen, J. A., & Johnston, G. H. (1963). Guide to a field description of permafrost for engineering purposes (Vol. 79, p. 21). National Research Council, Canada, Associate Committee on Soil and Snow Mechanics.
- Subcommittee, P. (1988). Glossary of permafrost and related ground-ice terms. *Associate Committee on Geotechnical Research, National Research Council of Canada, Ottawa, 156.*
- Porter, T. J., Froese, D. G., Feakins, S. J., Bindeman, I. N., Mahony, M. E., Pautler, B. G., ... Weijers, J. W. H. (2016). Multiple water isotope proxy reconstruction of extremely low last glacial temperatures in Eastern Beringia (Western Arctic). *Quaternary Science Reviews*, 137, 113–125. <https://doi.org/10.1016/j.quascirev.2016.02.006>
- Porter, T. J., Schoenemann, S. W., Davies, L. J., Steig, E. J., Bandara, S., & Froese, D. G. (2019). Recent summer warming in northwestern Canada exceeds the Holocene thermal maximum. *Nature communications*, 10(1), 1-10.
- Porter, T. J., & Opel, T. (2020). Recent advances in paleoclimatological studies of Arctic wedge- and pore-ice stable-water isotope records. *Permafrost and Periglacial Processes*.

- Riseborough, D., Shiklomanov, N., Etzelmuller, B., Gruber, S., & Marchenko, S. (2008). Recent Advances in Permafrost Modelling. *Permafrost and Periglacial Processes*, 19, 137–156. <https://doi.org/10.1002/ppp>
- Scapozza, C., Lambiel, C., Baron, L., Marescot, L., & Reynard, E. (2011). Internal structure and permafrost distribution in two alpine periglacial talus slopes, Valais, Swiss Alps. *Geomorphology*, 132(3–4), 208–221. <https://doi.org/10.1016/j.geomorph.2011.05.010>
- Schwamborn, G., Meyer, H., Fedorov, G., Schirrmeister, L., & Hubberten, H. W. (2006). Ground ice and slope sediments archiving late Quaternary paleoenvironment and paleoclimate signals at the margins of El'gygytgyn Impact Crater, NE Siberia. *Quaternary Research*, 66(2), 259–272. <https://doi.org/10.1016/j.yqres.2006.06.007>
- Shur, Y. L. (1988). Upper horizon of permafrost and thermokarst. *USSR Academy of Sciences, Siberian Branch: Novosibirsk, Russia*, 210.
- Shur, Y., Hinkel, K. M., & Nelson, F. E. (2005). The transition layer: implications for geocryology and climate-change science. *Permafrost and Periglacial Processes*, 16(1), 5–17. <https://doi.org/10.1002/ppp.518>
- Schuur, E. A., Bockheim, J., Canadell, J. G., Euskirchen, E., Field, C. B., Goryachkin, S. V., ... & Zimov, S. A. (2008). Vulnerability of permafrost carbon to climate change: Implications for the global carbon cycle. *BioScience*, 58(8), 701-714.
- Sjöberg, Y., Marklund, P., Pettersson, R., & Lyon, S. W. (2015). Geophysical mapping of peatland permafrost. *Cryosphere*, 9(2), 465–478. <https://doi.org/10.5194/tc-9-465-2015>
- Souchez, R. A., & Jouzel, J. (1984). On the isotopic composition in dD and d18O of water and ice during freezing. *Journal of Glaciology*, 30(106), 369–372. <https://doi.org/10.1017/S0022143000006249>
- Stephani, E., Fortier, D., & Shur, Y. (2010). Applications of cryofacies approach to frozen ground engineering – Case study of a road test site along the Alaska Highway (Beaver Creek, Yukon, Canada). 63rd Canadian Geotechnical Conference & 6th Canadian Permafrost Conference, (1963), 476–483. Retrieved from <http://136.159.35.81/cpc/CPC6-476.pdf>
- Stumpp, C., Klaus, J., & Stichler, W. (2014). Analysis of long-term stable isotopic composition in German precipitation. *Journal of Hydrology*, 517, 351-361.

- Subcommittee, P. (1988). Glossary of permafrost and related ground-ice terms. *Associate Committee on Geotechnical Research, National Research Council of Canada, Ottawa*, 156.
- Sugimoto, A., Naito, D., Yanagisawa, N., Ichianagi, K., Kurita, N., Kubota, J., ... Fedorov, A. N. (2003). Characteristics of soil moisture in permafrost observed in East Siberian taiga with stable isotopes of water. *Hydrological Processes*, 17, 1073–1092.
<https://doi.org/10.1002/hyp.1180>
- Suzuoki, T., & Kimura, T. (1973). D/H and 18O/16O Fractionation in Ice-Water System. *Journal of the Mass Spectrometry Society of Japan*, 21(3), 229–233.
<https://doi.org/10.5702/masspec1953.21.229>
- Throckmorton, H. M., Newman, B. D., Heikoop, J. M., Perkins, G. B., Feng, X., Graham, D. E., ... & Wilson, C. J. (2016). Active layer hydrology in an arctic tundra ecosystem: quantifying water sources and cycling using water stable isotopes. *Hydrological Processes*, 30(26), 4972-4986.
- Throop, J., Lewkowicz, A. G., & Smith, S. L. (2012). Climate and ground temperature relations at sites across the continuous and discontinuous permafrost zones, northern Canada. *Canadian Journal of Earth Sciences*, 49(8), 865–876. <https://doi.org/10.1139/E11-075>
- Van Everdingen, R. O. (1982). Frost Blisters of the Bear Rock Spring Area near Fort Norman, N.W.T. *Arctic*, 35(2), 243–265.
- Vanhala, H., Lintinen, P., & Ojala, A. (2009). Electrical resistivity study of permafrost on Ridnitšohkka fell in northwest Lapland, Finland. *Geophysica*, 45(1–2), 103–118.
- Vardy, S. R., Warner, B. G., & Aravena, R. (1997). Holocene climate effects on the development of a peatland on the Tuktoyaktuk Peninsula, northwest territories. *Quaternary Research*, 47(1), 90–104. <https://doi.org/10.1006/qres.1996.1869>
- Vardy, S. R., Warner, B. G., & Aravena, R. (1998). Holocene climate and the development of a subarctic peatland near Inuvik, Northwest Territories, Canada. *Climate Change*, 40, 285–313.
- Vasil'chuk, Y. K., Vasil'chuk, A. C., Rank, D., Kutschera, W., & Kim, J. C. (2001). Radiocarbon dating of $\delta^{18}\text{O}$ - δD plots in late pleistocene ice-wedges of the duvanny yar (Lower Kolyma River, Northern Yakutia). *Radiocarbon*, 43(2 PART II), 541–553.
<https://doi.org/10.1017/s0033822200041199>

- Vasil'chuk, Y., & Vasil'chuk, A. (2014). Spatial distribution of mean winter air temperatures in Siberian permafrost at 20-18 ka BP using oxygen isotope data. *Boreas*, 43(3), 678–687. <https://doi.org/10.1111/bor.12033>
- Vasil'chuk, Y. K., Lawson, D. E., Yoshikawa, K., Budantseva, N. A., Chizhova, J. N., Podborny, Y. Y., & Vasil'chuk, A. C. (2016). Stable isotopes in the closed-system Weather Pingo, Alaska and Pestsovoye Pingo, northwestern Siberia. *Cold Regions Science and Technology*. <https://doi.org/10.1016/j.coldregions.2016.05.001>
- Wang, Y., Jin, H., & Li, G. (2016). Investigation of the freeze-thaw states of foundation soils in permafrost areas along the China-Russia Crude Oil Pipeline (CRCOP) route using ground-penetrating radar (GPR). *Cold Regions Science and Technology*, 126, 10–21. <https://doi.org/10.1016/j.coldregions.2016.02.013>
- Watanabe, K., & Wake, T. (2009). Measurement of unfrozen water content and relative permittivity of frozen unsaturated soil using NMR and TDR. *Cold Regions Science and Technology*, 59(1), 34–41. <https://doi.org/10.1016/j.coldregions.2009.05.011>
- Watson, G. H., Slusarchuk, W. A., & Rowley, R. K. (1973). Determination of Some Frozen and Thawed Properties of Permafrost Soils. *Canadian Geotechnical Journal*, 10(4), 592–606. <https://doi.org/10.1139/t73-055>
- Wentworth, C. K. (1922). A Scale of Grade and Class Terms for Clastic Sediments. *The Journal of Geology*, 30(5), 377–392. <https://doi.org/10.1086/622910>
- Williams, P. J. (1995). Permafrost and climate change : geotechnical implications. *Philosophical Transaction of the Royal Society*, 352, 347–358.
- Wolter, J., Lantuit, H., Fritz, M., Macias-Fauria, M., Myers-Smith, I., & Herzschuh, U. (2016). Vegetation composition and shrub extent on the Yukon coast, Canada, are strongly linked to ice-wedge polygon degradation. *Polar Research*, 35(1), 27489.
- Woo, M. K. (1986). Permafrost hydrology in north america. *Atmosphere-Ocean*, 24(3), 201-234.
- Woo, M., & Steer, P. (1983). Slope hydrology as influenced by thawing of the active layer, Resolute, N. W.T. *Canadian Journal of Earth Sciences*, 20, 978–986.
- Wright, N., Hayashi, M., & Quinton, W. L. (2009). Spatial and temporal variations in active layer thawing and their implication on runoff generation in peat-covered permafrost terrain. *Water Resources Research*, 45(5).

- Yang, Y., Jiang, G., & Zhang, P. (2017). Stable Isotopic Stratification and Growth Patterns of Ground Ice in Permafrost on the Qinghai-Tibet Plateau, China. *Permafrost and Periglacial Processes*, 28, 119–129. <https://doi.org/10.1002/ppp.1892>
- Yanovsky, V. K. (1933). Expedition to Pechora River to determine the position of the southern permafrost boundary. *Reports of the Committee for Permafrost Investigations*, 5(2), 65-149.
- Yershov, E. D. (2004). *General geocryology*. Cambridge university press.
- Yoshikawa, K., Sharkhuu, N., & Sharkhuu, A. (2013). Groundwater hydrology and stable isotope analysis of an open-system pingo in Northwestern Mongolia. *Permafrost and Periglacial Processes*, 24(3), 175–183. <https://doi.org/10.1002/ppp.1773>
- Zhang, T., Heginbottom, J. A., Barry, R. G., & Brown, J. (2000). Further statistics on the distribution of permafrost and ground ice in the Northern Hemisphere. *Polar geography*, 24(2), 126-131.
- Zhu, X., Wu, T., Li, R., Xie, C., Hu, G., Qin, Y., ... & Yang, C. (2017). Impacts of summer extreme precipitation events on the hydrothermal dynamics of the active layer in the Tanggula permafrost region on the Qinghai-Tibetan plateau. *Journal of Geophysical Research: Atmospheres*, 122(21), 11-54.

3. REGIONAL SETTING AND SITE DESCRIPTIONS

3.1. Geography

The study location for this project is physiographically located within the Southern Ogilvie Mountains, Yukon Territory, Canada (Gordey and Makepeace, 1999) (Fig. 1). This area is located within the traditional territory of the Tr'ondek Gwich'in, north of Tombstone Provincial Park along the Dempster Highway. At present, the region is accessed by the Dempster Highway. Built between 1959-1978, the Dempster Highway is an important supply route connecting communities between Dawson City, Y.T. and Inuvik, N.W.T. The road has been the focus of recent geotechnical projects concerned with road integrity and thaw degradation (e.g. Idrees et al., 2015), and provides access for permafrost-related research into an otherwise difficult to access region.

This project is focused on two locations along the Dempster Highway within the Southern Ogilvie Mountains. The Blackstone 2019 collection area (BS19) is located at 64.920°N, 138.284°W, at approximately kilometer 126 of the Dempster Highway (Fig. 1). This chapter describes the bedrock geology, Quaternary history, climate, vegetation, soils and permafrost conditions of the study region and collection area.

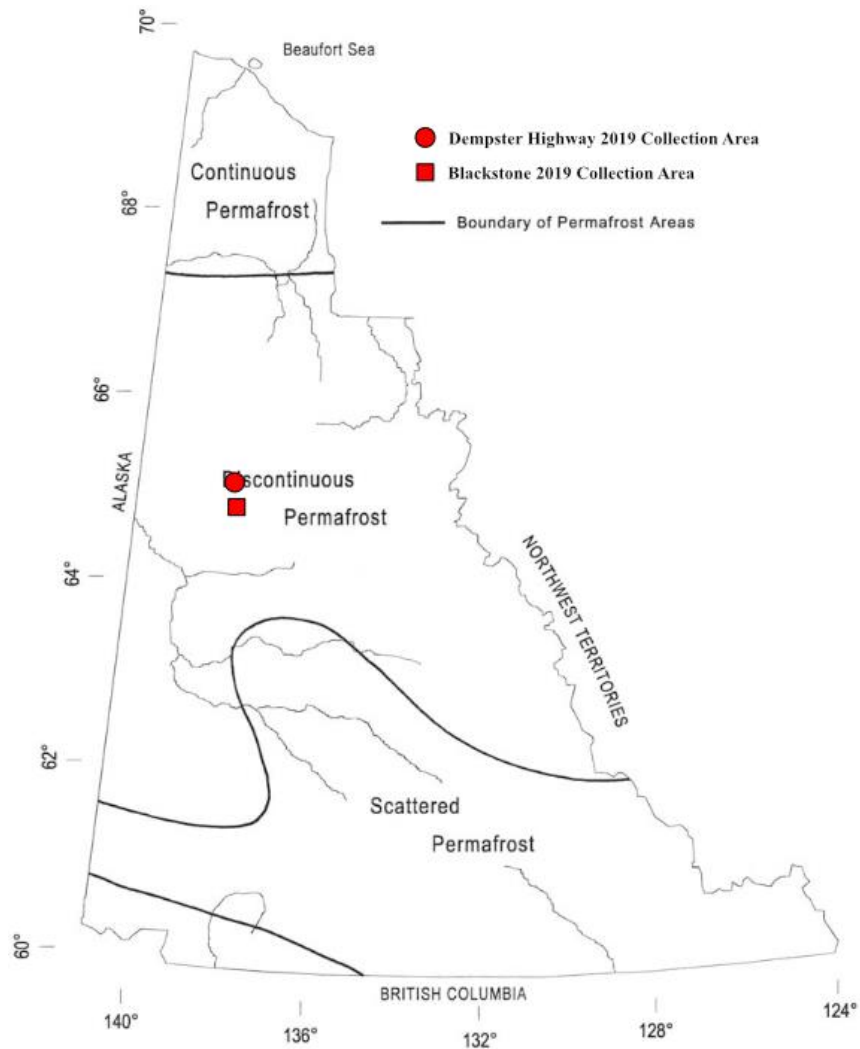


Figure 3.1. Regional map of the Yukon showing study site locations and general boundaries of permafrost zones. Adapted from Scudder (1997).

3.2. Bedrock Geology and Quaternary History

3.2.1. Bedrock geology

Local bedrock around the BS19 collection area include siltstones, sandstones, conglomerates, shales, slates, dolostone, and limestone ranging between the Paleoproterozoic to Middle Permian (Fig. 2).

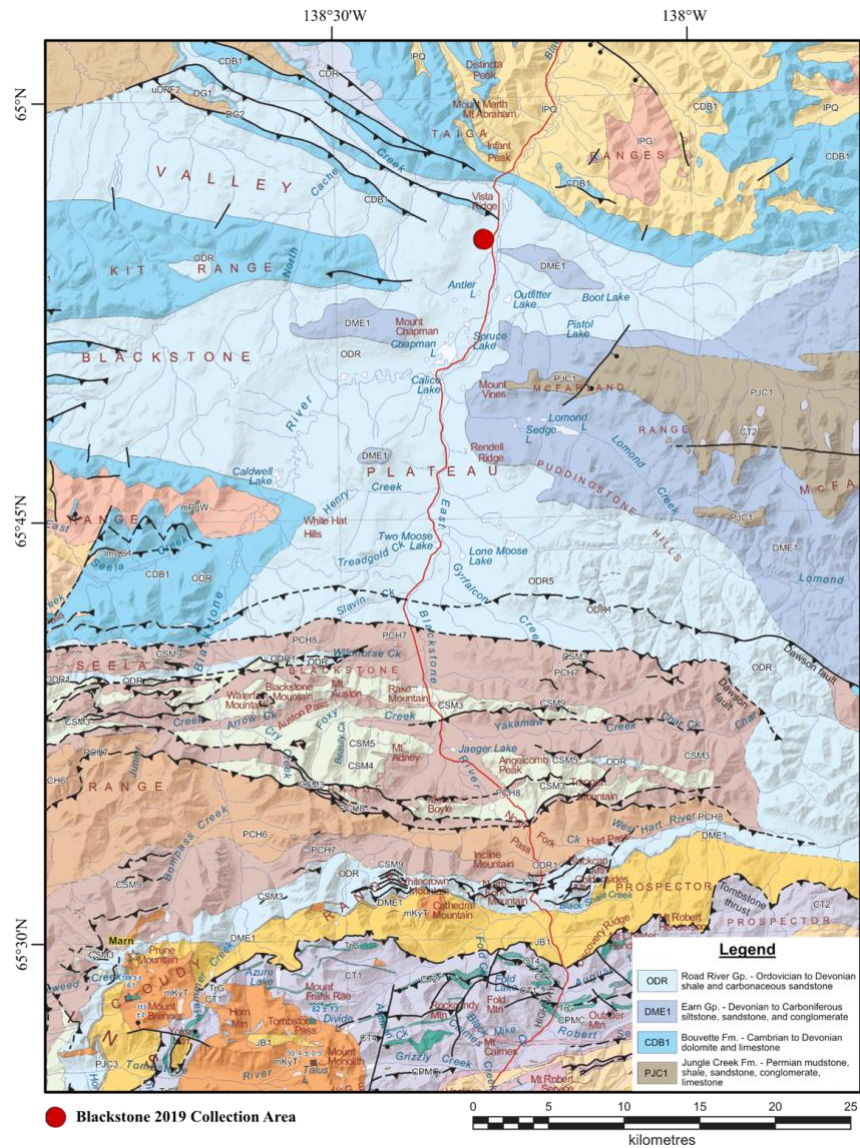


Figure 3.2. Bedrock geology within the Chapman Lake region. Red line represents the Dempster Highway. Location of the BS19 collection area is located at the red dot. Adapted from Yukon Geological Survey bedrock map for NTS regions 116B and 116C.

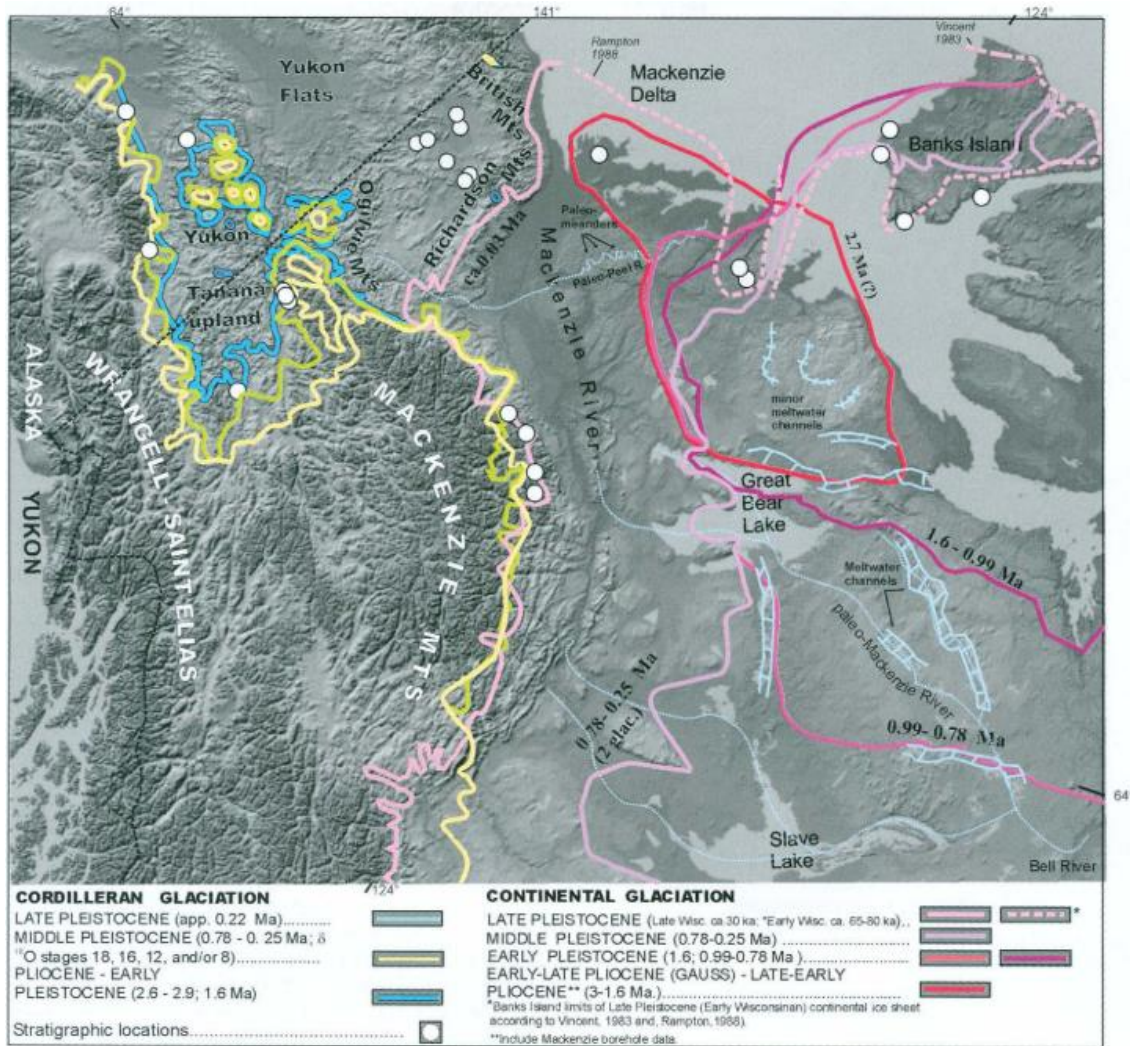


Figure 3.3. Extent of Pliocene and Pleistocene Cordilleran and continental glaciations in northwestern Canada and eastern Alaska (from Duk’Rodkin et al., 2004).

3.2.2. Quaternary history

Age correlations of glacial stratigraphy and geomorphology in the Tintina Trench region south of the Ogilvie Mountains are traditionally based on the degree of pedogenic development of paleosols within tills and geographic relations between moraines (Duk-Rodkin et al., 1996). Pre-Reid glaciations generally have thick Luvisols that developed during warmer periods (i.e. interglacials) (Westgate et al., 2001). Reduced extent of successive Late Cenozoic Cordilleran

glaciations was likely caused by uplift-driven aridification of accumulation areas in the St. Elias Mountains (Westgate et al., 2001; Duk-Rodkin et al., 2004).

Such correlations are relatively scarce for the Dempster Highway Corridor, leaving the glacial history of this region poorly constrained. Chapman Lake, a kettle lake in the Blackstone River Valley that is located a few kilometers south of BS19, and its associated Chapman Lake Moraine was initially ascribed a Reid age by Duk-Rodkin et al. (1996) and later a McConnell age by Beirele (2002). However, it is now understood that the Chapman Lake Moraine is pre-McConnell in age, likely deposited during MIS-4 (Briner et al., 2005).

The spatial relation of BS19 with the Chapman Lake Moraine provides broad maximum ages on the stratigraphy of the site. BS19 is located a few kilometers north of the hummocky Chapman Lake Moraine terrain, along a hillslope composed of cobble-silt diamict, overlain by a peat veneer. The location was mapped as a Reid-age moraine complex by Duk-Rodkin (1996). The shallow slope and well-rounded morphology of the hill suggest the terrain has been eroded by fluvial and slope processes since deposition.

3.3. Climate

Regional climate is subarctic continental (Wahl et al., 1987). At Dawson City, 1981-2010 climate normal data spanning 27 years indicate a mean annual temperature of -4.1°C. Mean annual precipitation was 324mm, 62% of which fell as rain. Most precipitation fell during the summer months (Environment and Climate Change Canada).

3.4. Soils, Vegetation and Hydrology

The BS19 collection area is located within the Northern Ogilvie Mountains ecoregion of the Taiga Cordillera ecozone (ESWG, 1996). The Northern Ogilvie Mountains ecoregion is associated with flat-topped and rounded hills and flat-bottomed river valleys sculpted from a former plain. Despite its broader inclusion within the discontinuous permafrost region, this ecoregion hosts continuous permafrost with medium to high ground ice contents owing to the higher elevation. Turbic and Static Cryosols are the dominant soil types within minor Eutric Brunisols and Melanic Brunisols within non-permafrost-affected soils (Fig. 3.4). Vegetation types are dominantly white spruce, ericaceous shrubs, dwarf willow, dwarf birch, with moss and lichen groundcover.

BS19 is located in the more locally defined Ogilvie River ecodistricts (ESWG, 1996). The Ogilvie River ecodistrict is characterized by broad valleys hosting an open vegetation structure dominated by ericaceous shrubs, dwarf species, mosses, and lichens, lacking taller vegetation types.

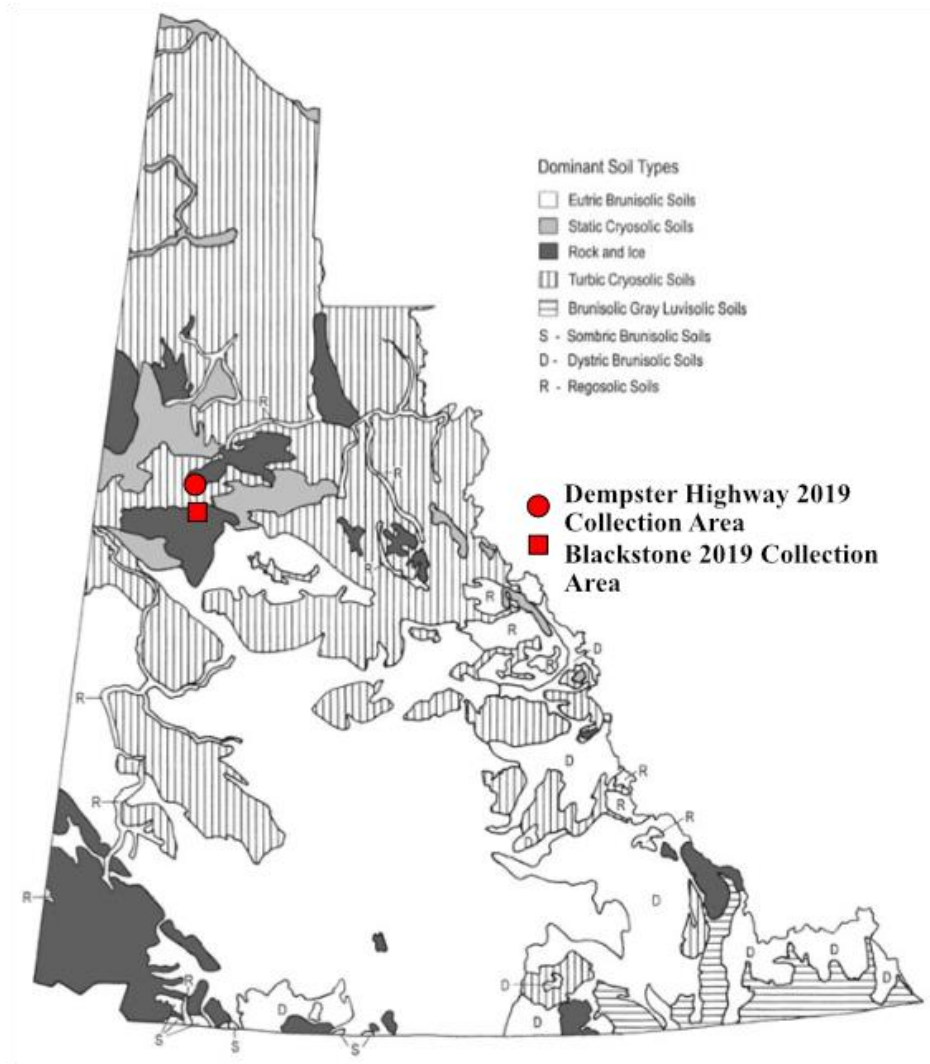


Figure 3.4. Soil classification map of Yukon Territory (from Scutter, 1997, after Agriculture Canada Expert Committee on Soil Survey 1987).

3.5. Collection Area Description

The Blackstone 2019 (BS19) collection area is located on the west side of the Dempster Highway ~10km north of Chapman Lake. Distance from the top of hill to the Dempster Highway is 1km, spanning an elevation range of 937 to 970m a.s.l. and an elevation difference of 33m. The hill slopes gently to the southeast. Progressing from northeast to southwest, the collection area is dominated by a broad, convex interfluvium bounded on its SW edge by a comparatively narrower gully oriented NW to SE. A concave region topographically separates the NW (upslope) end of the interfluvium from the greater valley side slope. Soil stratigraphy extending from the hilltop to the toeslope along the interfluvium is bimodal, with a relatively thin cover of Sphagnum-dominated peat underlain by pebbly-silty and sandy-silty diamicts. The thickness of the organic horizon is significantly greater between the interfluvium toe slope and Dempster Highway (Fig. 3.6D).

Turbic Cryosols (CSSC, 1998) are the dominant soil type in the BS19 collection area, particularly between the hillcrest and foot slope. They are also found in the bottom of the gully forming the southwest edge of the interfluve and on valley-bottom fen hummocks, though Organic Cryosols tend to be the dominant soil type in these zones. Static Cryosols are generally

less frequent in the BS19 collection area. They are more commonly found in the concave areas surrounding the interfluve.

Vegetation assemblages varied across the surface of the collection area with respect to local topography and soil moisture (Fig. 3.6). Drier soil moisture conditions generally coincided with more ericaceous shrubs, including *Betula nana* (dwarf birch) and *Salix spp.* These drier locations were found on tussocks within the gully riparian zone, on hummocks at proximal slope zones, and across the hilltop. By contrast, backslope positions hosted less ericaceous shrub cover and shorter average tussock heights, indicating that these tussocks were not as effective at providing the dry

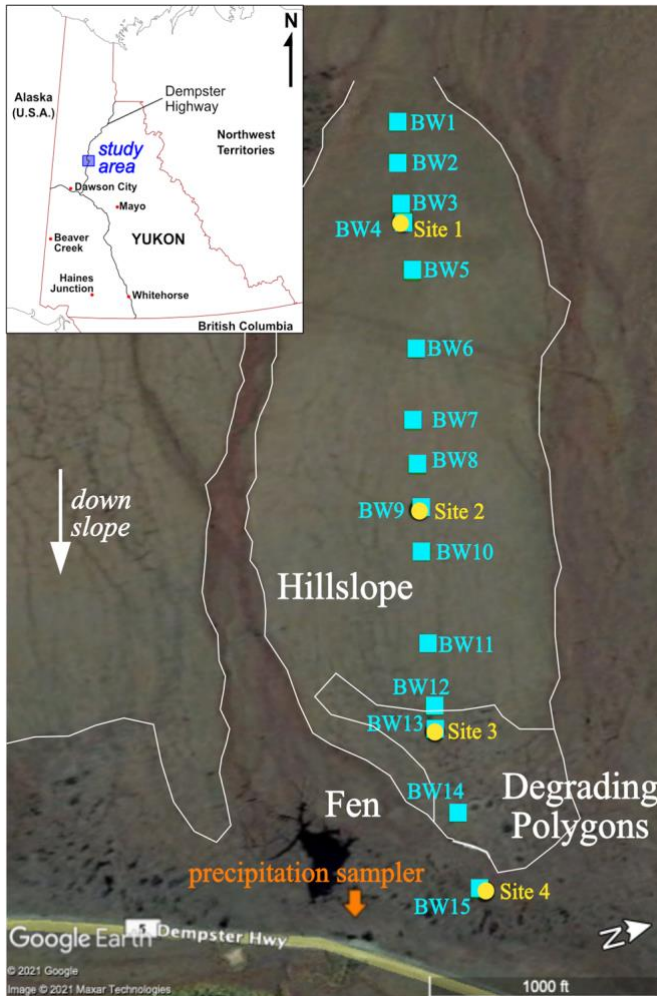


Figure 3.5. Map of sites and zones at the BS19 collection area. Satellite imagery from (Google Earth). *Blue squares* - September 2019 basal active layer waters; *yellow circles* - permafrost cores.

conditions favored by ericaceous shrubs. Consequently, these positions are characterized by low abundance of *Betula nana* and *Salix spp.*, but are most abundantly associated with *Eriophorum*

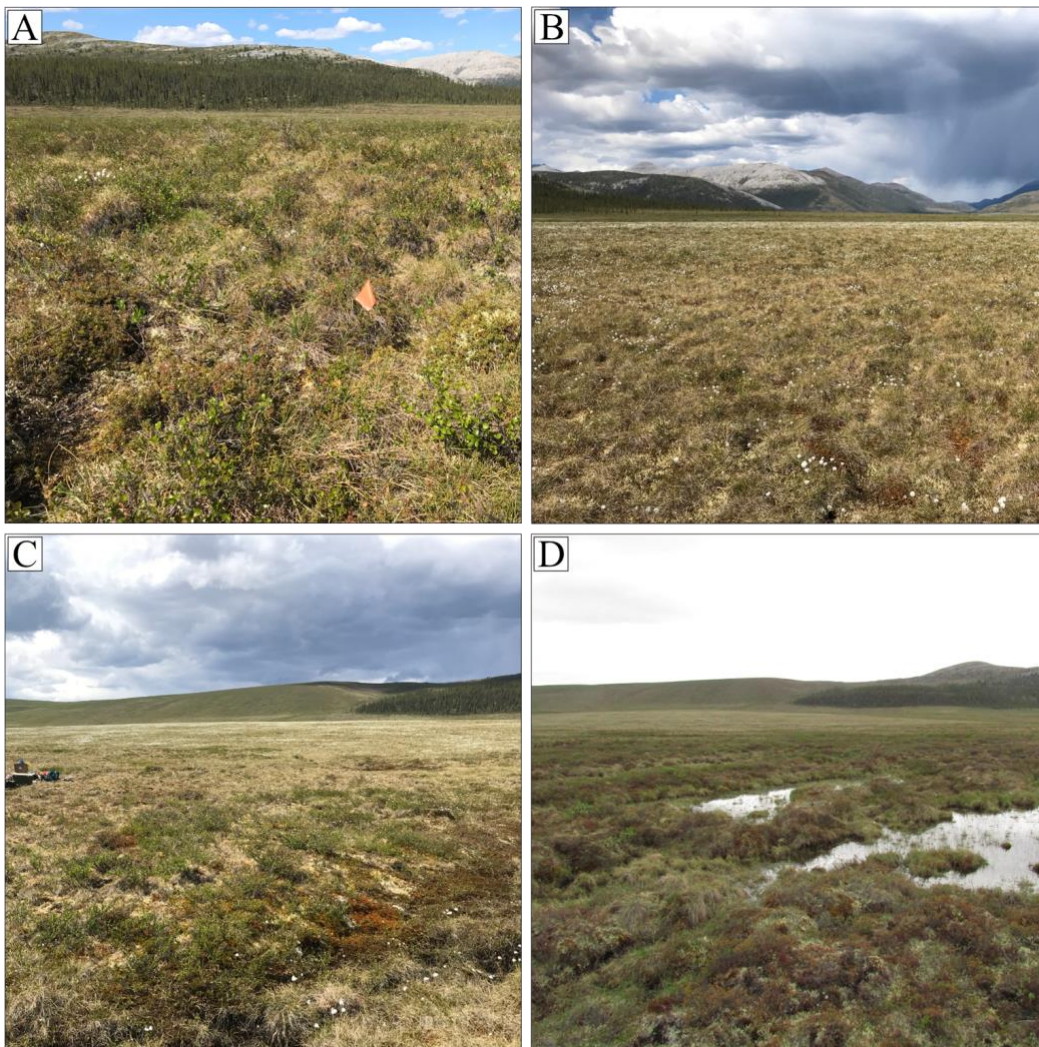


Figure 3.6. BS19 vegetation and topography at: A) hilltop - higher tussocks, dwarf birch and willows, thin peat; B) middle slope- shorter tussocks, more blooming tundra cotton, moss-covered wedges visible, thin peat; C) *degrading polygon area* - average surface water pH of 4.7, vegetation transitional between middle slope and fen, flat-centered ice wedge polygons, ice wedge surface troughs wetter and wider than on the hillslope with saturated moss lawns, thermokarst pools frequent at ice wedge intersections; D) *fen* - average surface water pH of 6.1, crude flark-and-hummock topography, moderate to high dwarf birch density on hummocks.

(cotton grass). These are generally found in association with small tussocks.

Peatland classifications ascribed to the BS19 collection area are based on the framework set out by the National Wetlands Working Group in 1997. BS19 is hydrologically classified as a bog, but can be further classified on the basis of ground morphology and water chemistry. The *hillslope* is best classified as a blanket bog, but also includes shallow ice wedge polygon troughs associated with lowland polygon bogs. The *degrading polygon zone* is a lowland polygon bog which, at the time of study, was experiencing the onset of thermal degradation, with standing water beginning to pool within polygon troughs and form budding thermokarst ponds at ice wedge intersections. The *fen* is transitional between a string bog, with crudely arranged strings and flarks generally oriented perpendicular to water flow from south to north, and a poor horizontal fen.

References

- Beierle, B. D. (2002). Late Quaternary glaciation in the Northern Ogilvie Mountains: revised correlations and implications for the stratigraphic record. *Canadian Journal of Earth Sciences*, 39(11), 1709-1717.
- Briner, J. P., Kaufman, D. S., Manley, W. F., Finkel, R. C., & Caffee, M. W. (2005). Cosmogenic exposure dating of late Pleistocene moraine stabilization in Alaska. *Geological Society of America Bulletin*, 117(7-8), 1108-1120.
- Canadian Agricultural Services Coordinating Committee. Soil Classification Working Group, Soil Classification Working Group, National Research Council Canada, Canada. Agriculture, & Agri-Food Canada. Research Branch. (1998). *The Canadian system of soil classification* (No. 1646). NRC Research Press.
- Cwynar, L. C., & Spear, R. W. (1995). Paleovegetation and Paleoclimatic Changes in the Yukon at 6 ka BP. *Géographie Physique et Quaternaire Paleovegetation*, 49(1), 29–35.
- Davies, L. J. (2018). The development of a Holocene cryptotephra framework in northwestern North America.
- Duk-Rodkin, A., & Hinds, S. J. (1996). *Surficial geology, Dawson, Yukon Territory*. Geological Survey of Canada.
- Duk-Rodkin, A., Barendregt, R. W., Tarnocai, C., & Phillips, F. M. (1996). Late Tertiary to late Quaternary record in the Mackenzie Mountains, Northwest Territories, Canada:

- stratigraphy, paleosols, paleomagnetism, and chlorine-36. *Canadian Journal of Earth Sciences*, 33(6), 875-895.
- Ecological Stratification Working Group (ESWG). 1996. *A national ecological framework for Canada*. Ottawa: Agriculture and Agri-Food Canada, Research Branch, Centre for Land and Biological Resources Research; and Ottawa: Environment Canada, State of the Environment Directorate, Ecozone Analysis Branch.
- Environment and Climate Change Canada. (2016). *Canadian Climate Normals*. Retrieved from https://climate.weather.gc.ca/climate_normals/index_e.html.
- Environment and Climate Change Canada. 1981-2010 Climate Normals & Averages. https://climate.weather.gc.ca/climate_normals/index_e.html
- Duk-Rodkin, A., Barendregt, R. W., Froese, D. G., Weber, F., Enkin, R., Smith, I. R., ... & Klassen, R. (2004). Timing and extent of Plio-Pleistocene glaciations in north-western Canada and east-central Alaska. In *Developments in Quaternary Sciences* (Vol. 2, pp. 313-345). Elsevier.
- Environment Yukon. (2014). *The Dempster Highway Travelogue*. Whitehorse, Yukon Territory, Canada: Yukon Government.
- Gordey, S.P. and Makepeace, A.J. (comp.) 1999: Yukon bedrock geology in Yukon digital geology, S.P. Gordey and A.J. Makepeace (comp.); Geological Survey of Canada Open File D3826 and Exploration and Geological Services Division, Yukon, Indian and Northern Affairs Canada, Open File 1999-1(D)
- Idrees, M., Burn, C. R., Moore, J. L., & Calmels, F. (2015, September). Monitoring permafrost conditions along the Dempster Highway. In *7th Canadian Permafrost Conference: Proceedings of a conference held* (pp. 20-23).
- National Wetlands Working Group (NWWG). (1997). *The Canadian wetland classification system*. Wetlands Research Branch, University of Waterloo.
- Porter, T. J., Schoenemann, S. W., Davies, L. J., Steig, E. J., Bandara, S., & Froese, D. G. (2019). Recent summer warming in northwestern Canada exceeds the Holocene thermal maximum. *Nature communications*, 10(1), 1-10.
- Prairie Climate Centre. *The Climate Atlas of Canada* (version 2, July 10, 2019). <https://climateatlas.ca>

- Froese, D. G., Zazula, G. D., Westgate, J. A., Preece, S. J., Sanborn, P. T., Reyes, A. V., & Pearce, N. J. G. (2009). The Klondike goldfields and Pleistocene environments of Beringia. *GSA Today*, 19(8), 4–10. <https://doi.org/10.1130/GSATG54A.1>
- Lacelle, D., Lauriol, B., Clark, I. D., Cardyn, R., & Zdanowicz, C. (2007). Nature and origin of a Pleistocene-age massive ground-ice body exposed in the Chapman Lake moraine complex, central Yukon Territory, Canada. *Quaternary Research*, 68(2), 249-260.
- Scudder, G. G. E. (1997). Environment of the Yukon. *Insects of the Yukon. Biological Survey of Canada (Terrestrial Arthropods)*, Ottawa, 13-57.
- Valentine, K. W. G., Tarnocai, C., Kimpe, C. D., King, R., Dormaar, J., Vreeken, W., & Harris, S. A. (1987). Some aspects of Quaternary soils in Canada. *Canadian journal of soil science*, 67(2), 221-247.
- Wahl, H. E., Fraser, D. B., Harvey, R. C., & Maxwell, J. B. (1987). Climate of Yukon. Environment Canada. *Atmospheric Environment Service, Climatological Studies*, 40(0).
- Westgate, J. A., Preece, S. J., Froese, D. G., Walter, R. C., Sandhu, A. S., & Schweger, C. E. (2001). Dating early and middle (Reid) Pleistocene glaciations in central Yukon by tephrochronology. *Quaternary Research*, 56(3), 335-348.
- Yukon Geological Survey. *Bedrock Geology, Dawson (116B & 116C), Yukon* [map]. 1:250,000. Centre for Topographical Information, Natural Resources Canada, May 2018.
- Yukon Geological Survey. *Bedrock Geology, Ogilvie River (116F & 116G), Yukon* [map]. 1:250,000. Centre for Topographical Information, Natural Resources Canada, May 2018.

4. METHODOLOGY

4.1. Water Sample Collection

Precipitation, active layer water, and surface water samples were collected during the second field period of September 11-18, 2019. Precipitation water was collected at two separate IAEA-designed rain samplers (Palmex) at KM126 and KM174 along the Dempster Highway. These rain samplers were designed to protect the waters contained within from significant fractionation that would enrich the $\delta^{18}\text{O}$ and δD values of the water. Old waters were emptied from the collector containers and reattached to the sampling funnel on September 17. Precipitation deposited the night of September 17 was collected the following day to inform geochemical inputs through precipitation at this location.

Active layer water samples were collected from the thawed portion of the active layer during the September 11-18 field period. Two types of these samples were collected: 1) basal active layer water and 2) active layer profile waters. Basal active layer waters were collected from free waters that seeped into the soil pits. Active layer profile waters were collected by cutting away a column of thawed active layer material from the wall of the soil pit, subsampling it into 5cm-depth intervals, and squeezing out the waters of each subsample by hand. All water samples were collected in polypropylene centrifuge tubes, prewashed in sample water.

Following collection, samples were placed in a refrigerator at $\sim 4^{\circ}\text{C}$. Samples were transported in a cooler with ice packs during transport from the field to Edmonton, where they were subsequently stored in a refrigerated environment at $\sim 4^{\circ}\text{C}$.

4.2. Permafrost Core Recovery, Subsampling, and Depth Corrections

Permafrost cores were collected between June 9-15, 2019 using a gas-powered earth auger with a coring bit attached to a segmented drill stem similar to the system described in Camels et al. (2005). Core segments were placed in coolers with ice packs following extraction and kept frozen until they could be placed inside a freezer at the end of the day. The core segments were frozen to -25°C and shipped from Dawson City to

Edmonton, followed by storage at -25°C. Subsampling of the permafrost materials was conducted using a bandsaw in a walk-in freezer held at -5°C. The upper ~30cm of each core was subsampled at a 2-cm depth resolution while depths between ~30-70cm were subsampled at a 1-cm depth resolution to resolve small isotopic variations in the shallow permafrost. Materials deeper than ~70cm were subsampled at 2-cm depth resolution. Depth corrections were made for the subsample intervals to make up for small, cumulative errors during coring and subsampling. These errors are the result of material lost from the saw blade, compounding uncertainty in manual measurement, and pre-existing discrepancies between borehole depths measured in the field and actual core segment lengths.

4.3. Thaw Depth Measurement

Linear thaw depth surveys were conducted in the BS19 collection area using a thaw probe. Thaw depth measurements were taken at 15cm intervals over distances totaling 250cm on either side of each soil pit. The microtopography of each thaw depth measurement was also noted to statistically compare the relationship of thaw depth with microtopography. Thaw depths could be reasonably estimated to an error of ~0.5cm using the thaw probe.

4.4. Thaw Depth Modeling

Thaw depth models were constructed for comparison with the isotope-estimated maximum active layer thickness (ALT_{max}), using probed thaw depths and cumulative thawing degree-days (TDDs) calculated for the year 2019. Using Eq. 4.1, cumulative thawing degree days were calculated from the “ERA5-Land hourly data from 1950 to present” dataset (Muñoz Sabater 2019, 2021), downloaded from the Copernicus Climate Change Service (C3S), for the vicinity around the study area (between 64-65°N and 138-139°W). This dataset contains hourly surface temperature values spatially gridded into 0.2°lat x 0.2°long blocks.

$$CTDDs = \sum_{i=0}^d \frac{T_{max} - T_{min}}{2} - 273.15 \quad (4.1)$$

where:

CTDDs: cumulative thawing degree days (K)

d: number day of the year up to and including which TDDs will be calculated

T_{max} : maximum daily temperature (K)

T_{min} : minimum daily temperature (K)

Thaw depth models for the study sites were constructed by fitting polynomial regressions to the cumulative TDDs and probed thaw depths measured in June and September of 2019.

These models were used to approximate ALT_{max} in 2018, with the assumption that conditions governing thawing at the study sites were similar in 2018 and 2019. Average daily temperatures were calculated from gridded hourly data, from which cumulative TDDs were also calculated, just as before. The day that the average daily surface temperature (ADST) dropped below 273.15K in 2018 was used to approximate the day that ALT_{max} was attained in 2018. To determine this date, 2018 ADSTs were plotted against time. The data were fitted with a rolling average and 95% confidence interval. The cumulative TDDs for the approximate date in 2018 that ALT_{max} was attained was then used as an input to the polynomial regression models to estimate the 2018 ALT_{max} for each site (the methods and R Studio script for thaw depth modeling are provided in greater detail in S11 and S12, respectively).

4.5. pH and Electrical Conductivity

pH and electrical conductivity (EC) were measured using a Mettler Toledo SevenExcellence. Both linear and 3-point segmented calibrations were used for pH, depending on the expected range of sample pH values. Because the pH of most samples from these sites are <5, linear calibration was sufficient. For samples pH values that range between 3.5 and 6.5, a 3-point segmented calibration was used. Both calibration methods use pH buffers of 4.01, 7.00, and 10.01. EC was calibrated using a single buffer solution of 1413 $\mu\text{S}/\text{cm}$. The calibrations were considered valid if subsequent analysis of the standards were within 1% of their accepted values. This validity test was repeated after every ten samples to check for instrumental drift and ensure data quality. The precision of pH and EC is therefore 1%. All measurements were conducted on unfiltered sample waters that were gently pre-mixed by shaking for ~3 seconds. This was done to re-homogenize suspended materials within the water, approximating the mixed state of the waters at the time of sampling in the field. Before measurement, care was taken to avoid contact

of the probe tips with trapped air bubbles. Between samples, the probes were rinsed with deionized water and patted dry with a Kim-Wipe.

4.6. Gravimetric Water Content

Gravimetric water (ice) content was determined using the following equation:

$$GWC(\%) = \left(\frac{\text{frozen sample mass (g)}}{\text{dry sample mass (g)}} \right) * 100 \quad (4.2)$$

Subsamples were dried in an oven at 110°C overnight. Samples that were difficult to extract all the moisture in this manner were instead dried in a freeze dryer overnight. Average error ranged between 1.9 and 4.5% for BS19-1, 2, and 3.

4.7. Stable Isotope Analysis

Analysis of $\delta^{18}\text{O}$ and δD of active layer waters, thawed ground ice, surface water, and precipitation, were analyzed by cavity ring-down laser absorption spectroscopy using a Picarro L-2130i at the PACS laboratory at the University of Alberta. Data were calibrated against USGS46 (-29.80‰ $\delta^{18}\text{O}$, -235.8‰ δD) and USGS48 (-2.22‰ $\delta^{18}\text{O}$, -2.0‰ δD) standards. An internal quality control (QC) water standard was run with each set of samples to monitor run consistency. Values are reported in values of “permil” (‰) with respect to Vienna-Standard Mean Ocean Water (V-SMOW). Uncertainty for $\delta^{18}\text{O}$ and δD values are estimated at $\pm 0.15\%$ and $\pm 0.5\%$, respectively, based on repeat measurement of the QC standard. *d*-excess was also calculated for individual water samples. For a water sample with observed $\delta^{18}\text{O}$ and δD values, defined by a point ($\delta^{18}\text{O}_{\text{obs}}, \delta\text{D}_{\text{obs}}$) in $\delta^{18}\text{O}$ - δD space, *d*-excess is the δD -intercept of a line that passes through ($\delta^{18}\text{O}_{\text{obs}}, \delta\text{D}_{\text{obs}}$) with a slope of 8. *D*-excess is described by the following equation:

$$d = \delta\text{D}_{\text{obs}} - (8 * \delta^{18}\text{O}_{\text{obs}}) \quad (4.3)$$

Using the uncertainties of $\delta^{18}\text{O}$ and δD given above, the propagated uncertain of *d*-excess is 1.3‰.

References

Muñoz Sabater, J. (2021). *ERA5-Land hourly data from 1950 to 1980* [data set]. Copernicus Climate Change Service (C3S) Climate Data Store (CDS). Retrieved January 26, 2022, from <https://cds.climate.copernicus.eu/cdsapp#!/dataset/10.24381/cds.e2161bac?tab=overview>

Muñoz Sabater, J., (2019): ERA5-Land hourly data from 1981 to present. Copernicus Climate Change Service (C3S) Climate Data Store (CDS). Retrieved January 26, 2022, from <https://cds.climate.copernicus.eu/cdsapp#!/dataset/10.24381/cds.e2161bac?tab=overview>

5. STABLE ISOTOPE DEVELOPMENT IN GROUND ICE ALONG AN ALPINE TUNDRA SLOPE IN THE OGILVIE MOUNTAINS, YUKON TERRITORY

The following chapter has been modified from its original publication manuscript format. As such, some information discussed previously in this thesis is repeated. The manuscript will be submitted for publication under the authorship of Casey A. Buchanan, Duane G. Froese, Trevor J. Porter, and Jeffrey L. Kavanaugh.

5.1. Introduction

Stable isotope ratios of oxygen and hydrogen ($\delta^{18}\text{O}$ and δD) from ground ice in permafrost regions have been used to reconstruct paleoclimate temperatures spanning the Late Pleistocene and Holocene in subarctic and arctic regions. This is possible due to the strong relations between the isotopic composition of atmospheric moisture and air temperature (Dansgaard, 1964). Ice wedges, for example, have been used to quantitatively constrain mean winter temperatures over past millennia (Vasil'chuk et al., 2000; Vasil'chuk et al., 2015). Paleoclimate temperature can be quantitatively estimated using ice wedge water isotopes because spring active layer meltwaters infilling and feeding ice wedge growth undergo very little to no isotopic modification due to rapid freezing (Opel et al., 2018).

Pore ice, ground ice generally too small to be seen by the naked eye that occurs interstitially between grains of sediment and organics, and texture ice, an umbrella term for ground ice distinguished by visible cryostructures, are promising candidates for reconstructing past temperatures. Some evidence indicates pore and texture ice primarily records summer temperature (Brosius et al., 2012; Meyer et al., 2010; Throckmorton et al., 2016). This summer temperature bias arises from the source water of pore and texture ice: a mixture primarily of summer precipitation, with potential minor contributions from snow melt and thawed active layer ice (Throckmorton et al., 2016, Bandera et al., 2020). Pore and texture ice have been used to *qualitatively* infer the timing of centennial- and millennial-scale climate fluctuations spanning the Holocene and late Pleistocene (e.g. Schwamborn et al., 2006, 2008; Dereviagin et al., 2003) as well as a boundary indicator between the Pleistocene and Holocene epochs (e.g. Lacelle et al., 2014; Schwamborn et al., 2008). More recently, Porter et al. (2019) presented evidence for

recent climate-induced change in the upper centimeters of relict permafrost just below the transition layer, the horizon separating the active layer from relict ground ice that thaws and refreezes over decadal time scales during especially warm years (Shur et al., 2005). However, these records are difficult to interpret because their source waters can become isotopically altered by local environmental conditions before undergoing long-term preservation into the underlying permafrost record (Dereviagin et al., 2003; Wetterich et al., 2014).

“Secondary” isotopic modification occurs within the active layer and underlying transition layer. In the active layer, surface evaporation, soil water mixing, pooling, and cryofractionation varyingly contribute to isotope modification during seasonal freeze-thaw cycles (Throckmorton et al., 2016).

The formation of "C"-shaped $\delta^{18}\text{O}$ and δD profiles in the active layer soil column is a notable form of secondary isotopic modification (Fig. 5.1). Documented by Michel and Fritz (1982), this unique stable isotope profile geometry develops from bi-directional freezing of the active layer in the fall and winter. During freezing, ^{18}O and D, heavier isotopologues of oxygen and hydrogen, are preferentially incorporated into the ice, where they form more stable bonds than in water. Consequently, the ice becomes more enriched in ^{18}O and D than the water. As freezing continues, both the ice and water become less enriched

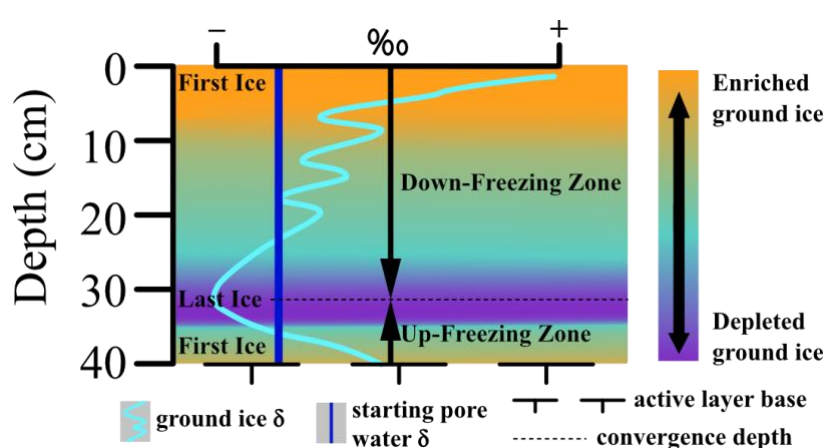


Figure 5.1. Conceptual model illustrating the development of a “C”-shaped $\delta^{18}\text{O}$ or δD profile in the active layer as a result of bi-directional freezing.

in ^{18}O and D as these heavier isotopes are depleted. This process results in C-shaped $\delta^{18}\text{O}$ and δD soil profiles, where the most enriched ice occurs at the top and bottom of the profile and isotopic ratios gradually decrease to a minimum in the lower to middle region of the active layer. The

vertex of this "C" indicates the depth at which the freezing fronts converged. Osterkamp and Romanovsky (1997) observed that freezing front convergence occurred in the lower active layer

at three continuous permafrost sites near Prudhoe Bay, Alaska due to a strong positive temperature gradient in the upper active layer during freeze-back.

When slow, bi-directional freezing occurs in a closed system, it can be approximated by Rayleigh-style equilibrium fractionation, in which ice is 2.8 to 3.1‰ $\delta^{18}\text{O}$ and 19.5 to 20.6‰ δD more enriched than the residual water at any given point during the freezing process (O’Neil, 1968; Suzuoki and Kimura, 1973). However, in natural settings, factors such as faster freezing under cold temperatures diminish the enrichment due to kinetic fractionation (Lacelle et al., 2014).

Ice from multiple years becomes averaged in the transition layer during periods of exceptionally deep thaw, which typically occurs on sub-decadal to multi-centennial time scales. Such low-frequency, greater thaw depth events are caused by significant changes to the environment or climate (Yanovsky, 1933; Shur et al., 2005). Materials deep within the transition layer might thus only rethaw once before further surface aggradation via sedimentation or organic matter accumulation places that material out of range of future thawing (Porter et al., 2019, *Supplementary*). In theory, the top of the transition layer can be identified isotopically at the base of the "C"-shaped isotope profile in the frozen active layer. The base of the transition layer is therefore defined by the depth of maximum (decadal- to centennial-order) thaw (ALT_{max}), below which resides stable, long-term “relict” ground ice.

Few studies documenting the isotopic characteristics and development of the transition layer exist. Lacelle et al. (2014) studied the geochemical and stable isotopic manifestation of downward water migration of active layer waters into the transition layer, and established these indicators as a means to identify thaw unconformities. Lacelle et al. (2019) studied stable isotopic and geochemical profiles across the mid-Holocene thaw unconformity in the Peel Plateau region of N.W.T., Canada. The latter study has implications for the isotopic and geochemical signatures of the transition layer because the base of the transition layer could be considered a recent thaw unconformity.

The widespread existence of pore ice and texture ice in northern regions makes it widely available for study. However, the extent of isotopic modification may reduce its reliability as an accurate paleoclimate proxy. In this study, we investigate spatially-varying processes driving isotopic development in pore and texture ice. The objectives of this study are to (1) establish the history of local permafrost formation using geochemical and traditional cryostructure analyses;

(2) examine the stable isotopic relations between the active layer, transition layer, and relict pore and texture ice; (3) assess the impacts of local processes on the stable isotope development of pore and texture ice; and (4) build upon existing evidence for 20th century warming captured by stable isotope records in pore and texture ice. Ultimately, we aim to improve the potential of stable isotopes in pore and texture ice for paleoclimate reconstruction.

5.2. Regional Setting and Site Description

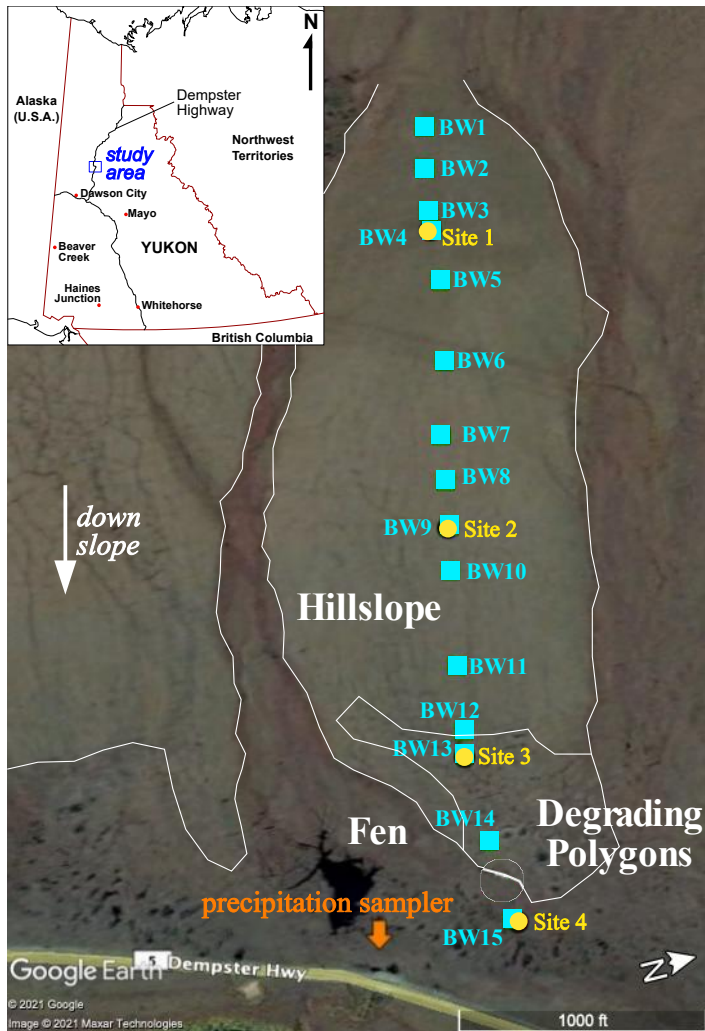


Figure 5.2. Map of the Blackstone 2019 collection area. Satellite imagery from (Google Earth). Blue squares - September 2019 basal active layer water sample pits (BW); yellow circles – core sites.

The Blackstone 2019 (BS19) study area spans a fen and hillslope peatland located within the Southern Ogilvie Mountains, Yukon Territory, Canada (64.920°N, 138.284°W, 940m elev. a.s.l.) at kilometer 126 of the Dempster Highway, just north of the Chapman Lake Moraine. Regional climate is subarctic continental (Wahl et al., 1987). At Dawson City, 1981-2010 climate normal data spanning 27 years indicate a mean annual temperature of -4.1°C. Over the 1981-2010 climate normal period, temperature data were not recorded for three of the thirty years at Dawson City. Mean annual precipitation was 324mm, 62% of which fell as rain. Most precipitation fell during the summer months (Environment and Climate Change Canada). Precipitation $\delta^{18}\text{O}$ and δD values fall along a Local Meteoric Water Line (LMWL) described by the equation $\delta\text{D} =$

$6.8\delta^{18}\text{O} - 24.5$ (Baranova, 2017; see S10 for more details). The area is broadly mapped within the extensive discontinuous permafrost region. However, permafrost extent is continuous within the study locale and encompassing valley due to the higher elevation.

The Blackstone collection area is divided into three zones (Figure 5.2, white labels, Fig 5.3). The *hillslope* (Fig. 5.3A,B) consists of an ~650m-long, east-facing gentle hillslope spanning an elevation difference of 26m. The slope is composed of strongly cryoturbated cobble-silt diamict mantled by a thin ombrotrophic blanket bog. The diamict was mapped as a moraine complex by Duk-Rodkin (1996) and is likely of pre-McConnell (MIS-4) in age (Briner et al., 2005). The diamict is cross-cut by a network of ice wedges identifiable on the peat surface by moisture-related differences in moss coloration and species and sometimes small surface troughs. The diamict contains a well-mixed fraction of fine, humified organics, likely the long-term product of cryoturbation and Turbic Cryosol formation. Based on soil texture and geographic position, this diamict is likely derived from glaciofluvial outwash contemporaneous with the Chapman Lake Moraine to the south, later reworked by colluvial and fluvial processes into its current form. The modern hillcrest (Site 1) is occupied by a short (25-71cm, avg. 44cm) overstory of *Betula nana* (dwarf birch), minor *Salix spp.* (willows) (25-48cm, avg. 37cm), and *Ledum groenlandicum* (Labrador tea), and an understory of tussock-forming *Eriophorum vaginatum* (cotton grass), *Sphagnum spp.*, *Cladonia rangiferina* and *Cladonia stellaris* (caribou lichens) (Figure 5.3). The middle backslope (Site 2) is occupied by significantly smaller abundance of *Betula nana*, *Cladonia spp.*, and *Ledum groenlandicum*, and *Sphagnum spp.*, and much more *Eriophorum vaginatum*. Backslope *Betula nana* heights (13-30cm, avg. 19cm) were also shorter than those on the hilltop. Furthermore, hillcrest tussocks were taller (28-30cm, avg. 29cm) than those in along the backslope (10-23cm, avg. 16 ± 5 cm).

The *degrading polygons* area (Fig. 5.3C) is a flatter area of thermally degrading ice wedge polygons. Thermal erosion of the tops of the wedges is indicated by the presence of pooling surface waters along ice wedge surface troughs and larger pools at wedge intersections. Vegetation is transitional between the hillslope and fen (the third zone). Most of the ground cover was *Cladonia spp.*, rather than *Eriophorum vaginatum* as it had been along the middle of the hillslope. There was also significantly more dwarf birch than in the middle hillslope and footslope. Minor amounts of *Rubus chamaemorus* (cloudberry) and *Ledum groenlandicum*

(Labrador tea) were also present. Thermal degradation ponds were occupied by saturated mats of

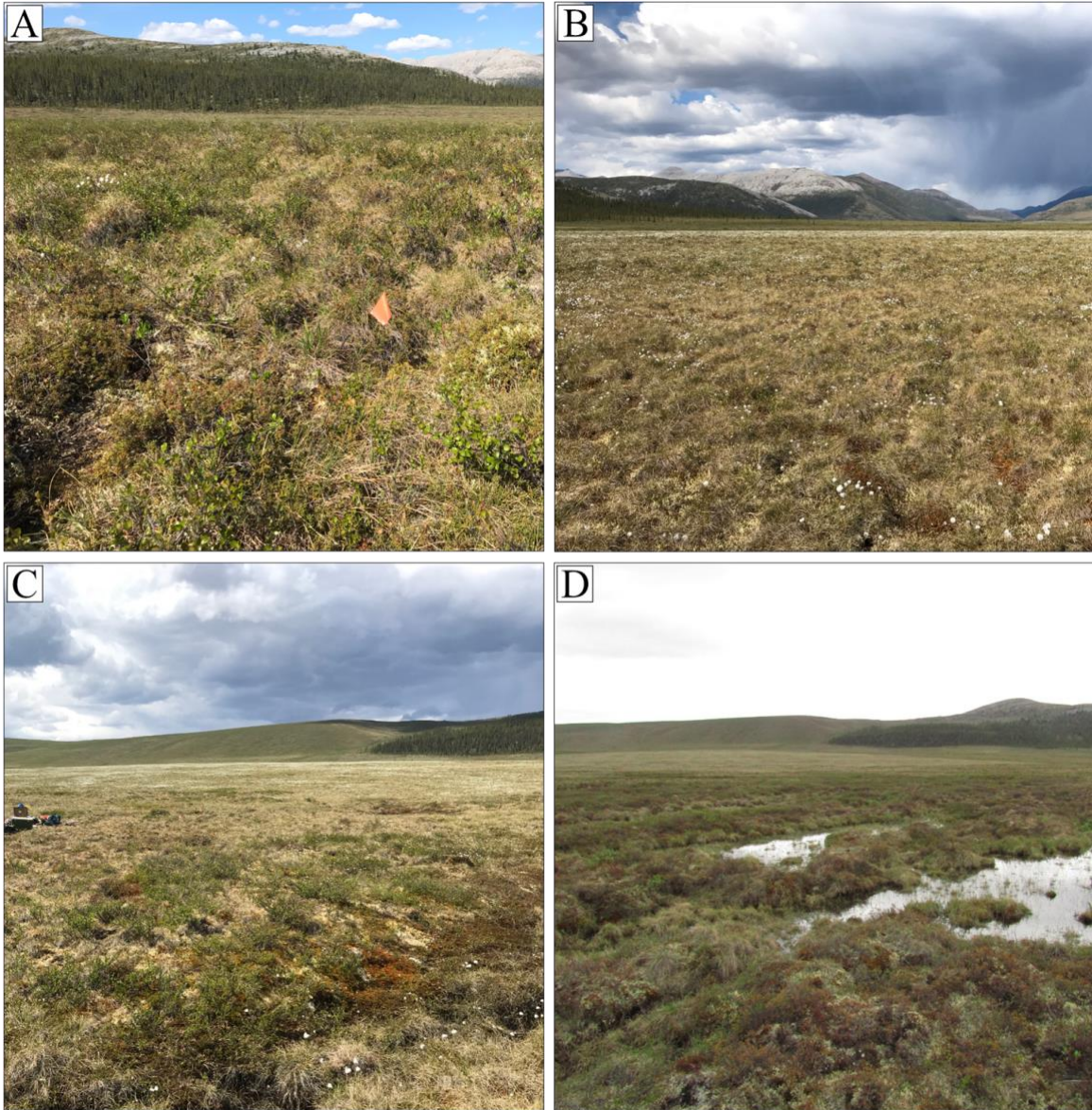


Figure 5.3. BS19 vegetation and topography at: A) *hillslope (top)* – higher tussocks, dwarf birch and willows, thin peat; B) *hillslope (middle)* – shorter tussocks, more blooming tundra cotton, moss-covered wedges visible, thin peat; C) *degrading polygon area* – average surface water pH of 4.7, vegetation transitional between middle slope and fen, flat-centered ice wedge polygons, ice wedge surface troughs wetter and wider than on the hillslope with saturated moss lawns, thermokarst pools frequent at ice wedge intersections; D) *fen* – average surface water pH of 6.1, crude flark-and-hummock topography, moderate to high dwarf birch density on hummocks.

grasses.

The *fen* (Fig. 5.3D) extends between the degraded polygon area and the Dempster Highway (Figure 5.2). The fen consists of strong microtopographic variations in the form of flarks and ombrotrophic and crude string-like hummocks. Surface waters in the fen have an average pH of 6.1, similar to sampled precipitation (6.6), indicating greater surface flow characteristic of fens. The presence of significantly thawed ice wedge troughs in the fen immediately southwest of the rain sampler indicates present day fen conditions might have developed from thermally-degraded polygonal ground. The stratigraphy consists of a deeper horizon of silty sands separated from an overlying blanket of peat by a gradational contact of varying depth. Flarks are occupied by saturated mats of grass while the drier hummocks host vegetation assemblages similar to the top of the hillslope - an overstory of *Betula nana* (dwarf birch) and *Ledum groenlandicum* (Labrador tea), and an understory of *Eriophorum vaginatum*, *Cladonia spp.*, and *Sphagnum spp.* with minor *Rubus chamaemorus* (cloudberry) and *Vaccinium vitis-idea* (lingonberry). The tops of hummocks within the fen contain much less *Cladonia spp.* and *Eriophorum vaginatum* and more *Ledum groenlandicum* compared to polygon surfaces in degrading polygon area. Cotton grass tussocks within polygons and on the tops of tussocks in the degraded polygon area are slightly taller (9-36cm, avg. 18 ± 7 cm) than middle slope tussocks.

5.3. Materials and Methods

5.3.1. Water sample collection

Precipitation, active layer water, and surface water samples were collected between September 11-18, 2019. Precipitation was collected at two separate Croatian rain samplers at KM126 (the BS19 collection area, Fig. 5.2, orange arrow) and KM174 (not show) of the Dempster Highway between September 17-18. These stations are designed to protect their sample waters from evaporative isotope enrichment. Old waters were emptied from the rain collectors and reattached to the sampling funnel on September 11. Captured precipitation was collected on September 18 to provide baseline isotopic input to the surface of the active later.

Active layer water samples were collected from the thawed active layer during the same interval as the water sampling described above. Two types of active layer water samples were collected: (1) “Basal active layer waters” were collected from standing water that pooled at the bottoms of fresh soil pits shortly after the monoliths were removed; and (2) “profile waters” were

collected by cutting away a column of monolith from the wall of the soil pit, subsampling it into 5cm-depth intervals, and squeezing out the liquid of each subsample by hand. All water samples were collected from bottom to top of the soil profile in polypropylene centrifuge tubes.

Following collection, samples were placed in a refrigerator at $\sim 4^{\circ}\text{C}$. Samples were transported in a cooler with ice packs during transport from the field to Edmonton, where they were subsequently stored in a refrigerated environment at $\sim 4^{\circ}\text{C}$.

5.3.2. Permafrost core recovery, subsampling, and depth corrections

Permafrost cores were collected between June 9-15, 2019 using a gas-powered earth auger with a coring bit attached to a segmented drill stem similar to the system described in Camels et al. (2005). Core segments were placed in coolers with ice packs following extraction and kept frozen until they could be placed inside a freezer at the end of the day. The core segments were frozen to -25°C and shipped from Dawson City to Edmonton, followed by storage at -25°C . Subsampling the permafrost materials was conducted using a bandsaw in a walk-in freezer held at -5°C . The upper $\sim 30\text{cm}$ of each core was subsampled at a 2-cm depth resolution while depths between $\sim 30\text{-}70\text{cm}$ were subsampled at a 1-cm depth resolution to resolve small isotopic variations in the shallow permafrost. Materials deeper than $\sim 70\text{cm}$ were subsampled at 2-cm depth resolution. Depth corrections were made for the subsample intervals to make up for small, cumulative errors during coring and subsampling. These errors are the result of material lost from the saw blade, compounding uncertainty in manual measurement, and pre-existing discrepancies between borehole depths measured in the field and actual core segment lengths.

5.3.3. Thaw depth measurement

Thaw depth surveys were conducted at the BS19 collection area by inserting a thin metal rod (thaw probe) into the ground until firm resistance was met. Thaw depth measurements were taken at 25cm intervals, totaling 250cm on either side of each soil pit, to capture local thaw depth variability. Measurements could be reasonably estimated to 1cm using markings along the side of the thaw probe. The microtopography of each thaw depth measurement was also noted to compare the relationship of thaw depth with microtopography. However, because cores were only drilled between tussocks (i.e. within hollows), only thaw depths taken between tussocks were used for comparisons with stable isotope and geochemical profiles.

5.3.4. Thaw depth modeling

Thaw depth models were constructed for comparison with the isotope-estimated maximum active layer thickness (ALT_{max}), using probed thaw depths and cumulative thawing degree-days (TDDs) calculated for the year 2019. Using Eq. 5.1, cumulative thawing degree days were calculated from the “ERA5-Land hourly data from 1950 to present” dataset (Muñoz Sabater 2019, 2021), downloaded from the Copernicus Climate Change Service (C3S), for the vicinity around the study area (between 64-65°N and 138-139°W). This dataset contains hourly surface temperature values spatially gridded into 0.2°latitude x 0.2°longitude blocks.

$$CTDDs = \sum_{i=0}^d \frac{T_{max} - T_{min}}{2} - 273.15 \quad (5.1)$$

where:

CTDDs: cumulative thawing degree days (K)

d: number day of the year up to and including which CTDDs will be calculated

T_{max} : maximum daily temperature (K)

T_{min} : minimum daily temperature (K)

Thaw depth models for the study sites were constructed by fitting polynomial regressions to the cumulative TDDs and probed thaw depths measured in June and September of 2019.

These models were used to approximate ALT_{max} in 2018, with the assumption that conditions governing thawing at the study sites were similar in 2018 and 2019. Average daily temperatures were calculated from gridded hourly data, from which cumulative TDDs were also calculated, just as before. The day that the average daily surface temperature (ADST) dropped below 273.15K in 2018 was used to approximate the day that ALT_{max} was attained in 2018. To determine this date, 2018 ADSTs were plotted against time. The data were fitted with a rolling average. The cumulative TDDs on the approximate date that ALT_{max} was attained in 2018 was then used as an input to the polynomial regression models to estimate the 2018 ALT_{max} for each site (see S11 for a more detailed description of 2018 thaw depth modeling using TDDs).

5.3.5. Stable isotope analysis

$\delta^{18}O$ and δD of active layer waters, thawed ground ice, surface water, and precipitation, were analyzed by cavity ring-down laser absorption spectroscopy using a Picarro L-2130i at the

PACS laboratory at the University of Alberta. Data were calibrated against USGS46 (-29.80‰ $\delta^{18}\text{O}$, -235.8‰ δD) and USGS48 (-2.22‰ $\delta^{18}\text{O}$, -2.0‰ δD) standards. An internal quality control (QC) water standard was run with each set of samples to monitor run consistency. Values are reported in values of “permil” (‰) with respect to Vienna-Standard Mean Ocean Water (V-SMOW). Uncertainty for $\delta^{18}\text{O}$ and δD values are estimated at $\pm 0.15\text{‰}$ and $\pm 0.5\text{‰}$, respectively, based on repeat measurement of the QC standard. *D*-excess was also calculated for individual water samples. For a water sample with observed $\delta^{18}\text{O}$ and δD values, defined by a point ($\delta^{18}\text{O}_{\text{obs}}, \delta\text{D}_{\text{obs}}$) in $\delta^{18}\text{O}$ - δD space, *d*-excess is the δD -intercept of a line that passes through ($\delta^{18}\text{O}_{\text{obs}}, \delta\text{D}_{\text{obs}}$) with a slope of 8. *D*-excess is described by the following equation:

$$d = \delta\text{D}_{\text{obs}} - (8 \times \delta^{18}\text{O}_{\text{obs}}) \quad (5.2)$$

Using the uncertainties of $\delta^{18}\text{O}$ and δD given above, the propagated uncertain of *d*-excess is 1.3‰.

5.3.6. Ice and water content

Gravimetric water (ice) content was determined as:

$$\text{GWC}(\%) = \left(\frac{\text{frozen sample mass (g)}}{\text{dry sample mass (g)}} \right) \times 100 \quad (5.3)$$

Subsamples were dried in an oven at 110°C overnight. Samples that were difficult to dry completely in this manner were instead dried in a freeze dryer overnight. Average error ranged between 1.9 and 4.5% for cores at Sites 2, 3, and 4. GWC was not available for Site 1.

5.3.7. Electrical conductivity and pH

Subsamples thawed overnight at 4°C and the thaw waters were squeezed out of each subsample, using a vice, into 15mL centrifuge tubes. The electrical conductivity and pH of each of the sample waters were measured using a Mettler Toledo SevenExcellence™. pH was calibrated with a set of standard solutions with pH values of 4.01, 7.00, and 10.01 which formed a three-point linear calibration curve. Electrical conductivity was calibrated using a single calibration solution of 1413 $\mu\text{S}/\text{cm}$. The calibrations were considered valid if subsequent analysis of the standards were within 1% of their accepted values. This validity test was repeated after every ten samples to check for instrumental drift and ensure data quality. The precision of pH and EC is therefore 1%.

5.4 Results

5.4.1. Precipitation and basal active layer water stable isotopes and geochemistry

Average isotopic values for local rain (-20.9‰ $\delta^{18}\text{O}$, 4.0‰ d -excess) sampled between September 11-18, 2019 were similar to the basal active layer waters at the hilltop (BW-1 to 4) (Figure 5.4). Along the hillslope (BW-1 to BW-12) basal waters became more enriched with lower slope position by $\sim 2.2\text{‰}$ $\delta^{18}\text{O}$, while d -excess was lower by $\sim 3.1\text{‰}$. d -excess values for BW7 and BW9 are lower than would be expected given the rest of the down-slope trend. This is unlikely due to evaporative enrichment during sample storage because the collection tubes were filled to the top to minimize head space, and were refrigerated during transport and storage. In the degrading polygon area and fen, basal waters (BW-13 to BW15) were less enriched in $\delta^{18}\text{O}$ than bottom slope waters, but still significantly more enriched than recent precipitation.

Stable isotope analyses of water samples obtained from thawed active layer profiles collected between September 11-18, 2019 at the Sites 1, 3, 4 show $\delta^{18}\text{O}$ enrichment in the upper 10-20cm centimeters of the thawed active layer by as much as 3.4‰ and d -excess depletion by as much as 12.2‰ relative to underlying soil water (Figure 5.5). The soil water profile at Site 2 was an exception. Although its thawed profile is isotopically homogeneous between 5-35cm

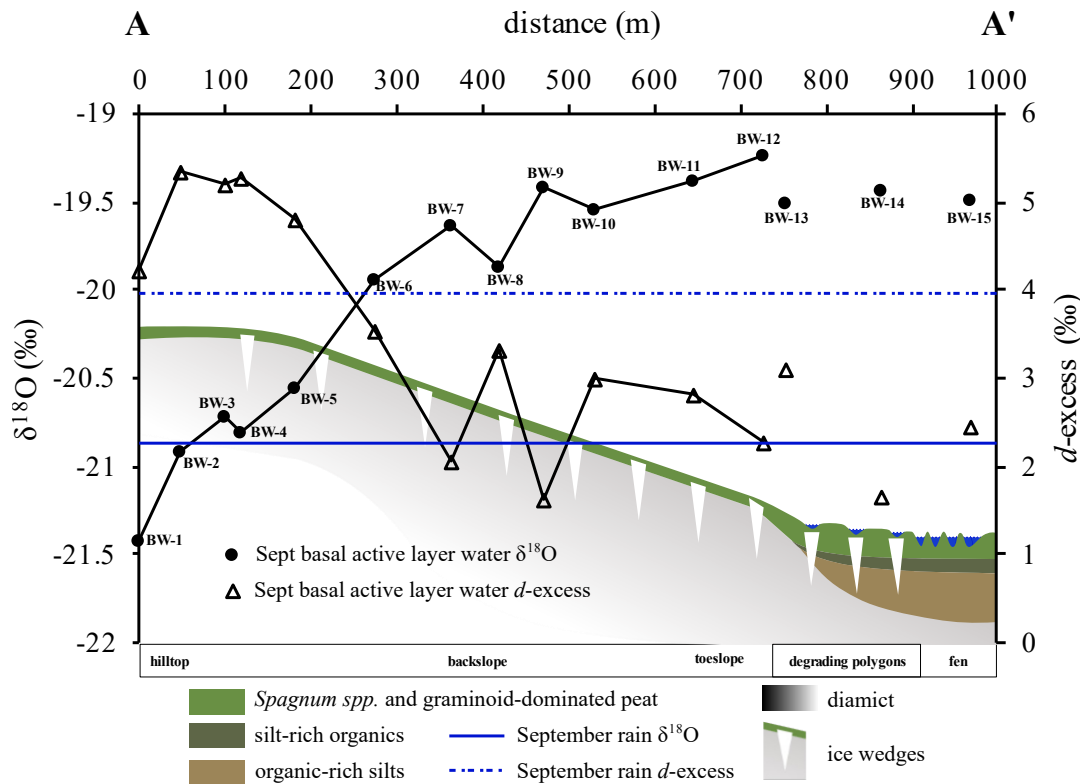


Figure 5.4. Stable isotope development of basal active layer waters (BW) at the BS19 study area. $\delta^{18}\text{O}$ enriches downslope while d -excess becomes more depleted. $\delta^{18}\text{O}$ and d -excess values from the degrading polygon area and fen are not linked by a line to emphasize the non-communicative hydrologies of these locations.

depth, d -excess varied considerably, with its lowest value (-0.6‰) at ~30cm depth, and highest value (3.0‰) at ~10cm depth.

Basal active layer water collected in September, 2019 had a pH similar to precipitation at the top of slope. pH then decreases downslope from 6.1 to 4.9 (BW2 to BW12). BW9 pH was anomalously high, at 6.0. BW13 and BW14 pH values were similar those from the lower hillslope, while BW15, at the fen hummock (Site 4), was slightly higher (pH = 5.2) than lower slope and degrading polygon values.

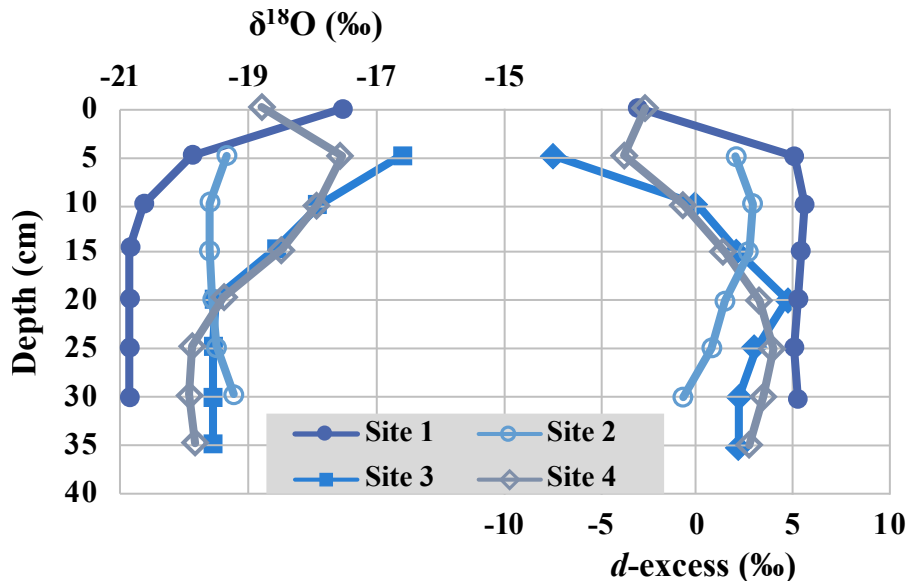


Figure 5.5. Stable isotopic profiles of June 2019 active layer waters from Sites 1, 2, 3, and 4. Note that the uppermost several centimeters are enriched in $\delta^{18}\text{O}$ and depleted in d -excess due to evaporation.

5.4.2. Stratigraphic framework

The cores examined in this study exhibited three distinct units on the basis of stable isotopes, GWC, cryostructures, and geochemistry. From top to bottom these are Units 1, 2, and 3, and correspond to the active layer, transition layer, and relict permafrost, respectively. This interpretation is presented in greater detail later in this work, but is included here to provide a clear framework for presenting results. Units were further subdivided alphabetically along natural, coinciding breaks in the physical and/or geochemical profiles. In this work, the depth in the active layer at which the upward- and downward-freezing fronts met during fall freeze-back is referred to as the ‘convergence depth’. We distinguish between the active layer regions above and below the convergence depth as the ‘downward-freezing zone’ and ‘upward-freezing zone’ (Figure 5.1), which correspond to Unit 1A and Unit 1B, respectively. The following is a description of typical characteristics associated with the two boundaries separating the three units, which are further summarized by Figure 5.6.

Unit 1 – Unit 2 Boundary. Cryostructure density and visible ice content increase just below the Unit 1-2 boundary (Site 2, Site 4), concomitant with an enrichment in GWC (Site 2, Site 3, Site 4). Typical cryostructures just beneath the Unit 1-2 boundary are micro-lenticular,

micro-braided lenticular, micro-braided, and crustal where the substrate is organic (Site 1, Site 4). Typical cryostructures just beneath the Unit 1-2 are lenticular, braided, and layered where the substrate is minerogenic (Site 1, Site 2). Upward- and downward-sweeping ice veins are sometimes appended to the bottom and top of the upper-most ice layer, respectively (Site 2). Unit 1 is typically characterized by a stable isotope C-profile (Site 1, Site 2, Site 4) formed by bi-directional freezing (see Discussion). The Unit 1-2 boundary is placed just below the most enriched values at the base of the C-profile. The base of the C-profile was the most diagnostic geochemical feature of the Unit 1-2 boundary.

Unit 2 – Unit 3 Boundary. Cryostructure density and visible ice content commonly increases just below the Unit 2-3 boundary (Site 2). GWC was observed to be more enriched beneath just below the prospective boundary (Site 2, Site 3, Site 4). A sharp spike of depleted (Site 4) or enriched (Site 2) $\delta^{18}\text{O}$ may also be found just below the boundary. Unit 2 may also exhibit an older C-profile, the base of which marks the Unit 2-3 boundary (Site 2, Site 3).

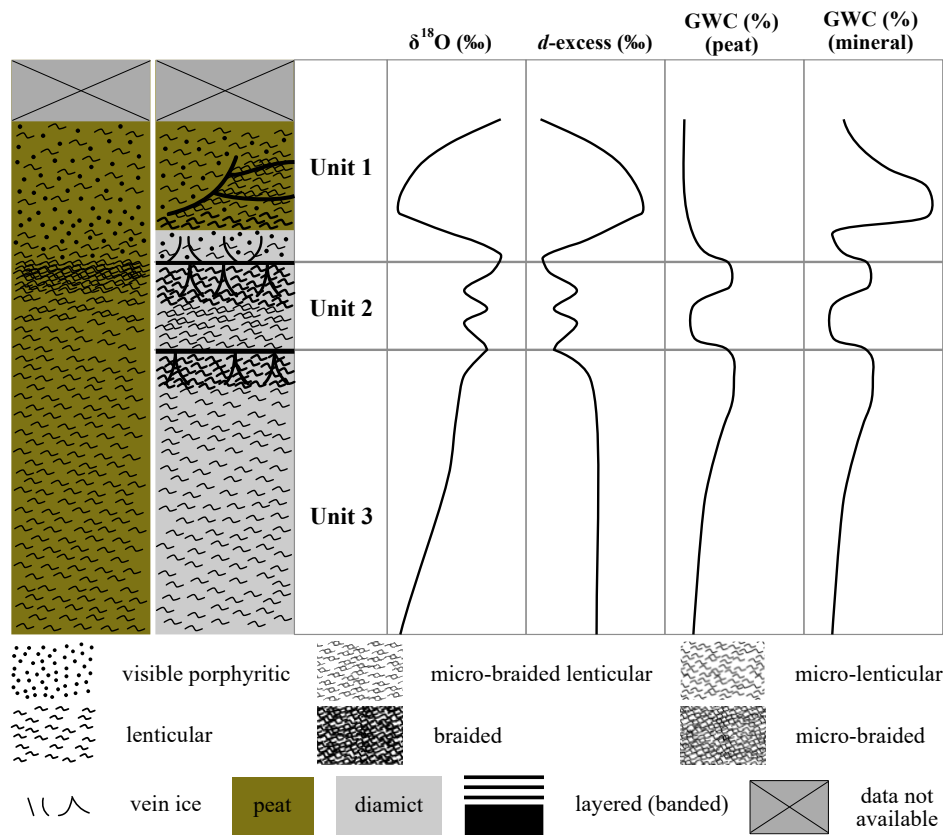


Figure 5.6. Representative stable isotope and GWC characteristics of the Unit 1-2 and Unit 2-3 boundaries.

Usually, Unit 3 was subdivided into subunits based on unique cryophysical, isotopic, and geochemical transitions. Unlike the main units, Unit 3 subunits do not necessarily share common traits between sites, and are defined for the purpose of discussion regarding the genesis of relict permafrost ice.

5.4.3. Ground ice geochemistry and stable isotopes

While the framework presented in the previous section details common characteristics of the boundaries between the three units, there also exists a high degree of site-specificity. The following section details the site-specific cryophysical and geochemical characteristics of Units 1, 2, and 3 in each core.

Site 1

The 2018 active layer (Unit 1, 0-42cm depth) at Site 1 was identified by a C-profile in both $\delta^{18}\text{O}$ and d -excess. Although this isotope-inferred 2018 thaw depth is close to the mean September, 2019 thaw depth (51cm), the high variability of in the probed 2019 thaw depth ($1\sigma = 13\text{cm}$) makes this comparison uncertain. Basal ice in the 2018 active layer attained $\delta^{18}\text{O}$ and d -excess values of -20.4‰ and 2.3‰, respectively. Despite considerable $\delta^{18}\text{O}$ and d -excess variability in profile, a convergence depth in the lower half of the active layer was still observable at 34cm depth. The convergence depth marks the boundary between the downward-freezing zone (Unit 1A) and upward-freezing zone (Unit 1B). Unit 1A (14-34cm) consists of a bimodal substrate of peat and silt. The silt domain contains interconnected ice veins in addition to micro-lenticular cryostructures, while the peat domain contains micro-lenticular and visible porphyritic cryostructures. Unit 1B (34-46cm) consists of only peat with micro-lenticular and visible porphyritic cryostructures.

The upper active layer (Unit 1A) at Site 1 is further divided into upper (15-21cm) and lower (21-34cm) domains (Figure 5.7). The upper domain has a δD - $\delta^{18}\text{O}$ slope of 7.9 (Figure 5.8, Table 5.1) and a horizontal d -excess- δD slope (Figure 5.8), while the lower domain has a δD - $\delta^{18}\text{O}$ slope of 6.5 and has a negative slope in d -excess- δD space displaced below that of the upper domain. Unit 1B has a δD - $\delta^{18}\text{O}$ slope of 7.2. However, in d -excess- δD space, Unit 1B is displaced below the upper domain of Unit 1A, closely matching the regression of the lower domain of Unit 1A.

The transition layer (Unit 2, 42-64cm depth) is divided into two subunits on the basis of soil matrix, cryostructures, and *d*-excess profile. The upper transition layer (Unit 2A, 42-52cm depth) is characterized by a peat substrate with micro-lenticular and micro-braided cryostructures. The Unit 2A-2B boundary coincides with the organo-mineral contact and a small offset in the *d*-excess profile. Unit 2B is characterized by a diamicton substrate with layered and lenticular cryostructures, and occasional small, orange, roughly circular mottles. Downward sweeping vein ice is appended to the top of the uppermost ice layer in Unit 2B. The two subunits were not differentiable in δD - $\delta^{18}O$ or *d*-excess- δD space. A sharp 2.5‰ offset in the *d*-excess profile at 63cm depth is taken to tentatively represent the base of the transition layer (Unit 2-3 boundary). An offset was not observed in the $\delta^{18}O$ profile at 63cm. Other geochemical and GWC data were not available to provide further clarity on the exact position of the transition layer base.

The upper $\sim 2/3$ of the transition layer decreases in $\delta^{18}O$ with depth by 1.7‰, while the entire transition layer decreases in *d*-excess with depth by 2.0‰. The transition layer has a δD - $\delta^{18}O$ slope of 6.7 and a negative *d*-excess- δD slope that overlaps with the lower domain of Unit 1A and is similar to Unit 1B. One outlier from the top of Unit 2 (-20.8‰ $\delta^{18}O$, -160.4‰ δD) was removed before the regression was calculated.

The relict ice at Site 1 (Unit 3, 64cm-unknown depth) contains a broad mix of cryostructures characterized by two domains. The ‘ice belt’ domain (i.e. Kanevskiy et al., 2011) has a high visible cryostructures density, and is dominated by micro-braided, lenticular, and suspended cryostructures. The ‘inter-belt’ domain has lower visible cryostructures density and is dominated by micro-lenticular, micro-braided-lenticular, micro-braided, and minor visible porphyritic. Occasional crustal ice is present, typically on the tops and bottoms of clasts, within both domains.

The relict ice was further divided into three separate subunits on the basis of cryostructural domain, stable isotope profile, and co-isotopic regressions. Unit 3A is characterized by a belted ice domain containing lenticular-suspended cryostructures with vertical bubble trains. $\delta^{18}O$ was stable at about -21.7‰, while *d*-excess decreased slightly with depth. Unit 3A is characterized by a well correlated ($r^2 = 0.81$) δD - $\delta^{18}O$ regression with a slope of 6.7 and is clustered tightly over Unit 2 in *d*-excess- δD space. Unit 3B is characterized by an inter-belt cryostructural domain containing mostly visible porphyritic, micro-lenticular, micro-

braided-lenticular, and micro-braided cryostructures, with a minor amount of braided and vein ice at the bottom. $\delta^{18}\text{O}$ decreases with depth, while d -excess is stable. Unit 3B has a well-correlated ($r^2 = 0.98$) δD - $\delta^{18}\text{O}$ regression with a slope of 7.2 and a negative slope in d -excess- δD space that overlaps with the active layer and transition layer. Unit 3C extends to an unknown depth and is characterized by an ice belt cryostructural domain with a suspended structure. The Unit 3B-3C boundary is sharp, but is not reflected in either the $\delta^{18}\text{O}$ or d -excess profiles.

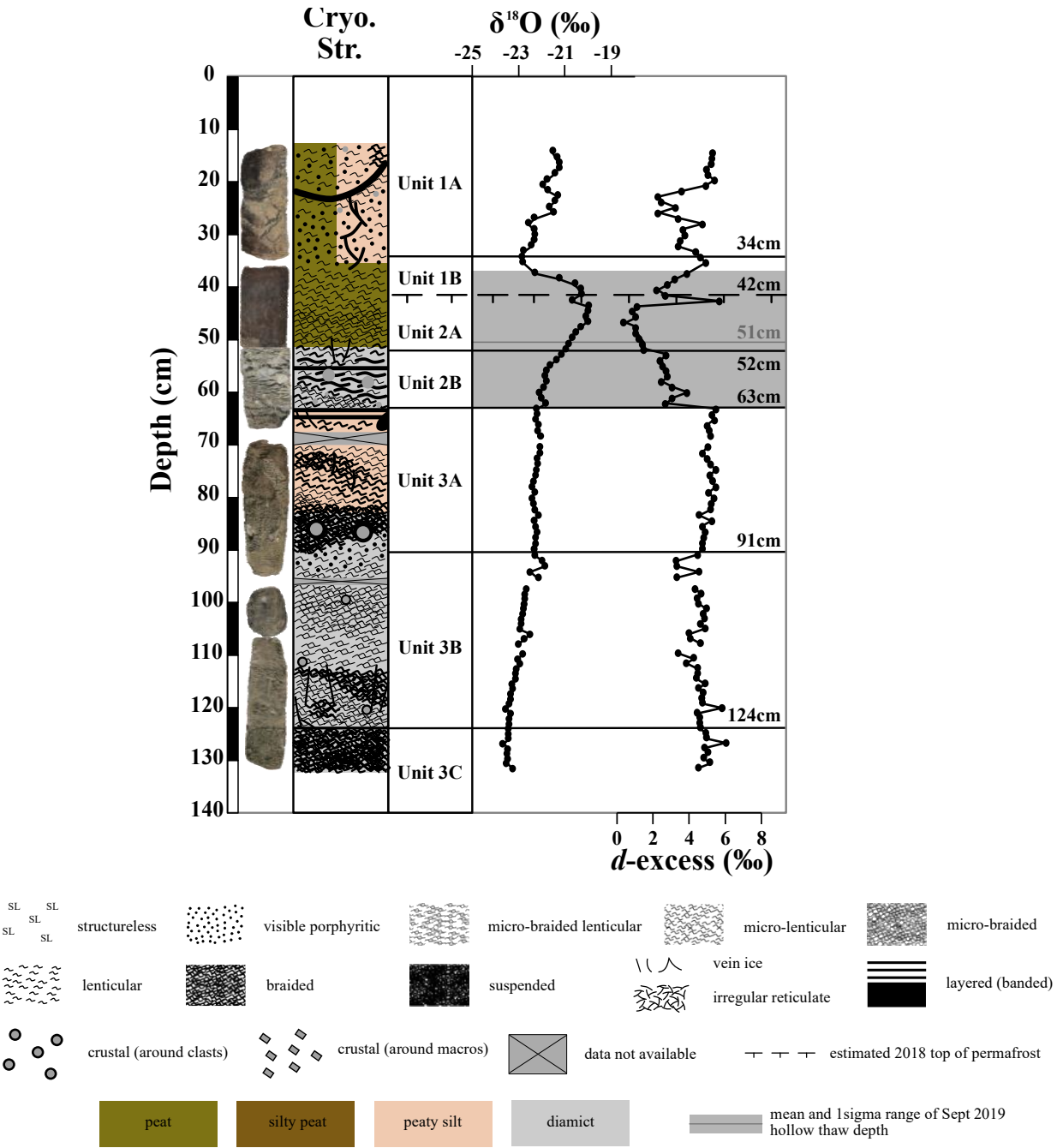


Figure 5.7. Cryostructures, stable isotopes, geochemistry, and unit divisions for Site 1.

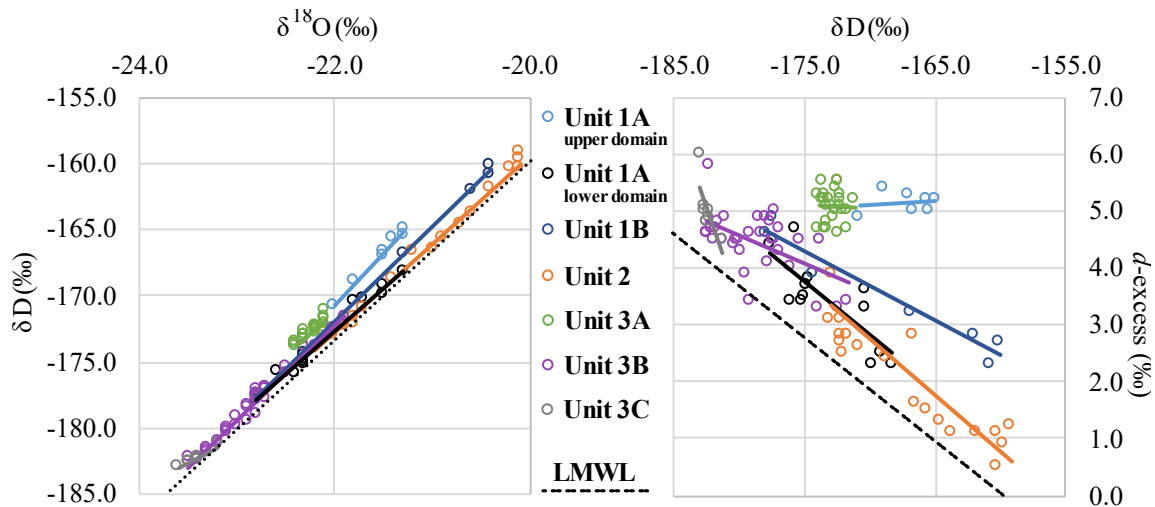


Figure 5.8. δD - $\delta^{18}O$ relations of stratigraphic units in Site 1. The LMWL is defined by the equation $\delta D = 6.8\delta^{18}O - 24.5$ (Baranova, 2017; dashed line). δD - $\delta^{18}O$ regressions are provided in Table 5.1.

Site 2

The active layer (Unit 1, 21-46cm depth) was identified by a C-profile in both $\delta^{18}O$ and d -excess (Figure 5.9). The inferred depth of the 2018 active layer is consistent with (within 1σ) the observed mean thaw depth (44cm) in September, 2019. The base of the active layer was characterized by high $\delta^{18}O$ (-19.3‰) and low d -excess values (0.6‰), a thick ice layer with downward-sweeping ice veins is appended to the top. A paucity of isotope data in the active layer makes the depth of freezing front convergence difficult to identify, though it likely occurs around 36cm depth, in the lower half of the active layer. The downward-freezing zone (Unit 1A, 20-36cm depth) has well correlated ($r^2 = 1.00$) δD - $\delta^{18}O$ regression with a slope of 6.2 (Figure 5.10). The upward-freezing zone (Unit 1B, 36-46cm depth) has a well correlated ($r^2 = 0.99$) δD - $\delta^{18}O$ regression with a slope of 6.5. However, the small number of points for the zones of downward freezing ($n = 5$) and upward freezing ($n = 6$) make the slope and intercept less certain.

The substrate in the active layer is bimodal, with a surface layer of peat 30-35cm deep underlain by organic-rich silt. The organic layer contains high GWC (340-1400%) with visible porphyritic, lenticular, and layered cryostructures. Downward-sweeping ice veins are appended to the top of the uppermost ice layer. GWC begins to decrease strongly with depth just above the organo-mineral contact. Within the organic-rich silts, GWC continues to decrease with depth into

a zone of visible porphyritic and structureless cryostructures. Much of the change in GWC is probably due to the change in density of the substrate. The ice content decrease is matched by visible porphyritic and structureless cryostructures.

The upper portion of the transition layer (Unit 2, 46-59cm depth) contains a banded ice domain with primarily lenticular and upward-sweeping ice veins appended to the base of the ice layer at the Unit 1-2 boundary. The lower transition layer contains visible porphyritic and micro-lenticular cryostructures and a decrease in GWC with depth. pH and EC are consistent at around 5.5 and 40uS/cm, respectively. The $\delta^{18}\text{O}$ and d -excess profiles appear to take the form of another C-profile, mainly due to the large enriched spike in $\delta^{18}\text{O}$ and decrease in d -excess at the base, and a spike in GWC, similar to the that observed at the Unit 1-2 boundary. The transition layer has a well correlated ($r^2 = 1.00$) δD - $\delta^{18}\text{O}$ regression with a slope of 6.5 and a negative slope in d -excess- δD space.

Relict ice (Unit 3, 59cm-unknown depth) is divided into four subunits. The uppermost relict ice (Unit 3A, 59-79cm depth) is characterized by a banded ice domain at the top containing lenticular and layered cryostructures. Vein ice converges upwards and are appended to the base of the ice layers. The bottom half is characterized by an inter-band domain with micro-lenticular cryostructures. $\delta^{18}\text{O}$ depletes steeply with depth in the upper 6cm, while d -excess steeply increases. This corresponds with a GWC spike just below the Unit 1-2 boundary. Below this, d -excess is stable at around 3‰. pH and EC are still stable around 5.3 and 40uS/cm, respectively, similar to the active layer and transition layer. $\delta^{18}\text{O}$ and δD in Unit 3A correlated well ($r^2 = 0.99$, $n = 14$) along a regression with a slope of 7.3 and a negative d -excess- δD regression.

Units 3B (79-91cm depth) and 3C (91-118cm) were differentiated mainly on differences in cryostructures and d -excess. GWC decreases with depth from 324% to 118% through these two subunits. Unit 3B was characterized by a banded ice domain of micro-braided and braided cryostructures with layered ice at the top, and a large increase in d -excess with depth. Sharp increases in pH and EC were observed at the upper boundary of Unit 3B. Through these two subunits, pH is consistent around 6.5, similar to rain water, and EC remained stable between

116-180uS/cm. Stable isotopes were spread along a poorly correlated ($r^2 = 0.69$) δD - $\delta^{18}O$ regression with a shallow slope of 2.4. The d -excess- δD regression is steep, negative, and has considerable spread. Unit 3C is characterized by an inter-band domain of layered, lenticular,

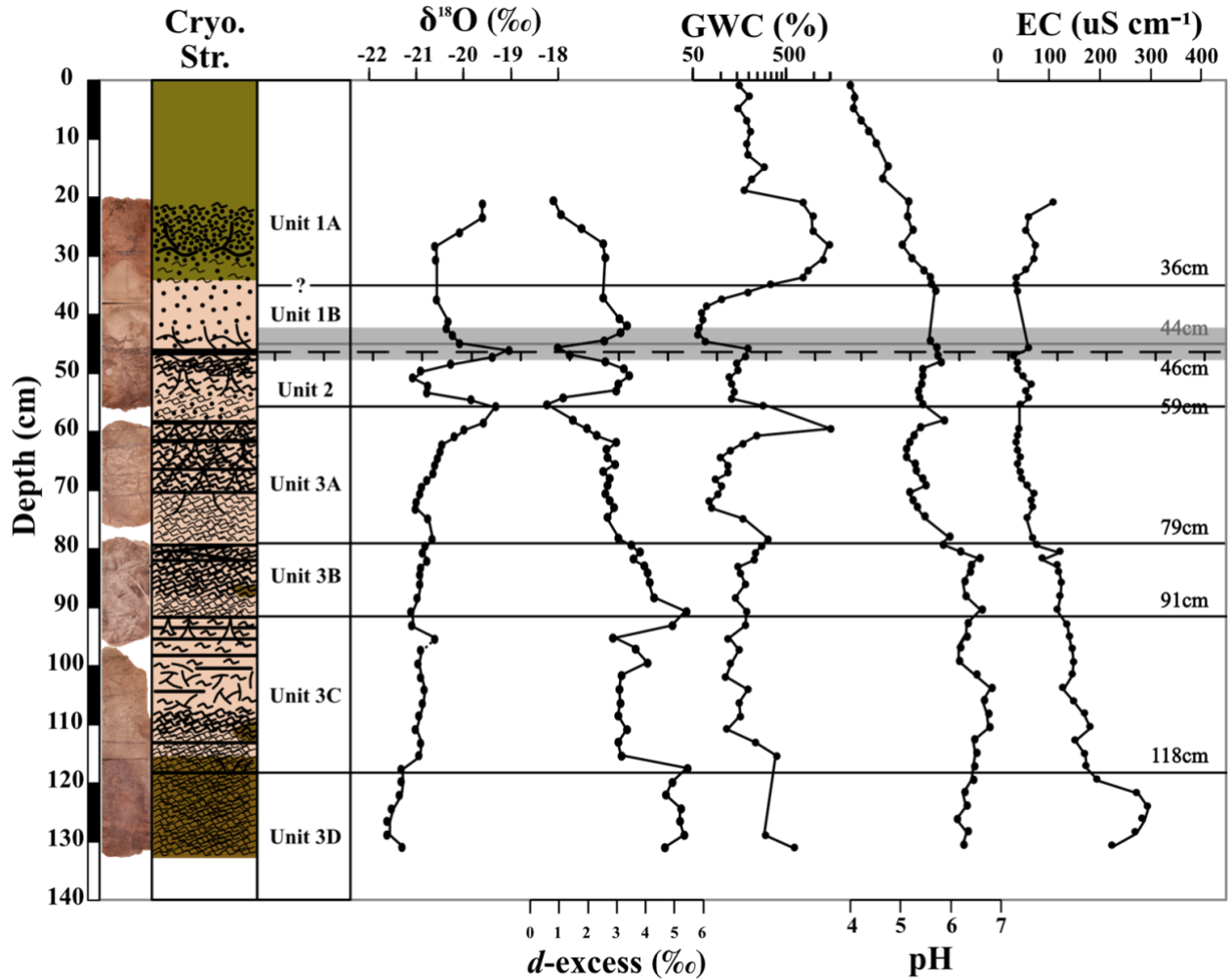


Figure 5.9. Cryostructures, stable isotopes, geochemistry, and unit divisions for Site 2. Legend is presented in Figure 5.7.

irregular reticulate, and braided cryostructures. pH and EC continue to remain stable with depth. d -excess was stable at about 3‰, similar to Unit 3A. $\delta^{18}O$ and δD are again poorly correlated ($r^2 = 0.65$) along a regression with a shallow slope of 3.9.

Unit 3D (118cm – unknown depth) is characterized by a banded ice domain of braided cryostructures hosted by a relict organic horizon. GWC is high and appears to decrease with depth. EC values are the highest observed in the Site 2 profile. $\delta^{18}O$ is the lowest in the Site 2

profile, while *d*-excess is high (~5‰). The stable isotopes are described by a well correlated ($r^2 = 0.99$) δD - $\delta^{18}O$ regression with a slope of 6.0.

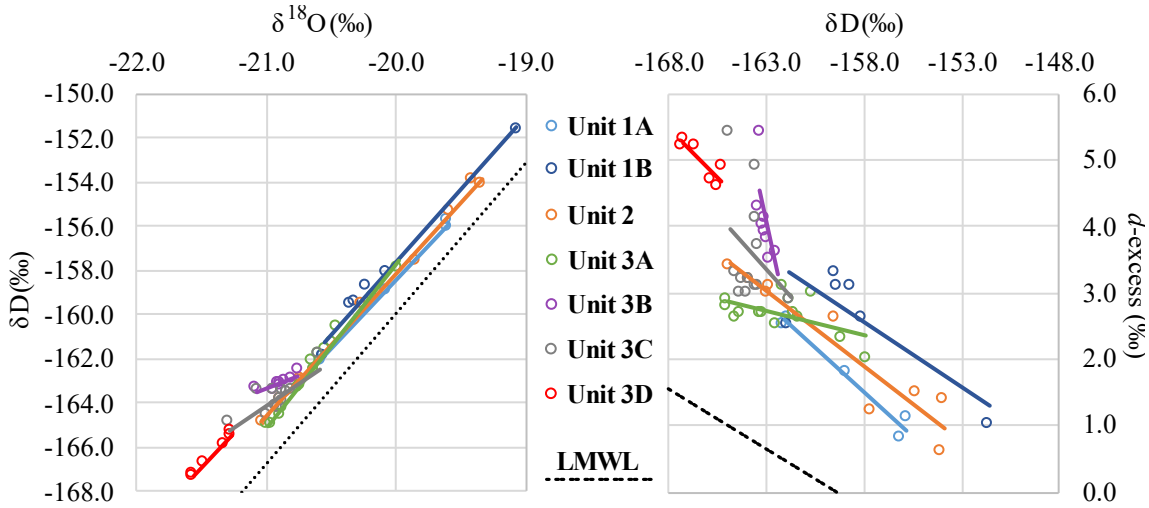


Figure 5.10. δD - $\delta^{18}O$ relations of stratigraphic units in Site 2. The LMWL is defined by the equation $\delta D = 6.8\delta^{18}O - 24.5$ (Baranova, 2017; dashed line). δD - $\delta^{18}O$ regressions are provided in Table 5.1.

Site 3

The Site 3 record was unique among the four sites for its almost entirely structureless ice morphology, exceedingly high ice content (mean GWC = 810%) and EC (mean EC = 444 μ S/cm), and entirely peat substrate (Figure 5.11). Rootlet density was also high, and increased in frequency and size from top to bottom. The active layer (Unit 1, 0-45cm depth) was identified by a C-profile in both $\delta^{18}O$ and *d*-excess, with the highest $\delta^{18}O$ and lowest *d*-excess values at the base. A convergence depth in the lower half of the active layer (31cm depth), was identified by the point most depleted $\delta^{18}O$ and highest in *d*-excess. The base of the isotope inferred active layer (45cm depth) was 6cm deeper than the mean September 2019 thaw depth (39cm). Unit 1A and 1B, representing the downward-freezing and upward-freezing zones of the active layer, respectively (c.f. Michel and Fritz, 1982), were described by δD - $\delta^{18}O$ regressions of $\delta D = 5.2\delta^{18}O - 53.1$ ($r^2 = 1.00$) and $\delta D = 4.9\delta^{18}O - 59.5$ ($r^2 = 0.80$), respectively (Figure 5.12). The downward freezing zone was characterized by a well-defined trend in *d*-excess- δD space, while isotopic data in the upward-freezing zone was relatively scattered. In the upward-freezing zone,

$\delta^{18}\text{O}$ and d -excess fluctuated strongly compared to the downward-freezing zone. The active layer was low in pH (~ 4.5) and EC (~ 100 uS/cm), similar to September 2019 basal active layer waters from the base of the slope (e.g. BW11 and BW12).

The upper half of the transition layer (45-67cm) was characterized by depleting $\delta^{18}\text{O}$ and increasing d -excess, while the lower half (67-83cm) was comparatively stable in $\delta^{18}\text{O}$ and d -excess. The transition layer was defined by a well-correlated ($r^2 = 0.98$) regression of $\delta\text{D} = 6.1\delta^{18}\text{O} - 35.8$. GWC in the upper few centimeters of the transition layer was similar to that of the active layer, though values were generally much higher ($>500\%$) through the rest of the layer, including a conspicuously high GWC at 54cm depth (1376%), associated with an ice layer. Acidity decreased slightly with depth, but was otherwise similar to the acidity of the active layer. A large increase in EC was observed with depth from 334uS/cm in the middle of the transition layer to 725uS/cm immediately below the active layer. EC data were not available for the upper active layer, but presumably also increases with depth. The Unit 2-3 boundary is characterized by small spikes in $\delta^{18}\text{O}$ and d -excess and a local maximum in GWC.

The relict permafrost (Unit 3, 83cm-undetermined depth) is characterized by stable $\delta^{18}\text{O}$ and d -excess of approximately -19.5% , slightly greater than the transition layer, and $1-2.5\%$, very similar to the transition layer, respectively. GWC is high, with most values above 600%. pH values are generally around 4.6 and only begin to substantially increase at about 134cm depth, though pH never exceeding 5.4. EC values fluctuated strongly between 282-817uS/cm. $\delta^{18}\text{O}$ and δD correlated well ($r^2 = 0.87$) along a regression of $\delta\text{D} = 7.8\delta^{18}\text{O} - 2.2$, but had a poorly defined slope in d -excess- δD space.

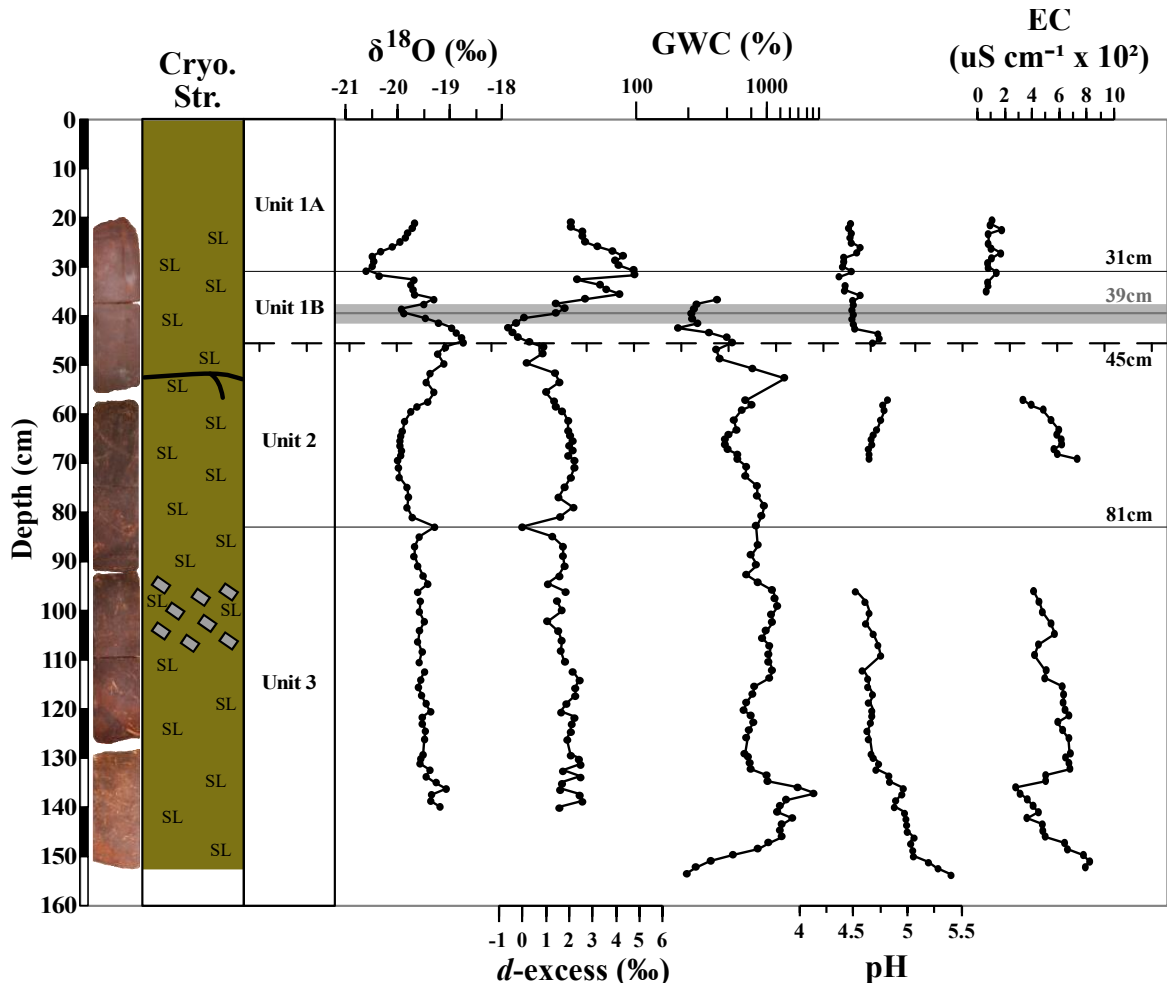


Figure 5.11. Cryostructures, stable isotopes, geochemistry, and unit divisions for Site 3. Legend is presented in Figure 5.7.

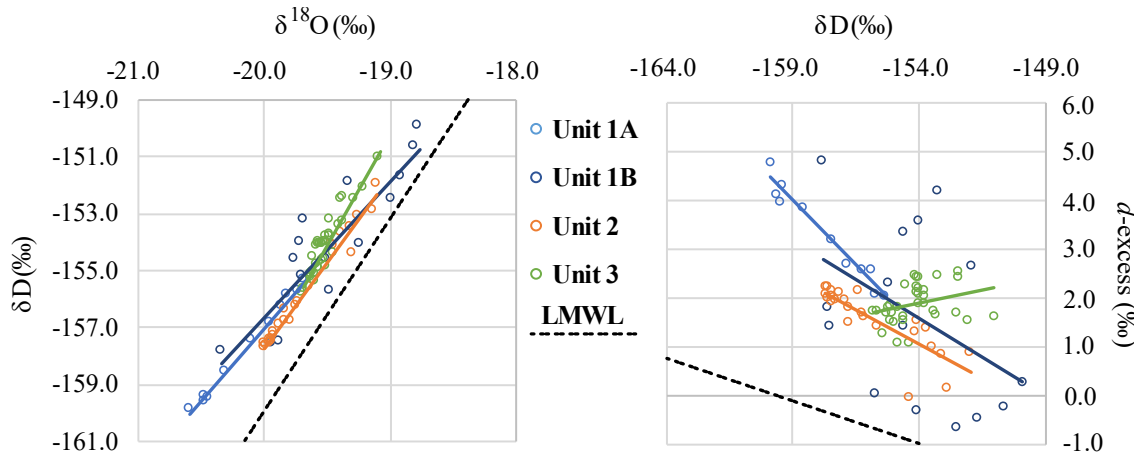


Figure 5.12. δD - $\delta^{18}\text{O}$ relations of stratigraphic units in Site 3. The LMWL is defined by the equation $\delta\text{D} = 6.8\delta^{18}\text{O} - 24.5$ (Baranova, 2017). δD - $\delta^{18}\text{O}$ regressions are provided in Table 5.1.

Site 4

Site 4 consists of peat down to a depth of 125cm, under which lies organic-rich silts (Figure 5.13). The active layer (Unit 1, 20-48cm depth) was identified by the C-profile in $\delta^{18}\text{O}$ and d -excess. Isotope-predicted 2018 thaw depth (48cm) was 7cm below mean September, 2019 thaw depth (41cm), and outside of 1σ . The convergence depth is in the lower active layer at 36cm depth, where a particularly sharp decrease in $\delta^{18}\text{O}$ and increase in d -excess was observed. The downward- and upward-freezing zones fall along similar, well-correlated regressions ($r^2 = 0.93$ and 0.98 , respectively) with slopes of 4.6 and 4.9, respectively (Figure 5.14). Cryostructures in the active layer are mostly micro-lenticular. However, in the upward-freezing zone, micro-braided, visible porphyritic, and structureless cryostructures were also observed. The active layer is low in GWC (<270%) except for steep increase up to 530% at the base. pH is consistently around 5.6, except in the upper 5cm of available data in the downward-freezing zone, where it increases from 4.9 to 5.1 with depth. EC is low; the highest value (87uS/cm) occurs just below convergence depth.

The transition layer (Unit 2, 48-58cm depth) is characterized by micro-braided cryostructures with crustal ice around macrofossils and small (<1cm diameter) mineral aggregates. $\delta^{18}\text{O}$ is consistent around -19.5‰, while d -excess depletes with depth. Diminished $\delta^{18}\text{O}$, and elevated d -excess and GWC mark the upper and lower boundaries of the transition

layer. Unlike other δD - $\delta^{18}O$ regressions in this study, $\delta^{18}O$ and δD are poorly correlated ($r^2 = 0.01$). pH is similar to active layer, while EC increases from 45-88uS/cm with depth.

The relict permafrost (Unit 3, 58cm-unknown depth) is divided into three subunits on the basis of stable isotope profiles and cryostructures. The lower-most subunit (Unit 3C), however, not discussed, as only a few data points are available. In Unit 3A (58-99cm depth), cryostructures are consistently micro-lenticular. $\delta^{18}O$ steadily decreases with depth, while d -excess steadily increases. $\delta^{18}O$ and δD are well-correlated ($r^2 = 0.89$) along a regression with a slope of 4.2. The data are tightly splayed along negatively sloping regression in d -excess- δD space. Like the top boundary, the lower boundary is marked by a thin layer depleted in $\delta^{18}O$ and high in d -excess. In the upper half of Unit 3A, GWC steadily decreases with depth from 631% to 347%, while pH and EC appear to increase. However, GWC, pH, EC are not available at deeper depths.

Unit 3B (99-123cm depth) is characterized by thick suspended or layered ice, along with braided and micro-braided cryostructures. $\delta^{18}O$ and d -excess values are consistently around -20‰ and 2‰, respectively. $\delta^{18}O$ and δD correlated well ($r^2 = 0.80$) along a regression with a slope of 4.3. The regression in d -excess- δD space was negative and poorly defined.

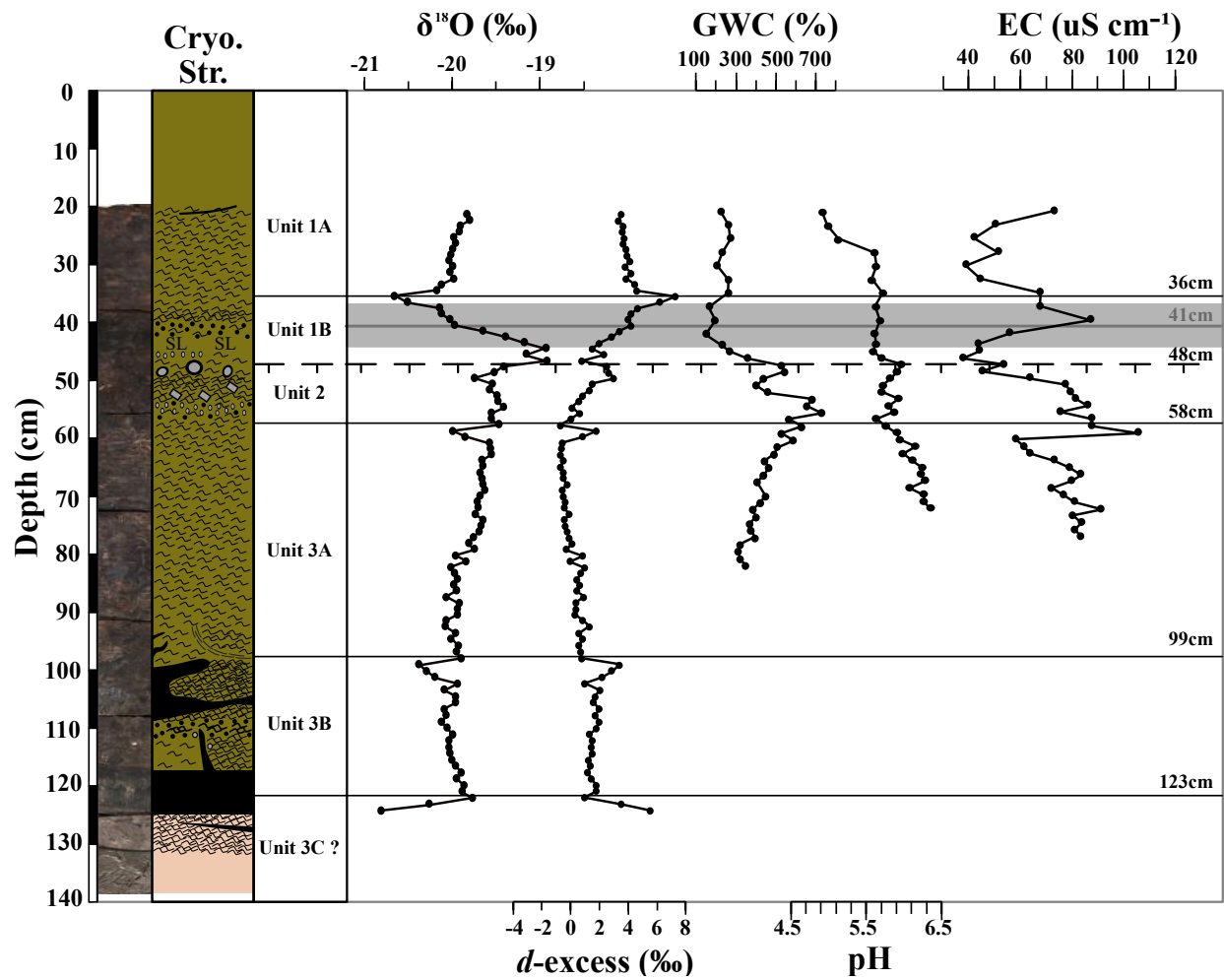


Figure 5.13. Cryostructures, stable isotopes, geochemistry, and unit divisions for Site 4. Legend is presented in Figure 5.7.

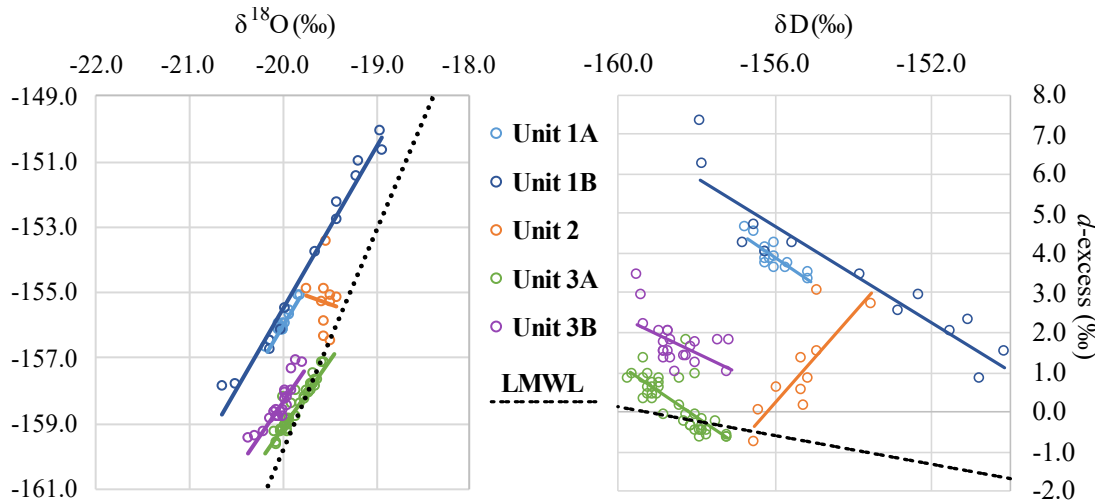


Figure 5.14. δD - $\delta^{18}O$ relations of stratigraphic units in Site 4. The LMWL is defined by the equation $\delta D = 6.8\delta^{18}O - 24.5$ (Baranova, 2017; dashed line). δD - $\delta^{18}O$ regressions are provided in Table 5.1.

Table 5.1. δD - $\delta^{18}O$ regressions of stratigraphic units for Site 1, Site 2, Site 3, and Site 4.

	<i>Site 1</i>			<i>Site 2</i>		
<i>Layer</i>	<i>Regression</i>	<i>r</i> ²	<i>n</i>	<i>Regression</i>	<i>r</i> ²	<i>n</i>
<i>Unit 1A</i>	$7.9(\delta^{18}O) + 3.3^*$	0.99	7	$6.2(\delta^{18}O) - 33.6$	1.00	5
	$6.5(\delta^{18}O) - 28.7^{**}$	0.97	12	n.a.	n.a.	n.a.
<i>Unit 1B</i>	$7.2(\delta^{18}O) - 13.8$	1	7	$6.5(\delta^{18}O) - 26.9$	0.99	6
<i>Unit 2</i>	$6.7(\delta^{18}O) - 25.3$	0.99	20	$6.5(\delta^{18}O) - 28.0$	1.00	9
<i>Unit 3A</i>	$6.7(\delta^{18}O) - 24.6$	0.81	24	$7.3(\delta^{18}O) - 10.9$	0.99	14
<i>Unit 3B</i>	$7.2(\delta^{18}O) - 13.4$	0.98	33	$2.4(\delta^{18}O) - 113.7$	0.69	8
<i>Unit 3C</i>	$4.0(\delta^{18}O) - 88.1$	0.91	8	$3.9(\delta^{18}O) - 82.8$	0.65	12
<i>Unit 3D</i>	n.a.	n.a.	n.a.	$6.0(\delta^{18}O) - 37.9$	0.99	6
	<i>Site 3</i>			<i>Site 4</i>		
<i>Layer</i>	<i>Regression</i>	<i>r</i> ²	<i>n</i>	<i>Regression</i>	<i>r</i> ²	<i>n</i>
<i>Unit 1A</i>	$5.2(\delta^{18}O) - 53.1$	1.00	11	$4.6(\delta^{18}O) - 64.5$	0.93	15
<i>Unit 1B</i>	$4.9(\delta^{18}O) - 59.5$	0.80	15	$4.9(\delta^{18}O) - 57.9$	0.98	13
<i>Unit 2</i>	$6.1(\delta^{18}O) - 35.8$	0.98	24	$-1.1(\delta^{18}O) - 176.0$	0.01	10
<i>Unit 3A</i>	$7.8(\delta^{18}O) - 2.2$	0.87	34	$4.2(\delta^{18}O) - 74.9$	0.89	39
<i>Unit 3B</i>	n.a.	n.a.	n.a.	$4.3(\delta^{18}O) - 73.3$	0.80	22

* upper domain ** lower domain

Average relict permafrost ice is more depleted than 2019 basal active layer waters, with the exception of Site 3, where the two values are approximately the same. First ice at the base of the 2018 active layer is consistently more enriched than 2019 basal active layer waters at all four sites (Figure 5.15, Table 2). At Site 1, 2019 basal active layer water (-20.8‰ $\delta^{18}\text{O}$) was 0.4‰ more depleted in $\delta^{18}\text{O}$ than 2018 first ice (-20.4‰ $\delta^{18}\text{O}$) and 1.4‰ more enriched in $\delta^{18}\text{O}$ than average relict permafrost (-22.2‰ $\delta^{18}\text{O}$). At Site 2, 2019 basal active layer water (-19.4‰ $\delta^{18}\text{O}$) was 0.3‰ more depleted in $\delta^{18}\text{O}$ than 2018 first ice (-19.1‰ $\delta^{18}\text{O}$) and 1.6‰ more enriched than average relict permafrost (-21.0‰ $\delta^{18}\text{O}$). At Site 3, 2019 basal active layer water (-19.5‰ $\delta^{18}\text{O}$)

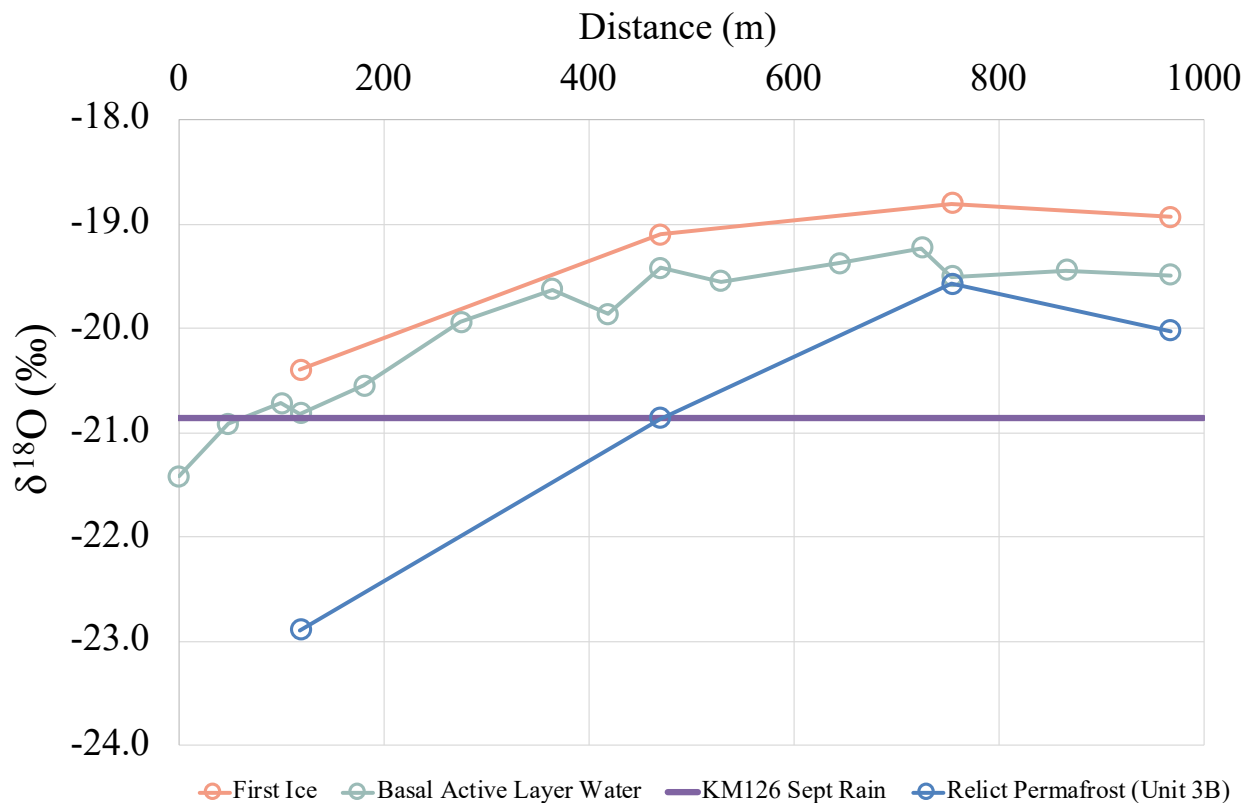


Figure 5.15. Comparison of the $\delta^{18}\text{O}$ values of average relict ground ice, 2018 first ice at the predicted 2018 active layer base, and September 2019 basal active layer water. Relict ground ice refers to ground ice below the transition layer (i.e. Unit 2). Note that the top 15cm were not included in the relict ice $\delta^{18}\text{O}$ average to avoid ice modified by cryotic water migration.

was 0.7‰ more depleted in $\delta^{18}\text{O}$ than 2018 first ice (-18.8 ‰ $\delta^{18}\text{O}$) and equal in value to average relict permafrost. At Site 4, 2019 basal active layer water (-19.5‰ $\delta^{18}\text{O}$) was 0.6‰ more depleted in $\delta^{18}\text{O}$ than 2018 first ice (-18.9‰ $\delta^{18}\text{O}$) and 0.5‰ more enriched than average relict permafrost (-20.0‰ $\delta^{18}\text{O}$).

Table 5.2. $\delta^{18}\text{O}$ values of 2019 basal active layer waters, 2018 first ice, and average relict permafrost ice for each of the four sites. Note that the upper 15cm were not used to calculate the average $\delta^{18}\text{O}$ of the relict permafrost ice to avoid altered ice values due to migrating cryotic waters.

	<i>Site 1</i>	<i>Site 2</i>	<i>Site 3</i>	<i>Site 4</i>
2019 Basal Active Layer Water (‰)	-20.8	-19.4	-19.5	-19.5
2018 First Ice (‰)	-20.4	-19.1	-18.8	-18.9
Average Relict Permafrost (‰)	-22.2	-21.0	-19.5	-20.0

The $\delta\text{D}-\delta^{18}\text{O}$ regressions of relict ice between sites were examined for systematic (consistently increasing or decreasing) variations in the co-isotopic composition of relict ice across the study area (Figure 5.16; Table 5.2, 5.3). The first 15cm of each relict ice record were not included in regression calculations to avoid potential influences from cryotic water migration that may have altered the isotopic composition at this depth. Relict ice from Sites 1-4 were characterized by $\delta\text{D}-\delta^{18}\text{O}$ regression slopes of 7.6, 5.2, 7.4, and 2.7, respectively, demonstrating no systematic variation in $\delta\text{D}-\delta^{18}\text{O}$ regression slope across the study area. With the exception of Site 4 ($r^2 = 0.54$), δD and $\delta^{18}\text{O}$ for a given site was generally well correlated ($r^2 > 0.85$). All $\delta\text{D}-\delta^{18}\text{O}$ values for relict ice fall along a well-correlated ($r^2 = 0.99$) regression ($\delta\text{D} = 6.8\delta^{18}\text{O} - 21.5$) that is nearly superimposed on the LMWL. With the exception of Site 4, each site, starting with Site 1 and moving down-slope, was translated up and to the right of the previous site along this regression. The basal active layer waters formed a well-correlated ($r^2 = 0.98$) $\delta\text{D}-\delta^{18}\text{O}$ regression with a slope of 6.4. The relict ice from Sites 2-4 were displaced below this line. Site 1 relict ice was more depleted than the basal active layer waters. Although collected on the same day, precipitation collected from GNIP stations at KM126 (the Blackstone collection area) and KM174 on the Dempster Highway differed in values.

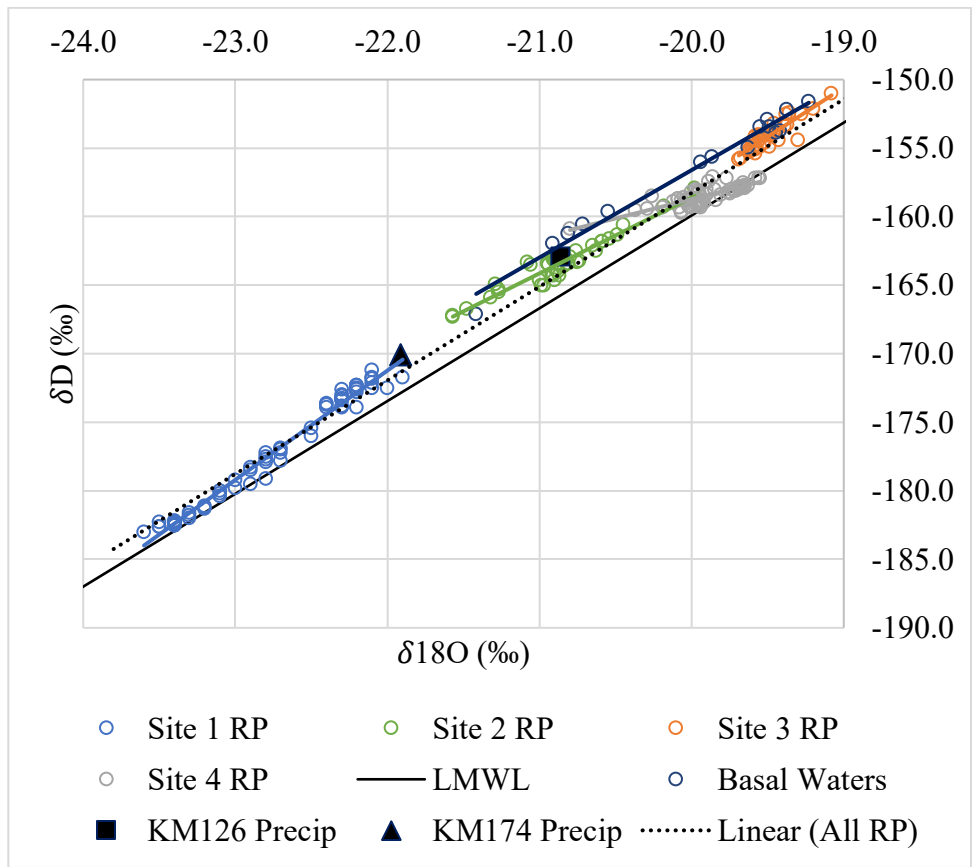


Figure 5.16. δD - $\delta^{18}O$ regressions of relict permafrost ice (RP) at each site, precipitation collected from local GNIP stations (collection on September 18, 2019), and basal active layer waters. Relict ice from all sites fall along a common regression of $\delta D = 6.8\delta^{18}O - 21.5$ ($r^2 = 0.99$). The Note that the top 15cm of relict ice at each site are not included in the regression calculation. LMWL (Baranova, 2017; solid line) has a regression of $\delta D = 6.8\delta^{18}O - 24.5$.

Table 5.3. δD - $\delta^{18}O$ regressions of relict permafrost ice and basal waters in Fig. 5.16.

	<i>Regression</i>
<i>Site 1 Relict Ice</i>	$\delta D = 8.0\delta^{18}O + 4.3$ ($r^2 = 0.98$)
<i>Site 2 Relict Ice</i>	$\delta D = 5.5\delta^{18}O - 47.8$ ($r^2 = 0.92$)
<i>Site 3 Relict Ice</i>	$\delta D = 7.2\delta^{18}O - 14.1$ ($r^2 = 0.78$)
<i>Site 4 Relict Ice</i>	$\delta D = 2.8\delta^{18}O - 102.4$ ($r^2 = 0.66$)
<i>All Relict Ice</i>	$\delta D = 6.8\delta^{18}O - 21.5$ ($r^2 = 0.99$)
<i>Basal Waters</i>	$\delta D = 6.4\delta^{18}O - 29.0$ ($r^2 = 0.98$)

5.4.4. Thaw depth modeling

Polynomial regressions were determined as the best fit for $TDD^{0.5}$ -Thaw Depth data (Figure. 5.17). With the exception of Site 1, for which the two different 2018 ALT_{max} estimations only differ by 1cm, TDD -modeled ALT_{max} is consistently shallower than the isotope-estimated ALT_{max} (Table 5.4).

These thaw depth models should be implemented with caution due to: 1) the overall limited number of thaw depth measurements used; and 2) only single thaw depth measurements were taken in June, 2019. Furthermore, linear regressions fitted to the same data produce non-zero y-intercepts, which represent unrealistic scenarios under the assumption that no thawing should have occurred prior to TDD accumulation.

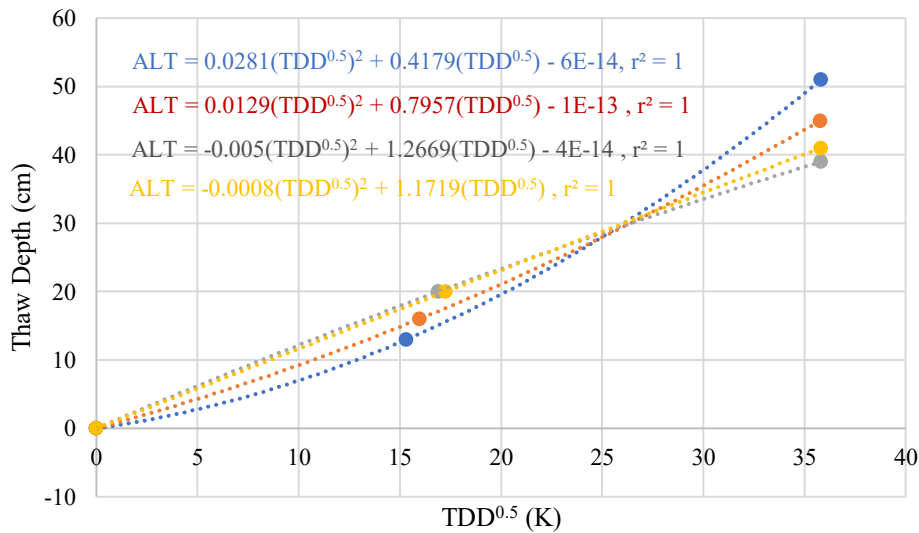


Figure 5.17. Relations between 2019 probed thaw depth and thawing degree-days (TDDs) for each of the four sites in the Blackstone study area. Data for each site were best fitted to a polynomial regression.

Table 5.4. Summary of TDD-modeled 2018 ALT_{max} and isotope-estimated 2018 ALT_{max}.

	Modeled Thaw Depth (cm)	Isotope-Estimated Thaw Depth (cm)
Site 1	43	42
Site 2	39	46
Site 3	36	45
Site 4	37	48

5.5. Discussion

5.5.1. Isotopic development of 2019 basal active layer waters

Isotopic similarity between basal active layer waters at the top of the hill and precipitation from September 2019 (Figure 5.4) indicate the hilltop waters had undergone less isotopic modification than basal active layer waters at the bottom of the slope. Basal water from the Site 2 June, 2019 monolith was also more enriched than June monolith of Site 1 (Figure. 5.5), which tentatively suggests downhill enrichment was also present in June. However, this would require more points along the slope for validation.

Downhill basal active layer water enrichment might have been caused by evaporative fractionation produced by upward vapor transport through air-filled pores in the acrotelm. Evaporative enrichment was active on the hillslope in June, as indicated by the dramatic $\delta^{18}\text{O}$ decrease and d -excess increase with depth in the June 2019 monoliths (Fig. 5.5). These evaporatively enriched acrotelm waters would likely have been flushed down into the catotelm by fresh precipitation. Although mixing with fresh precipitation would inevitably dilute and diminish the original evaporative enrichment, the effects amplify and become observable by repeating the cycle of evaporation and downward translocation as active layer waters flow downslope.

However, the δD - $\delta^{18}O$ regressions of relict ice at Sites 1, 2, and 3 (fig. 5.16, Table 5.3) do not support evaporative fractionation as a mechanism of downhill basal water enrichment. The slopes of these regressions would be expected to decrease with lower slope position as basal waters progressively accumulated more evaporatively enriched moisture or thawed first ice. However, consistent down-slope decrease in δD - $\delta^{18}O$ regression slope is absent in the study area, suggesting that, over the long-term, evaporative enrichment was not responsible for enriching the basal waters that fed the ground ice.

Evaporative fractionation is not the mechanism driving downslope basal water enrichment likely because acrotelm moisture does not have an effective manner of downward migration to the base of the active layer. Infiltration requires a sufficient downward soil water potential. This is easily achieved during periods of snowmelt or rain showers. However, at the time of sampling in September, 2019, most of the active layer was generally at field capacity; monoliths could be held without much water loss until a gentle squeeze was applied. The exception was the catotelm, through which basal waters usually leaked into the excavated soil pits.

Matric water infiltration by gravity could potentially be counteracted by various upward forces. Between precipitation events, upward migration of matric water through the soil column due to surface evaporation and capillary rise might work against downward migration of evaporatively enriched matric water by gravity. Similarly, cation enrichment in the acrotelm produced by surface evaporation might produce an osmotic gradient, pulling moisture upward into the acrotelm if the solute concentration gradient is great enough (Nassar and Horton, 1989; Kelly and Selker, 2001). This is because the air-filled pore space in the active layer would act as a semi-impermeable boundary between the ion-diluted phreatic waters and ion-enriched vadose waters (Kelly and Selker, 2001). Warming near the ground surface by solar radiation and cooling near the permafrost table could lead to a thermal gradient sufficiently stable enough to prevent soil water convection, since warmer soil water would remain higher in the soil column due to its lower density. However, because the maximum density of freshwater is reached at 4°C, solar radiation would need to warm the upper active layer moisture above this temperature. Thus, the downward pull of gravity on the evaporatively enriched matric waters would need to be greater than the combined forces of adsorption, capillarity, a negative ground temperature gradient, and a possible osmotic gradient for infiltration to occur during times of base flow. Ultimately,

however, more sampling and data are required to understand how these forces are interacting in the study area.

Melted ice from the permafrost table might also contribute to downhill active layer water enrichment. First ice formed at the bottom of the active layer during freeze-back is enriched in $\delta^{18}\text{O}$ and δD and has low d -excess relative to the original active layer water. When the active layer reaches its maximum thaw depth later in the following summer, the former first ice from previous years thaws and the released water mixes with the existing basal active layer water. These basal waters accrue more water from melted first ice as they flow down-hill, which progressively augments the enrichment.

In addition to melted first ice, a change in the δ values of precipitation as summer transitions into fall is more likely responsible for down-hill basal water enrichment. Because areas of higher topographic relief are generally better drained, basal waters higher up on the hillslope should contain a greater proportion of isotopically lighter fall precipitation than lower slope positions. Conversely, basal waters at progressively lower slope positions should contain a progressively greater fraction of older, isotopically enriched, summer precipitation. This is due to the greater amount of time these summer waters have had to migrate downslope. Therefore, basal waters further downslope, dominantly sourced from summer precipitation, should be more enriched in ^{18}O and D than waters further upslope.

Fresh precipitation input to the active layer would inevitably result in some degree of mixing between old summer waters and new fall waters in the active layer. The amount of isotopic depletion in the active layer as a consequence of this mixing with fresh fall precipitation might depend on a number of factors, such as the intensity and duration of the precipitation event, the isotopic difference between the old and new waters, active layer depth and corresponding storage capacity, and the unsaturated and saturated hydraulic conductivities of the soil. For example, water infiltration from a low-intensity, short-lived rain shower may be retarded by the unsaturated conditions of the soil at field capacity, and consequently not have time to infiltrate to the base of a deep active layer before it becomes evaporatively enriched. By the time mixing does occur, such as by isotopic diffusion along adsorbed water and capillary water conduits, the isotopic difference between the now evaporatively enriched pluvial water and older, enriched summer water is small, and the bulk isotopic composition of the soil changes little.

Following larger precipitation events and subsequent down-slope macro-pore drainage, the isotopic composition of the remaining matric waters would probably represent a mixture of the older summer precipitation and the newer, more depleted precipitation. By retaining some portion of older precipitation along the slope, matric waters could potentially promote the formation of a smooth isotopic trend in the basal waters along slope, similar to the smooth profile observed in the study area. In contrast, because saturated conditions are likely to persist longer in soils at lower slope positions, they likely do not decrease in saturation to field capacity as frequently as soils further upslope, which would diminish mixing between old basal waters and new precipitation at lower slope positions, preserving the $\delta^{18}\text{O}$ -enriched signature of older summer waters.

Local variations in the degree of down-slope $\delta^{18}\text{O}$ enrichment, notably BW8 and BW10, likely arose from site-specific amounts of thawed first ice and the degree of vertical and lateral mixing. The retention of a minor fraction of snow melt at BW8 could produce lower $\delta^{18}\text{O}$ values relative to adjacent sites. However, snow melt is usually shed relative quickly through the hydraulically conductive acrotelm in spring and early summer when the thaw front is still at a shallow depth (Quinton et al., 2004). Instead, the lower $\delta^{18}\text{O}$ value of BW8 may be due to input of water liberated from the top of a thawing ice wedge upslope. In contrast, however, BW9 (Site 2) was located 13m downslope from an ice wedge, yet its $\delta^{18}\text{O}$ value did not vary greatly from the overall down-slope trend, though this could equally be due to a lack ice wedge thawing at BW9 at the time of sampling.

Alternatively, these variations potentially arise from unique progressions of isotopic development along different water migration routes. The ultimate amount of basal water enrichment at a given point along the base of the hillslope should represent the cumulative effects of enrichment mechanisms along the given water migration route(s) leading to that point. The relative contribution of various processes to down-slope enrichment may vary for different routes. The transect along which basal waters were collected could cross multiple flow paths if the transect was oblique to the general direction of flow. For example, basal water sites BW1, BW2, BW3, BW6, BW7, and BW9 could represent the isotopic development of waters flowing along one migration route, while sites BW4, BW5, BW8, and BW10 could represent isotopic enrichment along a separate migration route.

Basal active layer waters in the degrading polygon area and fen are isotopically similar to those at the base of the hill (Figure 5.4). As explained later, the degrading polygon area likely receives waters flowing off the hillslope even though it is surrounded by ice wedge surface troughs, and thus can be considered as a contiguous component of the downhill enrichment profile. Basal active layer waters from the fen hummock are isotopically similar to those at the base of the hill (Figure 5.4). However, while the possible factors that lead to $\delta^{18}\text{O}$ enrichment (a change in the isotopic composition of the precipitation and introduction of thawed first ice) in all three areas are likely the same, down-slope water migration could not have played a significant role in the isotopic development of BW14 and BW15 basal active layer waters which were sampled from topographically isolated hummocks. Vertical soil water mixing was therefore likely more important than horizontal mixing at BW14 and BW15. Because hydrology of these two sites is not controlled by a continuous hillslope, thawed active layer ice may have been a more significant contributor to the basal active layer water since thaw waters are not mobilized downslope.

Basal active layer water development at BW13, on the other hand, is potentially complicated by its proximity to an ice wedge. Although the ground surface within high-centered ice wedge polygons are nominally higher than surrounding ice wedge surface troughs, and the surface water that pools in them, the BW13 was extracted adjacent to a wedge trough. While this particular spot within the polygon may be hydraulically isolated from trough waters in the spring, and perhaps through mid-summer, late-summer active layer thaw depths may extend below the surface height of standing trough waters, allowing them to infiltrate into the adjacent active layer and influence the isotopic and geochemical development of subsequent ice formation.

5.5.2. Geochemical and isotopic development of the 2018 active layer ice

C-profile development

The active layer (Unit 1) at all four sites are characterized by a “C”-shaped isotope pattern with the most enriched values at the top and bottom of the active layer, and most depleted values in the mid- to lower-mid center (Figure 5.7, Figure 5.9, Figure 5.11, Figure 5.13). Michel and Fritz (1982) report similar observations for the frozen active layer near Illisarvik, N.W.T., and suggest the pattern is attributable to isotopic fractionation during bi-directional freezing.

According to laboratory experiments (e.g. Mageau and Morgenstern, 1980; Suzuoki and Kimura, 1973) and field observations of freezing in frost blisters (e.g. Michel, 1986) and pingos (e.g. Vasil'chuk et al., 2016), for this progressive depletion to occur, the system must be closed or at least partly closed such that there is minimal external water input during freeze-back. However, this assumes that the isotopic composition of waters outside of the system are substantially different from those of the freezing water reservoir. In other words, any input of external water to the reservoir would disrupt the formation of a smooth, progressively depleting isotopic profile in the forming ice.

In contrast, the circumstances of C-profile formation along the hillslope may suggest the system was hydraulically open (i.e. laterally communicative) between the freezing fronts, and was still able to produce progressive, inward depletion consistent with Rayleigh fractionation. However, this is provided that gravity can overcome the force of cryosuction and matric forces, and the progress and extent of cryofractionation was fairly consistent across the hillslope at any given point in time. What remains uncertain is whether cryodesiccation of the inner active layer due to cryosuction would deprive this inner region of the necessary volume of water needed to generate a gravitationally-induced hydraulic potential strong enough to overcome both cryosuction and the matric forces of the soil, and move downhill under gravity. If not, water between the freezing fronts should migrate only to the freezing fronts and not down-slope, and C-profile formation should proceed as it would on level terrain. Ultimately, further testing is required to discern how these competing forces interact.

At all four sites, the upward-freezing zone (Unit 1B) was thinner than the downward-freezing zone (Unit 1A) (Figs. Figure 5.7, Figure 5.9, Figure 5.11, Figure 5.13). This is consistent with Osterkamp and Romanovsky (1997) who used a simple energy balance equation, in addition to known thermodynamic parameters pertaining to the upward-freezing front, to reproduce the thickness of upward freezing. Their findings show that the thermal gradient from the surface downward must be steeper than the thermal gradient from the bottom up to produce a freezing front convergence depth in the lower active layer. Boike et al. (1998) observed that while the full active layer reached 0°C (i.e. started freezing) at practically the same time, continued freezing varied through the active layer in relation to initial water content, which controlled the amount of latent heat released. In this sense, higher water content in the catotelm at the Blackstone study area prior to freeze-back, as was observed in September, 2019, should

maintain the zero-curtain effect longer in the lower active layer, allowing downward-freezing to reach the lower active layer before the conclusion of freeze-back. Luo et al. (2014) showed that the relative rates of freezing between the downward- and upward-freezing zones depends on the temperature at the top of permafrost (TTOP) at maximum thaw depth. In their study, two sites with TTOPs of -1.9°C and -0.9°C had convergence depths within the upper half of the active layer, while two sites with TTOPs $>-0.5^{\circ}\text{C}$ had convergence depths within the lower half of the active layer.

Down-slope first ice enrichment

First ice at the base of the 2018 active layer (i.e base of the C-profile) was progressively more enriched in $\delta^{18}\text{O}$ from the top to the bottom of the hillslope. Down-slope first ice enrichment was most likely the consequence of down-slope basal water enrichment previously described in the 2019 active layer waters. Other processes, such as cryostatic water migration, do not sufficiently explain this behavior. Cryostatic pressure between the advancing freezing fronts could potentially force progressively $\delta^{18}\text{O}$ -depleted water uphill if freezing front convergence progressed from the bottom of the slope to the top. However, to the authors knowledge, this has never been documented. Furthermore, cryostatic pressure would need to force active layer waters upslope and establish the observed stable isotope gradient in waters at the base of the active layer before upward freezing began. This could not be possible given cryostatic pressure is itself produced by propagating freezing fronts and there is no other conceivable force that could redistribute the active layer water up-slope. Neither could down-slope first ice enrichment be explained by migration of active layer waters under cryostatic pressure if the lateral direction of freezing along the slope was reversed (from top to bottom), as this would entail forcing progressively $\delta^{18}\text{O}$ -depleted waters downslope.

Site 1

Stable isotope patterns indicate the depth of maximum 2018 active layer thaw at Site 1 was 42cm. The $\delta^{18}\text{O}$ values above 42cm form a C-profile with a convergence depth of 34cm. The upward-freezing zone (Unit 1B) is thinner than the downward-freezing zone (Unit 1A) indicating upward freezing was slower than downward freezing. Although the isotope-derived 2018 thaw depth estimation falls within falls within 1σ of the average September 2019 thaw

depth (51 ± 13 cm), the 9cm difference between the two measurements, as well as the high September thaw depth variability, make the isotope-estimated thaw depth less certain. This variability is likely caused by localized subsurface pooling or channeling of hilltop active layer waters within thermal erosion depressions in the permafrost table, which are more likely to develop on flatter terrain. This is supported by the high variability of soil saturation between hummocks observed in the field. In contrast to Sites 2-4, the isotope-derived 2018 thaw depth estimation for Site 1 also compares well with TDD-modeled 2018 ALT_{\max} (43cm) (Table 5.4), which further suggests active layer thaw at the Site 1 borehole, was more influenced by air temperature than soil moisture.

Most of the isotopic variations within the downward-freezing zone are likely attributable, in part, to variations in freezing rate and / or effective boundary layer thickness during upward migration of active layer waters by cryosuction. Isolation of small water pockets behind the freezing front during its advance could also reduce overall cryofractionation during ice formation (Suzuoki and Kimura, 1973). The upper domain of the downward-freezing zone (15-21cm) is associated with a curved ice layer. The δD - $\delta^{18}O$ slope of 7.9 is greater than that previously attributed to equilibrium fractionation (6.2-7.3, Lacelle, 2011), which suggests this domain formed from source water of a different isotopic composition than that found lower in the active layer. This could represent either input from precipitation or lateral migration of active layer waters during freeze-back. The isotopic composition of the lower domain of downward freezing ($S_{\delta D-\delta^{18}O} = 6.5$) and of the upward-freezing zone ($S_{\delta D-\delta^{18}O} = 7.2$) are consistent with development by equilibrium fractionation. The spikes in $\delta^{18}O$ and d -excess immediately below the 2018 active layer are likely due to kinetic fractionation of a very limited water reservoir, perhaps trapped behind the upward-propagating freezing front at the start of freeze-back.

Site 2

The base of the 2018 active layer at Site 2 was located at 46cm depth. This is consistent with the average 2019 thaw depth of 44cm, but is inconsistent with TDD-modeled 2018 ALT_{\max} (39cm), potentially due to the thermal effects of soil moisture. The paucity of $\delta^{18}O$ and δD data points within the active layer make observation of a C-profile difficult, though the convergence depth is likely around 36cm. The downward-freezing zone (Unit 1A) was thicker than the upward-freezing zone (Unit 1B), indicating downward freezing occurred more rapidly. This is

supported by the shallower δD - $\delta^{18}O$ regression of the downward-freezing zone ($S_{\delta D-\delta^{18}O} = 6.2$) compared to the upward-freezing zone ($S_{\delta D-\delta^{18}O} = 6.5$), though both slopes indicate freezing in both directions was slow enough to promote equilibrium fractionation ($S_{\delta D-\delta^{18}O} > 6.2$). The geometry of the stable isotope profile between 46-58cm is interpreted as a second C-profile below 46cm, produced by deeper thaw penetration to 58cm depth some time prior to 2018. This is supported by a GWC spike at 58cm. This older C-profile could not have formed during the 2018 freeze-back as this would preclude formation of the C-profile above.

Site 3

The isotope-estimated 2018 ALT_{max} (45cm) at Site 3 is greater than both the September 2019 thawing probing thickness (39 ± 3 cm) and the TDD-estimated 2018 ALT_{max} (36cm). The 6cm discrepancy between the isotope-estimated 2018 ALT_{max} and September 2019 thaw probing thickness potentially arises from greater thermal effects from higher soil moisture content in 2018 than in 2019, while the discrepancy between the TDD-modeled 2018 ALT_{max} and the other two measurements is potentially because the TDD does not account for the thermal effects of soil moisture.

$\delta^{18}O$ and d -excess variability in the upward-freezing zone was potentially caused by kinetic fractionation (scatter in d -excess- δD space, Figure 5.12) and/or an open hydraulic system with variable isotopic input during freeze-back in 2018. Shallow δD - $\delta^{18}O$ regression slopes for downward- and upward-freezing (5.2 and 4.9, respectively, Table 5.1) further support the occurrence of kinetic fractionation during freeze-back. Whether the hydraulic system was open or not, it is unlikely that the active layer was saturated during freeze-back, because the high volume of water should buffer freezing velocity and promote advective heat flow, which would slow freezing rates. Therefore, kinetic fractionation likely occurred because the active layer was not fully saturated.

As previously discussed, a convergence depth in the lower half of the 2018 active layer indicates downward freezing was faster than upward freezing (Osterkamp and Romanovsky (1997); Luo et al., 2014). This further suggests that the temperature at the top of permafrost (TTOP) was $> -0.5^{\circ}C$ prior to freeze-back. Additionally, higher moisture content at the base of the active layer (as observed in during September, 2019 field work) could slow the rate of upward freezing due to greater latent heat release relative to downward freezing.

Open system conditions at Site 3 implies that water at the site is received from upslope. However, this conflicts with the presence of ice wedge surface troughs surrounding the site, which could divert slope waters around the site. Basal waters could bridge these wedge troughs during the summer when active layer thaw within the polygon becomes deep enough and the water table in the troughs become high enough. A high water table in the troughs is a reasonable assumption given the poorly drained conditions in the troughs observed in September, 2019, as evidenced by the presence of standing water. These conditions could initiate a ‘fill-and-spill’ process, similar to that proposed by Spence and Woo (2003) for ground water flow across bedrock, and later adapted by Wright et al. (2009) to describe similar processes across and evolving, semi-impermeable permafrost table during summer. Low pH may also support slope water source, but acidification could equally have occurred more-or-less *in-situ*. Low EC in the active layer, on the other hand, contrasts with much higher EC in transition layer and relict permafrost below, indicating dissolved ions have been concentrating at the bottom of the slope and in the permafrost over time.

Site 4

Stable isotope values of ground ice above 48cm form a C-profile indicative of bi-directional freezing. The GWC spike just below the base of the isotope-estimated 2018 active layer (48cm depth), in addition to the jump in EC, indicates that coupled downward translocation of soil waters and dissolved ions occurred (Figure 5.13). The local $\delta^{18}\text{O}$ minimum, *d*-excess maxima, and a local EC maximum at 37cm depth are indicative of the freezing front convergence depth. The low co-isotopic slopes of the downward- (Unit 1A, $S_{\delta\text{D}-\delta^{18}\text{O}} = 4.6$) and upward-freezing active layer (Unit 1B, $S_{\delta\text{D}-\delta^{18}\text{O}} = 4.9$) indicate freezing fractionation was dominantly kinetic, potentially due to rapid freezing and/or a thick boundary layer between the freezing fronts (Lacelle, 2011). A thicker boundary layer at Site 4 could be related to closed system conditions that mitigated mixing of the inter-front reservoir. The greater thickness of the downward-freezing zone relative to the upward-freezing zone indicates downward freezing was faster than upward freezing. This is further supported by the limited $\delta^{18}\text{O}$ range in the downward-freezing zone compared to the upward-freezing zone, indicating less ideal cryofractionation conditions. The isotope-estimated 2018 ALT_{max} (48cm) is greater than the September 2019 probed thaw depth ($41 \pm 3\text{cm}$) and the TDD-modeled 2018 ALT_{max} . Like Site 3,

this may be because soil moisture at Site 4 was higher than in 2019, and because the TDD thaw depth model does not account directly for the thermal effects of soil moisture.

5.5.3. Cryophysical, geochemical, and isotopic development of hillslope ground ice

The co-occurrence of lenticular and braided cryostructures separated by ice layers indicates that the hillslope permafrost most likely formed syngenetically (French and Shur, 2010; Kanevskiy et al., 2014; Stephani et al., 2014). The presence of organic material at depth further supports a syngenetic origin. Angular inclusions of organics and fine mixing with silt are indicative of cryoturbation. However, modern day cryoturbation is unlikely to reach the lower portions of these cores, indicating aggradation due to sedimentation has taken place, followed by continued cryoturbation. Despite this commonality between Site 1 and Site 2, differences in cryostratigraphy, geochemistry, and stable isotope profiles indicate that deposition and the history of ice formation differed between the two sites.

Site 1

The lower transition layer at Site 1 (Fig. 5.7, Unit 2B) appears to contain fairly high visible ice content in the form of layered and lenticular cryostructures, and its lower boundary is defined by a sharp shift in *d*-excess. These characteristics suggest a period of deep thaw (or multiple periods of deep thaw) followed by a slow frost table recovery to its present depth around the isotope-inferred 2018 thaw depth. This contrasts with most of record, which contains predominantly micro-lenticular and micro-braided cryostructures, suggestive of syngenetic formation. Some intervals containing suspended cryostructures (e.g. Unit 3A, 3C) are perhaps suggestive of pseudo-syngenetic ice growth (c.f. Kanevskiy et al., 2011).

Homogeneous mixing of organic and minerogenic silts indicates the organics were either deposited as loess or displaced from an organic horizon by cryoturbation. However, the latter case lacks support from evidence of deeper cryoturbation, such as the presence of large peaty domains. Although GWC data are not available for this record, visible ice content appears significant. Given the well-drained hydrology of the site, significant ice accumulation most likely developed syngenetically with punctuated periods of thawing, basal thaw water concentration, and permafrost recovery rather than by a single stage of initial downward freezing as primary

epigenesis, the latter of which is conducive to the formation of an ice-poor cryofacies (Kanevskiy et al., 2014; Gilbert et al., 2016).

The upper transition layer (subunit 2A) contains micro-braided and micro-lenticular cryostructures typical of syngenetic ground ice growth. The lower transition layer (subunit 2B) contains layered ice, which is generally an indicator of epigenetic growth – though, in combination with lenticular cryostructures, more likely indicates slow syngenetic growth (Stephanie et al., 2014) or pseudo-syngeneses (Kanevskiy et al., 2014). The cryostructural difference between these two subunits is governed by the difference in substrate. Occasional small, orange mottles in subunit 2B and reticulated ice veins just under the 2A-2B contact, produced by the contraction of the minerogenic material during freezing (Mackay, 1974), both attest to intermittent (decadal-scale) thawing and refreezing which characterizes the transition layer. The sharp shift in *d*-excess at the base of the transition layer represents a thaw unconformity produced by exceptionally deep thawing during a previous year.

A δD - $\delta^{18}O$ slope of 6.7 and negative *d*-excess- δD slope indicates the isotopic composition of transition layer ice developed by equilibrium fractionation (Fig. 5.8). This regression shares overlap with the lower domain of the downward-freezing zone and the upward-freezing zone. The transition layer lacks a C-profile like that in Unit 2 of Site 2 and Site 3, which indicates Unit 2 consists of aggradational pore and texture ice that formed over successive thawing and freezing cycles.

Unit 3A is interpreted as a relict intermediate horizon on the basis of high visible ice content in the form and pseudo-syngenetic lenticular-suspended cryostructures. Pseudo-syngenetic ground ice development was produced by the cessation of sediment deposition, the onset of organic growth, and thinning of the active layer during these processes and aggradational ice accumulation. The silty organics are mixed nearly homogeneously into Units 3A, 3B, and 3C, which indicates plant growth began prior to the cessation of sedimentation, and were consequently reworked by cryoturbation following further sedimentation. The stability of $\delta^{18}O$ and *d*-excess values in Unit 3A suggest that freezing conditions and stable isotopic composition of basal active layer waters (and therefore of precipitation) were stable over the course of ice development. The stability of cryofractionation conditions is further supported by the homogeneity of the soil matrix, which promotes boundary layer thickness regularity and the presence of long, vertical bubble trains indicating consistent, slow freezing conditions. Although

the lack of other geochemical data makes it difficult to ascertain the cause for the isotopic inflection at the Unit 3A-3B boundary, it could have been caused by a shift in either basal active layer water composition, freezing conditions, a change in aggradation rate, or a composite response of different these factors.

Units 3B and 3C are interpreted as syngenetic and pseudo-syngenetic (relict intermediate horizon), respectively. Syngenetic growth of Unit 3B was driven by loess deposition that produced lenticular and micro-lenticular cryostructures of moderate ice content. Unit 3C is potentially pseudo-syngenetic on the basis of a suspended cryostructures. The lack of isotopic inflection across the Unit 3B-3C boundary indicates that although excessive water was available for ice formation, freezing conditions and initial source water isotopic values did not significantly change between the two units.

The δD - $\delta^{18}O$ slope of 6.7 indicates the isotopic composition of Unit 3A (65-90cm) relict ice formed under equilibrium fractionation. The tight cluster of Unit 3A ice above the transition layer in d -excess- δD space indicates both freezing conditions and source water isotope composition were stable during ice development. The discrepancy between Unit 3A and Unit 3B in d -excess- δD space most likely reflects a thaw unconformity at the base of the transition layer, as suggested depth profiles of $\delta^{18}O$ and d -excess.

Site 2

The co-occurrence of micro-lenticular, lenticular, and layered cryostructures in Site 2 indicate ground ice formation probably mostly syngenetic (French and Shur, 2010; Kanevskiy et al., 2014; Stephani et al., 2014) (Fig. 5.9). The rate of syngenetic ground ice aggradation was not steady over time; repeated, individual ice layers are interpreted to have formed during periods of stationary transition layer position (French and Shur, 2010), whereas the lenticular domains represent periods when the transition layer was migrating upwards (French and Shur, 2010). The ice layer (and accompanying veins) and lenticular domains comprising Unit 2 directly beneath the 2018 active layer are likely the most modern iteration of the syngenetic ice sequence, and indicate the top of the modern transition layer (i.e. active layer thickness) has been relatively consistent at this site. Under modern conditions, syngenetic ice growth at the base of the transition layer at the site is likely driven by surface organic accumulation rather than sedimentation. Vein ice found appended to the bottoms of ice layers likely to have formed by the

upward migration of cryotic waters to these layers and desiccation of the surrounding sediment. The presence of cryotic water is likely due to dissolved solutes (Kokelj and Burn, 2003) and influence of Van der Waals forces along soil grain boundaries (Lacelle et al., 2014). Thus, while syngenetic ground ice formation is traditionally envisioned as an aggradational process (i.e. the formation of aggradation ice), the presence of layered and vein ice at Site 2 suggests syngeneses can be augmented by segregational processes. The upward migration of unfrozen, cryotic waters from deeper in the permafrost also explains domains of upward-increasing GWC observed in Units 2 & 3.

The brown coloration of the Site 2 soil profile indicates organic matter is mixed into the silty, minerogenic matrix and provides further evidence for syngenetic ground ice formation. In addition to the fine mixture of organics and silt, larger organic-rich domains are found closer to the bottom of the core. Either this organic horizon represents primary peat deposition prior to sedimentation or is composed of organics that were cryoturbated following initial sedimentation due to repeated freezing and thawing in the active layer (Schaetzl and Thompson, 2015). In either case, the presence of this organic horizon much deeper than the modern active layer indicates materials here must have once been closer to the ground surface, and that further sedimentation has since taken place. This further indicates that there is a transition from sedimentation-driven syngenetic permafrost growth to organic accumulation-driven syngenetic permafrost growth.

The dominantly silty texture of the hillslope soil matrix and syngenetic origin of the ground ice suggest an aeolian origin. Loess formation may have been locally prolific during the retreat of montane glaciers, such as the one that formed the Chapman Lake Moraine located just south of the study area. The finer fraction of organic matter in these silts may be sourced from cryoturbated surface organics, and some deposited as loess. The presence of pebbles and cobbles in the soil is most likely the result of the slow, upward mobility of these clasts due to cryoturbation from a deeper, coarser-textured horizon, potentially a paleo-outwash plain geographically associated with the Chapman Lake Moraine.

The 2018 transition layer in Site 2 corresponds with Unit 2. The bottom limit (59cm) is defined by a spike in GWC associated with a visible ice layer that likely formed during an older, deeper thawing event. This ice layer is likely formed of first ice as indicated by the isotope C-profile. Ice veins in the transition layer are interpreted to have formed due to upward cryosuction

of cryotic waters to the bottom of the active layer during freeze-back, likely over multiple freeze-thaw cycles, helping to feed the growth of the ice layer at the base of the modern active layer. A δD - $\delta^{18}O$ slope of 6.5 (Fig. 5.10) suggests the transition layer formed by equilibrium fractionation during C-profile formation. The well preserved C-profile also suggests that 2018 thawing and freeze-back did little to isotopically alter the transition layer ice below.

Ground ice in Unit 3A is interpreted as relict syngenetic ice, as indicated by a similar repetition of layered and lenticular ice. Syngensis in this subunit was most likely driven by slow upward migration of the transition layer base in response to slow surface peat accumulation. In a syngenetic context, the stable *d*-excess sequence suggests freezing conditions (freezing rate, effective boundary layer thickness) over the course of texture ice formation were consistent, and that upward $\delta^{18}O$ enrichment was mainly driven by changing basal active layer water isotopic composition. Like those in the transition layer, ice veins likely formed due to upward cryosuction of cryotic waters during ice layer formation. The lower acidity of the ice (pH<6) suggests it formed from waters that had previously resided in a Sphagnum-rich organic active layer because of the natural acidifying activity of Sphagnum peat (Kuhry et al., 1992) before migrating down into the mineral horizon. Isotopic scatter in *d*-excess- δD space reflects changing freezing conditions and/or source water isotope composition over time. A δD - $\delta^{18}O$ slope of 7.3 (Figure 5.10, Table 5.1) indicates Unit 3A developed by equilibrium fractionation (Lacelle et al. 2011). In *d*-excess- δD space, Unit 3A overlaps completely with transition layer ice. The isotopic continuity of the two tentatively suggests the ice above and below the Unit 2 – Unit 3A contact is conformable. However, the 1.11‰ $\delta^{18}O$ depletion and 2.39‰ *d*-excess enrichment with depth within in the uppermost 3cm of Unit 3A (59-62cm) suggests this ice was altered by cryotic water migration during transition layer thaw to 59cm (Lacelle et al., 2014). Cryotic water migration is supported by the presence of vein ice.

Unit 3B is interpreted as a relict intermediate horizon on the basis of its greater visible ice content and layered-suspended cryostructure. GWC values in Unit 3B closely compare with reported GWC values from Yedoma sequences in Alaska (Kanevskiy et al., 2014). This relict intermediate horizon likely formed after surface sedimentation stopped and as organics began to accumulate, resulting in active layer thinning and aggradational ice formation. High pH values approximating those typical of precipitation indicate Sphagnum was not among this primary vegetation succession. The upward gradation from micro-lenticular to lenticular to a suspended

cryostructure, accompanied by increasing GWC, suggests that rate of intermediate horizon formation progressively slowed, potentially due to increased thermal buffering by the increasing ice content. Given that the onset of intermediate horizon growth was induced by the cessation of surface sedimentation, the former active layer prior to onset of organic growth would have operated across the depth interval between the top of the sediments (~32cm) and the bottom of the intermediate horizon (92cm).

The irregular-reticulate cryostructures in Unit 3C diverge from the syngenetic facies of the rest of this sequence. Reticulate structures typically indicate epigenetic growth, with irregular-reticulate structures forming in slightly coarser-grained, potentially more heterogeneous mineral materials (French and Shur, 2010). Fortier et al. (2008) conducted lab experiments demonstrating the formation of irregular-reticulate cryostructures in water-rich slurries frozen slowly within a confined system (multi-directional freezing) as a potential analogue for their formation in subterranean soil channels observed in the CRREL permafrost tunnel. Ice in Unit 3C is thus interpreted to have formed slowly from a similar mud slurry while lacking a clear freezing front direction. The exact circumstances in which this scenario occurred are unclear, but may have been a consequence of shifting ground temperature regime following initial loess deposition. High pH, in this case, indicates surface organics were not present at the time of ice formation.

Peats in Unit 3D are interpreted as a buried O-horizon. Organic fragments in Unit 3B and 3C likely originated from Unit 3D and were displaced upwards by cryoturbation after the onset of silt deposition. The micro-braided cryostructure in the peat indicates a syngenetic origin, although ice formation in Unit 5 is not associated with the peat itself, but rather sediment deposition above. The jump in EC may have been formed by the concentration of solutes leached out of freshly deposited loess.

5.5.4. Cryophysical, geochemical, and isotopic development of ground ice in the degrading polygon area and fen

Site 3

High ice content and EC throughout the record is likely related to water and dissolved ion accumulation at the base of the slope (Fig. 5.11). Although the ice wedge trough observed just upslope of Site 4 seemed like it might redirect active layer waters around the site, standing water

in the troughs indicated they are not well drained. Therefore, if the elevation of the water table were to increase from basal water input from the slope, in addition to a thawing active layer within the polygon, a ‘fill-and-spill’ mechanism could develop, allowing basal slope waters to migrate into the polygon (Spence and Woo, 2003; Wright et al., 2009). Delivery of basal water to the base of the hillslope paired with ‘fill-and-spill’ activity into the polygon active layer may result in greater inter-annual fluctuations in maximum active layer thaw, which could explain why the Site 3 transition layer is thicker than at the other three sites.

The isotopic gradient with depth in the upper ~15cm of the transition layer was likely produced by downward infiltration of basal active layer waters into the upper permafrost. Infiltration probably occurred during summer 2018, when the active layer thawed and liberated large amounts of water, which accumulated above the thaw front, and above the permafrost table later in the summer (c.f. Mackay, 1983; Cheng, 1983). Considerable amounts of liquid-filled pore space can exist below the thaw front, where temperatures are at or slightly below freezing due to surface boundary forces between the water and ice and the presence of dissolved solutes (Hivon and Segó, 1995). This allows basal waters to move downward by cryosuction along a negative temperature gradient and by gravity (Mackay, 1983). As temperature decreases with depth, the amount of cracks and pore space decreases, progressively limiting the amount of basal water penetration with depth. Consequently, the bulk isotopic composition of the ice and cryotic water deeper in this ‘zone of infiltration’ remains more similar to that of the original ice. In contrast, the relatively greater amount of basal waters near the base of the active layer results in a bulk isotopic composition closer to that of the basal waters. The resulting isotopic gradient might also have been accentuated by increasing kinetic fractionation with depth during freezing due to a limited water supply (Lacelle et al., 2014). However, a δD - $\delta^{18}O$ regression slope of 6.1 ($r^2 = 0.98$) (Fig. 5.12) indicates cryofractionation was close to equilibrium (Lacelle, 2011). Additionally, the well-defined regression in d -excess- δD space also suggests fractionation occurred under equilibrium conditions (Lacelle et al., 2014).

The influence of downward-migrating basal waters into the transition layer is further supported by the sudden, large increase in GWC observed just below the top of the transition layer (Lacelle et al., 2014). GWC decreases with depth from this point, likely because of decreasing porosity and permeability at the time water migration occurred. Increasing EC with

depth indicates dissolved ions were drawn down into the ice with the basal water (c.f. Lacelle et al., 2014).

Some isotopic modification may also occur during freeze-back and throughout winter, when cryotic waters migrate upwards from deeper in transition layer toward the top of permafrost and lower active layer along a negative temperature gradient. However, isotopic modification from upward migration is probably less significant, since the volume of upward water migration in winter is smaller than during downward migration in the summer (Cheng, 1983).

$\delta^{18}\text{O}$ is slightly more depleted in the lower two thirds of the transition layer than in the relict permafrost. This is potentially because the transition layer has not yet undergone a sufficient number of freeze-thaw cycles to allow enriched basal waters to infiltrate and modify the original ice at lower depths.

The base of the transition layer (Unit 2-3 boundary, 81cm depth) is characterized by a sharp local increase in $\delta^{18}\text{O}$ and decrease in d -excess. These spikes are interpreted as a remnant of former first ice that formed after deep thaw penetration, and may not have been smoothed over by infiltrating basal waters if freeze-back was fast enough to prevent significant infiltration.

Site 4

The 2018 transition layer (Unit 2) at Site 4 is between 48-58cm depth. This is supported by relatively high EC and GWC values (Fig. 5.13) produced from downward translocation and concentration of thaw waters and dissolved ions during deep thaw penetration (Kokelj and Burn, 2003). EC at 58cm shifts abruptly, indicating a thaw unconformity. The absolute GWC maximum at 56cm also corresponds with this unconformity. Similarly, the GWC local maximum at 49cm likely corresponds to the upper boundary of the transition layer. The depth offset in the GWC profile here is likely a product of human error and material loss during subsampling, as core materials were subsampled later and therefore separately from subsampling for isotopes and geochemistry. Scattered δD - $\delta^{18}\text{O}$ data in the transition layer (Fig. 5.14), which fell between value of active layer and relict permafrost ice, suggests infiltration of basal active layer waters into the transition layer during summer of 2018. The positive regression in d -excess- δD space systematically varies with depth in the transition layer, reflecting a decreasing proportion of basal active layer waters.

Unit 3 corresponds to relict pore and texture ice. Stable isotopes in Unit 3 of Site 4 are relatively clustered in *d*-excess- δD space compared with Unit 3 ground ice in the other three cores, suggesting relatively consistent freezing conditions and source water isotope composition over time. The low δD - $\delta^{18}O$ slope of 4.2 in Unit 3A indicates kinetic fractionation was the most dominant during ice aggradation in the upper relict ice. Depleted values at the base of the transition layer match well with enriched values in the relict ice of Unit 3A, suggesting that ground ice above and below the Unit 2 – Unit 3A boundary is conformable. However, sudden $\delta^{18}O$ depletion and *d*-excess enrichment in the upper 3cm (58-61cm) of Unit 3A suggests basal active layer waters penetrated the top of permafrost during transition layer thaw, which subsequently froze rapidly with the limited amount of interstitial cryotic waters (Lacelle et al., 2014). Basal water migration into the top of permafrost during this thaw is supported by the EC maximum at 2cm below the estimated transition layer base. This pattern is also observed at the top of Unit 3B (99-103cm).

5.5.5. Role of down-hill enrichment in the isotopic development of ground ice

The isotopic averages of the relict ground ice profiles along the hillslope enrich downslope, mirroring enrichment of 2019 basal active layer waters and 2018 first ice (Figure 5.15). This suggests that (1) down-slope basal active layer water enrichment has been a reoccurring late-summer pattern across this hillslope over past millennia, and (2) down-slope basal active layer water enrichment seems to be an important modulator of isotope record development in ground ice along the hill slope over millennial time scales. Because basal active layer waters are less isotopically modified at the top of the hillslope, hilltop ground ice records, such as at Site 1, likely provide more accurate records of the original isotopic composition of precipitation. In contrast, ground ice at lower hillslope positions are sourced from secondarily-enriched active layer waters, and are therefore less reliable for determining the isotopic composition of the original precipitation. This does not mean, however, that ground ice at hilltop positions escape the effects of basal active layer migration down into the upper permafrost by cryosuction during the summer. Figure 5.18 conceptually summarizes how the isotopic profiles of relict ice isotopically shift in a positive direction with further downslope position and the processes responsible for this shift.

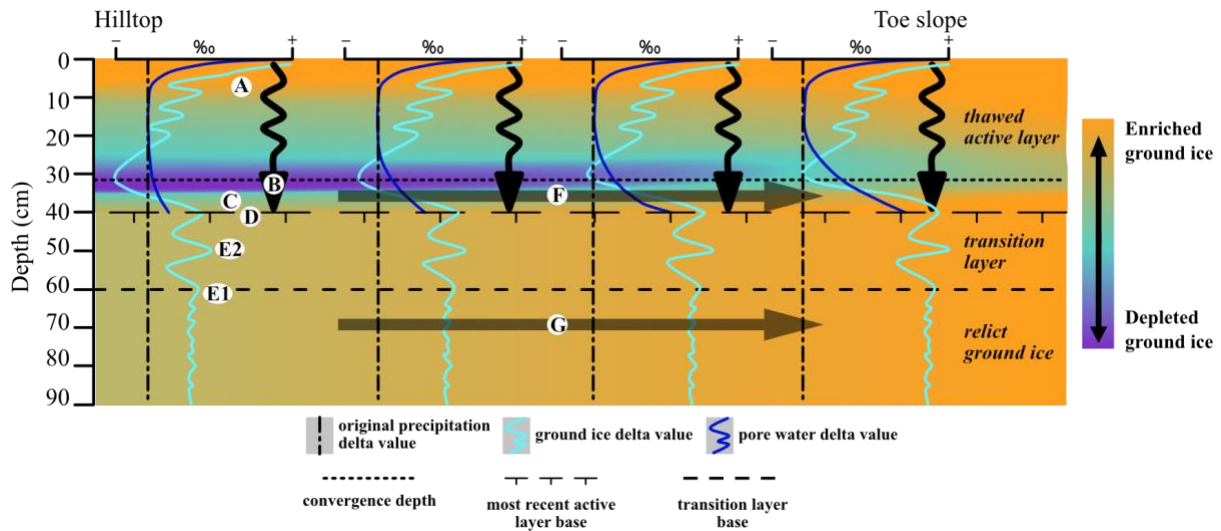


Figure 5.18. Conceptual model of stable isotope development in ground ice along sloping terrain. Common mechanisms of isotopic development include: A) Evaporative enrichment; B) rainwater infiltration to the active layer base; C) transition layer recycling and active layer water accumulation; D) cryofractionation-enriched first ice; E1,2) enriched first ice from an older freeze-back; F) basal active layer waters enrich in $\delta^{18}\text{O}$ and δD as they move downslope; G) downslope relict ground ice enrichment in $\delta^{18}\text{O}$ and δD .

5.5.6. Modern climate change and recent stable isotope record formation

Site 1 and Site 2 show some evidence that they are beginning to reflect modern climate warming in their stable isotope records (Figs. 5.7, 5.9). In Unit 3A of Site 2 (Figure 5.9), the $\delta^{18}\text{O}$ enrichment of 0.53‰ and stable *d*-excess values between 62-73cm indicates the basal active layer water isotope composition was becoming more enriched as ice aggraded, following a δD - $\delta^{18}\text{O}$ regression with a slope of ~ 8 . As previously discussed, ice between 59-62cm is likely altered by cryotic water migration and is therefore not considered part of the final isotopic record of modern climate warming in this core. $\delta^{18}\text{O}$ values in Unit 3A do not surpass those of Unit 3B until 67cm depth, which means the isotopic signal that can be attributed to modern climate warming is small, with a thickness of 5cm (62-67cm) and $\delta^{18}\text{O}$ difference of 0.16‰.

In contrast, $\delta^{18}\text{O}$ enrichment of 0.5‰ at Site 1 (Figure 5.7) starts within the transition layer at a depth of 55cm (upper Unit 2B). Although the onset of isotopic enrichment here is provisional, its position within the estimated transition layer means the modern climate warming signal here may still be subject to decadal-scale thaw depth variations, isotopic mixing, and

isotopic alteration. Slower rates of surface aggradation at Site 1 may explain why this signal is within the transition layer compared to potentially faster surface aggradation rates at Site 2.

Climate-driven $\delta^{18}\text{O}$ enrichment in the transition layer or upper relict ice was not observed at Site 3 and Site 4. As previously discussed, the enriched $\delta^{18}\text{O}$ and low d -excess values in the upper transition layer of Site 3 (Fig. 5.11) are most likely due to the infiltration of basal waters into the upper permafrost during summer active layer thawing. If climate-related warming did exist in the upper relict ice at Site 3, it has likely been erased by deep thaw penetration to the base of the active layer. The reason for a lack of a modern warming signal in the Site 4 isotope record is less clear. Despite the lack of chronology, $\delta^{18}\text{O}$ enrichment beginning at ~80cm depth is likely not related to modern climate warming, as the 22cm thickness between the start of enrichment and estimated transition layer base would imply unprecedented aggradation rates at the site. The lack of modern warming signal at Site 4 (Fig. 5.13) may be attributed to a static surface elevation if organic decomposition and compaction is keeping pace with the rate of organic accumulation. While rates of organic matter input and decomposition are not available, the advanced stages of organic decomposition in much of the core suggest the material has undergone considerable compaction.

5.6. Conclusions

Electrical conductivity, pH, and stable isotope analysis, in combination with traditional cryostructures analysis, proved effective for identifying key stratigraphic units, including the transition layer. The frozen active layer is characterized by a “C”-shaped stable isotope profile produced by Rayleigh fractionation or near-Rayleigh fractionation during bi-directional freezing. Maximum thaw depths, predicted from the base of the C-profiles, generally agree with 2019 thaw depth probing. Discrepancies between the two were most likely due to inter-annual differences in thaw depth, as in the case of Site 4, or local thaw depth heterogeneity, which makes comparison difficult, as in the case of Site 1. Conversely, stable isotopes alone did not always reliably predict the base of the transition layer. Instead, this boundary was identified using a combination of electrical conductivity, pH, $\delta^{18}\text{O}$, d -excess, and GWC, where they exhibited strong, coinciding inflections.

Active layer ice from 2018 was characterized by C-profiles produced by Rayleigh fractionation or near-Rayleigh fractionation during bi-directional freezing. Upward-freezing

zones in these C-profiles were thinner than downward-freezing zones because downward freezing occurred faster due to a steeper thermal gradient in the upper active layer. Isotopic fractionation occurred by equilibrium fractionation within the hillslope active layers (Sites 1 and 2) and by kinetic fractionation at the degrading ice wedge site (Site 3) and fen hummock site (Site 4). The depth of basal first ice enrichment in the active layer overall proved reliable as an estimator of maximum thaw depth from the previous year. The results of this study indicate that, while first ice can be more enriched than underlying transition layer ice, this is not always the case, suggesting maximum enrichment of basal active layer first ice is more likely a product of freezing conditions and source water composition for a given year rather than an innate isotopic relation between active layer and transition layer ice.

The transition layer at Site 2 preserved a C-profile that formed during a summer thaw some time prior to 2018. C-profile preservation suggests that the Site 2 transition layer has undergone very few cycles of thawing and refreezing since C-profile formation, and therefore possibly exemplifies an isotopically ‘immature’ transition layer. The same could be said for the transition layer at Site 3. While the Site 3 transition layer does not appear to be characterized by a C-profile, its $\delta^{18}\text{O}$ values are less than those of the underlying relict ice.

Co-isotopic regressions indicated equilibrium conditions or near-equilibrium cryofractionation generally prevailed during pore and texture ice formation at the base of the active layer and upper permafrost. Except at Site 1 where a thaw unconformity was identified, the isotopic composition of the upper relict ice inherited the isotopic composition of basal transition layer ice as the permafrost aggraded due to sedimentation and later peat accumulation. At Sites 2 and 3, there is also evidence that downward-migrating basal active layer waters by cryosuction during summer altered the isotopic composition of transition layer ice and relict permafrost ice, which manifests as a downward decrease in $\delta^{18}\text{O}$ and increase in *d*-excess.

The compounding effects of surface evaporation and recycling of transition layer ice enriched basal active layer waters as they moved downslope. This effect appears to have been a recurring phenomenon over past millennia as relict pore and texture ice are increasingly enriched relative to local precipitation at lower slope position on the hillslope. Relict pore and texture ice from the degrading polygon area and fen achieved similar enrichment, indicating the same active layer and transition layer processes influenced isotopic development in non-sloping areas. These findings suggest that hilltop stable isotope records in pore and texture ice are more representative

of local precipitation, whereas ground ice further downslope is more influenced by secondary isotopic fractionation processes experienced by basal active layer waters prior to freeze-back.

Pore and texture ice along the hillslope exhibited some evidence of isotopic enrichment in the top of permafrost driven by recent warming. At Sites 1 and 3 this enrichment was restricted to the transition layer, where it is potentially subject to future thawing and isotopic blending. $\delta^{18}\text{O}$ enrichment in the upper relict ice of Site 2 suggests that a change in environmental conditions or climate has occurred. However, this enrichment does not significantly surpass maximum $\delta^{18}\text{O}$ values in older relict ice. Although the Site 3 and Site 4 records were hosted in thick syngenetic peats, enrichment at the top of the relict ice was not observed at either site. At Site 3 this is possibly due to deep thaw penetration to the base of the transition layer and erasure of climate-related isotopic enrichment. The lack of upper relict ice enrichment at Site 4 was not clear, but is potentially attributed to a lack of recent surface aggradation. Although evidence for climate warming in the stable isotope record of pore and texture ice in the study area is provisional, the results of this study nonetheless shed light on the isotopic development of pore and texture ice, especially with regard to the role of the transition layer.

References

- Bandara, S., Froese, D., Porter, T. J., & Calmels, F. (2020). Holocene pore-ice $\delta^{18}\text{O}$ and $\delta^2\text{H}$ records from drained thermokarst lake basins in the Old Crow Flats, Yukon, Canada. *Permafrost and Periglacial Processes*, 31(4), 497-508.
- Baranova, N. (2017). *Evaluating Groundwater In a Permafrost Watershed Using Seasonal Geochemical and Isotope Discharge Trends, Ogilvie River, Yukon* (Doctoral dissertation, Université d'Ottawa/University of Ottawa).
- Briner, J. P., Kaufman, D. S., Manley, W. F., Finkel, R. C., & Caffee, M. W. (2005). Cosmogenic exposure dating of late Pleistocene moraine stabilization in Alaska. *Geological Society of America Bulletin*, 117(7-8), 1108-1120.
- Brosius, L. S., Anthony, K. W., Grosse, G., Chanton, J. P., Farquharson, L. M., Overduin, P. P., & Meyer, H. (2012). Using the deuterium isotope composition of permafrost meltwater to constrain thermokarst lake contributions to atmospheric CH_4 during the last deglaciation. *Journal of Geophysical Research: Biogeosciences*, 117(G1).
- Craig, H. (1961). Isotopic variations in meteoric waters. *Science*, 133(3465), 1702-1703.
- Cheng, G. (1983). The mechanism of repeated-segregation for the formation of thick layered ground ice. *Cold Regions Science and Technology*, 8(1), 57-66.
- Dansgaard, W. (1964). Stable isotopes in precipitation. *Tellus*, 16(4), 436-468.

- Dereviagin, A. Y., Chizhov, A. B., Meyer, H., Hubberten, H. W., Siegert, C., Phillips, M., ... & Balkema, A. A. (2003, July). Recent ground ice and its formation on evidence of isotopic analysis. In *Proceedings of 8th International Conference on Permafrost* (pp. 21-25).
- Duk-Rodkin, A. (1996). Surficial Geology, Dawson, Yukon Territory. *Geological Survey of Canada, Open File*, **3288**, 1 map, scale 1:250 000.
- Environment and Climate Change Canada. (2016). *Canadian Climate Normals*. Retrieved from https://climate.weather.gc.ca/climate_normals/index_e.html.
- Fortier, D., Kanevskiy, M., & Shur, Y. (2008, June). Genesis of reticulate-chaotic cryostructure in permafrost. In *Proceedings of the Ninth International Conference on Permafrost* (Vol. 1, pp. 451-456). Fairbanks, AK: Institute of Northern Engineering, University of Alaska Fairbanks.
- French, H., & Shur, Y. (2010). The principles of cryostratigraphy. *Earth-Science Reviews*, *101*(3-4), 190-206.
- Gilbert, G. L., Kanevskiy, M., & Murton, J. B. (2016). Recent advances (2008–2015) in the study of ground ice and cryostratigraphy. *Permafrost and Periglacial Processes*, *27*(4), 377-389.
- Grinter, M., Lacelle, D., Baranova, N., Murseli, S., & Clark, I. D. (2019). Late Pleistocene and Holocene ice-wedge activity on the Blackstone Plateau, central Yukon, Canada. *Quaternary Research*, *91*(1), 179-193.
- Hivon, E. G., & Sego, D. C. (1995). Strength of frozen saline soils. *Canadian Geotechnical Journal*, *32*(2), 336-354.
- Kanevskiy, M., Jorgenson, T., Shur, Y., O'Donnell, J. A., Harden, J. W., Zhuang, Q., & Fortier, D. (2014). Cryostratigraphy and permafrost evolution in the lacustrine lowlands of west-central Alaska. *Permafrost and Periglacial Processes*, *25*(1), 14-34.
- Kanevskiy, M., Shur, Y., Fortier, D., Jorgenson, M. T., & Stephani, E. (2011). Cryostratigraphy of late Pleistocene syngenetic permafrost (yedoma) in northern Alaska, Itkillik River exposure. *Quaternary research*, *75*(3), 584-596.
- Kelly, S. F., & Selker, J. S. (2001). Osmotically driven water vapor transport in unsaturated soils. *Soil Science Society of America Journal*, *65*(6), 1634-1641.
- Kokelj, S. V., & Burn, C. R. (2003). Ground ice and soluble cations in near-surface permafrost, Inuvik, Northwest Territories, Canada. *Permafrost and Periglacial Processes*, *14*(3), 275-289.
- Kuhry, P., Halsey, L. A., Bayley, S. E., & Vitt, D. H. (1992). Peatland development in relation to Holocene climatic change in Manitoba and Saskatchewan (Canada). *Canadian Journal of Earth Sciences*, *29*(5), 1070-1090.
- Lacelle, D., Fontaine, M., Forest, A. P., & Kokelj, S. (2014). High-resolution stable water isotopes as tracers of thaw unconformities in permafrost: A case study from western Arctic Canada. *Chemical Geology*, *368*, 85-96.
- Lacelle, D., Fontaine, M., Pellerin, A., Kokelj, S. V., & Clark, I. D. (2019). Legacy of Holocene landscape changes on soil biogeochemistry: a perspective from paleo-active layers in

- Northwestern Canada. *Journal of Geophysical Research: Biogeosciences*, 124(9), 2662-2679.
- Lacelle, D. (2011). On the $\delta^{18}\text{O}$, δD and D-excess relations in meteoric precipitation and during equilibrium freezing: theoretical approach and field examples. *Permafrost and Periglacial Processes*, 22(1), 13-25.
- Luo, D., Jin, H., Lü, L., & Wu, Q. (2014). Spatiotemporal characteristics of freezing and thawing of the active layer in the source areas of the Yellow River (SAYR). *Chinese Science Bulletin*, 59(24), 3034-3045.
- Mackay, J. R. (1974). Reticulate ice veins in permafrost, Northern Canada. *Canadian Geotechnical Journal*, 11(2), 230-237.
- Mackay, J. R. (1983). Downward water movement into frozen ground, western arctic coast, Canada. *Canadian Journal of Earth Sciences*, 20(1), 120-134.
- Mageau, D. W., & Morgenstern, N. R. (1980). Observations on moisture migration in frozen soils. *Canadian Geotechnical Journal*, 17(1), 54-60.
- Meyer, H., Schirmer, L., Andreev, A., Wagner, D., Hubberten, H. W., Yoshikawa, K., ... & Brown, J. (2010). Lateglacial and Holocene isotopic and environmental history of northern coastal Alaska—Results from a buried ice-wedge system at Barrow. *Quaternary Science Reviews*, 29(27-28), 3720-3735.
- Michel, F. A. (1986). Isotope geochemistry of frost-blister ice, North Fork Pass, Yukon, Canada. *Canadian Journal of Earth Sciences*, 23(4), 543-549.
- Michel, F. A., Fritz, P., & French, H. M. (1982). Significance of isotope variations in permafrost waters at Illisarvik, NWT. In *Proceedings of the Fourth Canadian Permafrost Conference* (pp. 173-181). National Research Council of Canada.
- Muñoz Sabater, J. (2021). *ERA5-Land hourly data from 1950 to 1980* [data set]. Copernicus Climate Change Service (C3S) Climate Data Store (CDS). Retrieved January 26, 2022, from <https://cds.climate.copernicus.eu/cdsapp#!/dataset/10.24381/cds.e2161bac?tab=overview>
- Muñoz Sabater, J., (2019): ERA5-Land hourly data from 1981 to present. Copernicus Climate Change Service (C3S) Climate Data Store (CDS). Retrieved January 26, 2022, from <https://cds.climate.copernicus.eu/cdsapp#!/dataset/10.24381/cds.e2161bac?tab=overview>
- Nassar, I. N., & Horton, R. (1989). Water transport in unsaturated nonisothermal salty soil: II. Theoretical development. *Soil Science Society of America Journal*, 53(5), 1330-1337.
- NASA Goddard Institute for Space Studies. (2021). Panoply (Version 4.12.6) [Computer software]. National Aeronautics and Space Administration (NASA). Retrieved from <https://www.giss.nasa.gov/tools/panoply/>
- O'Neil, J. R. (1968). Hydrogen and oxygen isotope fractionation between ice and water. *The Journal of Physical Chemistry*, 72(10), 3683-3684.
- Opel, T., Meyer, H., Wetterich, S., Laepple, T., Dereviagin, A., & Murton, J. (2018). Ice wedges as archives of winter paleoclimate: A review. *Permafrost and Periglacial Processes*, 29(3), 199-209.

- Porter, T. J., Schoenemann, S. W., Davies, L. J., Steig, E. J., Bandara, S., & Froese, D. G. (2019). Recent summer warming in northwestern Canada exceeds the Holocene thermal maximum. *Nature communications*, *10*(1), 1-10.
- Quinton, W. L., Carey, S. K., & Goeller, N. T. (2004). Snowmelt runoff from northern alpine tundra hillslopes: major processes and methods of simulation. *Hydrology and Earth System Sciences*, *8*(5), 877-890.
- RStudio Team. (2016). RStudio: Integrated Development for R. RStudio, Inc., Boston, MA. <http://www.rstudio.com/>
- Schaetzl, R. J., & Thompson, M. L. (2015). *Soils*. Cambridge university press.
- Schwamborn, G., Meyer, H., Fedorov, G., Schirrmeister, L., & Hubberten, H. W. (2006). Ground ice and slope sediments archiving late Quaternary paleoenvironment and paleoclimate signals at the margins of El'gygytyn Impact Crater, NE Siberia. *Quaternary Research*, *66*(2), 259-272.
- Shur, Y., Hinkel, K. M., & Nelson, F. E. (2005). The transition layer: implications for geocryology and climate-change science. *Permafrost and Periglacial Processes*, *16*(1), 5-17.
- Spence, C., & Woo, M. K. (2003). Hydrology of subarctic Canadian shield: soil-filled valleys. *Journal of Hydrology*, *279*(1-4), 151-166.
- Stephani, E., Fortier, D., Shur, Y., Fortier, R., & Doré, G. (2014). A geosystems approach to permafrost investigations for engineering applications, an example from a road stabilization experiment, Beaver Creek, Yukon, Canada. *Cold regions science and technology*, *100*, 20-35.
- Suzuoki, T., & Kimura, T. (1973). D/H and 18O/16O fractionation in ice-water system. *Journal of the Mass Spectrometry Society of Japan*, *21*(3), 229-233.
- Throckmorton, H. M., Newman, B. D., Heikoop, J. M., Perkins, G. B., Feng, X., Graham, D. E., ... & Wilson, C. J. (2016). Active layer hydrology in an arctic tundra ecosystem: quantifying water sources and cycling using water stable isotopes. *Hydrological Processes*, *30*(26), 4972-4986.
- Vasil'chuk, Y. K., van der Plicht, J., Jungner, H., & Vasil'chuk, A. C. (2000). AMS-dating of Late Pleistocene and Holocene syngenetic ice-wedges. *Nuclear Instruments and Methods in Physics Research Section B: Beam Interactions with Materials and Atoms*, *172*(1-4), 637-641.
- Vasil'chuk, Y. K., Budantseva, N. A., Christiansen, H. H., Chizhova, J. N., Vasil'chuk, A. C., & Zemskova, A. M. (2015). Oxygen stable isotope variation in Late Holocene ice wedges in Yamal Peninsula and Svalbard. *Geography, environment, sustainability*, *8*(3), 36-54.
- Vasil'chuk, Y. K., Lawson, D. E., Yoshikawa, K., Budantseva, N. A., Chizhova, J. N., Podborny, Y. Y., & Vasil'chuk, A. C. (2016). Stable isotopes in the closed-system Weather Pingo, Alaska and Pestsovoye Pingo, northwestern Siberia. *Cold Regions Science and Technology*, *128*, 13-21.
- Wahl, H. E. (1987). *Climate of Yukon*. Environment Canada. Atmospheric Environment Service.

Wetterich, S., Tumskey, V., Rudaya, N., Andreev, A. A., Opel, T., Meyer, H., ... & Hüls, M. (2014). Ice Complex formation in arctic East Siberia during the MIS3 Interstadial. *Quaternary Science Reviews*, 84, 39-55.

Wickham, H. (2016). *ggplot2: elegant graphics for data analysis*. Springer.

Wright, N., Hayashi, M., & Quinton, W. L. (2009). Spatial and temporal variations in active layer thawing and their implication on runoff generation in peat-covered permafrost terrain. *Water Resources Research*, 45(5).

Yanovsky, V. K. (1933). Expedition to Pechora River to determine the position of the southern permafrost boundary. *Reports of the Committee for Permafrost Investigations*, 5(2), 65-149.

6. CONCLUSIONS AND FUTURE WORK

6.1. Conclusions

Stable isotopes in pore and texture ice in permafrost contain valuable paleoclimate proxies. However, how these isotopes become incorporated into permafrost is poorly understood. This work aimed to improve our understanding of the long-term preservation of stable isotopes in pore and texture ice. The main objectives were 1) establish the history of local permafrost formation using geochemical and traditional cryostructure methods, 2) infer the conditions of stable isotope development of pore and texture ice in the active layer, transition layer, and relict permafrost, 3) assess the impacts of the local environment on the stable isotope development of pore and texture ice, and 4) build upon existing evidence for 20th century warming captured by stable isotope records in pore and texture ice.

6.1.1. Cryostratigraphy and History of Ground Ice Formation

Each site was divided into three main stratigraphic units: the active layer (Unit 1), transition layer (Unit 2), and relict permafrost (Unit 3). Divisions between these three units were made on the basis of stable isotopes, GWC, cryostructures, and geochemistry. A stable isotope C-profile, produced by Rayleigh fractionation during bi-directional freezing, was commonly observed in the 2018 active layer ice. ALT_{max} values in 2018, predicted from the base of these C-profiles, generally agree with 2019 thaw depth probing. Discrepancies between the two were most likely due to inter-annual differences in thaw depth, as in the case of Site 4, or spatial thaw depth heterogeneity, which makes comparison difficult, as in the case of Site 1. Consequently, a combination of geochemical and stable isotope parameters was more effective than the use of a single parameter for determining the base of the transition layer. With the exception of Site 1, the isotope-estimated 2018 ALT_{max} and TDD-modeled 2018 ALT_{max} at each site are inconsistent. TDD-modeled 2018 ALT_{max} values are likely more conservative because they do not account for the thermal effects of soil moisture.

Sequences of pore and texture ice at the study area indicated permafrost developed syngenetically at all four sites. At Site 3 and Site 4 syngeneses is inferred from the peaty substrates, high ice contents, and the frequent occurrence of elongated bubble trains. Along the

hillslope, layers of greater ice content and/or greater prevalence of layered ice indicated periods of slower ground ice aggradation whereas layers chiefly characterized by lenticular cryostructures formed during periods of faster permafrost aggradation. Syngeneses was further supported by cryoturbated organics below the transition layers along the hillslope, which indicates that the ground surface was once lower than present and surface aggradation has taken place.

6.1.2. Formation of stable isotopic patterns in pore and texture ice

Active layer stable isotope formation

Rayleigh fractionation during bi-directional freezing produced C-profiles at all four sites. δD - $\delta^{18}O$ regressions for 2018 active layer ice at Sites 1 and 2 had slopes consistent with equilibrium fractionation. In contrast, the δD - $\delta^{18}O$ slopes for the upward- and downward-freezing active layer zones at Sites 3 and 4 indicated rapid freezing, likely due to warm temperatures ($> -0.5^{\circ}C$) at the top of permafrost at the end of the thaw season and/or greater water content at the base of the active layer at the start of freeze-back. The formation of C-profiles on a slope may indicate that C-profiles can still form in the presence of an open system if water between the fronts is still moving down-hill. Alternatively, hillslope C-profiles may have formed because the upward and downward force of cryosuction arrested the downslope movement of active layer water by gravity.

Transition layer stable isotope formation

Isotopic preservation of a past freeze-thaw cycle in the form of an old C-profile was visible in the transition layer of Site 2. Presumably, this older C-profile was preserved because successive transition layer thawing did not penetrate deep enough to completely erase deeper parts of the profile. In contrast, the transition layers of Sites 1, 3, and 4 did not preserve older C-profiles, either because active layer thaw in 2018 reached the base of the transition layer or the transition layer ice is composed of many aggradational first ice layers produced by from many repetitions of thawing and refreezing.

Prevalence of kinetic vs. equilibrium fractionation in the transition layer varied between sites. Co-isotopic trends of transition layer ice at Site 4 indicate that water froze rapidly, and the isotopic composition after freeze-back was governed by the amount of active layer water that had

penetrated into the transition layer during 2018. Co-isotopic trends for Site 3 transition layer ice indicated fractionation occurred under near-equilibrium. δD - $\delta^{18}O$ regressions also indicated equilibrium fractionation was also predominant during the formation of Site 1 and Site 2 transition layer ice. However, at Site 2, equilibrium fractionation more likely transpired during freezing of a single water reservoir (i.e. during C-profile formation), whereas the lack of one or more preserved C-profiles in the Site 1 transition layer indicated equilibrium fractionation dominated over the course of multiple thawing and freezing events.

Findings from this study also provide tentative evidence of basal active layer water infiltration into the top of permafrost. Co-isotopic scatter of Site 4 transition layer ice in δD - $\delta^{18}O$ space and the spread of points in d -excess- δD space indicate rapid freezing of interstitial waters, which decrease in abundance with depth. At Site 3, basal active layer water infiltration is indicated by a decrease in $\delta^{18}O$ and increase in d -excess with depth in the upper several centimeters of the transition layer. At Site 2, the sharp onset of d -excess depletion ~6cm below the transition layer base indicates first ice enrichment diminishes with depth below maximum thaw, potentially due to a related decrease in interstitial active layer water with depth. However, C-profile preservation in the Site 2 transition layer suggests any isotopic alterations arising from basal active layer water infiltration did not significantly affect the isotopic composition of the transition layer during the 2018 freeze-back.

Relict permafrost stable isotope formation

Stable isotopes of relict pore and texture ice were generally multi-modal in δD - $\delta^{18}O$ and d -excess- δD space, reflecting varying freezing conditions and/or basal active layer water isotope composition over time. Co-isotopic regressions indicated the isotopic composition of the uppermost relict ice in Site 4 developed by kinetic fractionation, similar to the transition layer and active layer ice above, while the uppermost relict ice at Site 1, Site 2, and Site 3 developed by equilibrium fractionation, likewise similar to overlying transition layer and active layer ice.

Comparing co-isotopic regressions of transition layer ice and the uppermost unit of relict ice shed some light on the long-term archival of transition layer isotopes. In Site 2 and Site 4, the transition layer and upper relict ice (Unit 3A) were isotopically comparable in both δD - $\delta^{18}O$ and d -excess- δD space, suggesting there is not a significant thaw unconformity between them. The same is true for the transition layer and relict ice at Site 3, albeit with considerably different

slopes. In contrast, co-isotopic comparisons indicate the transition layer and upper relict ice are isotopically distinct at Site 1, most likely related to a thaw unconformity.

6.1.3. Influence of downhill basal active layer water $\delta^{18}\text{O}$ increase on pore and texture ice isotope chemistry

Downhill $\delta^{18}\text{O}$ increase in basal active layer waters appears to have been a recurring phenomenon over past millennia, as relict pore and texture ice are increasingly enriched relative to local precipitation at lower slope position on the hillslope. The average isotope values of Site 4 relict ice were similar to the average relict ice values at the base of the slope (i.e. Site 3), suggesting that the mechanisms responsible for enriched $\delta^{18}\text{O}$ and depleted *d*-excess at the base of the hillslope produced a comparable magnitude of $\delta^{18}\text{O}$ enrichment in a non-sloping area. These findings suggest that hilltop ground ice is more likely to provide a stable isotope record with minimal secondary fractionation effects than locations further downslope or within poorly drained areas.

6.1.4. Evidence of recent warming in stable isotope records of pore and texture ice

Pore and texture ice along the hillslope exhibited tentative evidence of isotopic enrichment driven by recent climate warming. Isotopic enrichment at the top of the transition layer can be observed at Sites 1, 2 and 3, while isotopic enrichment at the top of the relict permafrost was only observed at Site 2. Enrichment in the upper transition layers could either be attributable to climate warming or downward infiltration of basal active layer waters during the summer. Either way, the signal is most likely temporary, as variable thaw penetration from year-to-year could erase this pattern and start anew. In contrast, enrichment in the upper relict ice at Site 2 suggests a broader-scale environmental or climatic change has occurred. However, maximum $\delta^{18}\text{O}$ enrichment at the top of the Site 2 relict ice did not significantly surpass maximum $\delta^{18}\text{O}$ values in older relict ice. Although the Site 4 record was hosted in thick syngenetic peats, a theoretically ideal medium for capturing changes in climate, enrichment at the top of relict permafrost, or in the transition layer, was not observed, potentially due to a lack of recent surface aggradation. Although evidence for a climate warming signal in the stable isotope record of pore and texture ice in the study area is provisional, the results of this study

nonetheless shed light on the isotopic development of pore and texture ice, especially with regard to the role of the transition layer.

6.2. Future Work

The findings of this study have shed light on the stable isotopic development of pore and texture ice. Future work will be conducted to better refine this investigation and inform future studies. Included in this work will be analysis of ice content, pH, and EC in Site 1. Line scanning techniques will be used to estimate volumetric ice content. Average stable isotope values, weighted by volumetric water content, of the active layer, transition layer, and the two of them combined will be calculated and compared with stable isotope values at the top of permafrost in each of the cores. This will help refine our understanding of the relationship between active layer waters isotope composition and that of relict ground ice.

The findings of this study prompt further questions about the isotopic development of pore and texture ice in the transition layer and relict permafrost. Stable isotope data from this study tentatively suggest basal active layer waters penetrate the upper 3-5cm of the top of permafrost during summer thaw within the study area. While the migration of cryotic waters in frozen ground has been well documented, its effects on the isotopic development of the ground ice is not well understood. Direct observations in the study area using methods such as tritium analysis and time-domain reflectometry would help identify the depth of modern active layer water penetration into the top of permafrost and inform further isotope analyses. Long-term observations of thaw depth, snow depth, ground temperature, and soil moisture, combined with thaw depth modeling, would help to inform geochemical and stable isotopic variations at the base of the transition layer.

Bibliography

- Anderson, D. M., & Tice, A. R. (1973). The unfrozen interfacial phase in frozen soil water systems. In *Physical aspects of soil water and salts in ecosystems* (pp. 107-124). Springer, Berlin, Heidelberg.
- Anisimov, O. A., & Nelson, F. E. (1996). Permafrost distribution in the Northern Hemisphere under scenarios of climatic change. *Global and Planetary Change*, 14(1-2), 59-72.
- Arcone, S. A., Lawson, D. E., Delaney, A. J., Strasser, J. C., & Strasser, J. D. (1998). Ground-penetrating radar reflection profiling of groundwater and bedrock in an area of discontinuous permafrost. *Geophysics*, 63(5), 1573-1584.
- Arenson, L. U., Springman, S. M., & Segó, D. C. (2007). The rheology of frozen soils. *Applied Rheology*, 17(1), 12147-1.
- Augustin, L., Barbante, C., Barnes, P. R., Barnola, J. M., Bigler, M., Castellano, E., ... & Dreyfus, G. (2004). Eight glacial cycles from an Antarctic ice core. *Nature*, 429, 623-628.
- Bandara, S., Froese, D. G., St Louis, V. L., Cooke, C. A., & Calmels, F. (2019). Postdepositional Mercury Mobility in a Permafrost Peatland from Central Yukon, Canada. *ACS Earth and Space Chemistry*, 3(5), 770-778.
<https://doi.org/10.1021/acsearthspacechem.9b00010>
- Bandara, S., Froese, D., Porter, T. J., & Calmels, F. (2020). Holocene pore-ice $\delta^{18}\text{O}$ and $\delta^2\text{H}$ records from drained thermokarst lake basins in the Old Crow Flats, Yukon, Canada. *Permafrost and Periglacial Processes*, 31(4), 497-508.
- Baranova, N. (2017). *Evaluating Groundwater In a Permafrost Watershed Using Seasonal Geochemical and Isotope Discharge Trends, Ogilvie River, Yukon* (Doctoral dissertation, Université d'Ottawa/University of Ottawa).
- Beierle, B. D. (2002). Late Quaternary glaciation in the Northern Ogilvie Mountains: revised correlations and implications for the stratigraphic record. *Canadian Journal of Earth Sciences*, 39(11), 1709-1717.
- Beuselinck, L., Govers, G., Poesen, J., Degraer, G., & Froyen, L. (1998). Grain-size analysis by laser diffractometry: comparison with the sieve-pipette method. *Catena*, 32(3-4), 193-208.
- Bockheim, J. G. (2015). *Cryopedology* (p. 173). London: Springer.
- Boike, J., Roth, K., & Overduin, P. P. (1998). Thermal and hydrologic dynamics of the active layer at a continuous permafrost site (Taymyr Peninsula, Siberia). *Water Resources Research*, 34(3), 355-363.
- Booth, R. K., Jackson, S. T., & Gray, C. E. (2004). Paleoecology and high-resolution paleohydrology of a kettle peatland in upper Michigan. *Quaternary Research*, 61(1), 1-13.
- Brandt, O., Langley, K., Kohler, J., & Hamran, S. E. (2007). Detection of buried ice and sediment layers in permafrost using multi-frequency Ground Penetrating Radar: A case examination on Svalbard. *Remote Sensing of Environment*, 111(2-3), 212-227.
- Briner, J. P., Kaufman, D. S., Manley, W. F., Finkel, R. C., & Caffee, M. W. (2005). Cosmogenic exposure dating of late Pleistocene moraine stabilization in Alaska. *Geological Society of America Bulletin*, 117(7-8), 1108-1120.

- Brook, E. J., & Buizert, C. (2018). Antarctic and global climate history viewed from ice cores. *Nature*, 558(7709), 200-208.
- Brooks, H., Doré, G., & Smith, S. L. (2018). Permafrost geotechnical index property variation and its effect on thermal conductivity calculations. *Cold Regions Science and Technology*, 148, 63-76.
- Brosius, L. S., Anthony, K. W., Grosse, G., Chanton, J. P., Farquharson, L. M., Overduin, P. P., & Meyer, H. (2012). Using the deuterium isotope composition of permafrost meltwater to constrain thermokarst lake contributions to atmospheric CH₄ during the last deglaciation. *Journal of Geophysical Research: Biogeosciences*, 117(G1).
- Burn, C. (2013). Permafrost. In *Encyclopedia of Quaternary Science: Second Edition* (pp. 464-471). doi:10.1016/B978-0-444-53643-3.00099-6
- Burn, C. R. (1994). Permafrost, tectonics, and past and future regional climate change, Yukon and adjacent Northwest Territories. *Canadian Journal of Earth Sciences*, 31(1), 182-191.
- Burn, C. R. (1998). The active layer: two contrasting definitions. *Permafrost and Periglacial Processes*, 9(4), 411-416.
- Burn, C. R., & Michel, F. A. (1988). Evidence for recent temperature-induced water migration into permafrost from the tritium content of ground ice near Mayo, Yukon Territory, Canada. *Canadian Journal of Earth Sciences*, 25(6), 909-915.
- Calmels, F., & Allard, M. (2004). Ice segregation and gas distribution in permafrost using tomodesitometric analysis. *Permafrost and Periglacial Processes*, 15(4), 367-378.
- Calmels, F., Clavano, W., & Froese, D. G. (2010). Progress on X-ray computed tomography (CT) scanning in permafrost studies. In *Proceedings of the 5th Canadian Conference on Permafrost, GEO2010 Calgary, Alberta* (pp. 1353-1358).
- Calmels, F., Delisle, G., & Allard, M. (2008). Internal structure and the thermal and hydrological regime of a typical lithalsa: significance for permafrost growth and decay. *Canadian Journal of Earth Sciences*, 45(1), 31-43.
- Canadian Agricultural Services Coordinating Committee. Soil Classification Working Group, Soil Classification Working Group, National Research Council Canada, Canada. Agriculture, & Agri-Food Canada. Research Branch. (1998). *The Canadian system of soil classification* (No. 1646). NRC Research Press.
- Carballeira, R., & Pontevedra-Pombal, X. (2020). Diatoms in Paleoenvironmental Studies of Peatlands. *Quaternary*, 3(2), 10.
- Cheng, G. (1983). The mechanism of repeated-segregation for the formation of thick layered ground ice. *Cold Regions Science and Technology*, 8(1), 57-66.
- Cook, F.A. (1955). Near Surface Soil Temperature Measurements at Resolute Bay, Northwest Territories. *Arctic*, 8(4), 237-249.
- Couture, N. J., & Pollard, W. H. (2007). Modelling geomorphic response to climatic change. *Climatic Change*, 85(3), 407-431.
- Couture, N. J., Irrgang, A., Pollard, W., Lantuit, H., & Fritz, M. (2018). Coastal erosion of permafrost soils along the Yukon Coastal Plain and fluxes of organic carbon to the Canadian Beaufort Sea. *Journal of Geophysical Research: Biogeosciences*, 123(2), 406-422.
- Craig, H. (1961). Isotopic variations in meteoric waters. *Science*, 133(3465), 1702-1703.
- Cwynar, L. C., & Spear, R. W. (1995). Paleovegetation and Paleoclimatic Changes in the Yukon at 6 ka BP. *Géographie Physique et Quaternaire Paleovegetation*, 49(1), 29-35.

- Dansgaard, W. (1964). Stable isotopes in precipitation. *tellus*, 16(4), 436-468.
- Davies, L. J. (2018). The development of a Holocene cryptotephra framework in northwestern North America.
- Dereviagin, A. Y., Chizhov, A. B., Meyer, H., Hubberten, H. W., Siegert, C. (2003). Recent ground ice and its formation on evidence of isotopic analysis. In *Proceedings of 8th International Conference on Permafrost* (pp. 21-25).
- Dereviagin, A. Y., Chizhov, A. B., Meyer, H., Hubberten, H. W., Siegert, C., Phillips, M., ... & Balkema, A. A. (2003, July). Recent ground ice and its formation on evidence of isotopic analysis. In *Proceedings of 8th International Conference on Permafrost* (pp. 21-25).
- Douglas, T. A., Fortier, D., Shur, Y. L., Kanevskiy, M. Z., Guo, L., Cai, Y., & Bray, M. T. (2011). Biogeochemical and geocryological characteristics of wedge and thermokarst-cave ice in the CRREL permafrost tunnel, Alaska. *Permafrost and Periglacial Processes*, 22(2), 120-128.
- Duk-Rodkin, A. (1996). Surficial Geology, Dawson, Yukon Territory. *Geological Survey of Canada, Open File*, 3288, 1 map, scale 1:250 000.
- Duk-Rodkin, A., & Hinds, S. J. (1996). *Surficial geology, Dawson, Yukon Territory*. Geological Survey of Canada.
- Duk-Rodkin, A., Barendregt, R. W., Froese, D. G., Weber, F., Enkin, R., Smith, I. R., ... & Klassen, R. (2004). Timing and extent of Plio-Pleistocene glaciations in north-western Canada and east-central Alaska. In *Developments in Quaternary Sciences* (Vol. 2, pp. 313-345). Elsevier.
- Duk-Rodkin, A., Barendregt, R. W., Tarnocai, C., & Phillips, F. M. (1996). Late Tertiary to late Quaternary record in the Mackenzie Mountains, Northwest Territories, Canada: stratigraphy, paleosols, paleomagnetism, and chlorine-36. *Canadian Journal of Earth Sciences*, 33(6), 875-895.
- Ecological Stratification Working Group (ESWG). 1996. *A national ecological framework for Canada*. Ottawa: Agriculture and Agri-Food Canada, Research Branch, Centre for Land and Biological Resources Research; and Ottawa: Environment Canada, State of the Environment Directorate, Ecozone Analysis Branch.
- Environment and Climate Change Canada. (2016). *Canadian Climate Normals*. Retrieved from https://climate.weather.gc.ca/climate_normals/index_e.html.
- Environment and Climate Change Canada. 1981-2010 Climate Normals & Averages. https://climate.weather.gc.ca/climate_normals/index_e.html
- Environment Yukon. (2014). *The Dempster Highway Travelogue*. Whitehorse, Yukon Territory, Canada: Yukon Government.
- Fisher, D. A., Lacelle, D., & Pollard, W. (2019). A model of unfrozen water content and its transport in icy permafrost soils: Effects on ground ice content and permafrost stability. *Permafrost and Periglacial Processes*, 31(1), 184-199.
- Fortier, D., Kanevskiy, M., & Shur, Y. (2008, June). Genesis of reticulate-chaotic cryostructure in permafrost. In *Proceedings of the Ninth International Conference on Permafrost* (Vol. 1, pp. 451-456). Fairbanks, AK: Institute of Northern Engineering, University of Alaska Fairbanks.
- French, H. M. (2017). *The periglacial environment*. John Wiley & Sons.
- French, H., & Shur, Y. (2010). The principles of cryostratigraphy. *Earth-Science Reviews*, 101(3-4), 190-206.

- Fritz, M., Wetterich, S., Meyer, H., Schirrmeister, L., Lantuit, H., & Pollard, W. H. (2011). Origin and characteristics of massive ground ice on Herschel Island (western Canadian Arctic) as revealed by stable water isotope and hydrochemical signatures. *Permafrost and Periglacial Processes*, 22(1), 26-38.
- Froehlich, K., Gibson, J. J., & Aggarwal, P. K. (2002). *Deuterium excess in precipitation and its climatological significance* (No. IAEA-CSP--13/P).
- Froese, D. G., Zazula, G. D., Westgate, J. A., Preece, S. J., Sanborn, P. T., Reyes, A. V., & Pearce, N. J. G. (2009). The Klondike goldfields and Pleistocene environments of Beringia. *GSA Today*, 19(8), 4–10. <https://doi.org/10.1130/GSATG54A.1>
- Gibson, J. J., & Prowse, T. D. (1999). Isotopic characteristics of ice cover in a large northern river basin. *Hydrological Processes*, 13(16), 2537-2548.
- Gibson, J. J., & Prowse, T. D. (2002). Stable isotopes in river ice: Identifying primary over-winter streamflow signals and their hydrological significance. *Hydrological Processes*, 16(4), 873-890.
- Gilbert, G. L., Kanevskiy, M., & Murton, J. B. (2016). Recent advances (2008–2015) in the study of ground ice and cryostratigraphy. *Permafrost and Periglacial Processes*, 27(4), 377-389.
- Gordey, S.P. and Makepeace, A.J. (comp.) 1999: Yukon bedrock geology in Yukon digital geology, S.P. Gordey and A.J. Makepeace (comp.); Geological Survey of Canada Open File D3826 and Exploration and Geological Services Division, Yukon, Indian and Northern Affairs Canada, Open File 1999-1(D)
- Grinter, M., Lacelle, D., Baranova, N., Murseli, S., & Clark, I. D. (2019). Late Pleistocene and Holocene ice-wedge activity on the Blackstone Plateau, central Yukon, Canada. *Quaternary Research*, 91(1), 179-193.
- Grosse, G., Romanovsky, V., Jorgenson, T., Anthony, K. W., Brown, J., & Overduin, P. P. (2011). Vulnerability and feedbacks of permafrost to climate change. *Eos, Transactions American Geophysical Union*, 92(9), 73-74.
- Harris, C., & Matthews, J. A. (1984). Some observations on boulder-cored frost boils. *Geographical Journal*, 63-73.
- Hayashi, M., McClymont, A., Christensen, B., Bentley, L., & Quinton, W. (2011). Thawing of permafrost peatlands: Effects of water-energy feedback on landscape evolution. In *Proceedings of the joint meeting of the International Association of Hydrogeologists Canadian National Chapter and the Canadian Quaternary Association*, Quebec City.
- Hilbich, C., Marescot, L., Hauck, C., Loke, M. H., & Mäusbacher, R. (2009). Applicability of electrical resistivity tomography monitoring to coarse blocky and ice-rich permafrost landforms. *Permafrost and Periglacial Processes*, 20(3), 269-284.
- Hivon, E. G., & Segó, D. C. (1995). Strength of frozen saline soils. *Canadian Geotechnical Journal*, 32(2), 336-354.
- Hoefs, J. (2015). *Stable isotope geochemistry* (Vol. 285). Berlin: Springer.
- Hossain, S., Kibria, G., & Khan, S. (2018). *Site Investigation Using Resistivity Imaging*. CRC Press.
- Idrees, M., Burn, C. R., Moore, J. L., & Calmels, F. (2015, September). Monitoring permafrost conditions along the Dempster Highway. In *7th Canadian Permafrost Conference: Proceedings of a conference held* (pp. 20-23).
- Jackson, S. T., Charman, D., Newman, L., & Kiefer, T. (2010). *Peatlands: Paleoenvironments and carbon dynamics*. Pages International Project Office.

- Johnsen, S. J., Dahl-Jensen, D., Gundestrup, N., Steffensen, J. P., Clausen, H. B., Miller, H., Masson-Delmotte, V., Sveinbjörnsdóttir, A. E., & White, J. (2001). Oxygen isotope and palaeotemperature records from six Greenland ice-core stations: Camp Century, Dye-3, GRIP, GISP2, Renland and NorthGRIP. *Journal of Quaternary Science: Published for the Quaternary Research Association*, 16(4), 299-307.
- Jørgensen, A. S., & Andreasen, F. (2007). Mapping of permafrost surface using ground-penetrating radar at Kangerlussuaq Airport, western Greenland. *Cold Regions Science and Technology*, 48(1), 64-72.
- Jouzel, J., & Souchez, R. A. (1982). Melting–refreezing at the glacier sole and the isotopic composition of the ice. *Journal of Glaciology*, 28(98), 35-42.
- Judge, A. S., Tucker, C. M., Pilon, J. A., & Moorman, B. J. (1991). Remote sensing of permafrost by ground-penetrating radar at two airports in Arctic Canada. *Arctic*, 40-48.
- Kanevskiy, M., Jorgenson, T., Shur, Y., O'Donnell, J. A., Harden, J. W., Zhuang, Q., & Fortier, D. (2014). Cryostratigraphy and permafrost evolution in the lacustrine lowlands of west-central Alaska. *Permafrost and Periglacial Processes*, 25(1), 14-34.
- Kanevskiy, M., Shur, Y., Fortier, D., Jorgenson, M. T., & Stephani, E. (2011). Cryostratigraphy of late Pleistocene syngenetic permafrost (yedoma) in northern Alaska, Itkillik River exposure. *Quaternary research*, 75(3), 584-596.
- Kanevskiy, M., Shur, Y., Jorgenson, M. T., Ping, C. L., Michaelson, G. J., Fortier, D., ... & Tumskoy, V. (2013). Ground ice in the upper permafrost of the Beaufort Sea coast of Alaska. *Cold Regions Science and Technology*, 85, 56-70.
- Kelly, S. F., & Selker, J. S. (2001). Osmotically driven water vapor transport in unsaturated soils. *Soil Science Society of America Journal*, 65(6), 1634-1641.
- Kokelj, S. V., & Burn, C. R. (2003). Ground ice and soluble cations in near-surface permafrost, Inuvik, Northwest Territories, Canada. *Permafrost and Periglacial Processes*, 14(3), 275-289.
- Kokelj, S. V., Zajdlik, B., & Thompson, M. S. (2009). The impacts of thawing permafrost on the chemistry of lakes across the subarctic boreal-tundra transition, Mackenzie Delta region, Canada. *Permafrost and Periglacial Processes*, 20(2), 185-199.
- Kuhry, P., Halsey, L. A., Bayley, S. E., & Vitt, D. H. (1992). Peatland development in relation to Holocene climatic change in Manitoba and Saskatchewan (Canada). *Canadian Journal of Earth Sciences*, 29(5), 1070-1090.
- Kurylyk, B. L., & Hayashi, M. (2016). Improved Stefan equation correction factors to accommodate sensible heat storage during soil freezing or thawing. *Permafrost and Periglacial Processes*, 27(2), 189-203.
- Lacelle, D. (2011). On the $\delta^{18}\text{O}$, δD and D-excess relations in meteoric precipitation and during equilibrium freezing: theoretical approach and field examples. *Permafrost and Periglacial Processes*, 22(1), 13-25.
- Lacelle, D., Fontaine, M., Forest, A. P., & Kokelj, S. (2014). High-resolution stable water isotopes as tracers of thaw unconformities in permafrost: A case study from western Arctic Canada. *Chemical Geology*, 368, 85-96.
- Lacelle, D., Fontaine, M., Pellerin, A., Kokelj, S. V., & Clark, I. D. (2019). Legacy of Holocene landscape changes on soil biogeochemistry: a perspective from paleo-active layers in Northwestern Canada. *Journal of Geophysical Research: Biogeosciences*, 124(9), 2662-2679.

- Lacelle, D., Lauriol, B., Clark, I. D., Cardyn, R., & Zdanowicz, C. (2007). Nature and origin of a Pleistocene-age massive ground-ice body exposed in the Chapman Lake moraine complex, central Yukon Territory, Canada. *Quaternary Research*, 68(2), 249-260.
- Lacelle, D., St-Jean, M., Lauriol, B., Clark, I. D., Lewkowicz, A., Froese, D. G., ... & Zazula, G. (2009). Burial and preservation of a 30,000 year old perennial snowbank in Red Creek valley, Ogilvie Mountains, central Yukon, Canada. *Quaternary Science Reviews*, 28(27-28), 3401-3413.
- Lachniet, M. S., Lawson, D. E., Stephen, H., Sloat, A. R., & Patterson, W. P. (2016). Isoscapes of $\delta^{18}\text{O}$ and $\delta^2\text{H}$ reveal climatic forcings on Alaska and Yukon precipitation. *Water Resources Research*, 52(8), 6575-6586.
- Lapalme, C. M., Lacelle, D., Davila, A. F., Pollard, W., Fortier, D., & McKay, C. P. (2015, September). Cryostratigraphy of near-surface permafrost in University Valley, McMurdo Dry Valleys of Antarctica. In Conference Paper: GeoQuebec (p. 2015).
- Lee, H., Swenson, S. C., Slater, A. G., & Lawrence, D. M. (2014). Effects of excess ground ice on projections of permafrost in a warming climate. *Environmental Research Letters*, 9(12), 124006.
- Lewkowicz, A. G., & Harris, C. (2005). Morphology and geotechnique of active-layer detachment failures in discontinuous and continuous permafrost, northern Canada. *Geomorphology*, 69(1-4), 275-297.
- Li, H., Yang, Z. J., & Wang, J. (2018). Unfrozen water content of permafrost during thawing by the capacitance technique. *Cold Regions Science and Technology*, 152, 15-22.
- Luo, D., Jin, H., Lü, L., & Wu, Q. (2014). Spatiotemporal characteristics of freezing and thawing of the active layer in the source areas of the Yellow River (SAYR). *Chinese Science Bulletin*, 59(24), 3034-3045.
- Mackay, J. R. (1972). The world of underground ice. *Annals of the Association of American Geographers*, 62(1), 1-22.
- Mackay, J. R. (1974). Reticulate ice veins in permafrost, Northern Canada. *Canadian Geotechnical Journal*, 11(2), 230-237.
- Mackay, J. R. (1983). Downward water movement into frozen ground, western arctic coast, Canada. *Canadian Journal of Earth Sciences*, 20(1), 120-134.
- Mackay, J. R. (1983). *Oxygen isotope variations in permafrost, Tuktoyaktuk Peninsula area, Northwest Territories* (No. GSCAN-P--83-1B).
- Mackay, J. R. (1990). Seasonal growth bands in pingo ice. *Canadian Journal of Earth Sciences*, 27(8), 1115-1125.
- Mackay, J. R., & Dallimore, S. R. (1992). Massive ice of the Tuktoyaktuk area, western Arctic coast, Canada. *Canadian Journal of Earth Sciences*, 29(6), 1235-1249.
- Mageau, D. W., & Morgenstern, N. R. (1980). Observations on moisture migration in frozen soils. *Canadian Geotechnical Journal*, 17(1), 54-60.
- Mann, D. H., Groves, P., Reanier, R. E., & Kunz, M. L. (2010). Floodplains, permafrost, cottonwood trees, and peat: What happened the last time climate warmed suddenly in arctic Alaska?. *Quaternary Science Reviews*, 29(27-28), 3812-3830.
- McCave, I. N., & Syvitski, J. P. (1991). Principles and methods of geological particle size analysis. *Principles, methods and application of particle size analysis*, 3-21.
- McClymont, A. F., Hayashi, M., Bentley, L. R., & Christensen, B. S. (2013). Geophysical imaging and thermal modeling of subsurface morphology and thaw evolution of

- discontinuous permafrost. *Journal of Geophysical Research: Earth Surface*, 118(3), 1826-1837.
- Meyer, H., Derevyagin, A., Siegert, C., Schirrmeister, L., & Hubberten, H. W. (2002). Palaeoclimate reconstruction on Big Lyakhovsky Island, North Siberia—hydrogen and oxygen isotopes in ice wedges. *Permafrost and periglacial processes*, 13(2), 91-105.
- Meyer, H., Derevyagin, A. Y., Siegert, C., & Hubberten, H. W. (2002). Paleoclimate studies on Bykovsky Peninsula, North Siberia—hydrogen and oxygen isotopes in ground ice. *Polarforschung*, 70, 37-51.
- Meyer, H., Schirrmeister, L., Andreev, A., Wagner, D., Hubberten, H. W., Yoshikawa, K., ... & Brown, J. (2010). Lateglacial and Holocene isotopic and environmental history of northern coastal Alaska—Results from a buried ice-wedge system at Barrow. *Quaternary Science Reviews*, 29(27-28), 3720-3735.
- Michel, F. A. (1986). Isotope geochemistry of frost-blister ice, North Fork Pass, Yukon, Canada. *Canadian Journal of Earth Sciences*, 23(4), 543-549.
- Michel, F. A. (1986). Isotope geochemistry of frost-blister ice, North Fork pass, Yukon, Canada. *Canadian Journal of Earth Sciences*, 23(4), 543-549.
<https://doi.org/10.1139/e86-054>
- Michel, F. A. (1990, June). Isotopic composition of ice-wedge ice in northwestern Canada. In *Proceedings, Fifth Canadian Permafrost Conference, Nordicana* (Vol. 54, pp. 5-9).
- Michel, F. A. (1990). Isotopic composition of ice-wedge ice in northwestern Canada. In *Proceedings, Fifth Canadian Permafrost Conference, Nordicana* (Vol. 54, pp. 5-9).
- Michel, F. A. (2011). Isotope Characterisation of Ground Ice in Northern Canada Eureka, 12(November 2009), 3–12. <https://doi.org/10.1002/ppp.721>
- Michel, F. A., Fritz, P., & French, H. M. (1982). Significance of isotope variations in permafrost waters at Illisarvik, NWT. In *Proceedings of the Fourth Canadian Permafrost Conference* (pp. 173-181). National Research Council of Canada.
- Muller, S. W. (1943). Permafrost or permanently frozen ground and related engineering problems. US. Engineer. Office, Strat. Engineer. Study Spec. Rep, 62.
- Muller, S. W. (1947). *Permafrost or permanently frozen ground and related engineering problems*. J.W. Edwards, Inc.
- Muñoz Sabater, J. (2021). *ERA5-Land hourly data from 1950 to 1980* [data set]. Copernicus Climate Change Service (C3S) Climate Data Store (CDS). Retrieved January 26, 2022, from <https://cds.climate.copernicus.eu/cdsapp#!/dataset/10.24381/cds.e2161bac?tab=overview>
- Muñoz Sabater, J., (2019): ERA5-Land hourly data from 1981 to present. Copernicus Climate Change Service (C3S) Climate Data Store (CDS). Retrieved January 26, 2022, from <https://cds.climate.copernicus.eu/cdsapp#!/dataset/10.24381/cds.e2161bac?tab=overview>
- Murton, B., & French, H. M. (1994). Cryostructures in permafrost, Tuktoyaktuk coastlands, western arctic Canada. *Canadian Journal of Earth Sciences*, 31, 737-747.
- NASA Goddard Institute for Space Studies. (2021). Panoply (Version 4.12.6) [Computer software]. National Aeronautics and Space Administration (NASA). Retrieved from <https://www.giss.nasa.gov/tools/panoply/>
- Nassar, I. N., & Horton, R. (1989). Water transport in unsaturated nonisothermal salty soil: II. Theoretical development. *Soil Science Society of America Journal*, 53(5), 1330-1337.

- National Research Council Canada (1989). Glossary of permafrost and related ground-ice terms. Associate Committee on Geotechnical Research, National Research Council of Canada, Ottawa, 156.
- National Snow and Ice Data Center. *SOTC: Permafrost and Frozen Ground | National Snow and Ice Data Center*, 4 Apr. 2017, nsidc.org/cryosphere/sotc/permafrost.html.
- National Wetlands Working Group (NWWG). (1997). *The Canadian wetland classification system*. Wetlands Research Branch, University of Waterloo.
- Nelson, F. E., & Outcalt, S. I. (1987). A computational method for prediction and regionalization of permafrost. *Arctic and Alpine Research*, 19(3), 279-288.
- Nikolayev, V. I., & Mikhalev, D. V. (1995). An oxygen-isotope paleothermometer from ice in siberian permafrost. *Quaternary Research*, 43, 14–21. <https://doi.org/10.1016/j.solener.2019.02.027>
- Nikolayev, V. I., & Mikhalev, D. V. (1995). An oxygen-isotope paleothermometer from ice in Siberian permafrost. *Quaternary Research*, 43(1), 14-21.
- O'Neil, J. R. (1968). Hydrogen and oxygen isotope fractionation between ice and water. *The Journal of Physical Chemistry*, 72(10), 3683-3684.
- O'Neil, J. R. (1968). Hydrogen and oxygen isotope fractionation between ice and water. *Journal of Physical Chemistry*, 72(10), 3683–3684. <https://doi.org/10.1021/j100856a060>
- Opel, T., Meyer, H., Wetterich, S., Laepple, T., Dereviagin, A., & Murton, J. (2018). Ice wedges as archives of winter paleoclimate: A review. *Permafrost and Periglacial Processes*, 29(3), 199-209.
- Opel, T., Wetterich, S., Meyer, H., Dereviagin, Y. A., Fuchs, C. M., & Schirmer, L. (2017). Ground-ice stable isotopes and cryostratigraphy reflect late Quaternary palaeoclimate in the Northeast Siberian Arctic (Oyogos Yar coast, Dmitry Laptev Strait). *Climate of the Past*, 13(6), 587–611. <https://doi.org/10.5194/cp-13-587-2017>
- Osterkamp, T. E., & Burn, C. R. (2003). Permafrost.
- Pihlainen, J. A., & Johnston, G. H. (1963). Guide to a field description of permafrost for engineering purposes (Vol. 79, p. 21). National Research Council, Canada, Associate Committee on Soil and Snow Mechanics.
- Porter, T. J., & Opel, T. (2020). Recent advances in paleoclimatological studies of Arctic wedge-and pore-ice stable-water isotope records. *Permafrost and Periglacial Processes*, 31(3), 429-441.
- Porter, T. J., & Opel, T. (2020). Recent advances in paleoclimatological studies of Arctic wedge-and pore-ice stable-water isotope records. *Permafrost and Periglacial Processes*.
- Porter, T. J., Froese, D. G., Feakins, S. J., Bindeman, I. N., Mahony, M. E., Pautler, B. G., ... & Weijers, J. W. (2016). Multiple water isotope proxy reconstruction of extremely low last glacial temperatures in Eastern Beringia (Western Arctic). *Quaternary Science Reviews*, 137, 113-125.
- Porter, T. J., Froese, D. G., Feakins, S. J., Bindeman, I. N., Mahony, M. E., Pautler, B. G., ... Weijers, J. W. H. (2016). Multiple water isotope proxy reconstruction of extremely low last glacial temperatures in Eastern Beringia (Western Arctic). *Quaternary Science Reviews*, 137, 113–125. <https://doi.org/10.1016/j.quascirev.2016.02.006>
- Porter, T. J., Schoenemann, S. W., Davies, L. J., Steig, E. J., Bandara, S., & Froese, D. G. (2019). Recent summer warming in northwestern Canada exceeds the Holocene thermal maximum. *Nature communications*, 10(1), 1-10.

- Prairie Climate Centre. *The Climate Atlas of Canada* (version 2, July 10, 2019).
<https://climateatlas.ca>
- Quinton, W. L., Carey, S. K., & Goeller, N. T. (2004). Snowmelt runoff from northern alpine tundra hillslopes: major processes and methods of simulation. *Hydrology and Earth System Sciences*, 8(5), 877-890.
- Rantala, M. V., Nevalainen, L., Rautio, M., Galkin, A., & Luoto, T. P. (2016). Sources and controls of organic carbon in lakes across the subarctic treeline. *Biogeochemistry*, 129(1-2), 235-253.
- Riseborough, D., Shiklomanov, N., Etzelmuller, B., Gruber, S., & Marchenko, S. (2008). Recent Advances in Permafrost Modelling. *Permafrost and Periglacial Processes*, 19, 137–156. <https://doi.org/10.1002/ppp>
- RStudio Team. (2016). RStudio: Integrated Development for R. RStudio, Inc., Boston, MA. <http://www.rstudio.com/>
- Scapozza, C., Lambiel, C., Baron, L., Marescot, L., & Reynard, E. (2011). Internal structure and permafrost distribution in two alpine periglacial talus slopes, Valais, Swiss Alps. *Geomorphology*, 132(3–4), 208–221. <https://doi.org/10.1016/j.geomorph.2011.05.010>
- Schaetzl, R. J., & Thompson, M. L. (2015). *Soils*. Cambridge university press.
- Schuur, E. A., Bockheim, J., Canadell, J. G., Euskirchen, E., Field, C. B., Goryachkin, S. V., ... & Zimov, S. A. (2008). Vulnerability of permafrost carbon to climate change: Implications for the global carbon cycle. *BioScience*, 58(8), 701-714.
- Schwamborn, G., Meyer, H., Fedorov, G., Schirrmeister, L., & Hubberten, H. W. (2006). Ground ice and slope sediments archiving late Quaternary paleoenvironment and paleoclimate signals at the margins of El'gygytyn Impact Crater, NE Siberia. *Quaternary Research*, 66(2), 259-272.
- Schwamborn, G., Meyer, H., Fedorov, G., Schirrmeister, L., & Hubberten, H. W. (2006). Ground ice and slope sediments archiving late Quaternary paleoenvironment and paleoclimate signals at the margins of El'gygytyn Impact Crater, NE Siberia. *Quaternary Research*, 66(2), 259–272. <https://doi.org/10.1016/j.yqres.2006.06.007>
- Scudder, G. G. E. (1997). Environment of the Yukon. *Insects of the Yukon. Biological Survey of Canada (Terrestrial Arthropods)*, Ottawa, 13-57.
- Shotyk, W. (1996). Peat bog archives of atmospheric metal deposition: geochemical evaluation of peat profiles, natural variations in metal concentrations, and metal enrichment factors. *Environmental Reviews*, 4(2), 149-183.
- Shur, Y. L. (1988). Upper horizon of permafrost and thermokarst. *USSR Academy of Sciences, Siberian Branch: Novosibirsk, Russia*, 210.
- Shur, Y., Hinkel, K. M., & Nelson, F. E. (2005). The transition layer: implications for geocryology and climate-change science. *Permafrost and Periglacial Processes*, 16(1), 5–17. <https://doi.org/10.1002/ppp.518>
- Shur, Y., Hinkel, K. M., & Nelson, F. E. (2005). The transition layer: implications for geocryology and climate-change science. *Permafrost and Periglacial Processes*, 16(1), 5-17.
- Sjöberg, Y., Marklund, P., Pettersson, R., & Lyon, S. W. (2015). Geophysical mapping of palsa peatland permafrost. *Cryosphere*, 9(2), 465–478. <https://doi.org/10.5194/tc-9-465-2015>

- Souchez, R. A., & Jouzel, J. (1984). On the isotopic composition in dD and d18O of water and ice during freezing. *Journal of Glaciology*, 30(106), 369–372.
<https://doi.org/10.1017/S0022143000006249>
- Spence, C., & Woo, M. K. (2003). Hydrology of subarctic Canadian shield: soil-filled valleys. *Journal of Hydrology*, 279(1-4), 151-166.
- Stephani, E., Fortier, D., & Shur, Y. (2010). Applications of cryofacies approach to frozen ground engineering – Case study of a road test site along the Alaska Highway (Beaver Creek, Yukon, Canada). 63rd Canadian Geotechnical Conference & 6th Canadian Permafrost Conference, (1963), 476–483. Retrieved from
<http://136.159.35.81/cpc/CPC6-476.pdf>
- Stephani, E., Fortier, D., Shur, Y., Fortier, R., & Doré, G. (2014). A geosystems approach to permafrost investigations for engineering applications, an example from a road stabilization experiment, Beaver Creek, Yukon, Canada. *Cold regions science and technology*, 100, 20-35.
- Stumpp, C., Klaus, J., & Stichler, W. (2014). Analysis of long-term stable isotopic composition in German precipitation. *Journal of Hydrology*, 517, 351-361.
- Subcommittee, P. (1988). Glossary of permafrost and related ground-ice terms. *Associate Committee on Geotechnical Research, National Research Council of Canada, Ottawa*, 156.
- Sugimoto, A., Naito, D., Yanagisawa, N., Ichiyanagi, K., Kurita, N., Kubota, J., ... Fedorov, A. N. (2003). Characteristics of soil moisture in permafrost observed in East Siberian taiga with stable isotopes of water. *Hydrological Processes*, 17, 1073–1092.
<https://doi.org/10.1002/hyp.1180>
- Suzuoki, T., & Kimura, T. (1973). D/H and 18O/16O fractionation in ice-water system. *Journal of the Mass Spectrometry Society of Japan*, 21(3), 229-233.
- Suzuoki, T., & Kimura, T. (1973). D/H and 18O/16O Fractionation in Ice-Water System. *Journal of the Mass Spectrometry Society of Japan*, 21(3), 229–233.
<https://doi.org/10.5702/massspec1953.21.229>
- Throckmorton, H. M., Newman, B. D., Heikoop, J. M., Perkins, G. B., Feng, X., Graham, D. E., ... & Wilson, C. J. (2016). Active layer hydrology in an arctic tundra ecosystem: quantifying water sources and cycling using water stable isotopes. *Hydrological Processes*, 30(26), 4972-4986.
- Throop, J., Lewkowicz, A. G., & Smith, S. L. (2012). Climate and ground temperature relations at sites across the continuous and discontinuous permafrost zones, northern Canada. *Canadian Journal of Earth Sciences*, 49(8), 865–876.
<https://doi.org/10.1139/E11-075>
- Turunen, C., & Turunen, J. (2003). Development history and carbon accumulation of a slope bog in oceanic British Columbia, Canada. *The Holocene*, 13(2), 225-238.
- Valentine, K. W. G., Tarnocai, C., Kimpe, C. D., King, R., Dormaar, J., Vreeken, W., & Harris, S. A. (1987). Some aspects of Quaternary soils in Canada. *Canadian journal of soil science*, 67(2), 221-247.
- Van Bellen, S., Garneau, M., & Booth, R. K. (2011). Holocene carbon accumulation rates from three ombrotrophic peatlands in boreal Quebec, Canada: impact of climate-driven ecohydrological change. *The Holocene*, 21(8), 1217-1231.
- van Bellen, S., Magnan, G., Davies, L., Froese, D., Mullan-Boudreau, G., Zaccone, C., ... & Shotyk, W. (2018). Testate amoeba records indicate regional 20th-century lowering of

- water tables in ombrotrophic peatlands in central-northern Alberta, Canada. *Global change biology*, 24(7), 2758-2774.
- Van Everdingen, R. O. (1982). Frost Blisters of the Bear Rock Spring Area near Fort Norman, N.W.T. Arctic, 35(2), 243–265.
- Vanhala, H., Lintinen, P., & Ojala, A. (2009). Electrical resistivity study of permafrost on Ridnišohkka fell in northwest Lapland, Finland. *Geophysica*, 45(1–2), 103–118.
- Vardy, S. R., Warner, B. G., & Aravena, R. (1997). Holocene climate effects on the development of a peatland on the Tuktoyaktuk Peninsula, northwest territories. *Quaternary Research*, 47(1), 90–104. <https://doi.org/10.1006/qres.1996.1869>
- Vardy, S. R., Warner, B. G., & Aravena, R. (1997). Holocene Climate Effects on the Development of a Peatland on the Tuktoyaktuk Peninsula, Northwest Territories I. *Quaternary Research*, 47(1), 90-104.
- Vardy, S. R., Warner, B. G., & Aravena, R. (1998). Holocene climate and the development of a subarctic peatland near Inuvik, Northwest Territories, Canada. *Climate Change*, 40, 285–313.
- Vasil'chuk, Y. K. (2013). Syngenetic Ice Wedges: Cyclical Formation, Radiocarbon Age and Stable Isotope Records by Yuriy K. Vasil'chuk, Moscow University Press, Moscow, 2006. 404 pp. ISBN 5-211-05212-9. *Permafrost and Periglacial Processes*, 24(1), 82-93.
- Vasil'chuk, Y. K., & Vasil'chuk, A. C. (1997). Radiocarbon dating and oxygen isotope variations in Late Pleistocene syngenetic ice-wedges, northern Siberia. *Permafrost and Periglacial Processes*, 8(3), 335-345.
- Vasil'chuk, Y. K., & Vasil'chuk, A. C. (1998). Oxygen-isotope and C14 data associated with Late Pleistocene syngenetic ice-wedges in mountains of Magadan region, Siberia. *Permafrost and Periglacial Processes*, 9(2), 177-183.
- Vasil'chuk, Y. K., Budantseva, N. A., Christiansen, H. H., Chizhova, J. N., Vasil'chuk, A. C., & Zemskova, A. M. (2015). Oxygen stable isotope variation in Late Holocene ice wedges in Yamal Peninsula and Svalbard. *Geography, environment, sustainability*, 8(3), 36-54.
- Vasil'chuk, Y. K., Lawson, D. E., Yoshikawa, K., Budantseva, N. A., Chizhova, J. N., Podborny, Y. Y., & Vasil'chuk, A. C. (2016). Stable isotopes in the closed-system Weather Pingo, Alaska and Pestsovoye Pingo, northwestern Siberia. *Cold Regions Science and Technology*, 128, 13-21.
- Vasil'chuk, Y. K., van der Plicht, J., Jungner, H., & Vasil'chuk, A. C. (2000). AMS-dating of Late Pleistocene and Holocene syngenetic ice-wedges. *Nuclear Instruments and Methods in Physics Research Section B: Beam Interactions with Materials and Atoms*, 172(1-4), 637-641.
- Vasil'chuk, Y. K., Vasil'chuk, A. C., & Stanilovskaya, J. V. (2017). Early Holocene climate signals from stable isotope composition of ice wedge in the Chara Basin, Northern Transbaikalia, Russia. *Geoscience Frontiers. Scopu*s, 8(5), 1.
- Vasil'chuk, Y., & Vasil'chuk, A. (2014). Spatial distribution of mean winter air temperatures in Siberian permafrost at 20– 18 ka BP using oxygen isotope data. *Boreas*, 43(3), 678-687.
- Vasil'chuk, Y. K., Lawson, D. E., Yoshikawa, K., Budantseva, N. A., Chizhova, J. N., Podborny, Y. Y., & Vasil'chuk, A. C. (2016). Stable isotopes in the closed-system

- Weather Pingo, Alaska and Pestsovoye Pingo, northwestern Siberia. *Cold Regions Science and Technology*. <https://doi.org/10.1016/j.coldregions.2016.05.001>
- Vasil'chuk, Y. K., Vasil'chuk, A. C., Rank, D., Kutschera, W., & Kim, J. C. (2001). Radiocarbon dating of $\delta^{18}\text{O}$ - δD plots in late pleistocene ice-wedges of the duvanny yar (Lower Kolyma River, Northern Yakutia). *Radiocarbon*, 43(2 PART II), 541–553. <https://doi.org/10.1017/s0033822200041199>
- Vasil'chuk, Y., & Vasil'chuk, A. (2014). Spatial distribution of mean winter air temperatures in Siberian permafrost at 20-18 ka BP using oxygen isotope data. *Boreas*, 43(3), 678–687. <https://doi.org/10.1111/bor.12033>
- Wahl, H. E. (1987). *Climate of Yukon*. Environment Canada. Atmospheric Environment Service.
- Wahl, H. E., Fraser, D. B., Harvey, R. C., & Maxwell, J. B. (1987). *Climate of Yukon*. Environment Canada. *Atmospheric Environment Service, Climatological Studies*, 40(0).
- Wang, Y., Jin, H., & Li, G. (2016). Investigation of the freeze-thaw states of foundation soils in permafrost areas along the China-Russia Crude Oil Pipeline (CRCOP) route using ground-penetrating radar (GPR). *Cold Regions Science and Technology*, 126, 10–21. <https://doi.org/10.1016/j.coldregions.2016.02.013>
- Watanabe, K., & Wake, T. (2009). Measurement of unfrozen water content and relative permittivity of frozen unsaturated soil using NMR and TDR. *Cold Regions Science and Technology*, 59(1), 34–41. <https://doi.org/10.1016/j.coldregions.2009.05.011>
- Watson, G. H., Slusarchuk, W. A., & Rowley, R. K. (1973). Determination of Some Frozen and Thawed Properties of Permafrost Soils. *Canadian Geotechnical Journal*, 10(4), 592–606. <https://doi.org/10.1139/t73-055>
- Wentworth, C. K. (1922). A Scale of Grade and Class Terms for Clastic Sediments. *The Journal of Geology*, 30(5), 377–392. <https://doi.org/10.1086/622910>
- Westgate, J. A., Preece, S. J., Froese, D. G., Walter, R. C., Sandhu, A. S., & Schweger, C. E. (2001). Dating early and middle (Reid) Pleistocene glaciations in central Yukon by tephrochronology. *Quaternary Research*, 56(3), 335–348.
- Wetterich, S., Tumskey, V., Rudaya, N., Andreev, A. A., Opel, T., Meyer, H., ... & Hüls, M. (2014). Ice Complex formation in arctic East Siberia during the MIS3 Interstadial. *Quaternary Science Reviews*, 84, 39–55.
- Wetterich, S., Tumskey, V., Rudaya, N., Andreev, A. A., Opel, T., Meyer, H., Schirrmeister, L., Hüls, M. (2014). Ice Complex formation in arctic East Siberia during the MIS3 Interstadial. *Quaternary Science Reviews*, 84, 39–55.
- Wickham, H. (2016). *ggplot2: elegant graphics for data analysis*. Springer.
- Williams, P. J. (1995). Permafrost and climate change : geotechnical implications. *Philosophical Transaction of the Royal Society*, 352, 347–358.
- Wolter, J., Lantuit, H., Fritz, M., Macias-Fauria, M., Myers-Smith, I., & Herzschuh, U. (2016). Vegetation composition and shrub extent on the Yukon coast, Canada, are strongly linked to ice-wedge polygon degradation. *Polar Research*, 35(1), 27489.
- Woo, M. K. (1986). Permafrost hydrology in north america. *Atmosphere-Ocean*, 24(3), 201–234.
- Woo, M., & Steer, P. (1983). Slope hydrology as influenced by thawing of the active layer, Resolute, N. W.T. *Canadian Journal of Earth Sciences*, 20, 978–986.

- Wright, N., Hayashi, M., & Quinton, W. L. (2009). Spatial and temporal variations in active layer thawing and their implication on runoff generation in peat-covered permafrost terrain. *Water Resources Research*, 45(5).
- Yang, Y., Jiang, G., & Zhang, P. (2017). Stable Isotopic Stratification and Growth Patterns of Ground Ice in Permafrost on the Qinghai-Tibet Plateau, China. *Permafrost and Periglacial Processes*, 28, 119–129. <https://doi.org/10.1002/ppp.1892>
- Yanovsky, V. K. (1933). Expedition to Pechora River to determine the position of the southern permafrost boundary. *Reports of the Committee for Permafrost Investigations*, 5(2), 65-149.
- Yershov, E. D. (2004). *General geocryology*. Cambridge university press.
- Yoshikawa, K., Sharkhuu, N., & Sharkhuu, A. (2013). Groundwater hydrology and stable isotope analysis of an open-system pingo in Northwestern Mongolia. *Permafrost and Periglacial Processes*, 24(3), 175–183. <https://doi.org/10.1002/ppp.1773>
- Yukon Geological Survey. *Bedrock Geology, Dawson (116B & 116C), Yukon* [map]. 1:250,000. Centre for Topographical Information, Natural Resources Canada, May 2018.
- Yukon Geological Survey. *Bedrock Geology, Ogilvie River (116F & 116G), Yukon* [map]. 1:250,000. Centre for Topographical Information, Natural Resources Canada, May 2018.
- Zaccone, C., Plaza, C., Ciavatta, C., Miano, T. M., & Shotyk, W. (2018). Advances in the determination of humification degree in peat since: Applications in geochemical and paleoenvironmental studies. *Earth-Science Reviews*, 185, 163-178.
- Zhang, T., Heginbottom, J. A., Barry, R. G., & Brown, J. (2000). Further statistics on the distribution of permafrost and ground ice in the Northern Hemisphere. *Polar geography*, 24(2), 126-131.
- Zhu, X., Wu, T., Li, R., Xie, C., Hu, G., Qin, Y., ... & Yang, C. (2017). Impacts of summer extreme precipitation events on the hydrothermal dynamics of the active layer in the Tanggula permafrost region on the Qinghai-Tibetan plateau. *Journal of Geophysical Research: Atmospheres*, 122(21), 11-549.

APPENDIX

Appendix 1. Stable isotope data of BS19 ground ice

Table A1.1. Stable isotope data for Site 4. Active layer isotope data is listed in a separate table in Supplementary 2. The entire core was subsampled at 1cm resolution. Precision for $\delta^{18}\text{O}$, δD , and d -excess are 0.15‰, 0.5‰, and 1.3‰, respectively.

<i>Segment</i>	<i>Midpoint Depth (cm)</i>	<i>$\delta^{18}\text{O}$(‰)</i>	<i>δD(‰)</i>	<i>d-excess(‰)</i>
A	20.5			
A	21.5	-19.83	-155.1	3.5
A	22.5	-19.81	-155.1	3.3
A	23.5	-19.91	-155.6	3.7
A	24.6	-19.92	-155.7	3.6
A	25.6	-19.99	-156.2	3.7
A	26.6	-19.96	-156.0	3.6
A	27.6	-20.00	-156.1	3.8
A	28.6	-20.02	-156.2	4.0
A	29.6	-20.03	-156.2	4.1
A	30.6	-20.00	-156.2	3.8
A	31.7	-20.03	-156.0	4.2
A	32.7	-19.98	-156.0	3.9
A	33.7	-20.12	-156.5	4.5
A	34.7	-20.17	-156.7	4.6
A	35.7	-20.65	-157.9	7.3
A	36.7	-20.50	-157.8	6.2
A	37.7	-20.14	-156.5	4.7
A	38.8	-20.12	-156.8	4.2

A	39.8	-20.02	-156.2	4.0
A	40.8	-19.97	-155.5	4.2
A	41.8	-19.65	-153.8	3.4
A	42.8	-19.40	-152.3	2.9
A	43.8	-19.19	-151.5	2.0
A	44.8	-18.95	-150.1	1.5
A	45.8	-19.17	-151.0	2.3
A	46.9	-18.93	-150.7	0.8
A	47.9	-19.42	-152.8	2.5
A	48.9	-19.52	-153.5	2.7
A	49.9	-19.74	-154.9	3.0
A	50.9	-19.54	-154.9	1.5
A	51.9	-19.58	-155.3	1.3
A	52.9	-19.49	-155.1	0.8
A	54.0	-19.48	-155.3	0.5
A	55.0	-19.42	-155.2	0.1
A	56.0	-19.56	-155.9	0.6
B	57.0	-19.56	-156.4	0.0
B	58.0	-19.47	-156.5	-0.8
B	59.1	-20.00	-158.2	1.8
B	60.1	-19.85	-158.0	0.9
B	61.1	-19.58	-157.2	-0.6
B	62.1	-19.56	-157.2	-0.7
B	63.2	-19.55	-157.2	-0.7
B	64.2	-19.66	-157.8	-0.5
B	65.2	-19.65	-157.9	-0.7
B	66.3	-19.69	-158.0	-0.5

B	67.3	-19.66	-157.8	-0.5
B	68.3	-19.66	-157.5	-0.3
B	69.3	-19.63	-157.7	-0.6
B	70.4	-19.68	-157.9	-0.5
B	71.4	-19.72	-158.1	-0.4
B	72.4	-19.71	-158.1	-0.4
B	73.5	-19.74	-158.0	-0.1
B	74.5	-19.65	-157.7	-0.5
B	75.5	-19.68	-157.8	-0.4
B	76.5	-19.69	-157.8	-0.2
B	77.6	-19.76	-158.2	-0.1
B	78.6	-19.81	-158.4	0.1
B	79.6	-19.75	-158.3	-0.3
B	80.7	-19.96	-158.9	0.8
B	81.7	-19.84	-158.8	-0.1
B	82.7	-20.02	-159.2	0.9
B	83.7	-19.97	-159.1	0.7
B	84.8	-19.94	-159.1	0.4
B	85.8	-19.98	-159.2	0.6
B	86.8	-19.95	-159.2	0.4
B	87.9	-20.07	-159.6	0.9
B	88.9	-19.92	-159.0	0.4
B	89.9	-19.94	-159.1	0.3
B	90.9	-19.94	-159.3	0.3
B	92.0	-20.07	-159.7	0.8
C	93.0	-20.08	-159.3	1.3
C	94.1	-19.96	-159.1	0.6

C	95.2	-20.01	-159.3	0.8
C	96.3	-19.93	-158.9	0.6
C	97.4	-19.95	-158.9	0.7
C	98.5	-19.90	-158.4	0.8
C	99.6	-20.37	-159.5	3.4
C	100.7	-20.29	-159.4	2.9
C	101.8	-20.19	-159.3	2.2
C	102.9	-19.94	-158.5	1.0
C	104.0	-20.09	-158.7	2.0
C	105.1	-19.97	-158.0	1.7
C	106.2	-19.96	-158.1	1.6
C	107.3	-20.09	-158.7	2.0
C	108.4	-20.07	-158.8	1.7
C	109.5	-20.12	-158.9	2.0
C	110.6	-20.05	-158.6	1.8
C	111.7	-20.00	-158.6	1.3
C	112.8	-20.04	-158.8	1.5
C	113.9	-20.03	-158.8	1.5
C	115.0	-20.02	-158.7	1.5
C	116.1	-20.00	-158.8	1.3
C	117.2	-19.96	-158.3	1.4
C	118.3	-19.90	-158.0	1.2
C	119.4	-19.95	-158.2	1.4
C	120.5	-19.86	-157.1	1.8
C	121.6	-19.89	-157.4	1.8
C	122.7	-19.77	-157.2	1.0
C	123.8	-20.26	-158.5	3.6

C	124.9	-20.80	-160.9	5.5
---	-------	--------	--------	-----

Table A1.2. Stable isotope data for Site 3. Active layer isotope data is listed in a separate table in Supplementary 2. The core was subsampled at 1cm resolution between 21 to 69.5cm and 119.0 to 140.2cm and at 2cm resolution between 69.5 to 119.0cm.

<i>Segment</i>	<i>Midpoint Depth (cm)</i>	<i>$\delta^{18}O$(‰)</i>	<i>δD(‰)</i>	<i>d-excess(‰)</i>
A	21.0	-19.31	-153.5	1.0
A	22.9	-19.45	-154.1	1.6
A	24.9	-19.39	-153.7	1.4
A	26.8	-19.13	-152.9	0.2
A	28.8	-19.24	-153.1	0.8
A	30.2	-19.11	-152.0	0.9
A	31.2	-18.77	-149.9	0.3
A	32.2	-18.80	-150.6	-0.2
A	33.1	-18.90	-151.7	-0.4
A	34.1	-18.98	-152.5	-0.6
A	35.1	-19.23	-154.1	-0.3
A	36.1	-19.47	-155.7	0.0
A	37.0	-19.87	-157.5	1.4
A	38.0	-19.92	-157.6	1.8
A	39.0	-19.50	-154.6	1.4
A	40.0	-19.32	-151.9	2.7
A	40.9	-19.68	-153.3	4.2
A	41.9	-19.70	-154.0	3.6
A	42.9	-19.74	-154.6	3.3

A	43.9	-19.69	-155.2	2.3
A	44.8	-20.33	-157.8	4.8
A	45.8	-20.58	-159.9	4.8
A	46.8	-20.47	-159.6	4.1
A	47.7	-20.43	-159.5	4.0
A	48.7	-20.47	-159.4	4.3
A	49.7	-20.30	-158.6	3.9
A	50.7	-20.08	-157.5	3.2
A	51.6	-19.94	-156.9	2.7
A	52.6	-19.85	-156.2	2.6
A	53.6	-19.81	-155.9	2.6
A	54.6	-19.72	-155.7	2.1
A	55.5	-19.67	-155.3	2.1
B	57.5	-19.43	-154.1	1.3
B	58.5	-19.63	-155.6	1.4
B	59.5	-19.74	-156.2	1.7
B	60.5			
B	61.5	-19.86	-156.9	2.0
B	62.5			
B	63.5	-19.91	-157.3	1.9
B	64.5	-19.93	-157.4	2.0
B	65.5	-19.95	-157.5	2.1
B	66.5	-19.95	-157.6	2.0
B	67.5	-19.91	-157.2	2.1
B	68.5	-19.93	-157.5	1.9
B	69.5	-19.99	-157.7	2.2
B	71.0	-19.98	-157.6	2.2

B	73.0	-19.97	-157.7	2.1
B	75.0	-19.82	-156.8	1.8
B	77.0	-19.79	-156.8	1.5
B	79.0	-19.82	-156.4	2.2
B	81.0	-19.72	-156.2	1.6
B	83.0	-19.30	-154.4	0.0
B	85.0	-19.58	-155.4	1.3
B	87.0	-19.68	-155.7	1.7
B	89.0	-19.69	-155.8	1.7
B	91.0	-19.62	-155.2	1.8
C	93.0	-19.52	-154.6	1.6
C	94.6	-19.43	-154.4	1.1
C	96.3	-19.62	-155.1	1.8
C	98.3	-19.55	-154.9	1.5
C	100.3	-19.60	-155.1	1.7
C	102.4	-19.49	-154.9	1.1
C	104.4	-19.58	-155.1	1.5
C	106.4	-19.62	-155.3	1.7
C	108.5	-19.53	-154.6	1.6
C	110.5	-19.58	-154.8	1.8
C	112.5	-19.49	-153.8	2.1
C	114.2	-19.56	-154.0	2.4
C	115.8	-19.60	-154.5	2.2
C	117.4	-19.54	-154.1	2.2
C	119.0	-19.46	-153.8	1.9
C	120.7	-19.37	-153.3	1.7
C	121.8	-19.53	-154.0	2.2

C	123.1	-19.52	-154.1	2.1
C	124.7	-19.48	-153.8	2.0
C	126.4	-19.49	-154.0	1.9
D	129.5	-19.51	-154.0	2.1
D	130.3	-19.56	-154.1	2.4
D	131.4	-19.58	-154.1	2.5
D	132.6	-19.39	-153.4	1.7
D	133.9	-19.46	-153.2	2.5
D	135.2	-19.28	-152.5	1.7
D	136.4	-19.08	-151.0	1.6
D	137.7	-19.36	-152.4	2.4
D	138.9	-19.38	-152.5	2.6
D	140.2	-19.20	-152.1	1.6

Table A1.3. Stable isotope data for Site 2. Active layer isotope data is listed in a separate table in Supplementary 2. The core was subsampled at 2cm resolution between 21 to 55.8cm and 80.9 to 131.3cm and at 1cm resolution between 55.8 to 80.9cm.

<i>Segment</i>	<i>Midpoint Depth (cm)</i>	<i>$\delta^{18}O$(‰)</i>	<i>δD(‰)</i>	<i>d-excess(‰)</i>
A	21.0	-19.61	-156.1	0.8
A	23.4	-19.60	-155.8	1.1
A	25.9	-20.08	-158.9	1.8
A	28.3	-20.58	-162.1	2.5
A	30.7	-20.57	-161.9	2.6
A	32.7			
A	33.9			
A	35.1			

A	36.3			
A	37.5	-20.56	-161.9	2.5
A	38.8			
A	40.0			
A	41.2	-20.31	-159.4	3.1
A	42.4	-20.36	-159.5	3.3
A	43.6	-20.23	-158.7	3.1
A	44.8	-20.08	-158.1	2.6
A	46.1	-19.07	-151.6	1.0
A	47.3	-19.41	-153.9	1.4
A	48.5	-20.26	-159.5	2.6
A	49.7	-20.89	-163.9	3.2
A	50.9	-21.04	-164.9	3.4
A	52.1	-20.74	-162.9	3.1
A	53.4	-20.74	-163.0	3.0
A	54.6	-19.85	-157.6	1.2
A	55.8	-19.34	-154.1	0.6
B	58.5	-19.59	-155.3	1.5
B	59.7	-19.98	-157.9	2.0
B	61.0	-20.18	-159.2	2.3
B	62.2	-20.45	-160.6	3.0
B	63.4	-20.49	-161.3	2.6
B	64.7	-20.54	-161.6	2.7
B	65.9	-20.59	-161.8	2.9
B	67.1	-20.63	-162.5	2.5
B	68.4	-20.75	-163.3	2.7
B	69.6	-20.87	-164.3	2.7

B	70.8	-20.90	-164.6	2.6
B	72.1	-20.97	-165.0	2.8
B	73.3	-20.99	-165.0	2.9
B	75.0	-20.74	-163.2	2.7
C	78.5	-20.65	-162.1	3.1
C	79.7	-20.80	-162.9	3.5
C	80.9	-20.85	-163.0	3.8
C	82.1	-20.76	-162.5	3.6
C	83.3	-20.89	-163.1	3.9
C	84.5	-20.90	-163.2	4.0
C	86.2	-20.91	-163.1	4.1
C	88.5	-20.95	-163.4	4.3
C	90.9	-21.08	-163.3	5.4
C	93.3	-21.06	-163.5	4.9
C	95.5	-20.59	-161.8	2.9
D	97.5	-20.88	-163.4	3.7
D	99.8	-20.94	-163.5	4.1
D	102.0	-20.89	-163.9	3.2
D	104.3	-20.81	-163.4	3.1
D	106.5	-20.84	-163.6	3.1
D	108.8	-20.91	-164.3	3.0
D	111.0	-21.00	-164.6	3.3
D	113.3	-20.88	-164.0	3.0
D	115.5	-20.92	-164.2	3.2
D	117.8	-21.29	-164.9	5.4
D	120.0	-21.27	-165.3	4.9
D	122.3	-21.32	-165.9	4.7

D	124.5	-21.48	-166.7	5.2
D	126.8	-21.57	-167.3	5.2
D	129.0	-21.57	-167.2	5.3
D	131.3	-21.27	-165.5	4.6

Table A1.4. Stable isotope data for Site 1. Active layer isotope data is listed in a separate table in Supplementary 2. The core was subsampled at 1cm resolution.

<i>Segment</i>	<i>Midpoint Depth (cm)</i>	<i>$\delta^{18}O$(‰)</i>	<i>δD(‰)</i>	<i>d-excess(‰)</i>
A	14.5	-21.5	-167.0	5.3
A	15.5	-21.4	-165.7	5.2
A	16.6	-21.3	-165.0	5.2
A	17.6	-21.3	-165.4	5.0
A	18.7	-21.5	-166.7	5.0
A	19.7	-21.8	-168.9	5.4
A	20.8	-22.0	-170.8	4.9
A	21.8	-21.8	-170.4	3.6
A	22.9	-21.3	-168.3	2.3
A	23.9	-21.5	-169.2	2.5
A	25.0	-21.7	-170.3	3.3
A	26.0	-21.5	-169.9	2.3
A	27.1	-22.3	-175.2	3.4
A	28.1	-22.6	-175.8	4.7
A	29.2	-22.3	-174.9	3.7
A	30.2	-22.3	-174.6	3.8
A	31.3	-22.3	-175.0	3.5
A	32.3	-22.4	-176.0	3.4
A	33.4	-22.8	-177.7	4.4

A	34.4	-22.8	-178.0	4.6
A	35.5	-22.8	-177.4	4.9
B	37.5	-22.3	-174.4	3.9
B	38.5	-21.3	-166.9	3.2
B	39.6	-20.6	-162.1	2.8
B	40.6	-20.4	-160.8	2.3
B	41.6	-20.4	-160.1	2.7
B	42.7	-20.8	-160.4	5.7
B	43.7	-20.1	-159.2	1.2
B	44.7	-20.1	-159.7	0.9
B	45.8	-20.2	-160.3	1.1
B	46.8	-20.1	-160.3	0.5
B	47.8	-20.4	-161.9	1.1
B	48.9	-20.6	-163.8	1.1
B	49.9	-20.7	-164.6	1.3
B	50.9	-20.9	-165.7	1.5
B	52.0	-21.0	-166.5	1.6
B	53.0	-21.2	-166.7	2.8
B	54.0	-21.4	-168.8	2.4
B	55.0	-21.7	-170.9	2.6
B	56.1	-21.8	-171.7	2.8
B	57.1	-21.9	-172.3	2.8
B	58.1	-21.8	-172.1	2.5
B	59.2	-21.9	-172.3	3.1
B	60.2	-22.1	-172.9	3.9
B	61.2	-22.0	-173.1	3.1
B	62.3	-21.9	-172.2	2.7
B	63.3	-22.2	-172.5	5.5
B	64.3	-22.2	-172.3	5.3

B	65.4	-22.3	-172.6	5.4
B	66.4	-22.1	-172.1	5.0
B	67.4	-22.2	-172.3	5.1
B	68.5	-22.1	-171.2	5.2
C	69.5			
C	70.6	-22.1	-171.7	5.0
C	71.7	-22.1	-171.8	4.7
C	72.7	-22.2	-172.6	5.0
C	73.8	-22.2	-172.3	5.2
C	74.9	-22.2	-172.5	5.5
C	76.0	-22.3	-173.0	5.1
C	77.0	-22.3	-173.4	5.3
C	78.1	-22.4	-173.7	5.5
C	79.2	-22.3	-173.3	5.1
C	80.3	-22.4	-173.9	5.3
C	81.3	-22.4	-173.6	5.2
C	82.4	-22.3	-173.1	5.2
C	83.5	-22.1	-172.5	4.6
C	84.6	-22.3	-173.4	5.2
C	85.7	-22.3	-173.3	4.7
C	86.7	-22.2	-172.8	4.9
C	87.8	-22.3	-173.3	4.8
C	88.9	-22.3	-173.4	4.7
C	90.0	-22.3	-173.9	4.7
C	91.0	-22.3	-173.8	4.5
C	92.1	-22.0	-172.5	3.3
C	93.2	-21.9	-171.7	3.4
C	94.3	-22.5	-175.4	4.5
C	95.3	-22.2	-173.9	3.3

C	96.4			
D	97.5	-22.7	-176.9	4.3
D	98.4	-22.7	-177.0	4.7
D	99.4	-22.7	-177.2	4.5
D	100.3	-22.8	-177.5	4.5
D	101.3	-22.8	-177.2	5.0
D	102.2	-22.8	-177.7	4.8
D	103.2	-22.8	-177.9	4.9
D	104.1	-22.9	-178.3	4.6
D	105.1	-22.9	-178.5	4.9
D	106.0	-22.5	-176.0	4.0
D	107.0	-22.7	-177.8	4.1
D	107.9	-23.0	-179.2	4.6
D	108.9			
D	109.8	-22.8	-179.1	3.4
D	110.7	-23.0	-179.8	4.3
D	111.7	-22.9	-179.5	3.9
D	112.6	-23.1	-180.0	4.5
D	113.6	-23.1	-180.2	4.5
D	114.5	-23.1	-180.4	4.4
D	115.5	-23.2	-181.1	4.9
D	116.4	-23.2	-181.2	4.5
D	117.4	-23.3	-181.6	4.8
D	118.3	-23.3	-181.8	4.7
D	119.3	-23.4	-182.2	4.7
D	120.2	-23.5	-182.3	5.8
D	121.1	-23.3	-182.0	4.5
D	122.1	-23.4	-182.4	4.6
D	123.0	-23.4	-182.4	4.6

D	124.0	-23.4	-182.5	4.6
D	124.9	-23.4	-182.3	4.9
D	125.9	-23.4	-182.3	5.0
D	126.8	-23.6	-183.0	6.0
D	127.8	-23.4	-182.5	4.8
D	128.7	-23.5	-182.6	5.0
D	129.7	-23.4	-182.5	4.8
D	130.6	-23.5	-182.6	5.1
D	131.6	-23.2	-181.3	4.5

Appendix 2. September 2019 Active Layer Profile Water Stable Isotopes

Table A2.1. Site 4

<i>Depth (cm)</i>	<i>$\delta^{18}\text{O}(\text{‰})$</i>	<i>$\delta\text{D}(\text{‰})$</i>	<i>d-excess(‰)</i>
0-5	-18.7	-152.5	-2.6
5-10	-17.5	-143.7	-3.6
10-15	-17.9	-143.8	-0.6
15-20	-18.4	-145.8	1.6
20-25	-19.3	-151.2	3.3
25-30	-19.9	-154.8	4.0
30-35	-19.9	-155.5	3.5
35-40	-19.8	-155.3	2.9
basal water	-19.5	-153.4	2.5

Table A2.2. Site 3

<i>Depth (cm)</i>	<i>$\delta^{18}\text{O}(\text{‰})$</i>	<i>$\delta\text{D}(\text{‰})$</i>	<i>d-excess(‰)</i>
5-10	-16.6	-139.8	-7.3
10-15	-17.8	-142.3	0.1

15-20	-18.5	-146.0	2.2
20-25	-19.5	-150.9	4.8
25-30	-19.5	-152.6	3.3
30-35	-19.5	-153.6	2.2
35-40	-19.5	-153.6	2.2
basal water	-19.5	-152.9	3.1

Table A2.3. Site 2

<i>Depth (cm)</i>	<i>$\delta^{18}\text{O}(\text{‰})$</i>	<i>$\delta\text{D}(\text{‰})$</i>	<i>d-excess(‰)</i>
5-10	-19.3	-152.1	2.0
10-15	-19.6	-153.5	3.0
15-20	-19.6	-153.7	2.8
20-25	-19.5	-154.4	1.5
25-30	-19.4	-154.6	0.9
30-35	-19.2	-153.8	-0.6
basal water	-19.4	-153.7	1.6

Table A2.4. Site 1

<i>Depth (cm)</i>	<i>$\delta^{18}\text{O}(\text{‰})$</i>	<i>$\delta\text{D}(\text{‰})$</i>	<i>d-excess(‰)</i>
0-5	-17.4	-142.3	-2.9
5-10	-19.8	-153.4	5.2
10-15	-20.6	-159	5.7
15-20	-20.8	-160.7	5.6
20-25	-20.8	-161.1	5.4
25-30	-20.8	-161.2	5.2
basal water	-20.8	-161.2	5.3

Appendix 3. September 2019 Basal Active Layer Waters

Table A3.1. Stable isotopes of free waters sampled at the base of thaw pits excavated in September 2019. Distance increases downslope. BW4, 9, 13, and 15 were sampled at the same locations as Sites 1, 2, 3, and 4, respectively.

<i>Original Name</i>	<i>Site</i>	<i>Distance (m)</i>	<i>$\delta^{18}\text{O}$ (‰)</i>	<i>δD (‰)</i>	<i>d-excess (‰)</i>
RZ-2	BW1	0.0	-21.4	-167.1	4.2
RZ-3	BW2	48.5	-20.9	-161.9	5.4
TZ-1	BW3	100.0	-20.7	-160.5	5.2
BS19-4-2 (BW)	BW4	118.7	-20.8	-161.2	5.3
TZ-2	BW5	180.7	-20.6	-159.6	4.8
TZ-3	BW6	275.6	-19.9	-156.0	3.5
TZ-4	BW7	364.4	-19.6	-155.0	2.1
TZ-5	BW8	419.1	-19.9	-155.6	3.3
BS19-3-2 (BW)	BW9	470.0	-19.4	-153.7	1.6
TZ-6	BW10	528.6	-19.6	-153.4	3.0
TZ-7	BW11	644.7	-19.4	-152.2	2.8
TZ-8	BW12	725.3	-19.2	-151.6	2.3
DZ-1	BW13	754.6	-19.5	-152.9	3.1
DZ-2	BW14	866.2	-19.4	-153.9	1.7
DZ-4	BW15	967.2	-19.5	-153.4	2.5

Appendix 4. September 2019 Thaw Depths

Table A4.1. Probed thaw depths from September 2019. BW4, 9, 13, and 15 were sampled at the same locations as Sites 1, 2, 3, and 4, respectively.

<i>Measurement Date</i>	<i>Site</i>	<i>Distance (m)</i>	<i>Average hollow thaw depth (cm)</i>	<i>1 σ hollow precision (cm)</i>	<i>n</i>
-------------------------	-------------	---------------------	---------------------------------------	--	----------

	BW1	0	52.5		
15-Sep-2019	BW2	49	46.1	9.2	16
15-Sep-2019	BW3	100	40.2	7.0	15
15-Sep-2019	BW4	119	50.7	13.0	9
15-Sep-2019	BW5	181	42.0	4.4	6
15-Sep-2019	BW6	276	42.1	2.0	9
	BW7	364	n.r.		
	BW8	419	n.r.		
12-Sep-2019	BW9	470	44.2	2.0	31
16-Sep-2019	BW10	529	48.7	1.2	3
16-Sep-2019	BW11	645	45.0		6
	BW12	725	45.0		
16-Sep-2019	BW13	755	38.7	2.5	6
17-Sep-2019	BW14	866	42.3	2.7	9
17-Sep-2019	BW14*	918	40.0	3.4	13
17-Sep-2019	BW15	967	40.5	3.3	6

Appendix 5. Electrical Conductivity, pH, and GWC of Permafrost Ice

Table A5.1. Site 4 permafrost ice pH and EC. Note the Site 4 core was re-subsampled for these analyses; depths may therefore vary slightly from those for the stable isotope values from Site 4.

<i>Segment</i>	<i>Midpoint Depth (cm)</i>	<i>pH</i>	<i>EC (uS/cm)</i>
A	21.0	4.9	73.2
A	23.4	5.0	50.2
A	25.7	5.1	42.1
A	28.1	5.6	51.4
A	30.4	5.6	38.8
A	32.8	5.6	44.6
A	35.1	5.7	67.7
A	37.5	5.6	67.6
A	39.8	5.7	87.3

A	42.2	5.6	55.8
A	44.0	5.6	43.8
A	45.2	5.6	44.1
A	46.4	5.7	37.8
A	47.6	6.0	53.3
A	48.8	5.9	45.0
A	49.9	5.8	63.8
A	51.1	5.7	77.4
A	52.3	5.7	79.5
A	53.5	5.9	81.4
A	54.6	5.8	86.2
A	55.8	5.9	75.4
B	57.0	5.6	87.7
B	58.2	5.8	87.9
B	59.4	5.9	105.9
B	60.6	5.9	58.2
B	61.8	6.2	61.3
B	63.0	6.0	63.8
B	64.2	6.1	73.2
B	65.4	6.3	79.0
B	66.6	6.2	83.4
B	67.8	6.3	79.9
B	69.0	6.1	72.2
B	70.2	6.3	76.9
B	71.4	6.3	81.3
B	72.6	6.4	91.5
B	73.8		80.3
B	75.0		83.7
B	76.2		81.2

B	77.4	83.4
B	78.6	321.1
B	79.8	308.8
B	81.0	322.6
B	82.2	347.2

Table A5.2 Site 3 pH, electrical conductivity, and gravimetric water content. Electrical conductivity and pH analyses marked with (*) between 97.9 to 110.9cm were conducted on a separate set of subsamples from GWC and are therefore presented in Table S5.3.

<i>Segment</i>	<i>Midpoint Depth (cm)</i>	<i>pH</i>	<i>EC (uS/cm)</i>	<i>GWC (%)</i>
A	21			
A	22.9			1376.0
A	24.9			782.9
A	26.8			434.6
A	28.8			411.2
A	30.2	4.7		546.0
A	31.2	4.8		492.9
A	32.2	4.7		362.3
A	33.1	4.5		206.2
A	34.1	4.5		291.2
A	35.1	4.5		267.1
A	36.1	4.5		262.3
A	37	4.5		275.7
A	38	4.5		289.7
A	39	4.5		414.8
A	40	4.6	66.9	
A	40.9	4.4	80.3	

A	41.9	4.4	77.5	
A	42.9			
A	43.9	4.4	141.0	
A	44.8	4.5	80.3	
A	45.8	4.4	77.9	
A	46.8	4.4	104.5	
A	47.7	4.4	170.7	
A	48.7	4.5	102.5	
A	49.7	4.6	82.9	
A	50.7	4.5		
A	51.6	4.5	81.6	
A	52.6	4.5	179.4	
A	53.6	4.5	96.8	
A	54.6	4.5	107.6	
A	55.5			
B	57.5	4.8	334.3	690.1
B	58.5	4.8	392.8	770.7
B	59.5	4.8	480.1	646.0
B	60.5			
B	61.5	4.8	536.9	559.6
B	62.5			
B	63.5	4.7	593.0	587.6
B	64.5	4.7	577.3	510.5
B	65.5	4.7	609.0	477.3
B	66.5	4.7	613.1	479.8
B	67.5	4.7	557.9	501.2

B	68.5		4.7	583.2	595.7
B	69.5		4.7	724.9	595.9
B	71				701.1
B	73				687.3
B	75				850.8
B	77				846.0
B	79				958.1
B	81				913.2
B	83				835.7
B	85				
B	87				859.2
B	89				762.7
B	91				836.8
C	93				701.7
C	94.6				864.3
C	96.3				1102.4
C	97.9		*	*	1158.9
C	99.5		*	*	1208.1
C	101.1		*	*	1086.4
C	102.8		*	*	1100.9
C	104.4		*	*	993.2
C	106		*	*	924.1
C	107.7		*	*	1055.1
C	109.3		*	*	1040.5
C	110.9		*	*	1035.2
C	112.5		4.6	499.4	1107.6

C	114.2	4.6	491.2	1048.8
C	115.8	4.6	616.1	804.3
C	117.4	4.7	627.2	779.2
C	119	4.7	624.9	699.3
C	120.7	4.7	636.3	662.2
C	121.8	4.7	665.0	752.9
C	123.1	4.7	584.1	790.7
C	124.7	4.6	621.6	731.0
C	126.4	4.7	663.8	704.5
D	129.5	4.7	675.8	677.8
D	130.3	4.7	641.7	722.4
D	131.4	4.7	664.7	748.8
D	132.6	4.7	673.3	755.6
D	133.9	4.8	497.1	1007.2
D	135.2	4.8	499.0	1027.2
D	136.4	5.0	282.4	1744.9
D	137.7	5.0	310.9	2334.3
D	138.9	5.0	365.2	1418.5
D	140.2	4.9	404.9	1276.4
D	141.4	5.0	445.7	1220.7
D	142.7	5.0	361.3	1577.6
D	143.9	5.0	474.0	1316.4
D	145.2	5.0	476.5	1271.2
D	146.5	5.1	495.1	1320.2
D	147.7	5.0	633.1	1045.0
D	149	5.1	656.2	860.3

D	150.2	5.1	769.3	553.3
D	151.5	5.2	816.9	371.5
D	152.7	5.3	785.3	286.0
E	154	5.4		242.8

Table A5.3 Site 3 subset(*) pH, electrical conductivity, and gravimetric water content. These analyses were performed on subsamples separate from those used for GWC. The depths for these two sets therefore differ slightly.

<i>Segment</i>	<i>Midpoint Depth (cm)</i>	<i>pH</i>	<i>EC (uS/cm)</i>
C	96.4	4.5	409.9
C	98.6	4.6	447.0
C	100.8	4.7	473.8
C	102.9	4.6	534.4
C	105.1	4.7	562.1
C	107.3	4.7	446.2
C	109.5	4.8	417.8

Table A5.4. Site 2 pH, electrical conductivity, and gravimetric water content.

<i>Segment</i>	<i>Midpoint Depth (cm)</i>	<i>pH</i>	<i>EC (uS/cm)</i>	<i>GWC (%)</i>
Mono	1.0	4.0		156.3
Mono	3.0	4.1		200.9
Mono	5.0	4.1		154.7
Mono	7.0	4.2		191.5
Mono	9.0	4.4		209.2
Mono	11.0	4.5		189.7
Mono	13.0			196.2
Mono	15.0	4.7		291.3

Mono	17.0	4.6		215.9
Mono	19.0			180.6
A	21.0	5.2	108.0	739.8
A	23.4	5.1	58.8	952.5
A	25.9	5.2	54.9	970.1
A	28.3	5.0	74.3	1406.1
A	30.7	5.2	69.2	1235.2
A	32.7	5.5	54.7	849.3
A	33.9	5.6	33.8	753.6
A	35.1	5.6	34.3	342.1
A	36.3	5.7	36.3	197.1
A	37.5			103.7
A	38.8			72.3
A	40.0			63.2
A	41.2			65.9
A	42.4			60.4
A	43.6			58.8
A	44.8	5.6		69.9
A	46.1	5.7	58.7	194.8
A	47.3	5.7	29.4	186.2
A	48.5	5.8	37.6	150.9
A	49.7	5.4	38.3	156.1
A	50.9	5.4	48.7	124.9
A	52.1	5.4	64.8	132.7
A	53.4	5.4	54.6	140.9
A	54.6	5.4	58.8	133.6
A	55.8	5.4	41.6	282.1
B	58.5	5.9		
B	59.7	5.4	39.7	1485.1

B	61.0	5.3	38.5	242.2
B	62.2	5.2	35.7	175.8
B	63.4	5.1	37.3	129.8
B	64.7	5.1	44.0	101.2
B	65.9	5.3	36.6	122.4
B	67.1	5.3	42.7	120.9
B	68.4	5.4	46.1	88.1
B	69.6	5.5	57.1	103.5
B	70.8	5.2	69.0	93.3
B	72.1	5.2	63.8	77.3
B	73.3	5.3	67.8	81.7
B	75.0	5.5	55.3	174.1
C	78.5	6.0	67.6	324.0
C	79.7	5.8	74.6	275.9
C	80.9	6.2	120.9	236.2
C	82.1	6.6	87.5	230.9
C	83.3	6.4	115.8	155.5
C	84.5	6.4	119.9	165.3
C	86.2	6.2	124.1	185.2
C	88.5	6.3	122.1	142.7
C	90.9	6.6	116.7	190.5
C	93.3	6.3	137.3	183.1
C	95.5	6.3	140.9	122.4
D	97.5	6.2	147.1	157.1
D	99.8	6.2	149.1	128.6
D	102.0	6.5	146.2	114.1
D	104.3	6.8	128.8	195.5
D	106.5	6.6	150.8	157.5
D	108.8	6.7	170.7	163.5

D	111.0	6.8	181.2	118.3
D	113.3	6.4	152.6	234.6
D	115.5	6.5	172.6	392.3
D	117.8	6.4	174.3	
D	120.0	6.4	196.9	
D	122.3	6.3	276.8	
D	124.5	6.3	296.7	
D	126.8	6.1	287.8	
D	129.0	6.3	272.5	298.2
D	131.3	6.2	227.3	599.0

Appendix 6. Core Names and Designations

Table A6.1. Comparison of naming systems used for permafrost core sites. “Archived name” is the core site written on the core storage bag inside the permafrost archive. “This work” is the equivalent name used for the core sites in this work.

<u>Archived Name</u>	<u>This Work</u>
BS19-4	Site 1
BS19-3	Site 2
BS19-2	Site 3
BS19-1	Site 4

Appendix 7. Methodology for correcting core segment depths

The difference between the length of a core segment calculated from bore hole depth measurements in the field (field length) and length of the same core segment when remeasured in the lab (lab length) is either caused by the loss of material from the top of the segment due to melting against the top of the core barrel or due to an uneven basal fracture (‘wedge break’) when the core was broken from the base of the bore hole.

Depth corrections can be made under three different conditions: one in which results in a field length greater than the lab length of the segment ($L_{field} > L_{lab}$) and two that result in the lab length of the segment being greater than the field length ($L_{lab} > L_{field}$).

Scenario 1: $L_{field} > L_{lab}$

Contact between the top of the core barrel (if positioned vertically) and the top of the segment while drilling melts material from the top of the segment. The top depth of the segment in question ($Top_{current}$) is deeper than the base of the previous segment ($Base_{previous}$). In this scenario, the lab length is used for the true length of the segment and the true top depth of the segment in question is estimated using Equation 1.

$$Top_{current} = Base_{previous} + (L_{field}^{current} - L_{lab}^{current}) \quad (S7.1)$$

Scenario 2A: $L_{lab} > L_{field}$

The base of the segment breaks off the bottom of the bore hole at an angle, leaving a small wedge of material attached to the bottom of the hole. The measuring tape is accidentally placed on top of the elevated part of the wedge, underestimating the field length of the segment. The true length of the segment can be easily determined after extraction from the bore hole or in the lab by measuring between the upper and lower extremes.

Scenario 2B: $L_{lab} > L_{field}$

The base of a segment (Seg A) breaks off the bottom of the bore hole at an angle, leaving a small wedge of material attached to the bottom of the hole, similar to Scenario 2A. However, this time the measuring tape is placed at the lowest point on the wedge such that the field length and lab length of Seg A are the same. This scenario now creates a problem for the segment below, for which the lab length is an overestimation due to Seg A wedge material appended to its top. The solution is to consider the $Base_{Seg A} = Top_{Seg B}$ and the true length of Seg B (L_{true}^B) = L_{lab}^* . Unfortunately it is not possible to determine whether, in the case that $L_{lab} > L_{field}$, it is because of Scenario 2A conditions or Scenario 2B conditions. In this thesis, Scenario 2A was always assumed if the $L_{lab} > L_{field}$ condition was met.

Appendix 8. Methodology for correcting subsample depths

Core segments were subsampled at either 1cm or 2cm intervals. Cumulative error, however, due to human error and loss of material from the saw blade, meant that midpoint depths for each subsample had to be corrected to fit within the upper and lower bounds of the core segment. This was done using Equation 2. The number of subsamples (*# subsamples*) refers to the number of subsamples for a core segment.

$$\text{subsample depth modifier} = 1 + \left[\frac{(\text{corrected core length} - \# \text{ subsamples})}{\# \text{ subsamples}} \right] \quad (\text{S8.1})$$

To find the corrected midpoint depth of a subsample, the subsample depth modifier is multiplied by the subsample resolution (either 1cm or 2cm) and added to the midpoint depth of the previous subsample.

$$CMD_{\text{current}} = CMD_{\text{previous}} + (R * SDM) \quad (\text{S8.2})$$

where:

CMD_{current} : corrected midpoint depth of the subsample in question

CMD_{previous} : corrected midpoint depth of the subsample above

R : target subsample resolution (either 1cm or 2cm in this thesis)

SDM : subsample depth modified

Appendix 9. Local Meteoric Water Line

Baranova (2017) presented elevation-corrected $\delta^{18}\text{O}$ and δD values of rain and snow data (Fig. 1, orange) collected at a highway maintenance camp on the Dempster Highway (65.36°N, 138.31°W), ~17km NNE of the Blackstone 2019 study area. Rain samples were collected in 2013 and 2014 and snow samples were collected in spring of 2015. This dataset was compared against a LMWL constructed from regional GNIP stations. Following Porter et al. (2016), stable isotope data from GNIP from GNIP stations located at Inuvik, Mayo, Snare Rapids, Whitehorse, and Yellowknife were used to construct a regional LMWL (Fig. 1, blue). The δD - $\delta^{18}\text{O}$ regression of the dataset from Baranova (2017) ($\delta\text{D} = 6.8\delta^{18}\text{O} - 24.5$) matched closely with the regional LMWL of the GNIP ensemble ($\delta\text{D} = 7.2\delta^{18}\text{O} - 12.8$). As such, the Baranova dataset was used as the LMWL for the Blackstone study area due to its close proximity to study area and elevation-corrected values.

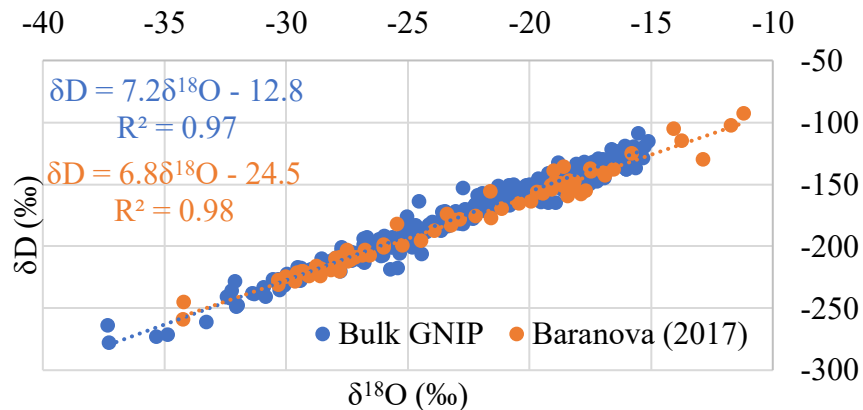


Fig S10.1. Comparison of the LMWL constructed from GNIP waters and the LMWL constructed from precipitation data presented by Baranova (2017). Data are sourced from the Global Network for Isotopes in Precipitation (GNIP) accessed through International Atomic Energy Agency (IAEA).

References

- Baranova, N. (2017). *Evaluating Groundwater In a Permafrost Watershed Using Seasonal Geochemical and Isotope Discharge Trends, Ogilvie River, Yukon* (Doctoral dissertation, Université d'Ottawa/University of Ottawa).
- Porter, T. J., Froese, D. G., Feakins, S. J., Bindeman, I. N., Mahony, M. E., Pautler, B. G., ... & Weijers, J. W. (2016). Multiple water isotope proxy reconstruction of extremely low last glacial temperatures in Eastern Beringia (Western Arctic). *Quaternary Science Reviews*, 137, 113-125.

Appendix 10. Correcting a flipped core segment at Site 3

During data analysis, it was discovered that the upper-most core segment (segment A) extracted at Site 3 record had accidentally been flipped some time during field work or during handling in the laboratory. This was discovered due to similarity between the vertical peat fabric in the “top” of core segment A and the top of core segment B. A general decrease in color value is also observed when core segment A is flipped over. The shapes of the “top” and “bottom” of core segment A also indicated the core had been reversed. The top of core segments are usually cone shaped due to wear on the top of the core barrel during drilling, while the base is more flat, having been snapped off from the base of the borehole for extraction. After flipping core

segment A over, the isotopic profile displays many features also shared by the other three sites, such as a strong C-profile and isotopic enrichment at the top of the transition layer due to cryotic water infiltration into the top of permafrost. Given multiple lines of strong evidence exist that the core segment had been accidentally flipped, we decided to present this piece of the record in its proper, upright form.

Appendix 11. Methods for modeling 2018 thaw depth using thawing degree-days

A thaw depth model was constructed for comparison with the isotope-estimated maximum active layer thickness (ALT_{max}). The thaw depth model was constructed using probed thaw depths from June and September, 2019 and thawing degree-days (TDDs) calculated for the year 2019. Thawing degree days were calculated from the “ERA5-Land hourly data from 1950 to present” between 64-65°N and 138-139°W, which contains hourly surface temperature values, gridded into 0.2°x0.2° blocks (e.g. Fig. 1).

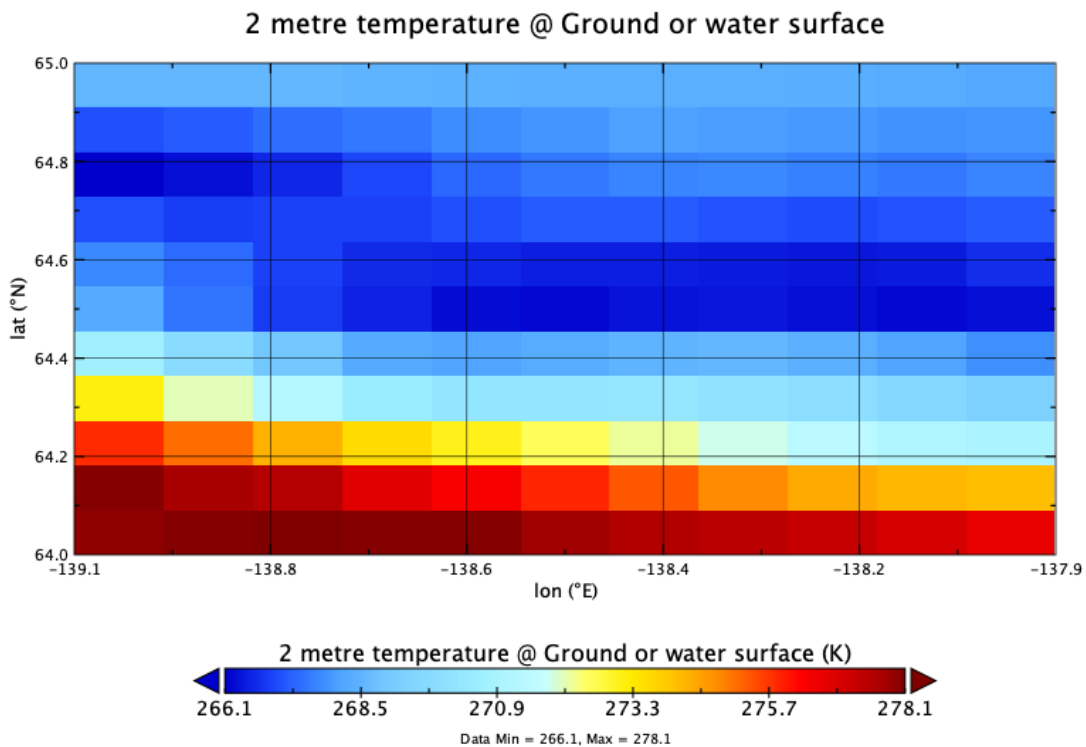


Figure 1. Example map of modeled surface temperature data at the Blackstone study area on May 5, 2019, 00:00. Map was produced in Panoply (NASA/GISS, 2021) using the “ERA5-Land hourly data from 1950 to present” dataset (Muñoz Sabater, 2019, 2021) from the Copernicus Climate Change Service (C3S).

The following parameters were provided as inputs to the Copernicus Climate Change Service (C3S) to access and download the “ERA5-Land hourly data from 1950 to present” dataset:

Variable Measured: 2m temperature

Years: 2019

Months: All

Days: All

Times: All

Subregion extraction: North 65deg, West -139deg, South 64deg, East -138deg

Format: GRIB

The same dataset was also downloaded for the year 2018:

Variable Measured: 2m temperature

Years: 2018

Months: All

Days: All

Times: All

Subregion extraction: North 65deg, West -139deg, South 64deg, East -138deg

Format: GRIB

Gridded surface temperature data, in the form of .grib files, downloaded from C3S, were read using Panoply (NASA/GISS, 2021), exported as .cvs files, and resaved as .xlsx files for further analyses in RStudio (RStudio Team, 2016).

Cumulative TDDs were calculated using eq.1:

$$CTDDs = \sum_{i=0}^d \frac{T_{max} - T_{min}}{2} - 273.15 \quad (1)$$

where:

d: day of the year (0 – 365) up to and including which TDDs will be calculated

T_{max} : maximum daily temperature (K)

T_{min} : minimum daily temperature (K)

R Studio was used to calculate cumulative TDDs for days on which thaw depth probing was conducted in 2019 (Table 1) (R Studio script for cumulative TDD computation is presented in S12). Microsoft Excel was used to construct thaw depth models from the 2019 probed thaw depths and corresponding cumulative TDDs, for the Blackstone study sites (Fig. 2).

Table 1. Summary of accumulated TDDs (in degrees K) calculated for thaw probing days at each site in 2019.

	JUNE 9	JUNE 11	JUNE 14	JUNE 15	SEPT 12	SEPT 15	SEPT 16	SEPT 17
SITE 1	235					1284		
SITE 2		255			1280			
SITE 3			286				1284	
SITE 4				298				1284

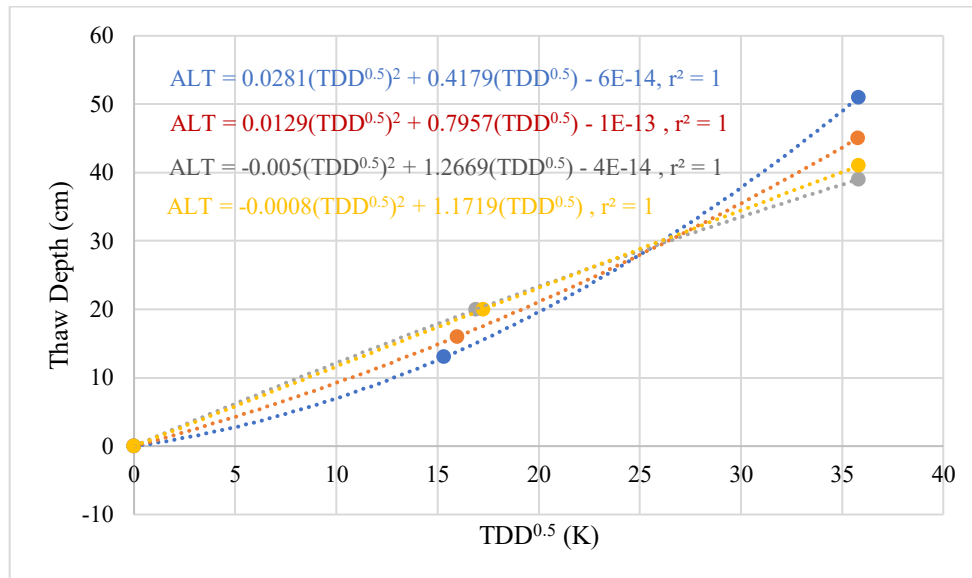


Figure 2. Relations between 2019 probed thaw depth and thawing degree-days (TDDs) for each of the four sites in the Blackstone study area. Data for each site were best fitted to a polynomial regression.

The date of 2018 of maximum thaw depth (ALT_{max}) was approximated by the day that the average daily surface temperature (ADST) dropped below $0^{\circ}C$. To determine this date, previously calculated ADSTs in 2018 were plotted against time using the *ggplot2* package in R Studio (Fig. 3). A rolling average and 95% confidence interval were plotted using the function *geom_smooth()*. The date on which the ADST dropped below $0^{\circ}C$ was approximated (day 275) by the intersection of the rolling average line with $0^{\circ}C$.

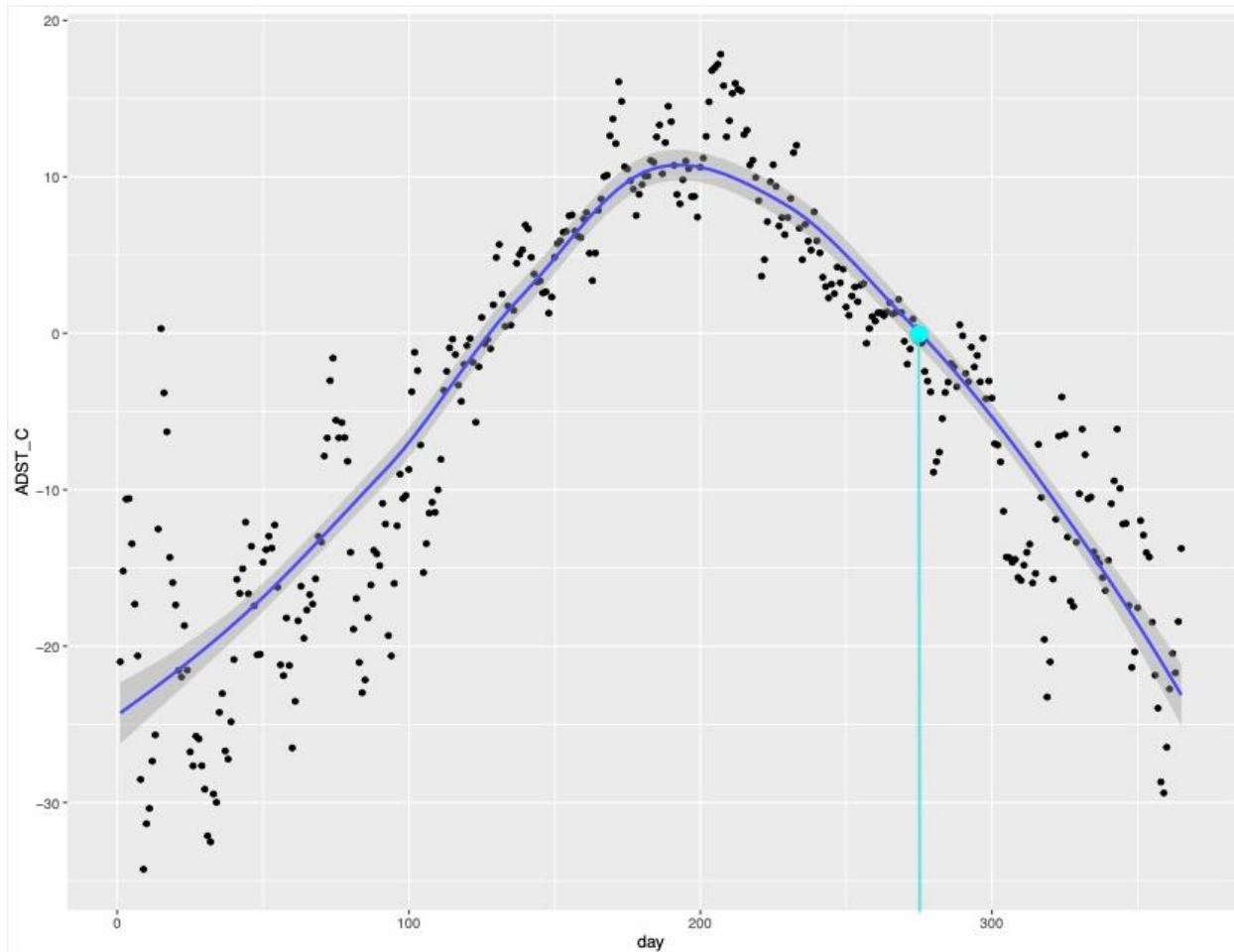


Figure 3. Average daily surface temperatures (black dots) plotted for each day during 2018. The blue line is a rolling average, while the dark grey region represents a 95% confidence interval. Light blue dot indicates the approximant date when the average daily surface temperature drops below 0°C. Data plotted using *ggplot2* in R Studio.

Cumulative TDDs were calculated for day 275 of year 2018 using the R Studio script previously presented. The cumulative TDDs was then used as an input to the polynomial regressions in Figure 3 to estimate the 2018 ALT_{max} for each site.

References

Muñoz Sabater, J. (2021). *ERA5-Land hourly data from 1950 to 1980* [data set]. Copernicus Climate Change Service (C3S) Climate Data Store (CDS). Retrieved January 26, 2022, from <https://cds.climate.copernicus.eu/cdsapp#!/dataset/10.24381/cds.e2161bac?tab=overview>

Muñoz Sabater, J., (2019): ERA5-Land hourly data from 1981 to present. Copernicus Climate Change Service (C3S) Climate Data Store (CDS). Retrieved January 26, 2022, from <https://cds.climate.copernicus.eu/cdsapp#!/dataset/10.24381/cds.e2161bac?tab=overview>

NASA Goddard Institute for Space Studies. (2021). Panoply (Version 4.12.6) [Computer software]. National Aeronautics and Space Administration (NASA). Retrieved from <https://www.giss.nasa.gov/tools/panoply/>

RStudio Team. (2016). RStudio: Integrated Development for R. RStudio, Inc., Boston, MA. <http://www.rstudio.com/>

Wickham, H. (2016). *ggplot2: elegant graphics for data analysis*. Springer.

Appendix 12. R Studio script for cumulative TDD calculations

The following script was used to calculate cumulative TDDs for specified days of a single given year from the “ERA5-Land hourly data from 1950 to present” (Copernicus Climate Services (C3S)).

```
#####==DOCUMENTATION==#####  
#Script written by: Casey Buchanan, MSc.  
#Source: https://cds.climate.copernicus.eu/cdsapp#!/dataset/reanalysis-era5-land?tab=overview  
#Dataset: “ERA5-Land hourly data from 1950 to present”  
#Dataset References:  
#Muñoz Sabater, J. (2021). ERA5-Land hourly data from 1950 to 1980 [data set]. Copernicus  
# Climate Change Service (C3S) Climate Data Store (CDS). Retrieved January 26, 2022, from  
# https://cds.climate.copernicus.eu/cdsapp#!/dataset/10.24381/cds.e2161bac?tab=overview  
#Muñoz Sabater, J., (2019): ERA5-Land hourly data from 1981 to present. Copernicus Climate  
# Change Service (C3S) Climate Data Store (CDS). Retrieved January 26, 2022, from  
# https://cds.climate.copernicus.eu/cdsapp#!/dataset/10.24381/cds.e2161bac?tab=overview  
  
#####==NOTES==#####  
#Total of 96456 observations  
#Observations 0-23 (i.e. the first full day; 2009-12-31) has all NaNs (later removed by script)  
#Observation 96456 (the last observation; first hour of 2021-01-01) has all NaNs (later  
#removed by script)  
  
#####==CUSTOM FUNCTIONS==#####  
#Function for cumulative TDDs up to a given date.  
TDDs=function(day){  
  integrate=vector()  
  for (i in DavgT[1:day,2]) {  
    if(i>0){integrate=c(integrate,i) }  
  }  
  tdds=sum(integrate)  
  return(tdds)  
}
```

```
#Function for creating a data frame containing chosen dates
#for cumulative TDD calculations.
```

```
TDDsTable=function(){
  x=readline("What days of the year would you like to
             calculate cumulative TDDs for? Format answer
             as '##,##,##,##,...'.")
  x=as.numeric(unlist(strsplit(x,",")))
  y=vector()
  for(i in x){
    z=TDDs(i)
    y=c(y,z)
  }
  output=data.frame("day"=x,"cumulativeTDDs"=y)
  return(output)
  rm(x,i)
}
```

```
#Function for exporting a .csv file of a data frame
#containing chosen dates and respective cumulative
#TDD calculations.
```

```
exportDF=function(df){
  exportname=readline("Write a file name. ")
  wd = getwd()
  path = paste0(wd,"/",exportname,".csv")
  write.csv(df,path)
}
```

```
#Function for exports .csv file containing cumulative TDDs
#for dates of interest.
```

```
exportDF2=function(){
  TDDs=function(day){
    integrate=vector()
    for (i in DavgT[1:day,2]) {
      if(i>0){integrate=c(integrate,i) }
    }
    tdds=sum(integrate)
    return(tdds)
  }
  TDDsTable=function(){
    x=readline("What days of the year would you like to
               calculate cumulative TDDs for? Format answer
               as '##,##,##,##,...'.")
    x=as.numeric(unlist(strsplit(x,",")))
    y=vector()
    for(i in x){
```

```

    z=TDDs(i)
    y=c(y,z)
  }
  output=data.frame("day"=x,"cumulativeTDDs"=y)
  return(output)
  rm(x,i)
}
df=TDDsTable()
exportname=readline("Write a file name. ")
wd = getwd()
path = paste0(wd,"/",exportname,".csv")
write.csv(df,path)
}

#####==SCRIPT==#####
#Imports the data file.
library(readxl)
data <- read_excel("2018 edited.xlsx", col_names = FALSE)
View(data)

#Formats data to a dataframe and adds longitude values column headers
data=data.frame(data); colnames(data)=seq(from=-139.0,to=-138.0,by=0.1)

#Removes NA rows.
id.nas = function() {
  i = 1; na.list=vector()
  while (i <= length(data[,1])) {
    if (is.na(data[i,1])) { na.list=c(na.list,i)
    }
    i = i+1
  }
  return(na.list)
  rm(i)
}
x=id.nas(); data=data[-x,]; rownames(data)=c(1:length(data[,1])); rm(x)

#Creates latitude labels for data
lat.list=seq(from=65.0,to=64.0,by=-0.1); i = 1; latitude=vector()
while (i <= 8760) { latitude=c(latitude,lat.list); i=i+1 }
latitude=as.numeric(latitude); data=cbind(latitude,data); rm(i)

#Labels the hour for each row in "data".
hour=rep(c(1:8760),each=11); hour=as.numeric(hour); data=cbind(hour,data)

#Creates temperature averages for each hour.
HavgT=data.frame(hour=1:8760); x=1; y=11; AvgHourlyTemps=vector(); i=1

```

```

while(i<=8760){matrix=as.matrix(data[x:y,3:13]); avg=mean(matrix);
AvgHourlyTemps=c(AvgHourlyTemps,avg); x=y+1; y=y+11; i=i+1 }
HavgT=cbind(HavgT,AvgHourlyTemps); Day = rep(c(1:365),each=24);
HavgT=cbind(Day,HavgT);
rm(avg,i,x,y,matrix)

#Finds the avg temperature of the min and max temperatures for each day
#and subtracts the freezing temp of water (273.15K) to get the number
#of thawing degree-days for each day.
DavdT=data.frame(day=1:365); x=1; y=24; TDD=vector(); i=1
while(i<=365) { working.temps=HavgT[x:y,3]; minimum=min(working.temps);
maximum=max(working.temps);
avg=mean(c(minimum,maximum)); tdd=avg-273.15; TDD=c(TDD,tdd); x=y+1; y=y+24;
i=i+1 }
DavdT=cbind(DavdT,TDD); rm(avg,i,x,y,minimum,maximum,working.temps,tdd)

#####==DATA EXPORT==#####
#Exports .csv file containing cumulative TDDs for dates of interest.
exportDF2()

```

References

- Muñoz Sabater, J. (2021). *ERA5-Land hourly data from 1950 to 1980* [data set]. Copernicus Climate Change Service (C3S) Climate Data Store (CDS). Retrieved January 26, 2022, from <https://cds.climate.copernicus.eu/cdsapp#!/dataset/10.24381/cds.e2161bac?tab=overview>
- Muñoz Sabater, J., (2019): ERA5-Land hourly data from 1981 to present. Copernicus Climate Change Service (C3S) Climate Data Store (CDS). Retrieved January 26, 2022, from <https://cds.climate.copernicus.eu/cdsapp#!/dataset/10.24381/cds.e2161bac?tab=overview>
- RStudio Team. (2016). RStudio: Integrated Development for R. RStudio, Inc., Boston, MA. <http://www.rstudio.com/>